UNIVERSIDADE FEDERAL DE PERNAMBUCO
CENTRO DE TECNOLOGIA E GEOCIÊNCIAS
DEPARTAMENTO DE OCEANOGRAFIA
PROGRAMA DE PÓS-GRADUAÇÃO EM OCEANOGRAFIA

DJOIRKA MINTO DIMOUNE

NEW INSIGHT OF THE WEST TROPICAL ATLANTIC CIRCULATION BASED ON 25 YEARS OF SATELLITE ALTIMETRY, PIRATA DATA AND GLORYS OCEAN REANALYSIS

Recife
2022

DJOIRKA MINTO DIMOUNE

NEW INSIGHT OF THE WEST TROPICAL ATLANTIC CIRCULATION BASED ON 25 YEARS OF SATELLITE ALTIMETRY, PIRATA DATA AND GLORYS OCEAN REANALYSIS

Thesis presented to the Post-graduate program in Oceanography at the Federal University of Pernambuco, as part of a requirement to obtain a doctorate in Science.

Research field: Physical Oceanography.

Supervisor: Prof. Dr. Moacyr Cunha de Araújo Filho.

Co-supervisor: Prof. Dr. Fabrice Hernandez.

Recife

2022

Catalogação na fonte
Bibliotecária Margareth Malta, CRB-4 / 1198

D582n Dimoune, Djoirka Minto.
New insight of the west tropical atlantic circulation based on 25 years of satellite altimetry, pirata data and glorys ocean reanalysis / Djoirka Minto Dimoune. - 2022.
220 folhas, il., gráfs., tabs.

Orientador: Prof. Dr. Moacyr Cunha de Araújo Filho.
Coorientador: Prof. Dr. Fabrice Hernandez.

Tese (Doutorado) – Universidade Federal de Pernambuco. CTG. Programa de Pós-Graduação em Oceanografia, 2022.
Inclui Referências e Apêndice.
Texto em Inglês.

1. Oceanografia. 2. Atlântico tropical oeste. 3. Variabilidade sazonal e interanual das correntes. 4. Rotacional do vento. 5. Modo climático do Atlântico. 6. Correntes geostróficas da altimetria. 7. Reanálise GLORYS12V1. I. Araújo Filho, Moacyr Cunha de (Orientador). II. Hernandez, Fabrice. (Coorientador). III. Título.

UFPE

551.46 CDD (22. ed.) BCTG/2022-77

DJOIRKA MINTO DIMOUNE

NEW INSIGHT OF THE WEST TROPICAL ATLANTIC CIRCULATION BASED ON 25 YEARS OF SATELLITE ALTIMETRY, PIRATA DATA AND GLORYS OCEAN REANALYSIS

Thesis presented to the Post-graduate program in Oceanography at the Federal University of Pernambuco, Center of Technology and Geoscience, as part of a requirement to obtain a doctorate in Science, in the research field of Physical Oceanography

.

Evaluated on: January 27, 2022

EXAMINATION COMMISSION

_____
Prof. Dr. Fabrice Hernandez (Co-supervisor)
Institute of Research for Development

_____
Prof. Dr. Alex Costa da Silva (Internal examiner)
Federal University of Pernambuco

_____
Prof. Dr. Carmen Medeiros Limongi (Internal examiner)
Federal University of Pernambuco

_____
Prof. Dr. Agré Kousso Sandrine Djakouré (External examiner)
Felix Houphouet-Boigny University

_____
Prof. Dr. Bernard Bourlès (External examiner)
Institute of Research for Development

Aos

Meu pai, Djoirka Dimoune, que nunca viu essa aventura,

minha mãe, Poubiki Douti,

minha noiva, Angèle Midrah,

meus irmãos, Kouassoube Dimoune e Wenpo Dimoune,

pelo amor e apoio que recebi durante todo esse período de aprendizado

ACKNOWLEDGMENTS

À Deus que, a quem devo a saúde e a força que me permitiram concluir esta tese.

À minha mãe, minha noiva e meus irmãos, pela presença deles na minha vida, e principalmente pelo apoio recebido ao longo desse período de tese.

Aos meus orientadores, Prof. Dr. Moacyr Araujo e Dr. Fabrice Hernandez, pelas suas orientações, confiança, incentivo e apoio ao longo desse período.

À Dra. Florence Birol e ao Sr. Fabien Leger, pela colaboração, confiança, e conselhos durante minha visita no LEGOS e depois. Meus sinceros agradecimentos também ao Dr. Gerard Eldin, pela colloboração.

À CAPES e à CAPES-Print, pela concessão de bolsa de Doutorado aqui no Brasil (Processo 88882.379448/2019-01), e na França durante a realização do Estágio de Doutorado "Sanduiche" (Processo 88887.467360/2019-00), realizado no Laboratoire d'Etudes en Géophysique et Océanographie Spatiale – LEGOS, Toulouse, France. Meus agradecimentos também ao LEGOS, que me recebeu e me deu todo o apoio que necessitava.

Aos Prof. Dr. Jesser Fidelis e Profa. Dra. Mônica Fereira, coordenadores do PPGO-UFPE, pelas suas disponibilidades de sempre ajudar.

Aos Laboratoire Mixte International TAPIOCA – LMI-TAPIOCA, e Institut de Recherche pour le Développement – IRD, pelo apoio.

Aos professores de DOCEAN, que me ensinaram muito sobre suas respectivas disciplinas, e pelos seus conselhos. Um agradecimento também ao Dr. Marcus Silva pela collaboração.

Aos meus amigos do CEERMA e do LOFEC, Nathanaël Dossa, Aubains Hounsou-gbo, Humberto Varona, Carlos Noriega, Ramila Assunção, Paulo, Everton, Isabelle, Syumara, pelo companheirismo e amizade ao longo desses anos. Um agradecimento especial ao amigo Nathanaël Dossa, com quem aprendi muito ao longo desse periodo de tese.

Aos funcionários do CEERMA e do DOCEAN pela amizade e ajuda, especialmente aos Sra. Claudia von Shosten, Dra. Fabiana Soares, Dr. Leonardo Bruto e Sra. Izabele Cabral.

Finalmente, minha sincera gratidão a todos(as) aqueles(as) que, de uma forma ou de outra, ajudaram para a realização deste trabalho.

ABSTRACT

The western tropical Atlantic is one of the most dynamic regions of the whole ocean where most of the zonal currents flows transporting water masses with salt and heat. Its importance is mostly due to its interactions with atmosphere which influence the regional climate and the precipitations of the region. During this thesis, the main goal was to take advantage of the larger dataset of the altimetry-geostrophic currents and the GLORYS12V1 (G12V1) reanalysis available over the 1993-2017 period to revisit the western tropical Atlantic circulation and improve the knowledge about the spatiotemporal variability of the currents at the seasonal and interannual timescales. To do so, 9 sections crossing the currents were used to follow the evolution of the currents and the redistribution of the water masses. Data from Ship-mounted acoustic Doppler current profiler (SADCP) and near-surface drifter were used to prove the effectiveness of the G12V1. From both the altimetry-geostrophic currents data and the G12V1 reanalysis we found 2 different behaviours of the North Brazil Current (NBC) strength. In the southern hemisphere, the NBC depicts an annual cycle with a maximum (minimum) amplitude/transport during boreal spring (fall) while in the northern hemisphere, its cycle reverses. During boreal spring, the southward recirculation of the northern branch of the South Equatorial Current (nSEC) joins the weak NBC retroflected branch (rNBC) to feed a surface eastward flow along the equatorial region and to generate a cyclonic circulation between 0°-5°N, 35°W-45°W. The volume transport of the NBC in the upper layer (0-100 m) shows an equatorial retroflection of 1.8 Sv joining the weak flow from the rNBC-nSEC (4.6 Sv) to maintain this cyclonic circulation. From September to December, the NBC shows another retroflection region in the upper layer between 4-6°N which is particularly intense in October. During boreal fall, the upper rNBC connects to the North Equatorial Countercurrent (NECC) which shows a two-core structure, and eventually 2 separated branches from November to the first half of the year. The seasonal variability of the transport/amplitude/core location of both branches and the currents in the northern hemisphere respond to the remote wind seasonal changes in the eastern basin. The higher contribution of the rNBC to the NECC occurs during boreal fall with an input of 15.2 Sv. In the thermocline layer (100-350 m), the higher contribution to the Equatorial Undercurrent (EUC) occurs during boreal spring and fall (22.3 Sv and 20 Sv, respectively) when the contribution of the northern hemisphere waters to the rNBC is also higher. The investigation of the year-to-year variations of the altimetry-geostrophic currents crossing the 9 sections (amplitude and core velocity/location) show that

the interannual variability of the NECC amplitude/location and the nSEC amplitude at 42°W might be associated to the Atlantic meridional mode (AMM) phases whereas it is associated to the zonal mode (AZM) phases at 32°W. Unlike, the interannual variability of the NECC transport at 38°W and of the surface equatorial eastward flow amplitude at 32°W appears to be associated to both modes.

Keywords: western tropical Atlantic; seasonal and interannual variability of the currents; wind stress curl; Atlantic climate modes; altimetry-geostrophic currents; GLORYS12V1 reanalysis.

RESUMO

O Atlântico tropical oeste é uma das regiões mais dinâmicas de todo o oceano, para onde a maioria das correntes zonais vão, transportando massas de água e calor. A sua importância deve-se principalmente às suas interações com a atmosfera, que influenciam o clima regional e as precipitações das regiões circundantes. O principal objetivo dessa tese foi aproveitar o maior banco de dados das correntes derivadas da altimetria e das reanálises GLORYS12V1 (G12V1) disponíveis durante o período 1993-2017 para revisitar a circulação na região oeste do Atlântico tropical e aprofundar o conhecimento sobre a variabilidade espaço-temporal das correntes nas escalas sazonal e interanual. Para tal, foram utilzadas 9 secções transversais das correntes a fim de avaliar a evolução da circulação e a redistribuição das massas de água. Os dados de correntes obtidos de SADCP (Ship-mounted acoustic Doppler current profiler) e de derivadores foram utilizados para comprovar a acurácia do reanálise numérica G12V1. Ambos os dados da altimetria e do reanálise numérica mostram dois comportamentos diferentes da Corrente Norte do Brasil (CNB). No hemisfério sul, o transporte/amplitude da CNB mostra um ciclo anual com um máximo (mínimo) durante a primavera boreal (outono) enquanto no hemisfério norte, o seu ciclo inverte-se. Na primavera boreal a recirculação do ramo norte da Corrente Sul Equatorial (nCSE) para o sul junta-se com o fraco ramo retroflectado da CNB (rCNB) para alimentar uma corrente da superfície para leste ao longo da região equatorial e gerar uma circulação ciclônica entre 0°-5°N, 35°W-45°W. O transporte da CNB na camada superior (0-100 m) durante a primavera boreal indica uma retroflexão equatorial da CNB com 1,8 Sv juntando ao fluxo da rCNB-nCSE (4,6 Sv) para manter esta circulação ciclônica. De Setembro até Dezembro, a CNB mostra na camada superior uma outra região de retroflexão entre 4°-6°N que é particularmente intenso em Outubro. Durante o outono boreal, a rCNB da camada superior conecta-se a Contracorrente Norte Equatorial (CCNE) que presenta uma estrutura com dois núcleos, e até mesmo dois ramos separados no final do ano. A variabilidade sazonal do transporte/amplitude/localização do núcleo de ambos os ramos e das correntes no hemisfério norte é influenciado pela variabilidade sazonal do vento remoto na bacia oriental. A maior contribuição da rCNB para a CCNE ocorre durante o outono boreal (15,2 Sv). Na camada inferior (100-350 m), a maior contribuição para a Subcorrente Equatorial (SCE) ocorre durante a primavera e o outono boreais (22,3 Sv e 20 Sv, respectivamente) quando a contribuição das águas do hemisfério norte para a rNBC está também maior. A investigação das variações interanuais das correntes derivadas da altimetria (amplitude/localização do núcleo) mostra que

a variabilidade da amplitude/localização da CCNE e da amplitude da nCES a 42°W está associada às diferentes fases do modo de variabilidade meridional do Atlântico tropical (AMM) enquanto está associada às fases do modo zonal (AZM). Ao contrário, a variabilidade interanual do transporte da CCNE a 38°W e da amplitude da corrente equatorial da superfície para o leste está associada a ambos os modos.

Palavras-chave: Atlântico tropical oeste; variabilidade sazonal e interanual das correntes; rotacional do vento; modo climático do Atlântico; correntes geostróficas da altimetria; reanálise GLORYS12V1.

LIST OF FIGURES

ARTICLE 1

ARTICLE 2

TABLES LIST

ARTICLE 1

ARTICLE 2

LIST OF ABBREVIATIONS

ADCP	Acoustic Doppler Current Profilers
ADT	Absolute Dynamic Topography
ACM	Atlantic Climate Modes
AOML	Atlantic Oceanographic and Meteorological Laboratory
AMM	Atlantic Meridional Modes
AMO	Atlantic Multidecadal Oscillation
AMOC	Atlantic Meridional Overturning Circulation
AZM	Atlantic Zonal Mode
CASCADE	Chaîne Automatisée de Suivi des Courantomètres Acoustiques Doppler Embarqués
CEOF	Complex Empirical Orthogonal Function
CMEMS	Copernicus Marine Environment Monitoring Service
cSEC	Central branch of the South Equatorial Current
CTD	Conductivity Temperature Depth
DOCEAN	Departamento De Oceanografia
ECI	Echo Intensity
ECMWF	European Centre for Medium-Range Weather Forecast
EKE	Eddy Kinematic Energy
ENSO	El Niño-Southern Oscillation
EOF	Empirical Orthogonal Function
eSEC	Equatorial branch of the South Equatorial Current
EUC	Equatorial Undercurrent
GDP	Global Drifters Program
GPS	Global Positioning System
GLORYS	Global Reanalysis
IES	Inverted Echo Sounders
IL/ILD	Isotherm Layer/Isotherm Layer Depth
ITCZ	Intertropical Convergence Zone
KWs	Kelvin Waves

LPO	Laboratoire de Physique de Océans
LTA	Long-term Averaged Files
ML/MLD	Mixed Layer/Mixed Layer Depth
NAO	North Atlantic Oscillation
NBUC/NBC	North Brazil Undercurrent/North Brazil Current
NBCR	North Brazil Current Retroflection
NECC	North Equatorial Countercurrent
NH	Northern Hemisphere
nNECC	Northern branch of the North Equatorial Countercurrent
NEUC	North Equatorial Undercurrent
nNBCR	Northern branch of the North Brazil Current Retroflection
NOAA	National Oceanic and Atmospheric Administration
NRT	Near Real Time
nSEC	Northern branch of the South Equatorial Current
PGOOD	Percentage of Good Data
PIRATA/PIRATA-BR	Prediction and Research Moored Array in the Tropical/ Prediction and Research Moored Array in the Tropical – Brazil
PPGO	Programa de Pós-graduação em Oceanografia
PW	Petawatt
rNBC	Retroflected branch of the NBC
RWs	Rossby Waves
SADCP	Ship-mounted Acoustic Doppler Current Profilers
SLP	Sea Level Pressure
SEC	South Equatorial Current
SEUC	South Equatorial Undercurrent
SH	Southern Hemisphere
sNBCR	Southern branch of the North Brazil Current Retroflection
sNECC	Southern branch of the North Equatorial Countercurrent
SSH	Sea Surface Height
SSS	Sea Surface Salinity

SST	Sea Surface Temperature
STA	Short-term Averaged Files
SVP	Surface Velocity Program
TA	Tropical Atlantic
TIWs	Tropical Instabilities Waves
VmDAS	Vessel-mounted Data Acquisition System software
WAF	West African Monsoon
WB	Western Boundary
WBS/WBSC	Western Boundary Surface /Western Boundary Surface Circulation
WS/WSC	Wind Stress /Wind Stress Curl
WTA/WTNA	Western Tropical Atlantic/Western Tropical North Atlantic

LIST OF SYMBOLS

A_h	Horizontal friction coefficient of the ocean water
A_v	Vertical friction coefficients of the ocean water
C_D	Drag coefficient at the ocean surface
ECI	Mean echo intensity of the ADCP
f	Coriolis parameter due to the Earth's rotation
g	Gravitational acceleration of the Earth
p	Pressure of the ocean water
R_t	Radius of the Earth
U	Zonal wind velocity components
u	Zonal component of a particle of water
$\underline{U_f}$	Velocity of the oceanic current
ug	Zonal component of the geostrophic current
V	Meridional wind velocity components
v	Meridional component of a particle of water
vg	Meridional component of the geostrophic current
W	Wind speed
β	Rossby parameter
Δσ	Variation of the density corresponding to a given variation of temperature in the surface layer.
ΔT	Variation of the temperature in the surface layer
ρ	Density of ocean water
ρ_{air}	Density of air
τ_s	Wind speed at the surface
ζ_x	Zonal component of the wind stress
ζ_y	Meridional component of the wind stress

CONTENTS

1 MOTIVATION AND OBJECTIVES

The tropical Atlantic (TA) is the place of a dynamic ocean-atmosphere interaction, multiples interactions between the oceanic currents, and phenomena such as the waves propagations, and mesoscale activities. Its western boundary circulation surface (WBSC) contributes to the return branch of the global thermohaline circulation so-called the Atlantic meridional overturning circulation (AMOC) and the wind-driven subtropical cells (Lumpkin and Speer, 2003; Hazeleger and de Vries, 2003; Hazeleger et al., 2003, Schott et al., 2004, 2005; Brandt et al., 2016), which connects the southern warm surface waters to the northern hemisphere, crossing the TA (Gordon, 1986). North of 10°S, the WBSC is represented by the North Brazil Undercurrent/North Brazil Current (NBUC/NBC) system which flows northward along the Brazilian coast and is primarily fed by the northern branch of the wind-driven southern subtropical gyre which is the South Equatorial Current (SEC) (Rodrigues et al., 2007). This NBUC/NBC system is one of the most powerful tropical western boundary currents system in the world Ocean. It almost feeds all the eastward currents of the upper-thermocline and below. As part of the return branch of AMOC, it exchanges mass, salt and heat, especially in the surface layers, and affects directly the heat content of the mixed layer in the entire TA basin through the eastward North Equatorial Countercurrent (NECC) (Philander and Pacanowski, 1986), and indirectly the precipitations together with the winds (Foltz et al., 2012).

The western boundary surface (WBS) circulation in the entire TA includes all the multiples surface currents flowing (Figure 1) and can be subdivided in three areas relatively to the dynamics and the singularities of each of them. These areas are: the equatorial area between 2°S and 2°N, the western boundary near to the Brazilian coasts, and the rest of the area outside of the first two areas.

The dynamics of the first area is considered as the more complex due to the Coriolis force which is too smaller and almost null making the geostrophic balance difficult for use there. The main current flowing is the Equatorial Undercurrent (EUC) which has its core in the thermocline layer, with a core mean position located about 100-m depth (Hormann and Brandt, 2007; Brandt et al., 2016). It is supplied by the NBC retroflection (NBCR) (Schott et al., 1995, 1998; Bourlès et al., 1999a, Goes et al., 2005). The second area is the area close to the south America coast, where the main current flowing is the NBC which is the more intense surface current in the TA, and is

partly formed by the NBUC. The third area is composed by the central branch of the SEC (cSEC), which also contributes to the formation of the NBC approximately at 5°S. North of the equator, the northern branch of SEC (nSEC) also connects with the NBC to strengthen him. At the northern flank of nSEC, the NECC flows in the opposite direction and penetrates into the Gulf of Guinea at approximately 10°-15°W (Lumpkin and Garzoli, 2005). It is partly fed by at its western side by the NBCR. Below the upper-thermocline, there are two symmetric eastward currents flowing: the North Equatorial Undercurrent (NEUC) and the South Equatorial Undercurrent (SEUC) (Castellanos et al., 2015). They are respectively fed by partly the NBCR and by a mixture of NBUC and the interior recirculation of the SEC (Schott et al., 2004; Dossa et al. 2020).

The three areas are characterized by an intense mesoscale activity and waves propagations which participate to the dynamic of the entire TA and explain the large mesoscale energy which induces the intraseasonal variability of the currents in these areas, especially in the western boundary (WB) (Johns et al., 1990, 1998; Didden and Schott, 1993, Schott et al., 2003). The mesoscale activities are characterized by eddies generations and propagations due to barotropic and/or baroclinic instabilities, or other processes such as the NBC retroflection imbalance or waves reflection (Johns et al., 1990; Ma, 1996; Not and Pichevin, 1996; Aguedjou et al., 2019). They contribute to the nonlinear terms in the vorticity balance west 32°W in the northern TA (Verdy and Jochum, 2005). One of the important mesoscale features of the WB is the NBC rings (e.g., Jochum and Malanotte-Rizzoli, 2003) which contributes to an important northward transfer of the heat through the volume transport of the return branch of the AMOC. About 22% of the total volume transport were found by Fratantoni et al. (2000). The waves which propagate in the TA are mostly the eastward equatorial Kelvin waves (KWs), the westward planetary waves (Rossby waves), and the tropical instabilities waves (TIWs). The KWs are generated by the thermocline oscillation due the weakening/strengthening of the trade winds west of the basin. They reflect to the western coast of Africa, become the coastal KWs, and later the downwelling Rossby waves (RWs), which deepen the thermocline in the WB and favour an increase of the NECC transport in the upper-thermocline (Garzoli and Katz, 1983; Fonseca et al., 2004). The RWs found in the TA basin are generally of the three first baroclinic modes and are captured by the anomalies of the sea surface height (SSH) (Schouten et al., 2005). In the equatorial region, the tropical instabilities waves (TIWs) are generated by the barotropic instability of the horizontal shear between the nSEC and the NECC

and/or the vertical shear between the nSEC/cSEC and the EUC (Jochum et al., 2004; von Schuckmann et al., 2008, Athié and Marin, 2008, Foltz et al., 2020).

All these aspects of the TA dynamics mentioned above justify the complexity of its circulation and mostly of its surface circulation. The trade winds play a key role on its variabilities and drive the whole surface circulation starting from the subtropical gyres. In the upper layer, they influence the mixed layer depth (MLD) and create a complex interdependence relationship between the ocean and atmosphere by the exchanges through their common thin interface layer. This layer is characterized by a Sea Surface Temperature (SST) and a Sea Surface Salinity (SSS) which vary seasonally. The exchanges between the warmer mixed layer (ML) and atmosphere are one of the causes of the precipitations in the TA and the surrounding regions, and affect even the regional climate which is controlled by the tropical Atlantic meridional (AMM) and zonal (AZM) modes (Foltz and McPhaden, 2006, 2010; Foltz et al., 2012; Hounsou-gbo et al., 2015, 2016).

Over the past few years, several studies have been conducted to understand the spatial and temporal variabilities of the currents of the TA, and explain the mechanisms driving these variabilities, especially in the western TA (WTA). Despite the research efforts, there are still many questions regarding the circulation that need to be answered. The main questions that motivated this thesis are: How does the NBC behave in both sides of the equator? What is the proportion of the NBC in the other surface currents or vice versa? How do the trade winds and waves propagation affect the seasonal variabilities of the different surface currents? And what relationship can exist between their interannual variability and the tropical Atlantic climate modes (ACM)?

These questions have been motivated by the previous studies carried out. For example, concerning the NBC variability, many studies showed that, approximately at 5°S, the NBC appears as the merging of the NBUC which contributes to approximately 15-20 Sverdrup (Sv), and the cSEC, which increases the NBC transport to an annual mean of 32 Sv in the upper 600m before reaching the equator (Stramma, 1991; Stramma et al., 1995; Schott et al., 1993, 1995, 2005). Using the shipboard profiling sections and short period of currentmeters data, it has been also shown that, south of the equator the NBC transport follows an annual cycle of small variations (±3-4 Sv) (e.g. Stramma et al., 1995; Bourlès et al., 1999b), with a maximum transport during June-August and minimum during December-February. The investigations showed that only less than third of the total transport occurs in the upper-thermocline. Unlike, north of the equator, Johns et al. (1998), using two years of current meter observations at ~4°N, showed that the NBC transport has an

annual cycle which reaches a maximum during July-August (36 Sv) and a minimum during April-May (13 Sv). They found that, at this location the mean transport is dominated by the flow in the upper 150 m and is driven by the remote winds forcing while the increase in the total transport is explained by the thermohaline component of the flow. Before 4°N, Garzoli et al. (2004) used inverted echo sounders (IES) and pressure Gauge data approximately at 2°N to investigate the NBC variability and also showed a different result. The authors couldn't find a strong annual cycle like described by John et al. (1998). However, they found an increase of transport ranging from ~6 Sv in May to ~20 Sv during August-October. They also found a secondary minimum in July and explained the differences in strength and variability of the NBC with Johns et al. (1998) by the difference in locations or a small period during which the data overlap twice. These different results raise questions about the variability of the NBC on its pathway and motivate our will to deepen the understanding of its seasonal variability.

On its way to the north, the NBC undergoes seasonally a retroflection during which a cyclonic ring is shed, transporting the warm water of AMOC to the north. Garzoli et al. (2003) found that, annually, these rings transport 8 Sv of warm waters and an equivalent of 0.54 Petawatt (PW) heat to the north. The NBC retroflected branch (rNBC) toward the east partly feeds the NECC which is the largest and strongest zonal surface current in TA and contributes to the variability of this latter. The studies made in the last few years about the NECC variabilities have proposed different latitudinal coverage for the NECC going from 3°N to north of 13°N. Richardson and McKee (1984) used historic ship drift data and show that the NECC is located between 3°-10°N. Garzoli and Richardson (1989) and Garzoli (1992) used the IES installed at 28°W and 38.5°W and found that the NECC is located between 3°N and 9°N. More recent studies of Urbano et al. (2006, 2008) who used modelling and some sections of direct velocity measurements available at respectively 35°W and 38°W showed that the NECC could extend up to 13°N. They also confirmed a particular two-core/branch structure of the NECC, specific to the tropical Atlantic in the upper-thermocline, which has been mentioned previously by Schott and Böning (1991), Didden and Schott (1992) and Stramma et al. (2005). Urbano et al. (2006, 2008) are the first to investigate the existence of the secondary core to the north and have showed that the two cores are wind-driven and are the result of the finite width of the intertropical convergence zone (ITCZ). The seasonal variability of the NECC transport have been investigated in the region limited by 30°–45°W and 2°–12°N by Fonseca et al. (2004) who used hydrographic and altimetry data from 1993 to 2000

and showed that it follows an annual cycle with maximum strength of 12 Sv during boreal fall (October-November). This annual cycle was explained by the influence of the remote wind stress curl (WSC) strength which peaks in August, 1-3 months before the peak of the NBC transport found by Johns et al. (1998). The delay was found consistent with the expected time delay of the RWs propagation at this latitude, and with Garzoli and Katz (1983). The model results of Urbano et al. (2006) at 35°W showed that the total transport of the NECC is approximately in Sverdrup balance and only 60% of this transport is above the thermocline. They found that the seasonal changes in the wind stress curl lead the transport expected by applying the Sverdup balance, by one month. They showed that the time delay found corresponds to the time necessary to the first mode baroclinic RWs to cross the TA, propagating from the Africa coast to 35°W. Investigating the core positions of the NECC, Fonseca et al. (2004) and Urbano et al. (2008) found two northward migrations of the NECC, and showed that these migrations throughout the year were driven by the local winds. With regards to all these studies about the seasonal and spatial variability of the NECC vertical structure, and its transport which have been investigated with short period of data, there are still some aspects that need to be deepened like: the particularities of its changes at different locations of the western tropical north Atlantic (WTNA), the spatial and temporal variability of its cores, and the mechanism which can influence the changes at different locations.

The seasonal variability of the nSEC and cSEC have received less attention in the TA, and few studies have mentioned the presence of an equatorial branch of the SEC (eSEC) flowing near to the equator if it does exist (Stramma and Schott, 1999; Schott et al., 2004; Lumpkin and Garzoli, 2005). Few studies have been carries out and showed that both the cSEC and the nSEC are wind-driven. Using the Argo-inferred velocities from November 2007 to up to September 2013, Rosell-Fieschi et al. (2015) have shown that the annual mean of the surface currents is dominated in the equatorial region by the cSEC and nSEC. Their study showed that the cSEC follows an annual cycle with a maximum (minimum) in May-June (October-November) while the nSEC follows a semi-annual cycle intensified during boreal summer and early winter. The latter core position is located between 1°N and 2°N, and migrates northward in spring when the NECC is weak or almost disappeared. So far, the volume transport of both nSEC and cSEC have been computed from few individual sections of observations data, but the seasonal variability is still weakly documented, and is one of the aspects that motivates this study.

The studies of the EUC variability in the TA showed a strong semi-annual cycle mainly driven by the wind field over the whole basin, and its transport maxima is reached in boreal spring and fall (Hormann and Brandt, 2007; Urbano et al., 2008; Brandt et al., 2016). It has been mentioned by Hisard and Hénin (1987) the presence of an eastward currents which can reach a velocity of 50 cm/s above the EUC, and is difficult to be captured by the current profilers because it is shallower. Bourlès et al. (1999b) using acoustic Doppler current profiler (ADCP) section west of 44°W also confirm a presence of a weak eastward flow above the EUC. However, this eastward flow remains poorly documented because of the difficulty to be captured in the shipboard profiling sections. The results of the altimetry and improvement of the recent years to capture well the surface circulation and reduce the errors of measurements and calculations, especially in the equatorial region can be helpful for this investigation and is one of the hopes in the investigation of the near-surface currents of this study.

With regard to the interannual variability of the surface currents in the WTA, few studies have been conducted so far, certainly due to the short period of observational data that doesn't allow to have significant results. Nevertheless, because the year-to-year variations observed with the currents, some investigations have been initiated. Most of them which have been conducted to date focus on the NECC. For example, Hormann et al. (2012) used seventeen years of geostrophic currents from altimetry in the NECC region to investigate the interannual variability of this latter in relation to the AMM and AZM. From the complex empirical orthogonal function (CEOF) decomposition of zonal geostrophic velocity, the authors conclude to the relationships between the NECC's strength and the AZM, and between the NECC's core position and the AMM.

The purpose of this thesis is to take advantage of fifteen 38°W ADCP sections from the Prediction and Research Moored Array in the Tropical Atlantic program cruises maintained by Brazil (PIRATA-BR) and the CAMADAS FINAS program cruise held in 2012, GLORYS12V1 (G12V1) reanalysis which is assimilated with many observational data of the global ocean and available from 1993 to 2018 with a spatial resolution of 1/12°. and 25 years of altimetry-geostrophic derived currents data from 1993 to 2017, with a spatial resolution of 1/4° to revisit the seasonal and interannual variability of the surface currents of the WTA.

The approach to achieve our objectives will be as follows:

- Define sections crossing all the currents in order to analyze the variabilities of the cross-currents to these latter.

- Use the 38°W ADCP section from PIRATA and the climatology of the near-surface currents from drifters to reassess the consistency of G12V1 reanalysis, already proven in the other regions of the Atlantic; and investigate with G12V1 to the seasonal and interannual variability of the two-core structure of the NECC in relation to winds and the tropical Atlantic modes;
- Then, use the altimetry-geostrophic currents to analyze the spatial and the temporal variabilities of the characteristics of all the upper layer currents of WB (amplitude, core velocity and core position) by using six (06) selected sections crossing the currents out of the equatorial region; and propose an updated seasonal circulation map of the surface circulation.
- And, use the 3D G12V1 reanalysis to deepen the understanding of WBC by analyzing the vertical structure of the cross-currents of all the sections defined, their associated volume transport in both the upper and thermocline layers, and propose a seasonal map of the NBC contribution to the other currents and vice versa.

This manuscript is organized as follows: the next chapter presents the general aspects of the TA dynamics. The study area and data analysis follow, to present the different sections used to study the surface currents, the data used and their analysis. Chapter 4 is dedicated to the assessment of G12V1 realism in the WTNA comparing with near-surface drifters' monthly climatology and the ADCP data at 38°W section; and the investigation of the NECC variability at this section. The following chapter is dedicated to the seasonal and interannual variability of the WB currents using the altimetry-derived current data over 1993-2017 period and the selected cross-sections of the currents. It is followed by the study of the WB currents seasonal variability using the G12V1 reanalysis over the 1993-2018 period to analyze the vertical structure and the transport of the currents, and complement the study of the previous chapter. Finally, the chapter 7 provides a synthesis of the thesis work and conclusions before to give some perspectives.

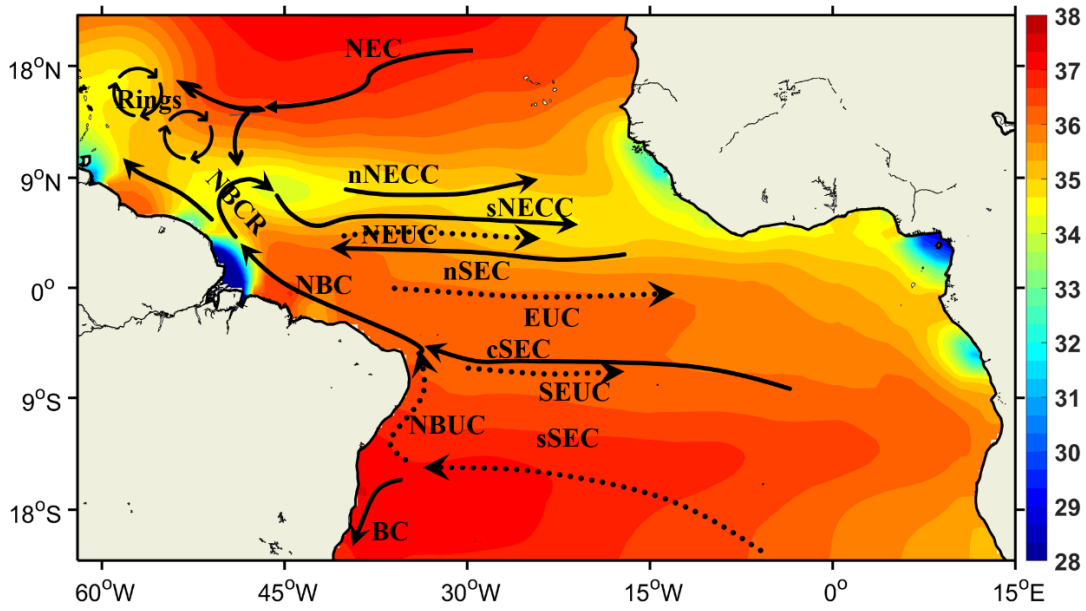

Source: The author (2022).

Figure 1. Upper and thermocline layers currents (respectively thick solid and dashed black lines) in the western tropical Atlantic based on John et al. (1990), Schott et al. (2004) and Halm et al. (2017): North Equatorial Current (NEC), North Equatorial Undercurrent (NEUC), North Equatorial Countercurrent (NECC), its northern branch (nNECC), Equatorial Undercurrent (EUC), southern, northern and central branches of the South Equatorial Current (sSEC, nSEC, cSEC), North Brazil Undercurrent (NBUC), North Brazil Current and its retroflection (respectively, NBC and NBCR), the rings shed during the NBCR; and Brazil Current (BC). The currents are superimposed on the September-October-November mean of the CORA Sea Surface Salinity (SSS) reanalysis (INSITU_GLO_TS_OA_REP_OBSERVATIONS_013_002_b product) made available by Copernicus Marine Service (CMEMS at https://resources.marine.copernicus.eu/products) over 1993-2018 period.

2 GENERAL ASPECTS OF THE TROPICAL ATLANTIC

The Tropical Atlantic (TA) dynamics in the surface layers is part of the complex ocean-atmosphere dynamics which involves the interactions between the ocean and atmosphere and affects the regional climate. This ocean dynamics is maintained by the northeast and the southeast trade winds which blow toward the western basin and are responsible for the movement of the water masses in the surface layers through the surface currents which are the main components of the dynamics. During the displacements of the water masses, they can mix, change density, the heat content; and generally, create the barotropic or baroclinic instabilities. The trade winds are also responsible of the accumulation of water in the western boundary (WB) of the TA, which generally affects the sea level gradient and deepens the thermocline and the mixed layer (ML) in the WB. The changes of the wind regime and the shear between the currents are responsible of the generation and propagation of waves in the surface layers. The surface layers which are constantly interacting with the atmosphere are impacted and undergoes changes that are reflected on the sea surface temperature (SST) and the sea surface salinity (SSS) pattern which can be indicators of the regional climate changes.

In this chapter, we are going to introduce the variability of the components which are part of the ocean-atmosphere dynamics in the TA and remind the main equations which gouvern the ocean circulation. We will also introduce the two climate modes of the TA in order to understand the ocean-atmosphere mechanisms which maintain these modes.

2.1 VARIABILITY OF THE TRADE WINDS IN THE TROPICAL ATLANTIC

The winds blowing in the TA are exclusively the trade winds which are characterized by a strong seasonal variability. They are directed from semi-permanent high atmospheric pressures of south Atlantic (Saint Helena High centered approximately at 25°S of latitude) and of the north Atlantic (Azores high centered approximately at 30°W) to the low atmospheric pressure located between both high-pressure zones and are deviated to the west under the influence of the Coriolis force. In the northern and southern hemispheres (NH and SH, respectively), they are called respectively the northeast and southeast trade winds and are components of the Hadley cells. They are generated by the pressure gradients between the areas of high pressure (~30° latitude) and low

pressure (around the thermal equator), and creates on both side of the latter area the north-south and south-north cycling Hadley cells respectively, in the southern and northern hemisphere (Wallace and Hobbs, 1977). The low-pressure area is also known as the intertropical convergence zone (ITCZ) where trade winds converge and rise up into the atmosphere with warm and humid air. The strengthening (weakening) of the trade winds during the year is due the southernmost (northernmost) position of the high atmospheric pressure zones in both hemisphere (Peterson and Stramma, 1991).

The ITCZ is usually used as the main markers of the seasonal variability of the trade winds in the TA and the convective activities related to him due the rise up of warm and humid air as mentioned above generate cumulonimbus cells in altitude when cooling, and precipitations over large areas surrounding its position. Both the seasonal changes of its latitudinal position from south to north and vice versa, and the strength and direction of the trade winds in both hemispheres are the result of the solar heating, the continental land masses and the circulation of winds in a vertical plane in the atmosphere.

During the boreal fall-winter (spring-summer), the ITCZ shifts southward (northward) when the trade winds are strengthening (weakening) in the northern hemisphere and weakening (strengthening) the southern hemisphere. The southernmost position of the ITCZ is located between the equator in the western part of basin, and approximately at 5°N in the eastern part (Figure 2) in February-March. It reaches its northernmost position in July-August between 8°-12°N at the surface of the ocean and is framed throughout the year by two zero lines of the wind stress curl (WSC) in both side the equator.

The two zero lines of the WSC are characterized by a transition zone between opposite sign of the WSC (Figure 2). In the NH, the zero-line varies between the positive WSC north of the ITCZ and the negative WSC further north. It seems to follow the same latitudinal movement of the ITCZ, with the southernmost (northernmost) position at approximately 10°-12°N (15°-20°N) in western side of the basin, and 20°-22°N (up to 22°N) in the eastern side of the basin during boreal winter-spring (summer-fall) due to the strengthening (weakening) of the northeast trade winds. Unlike, in the SH, the zero line of the WSC position varies less in the eastern side of the basin but leads the ITCZ by one to two months in the central part of the basin and varies between 5°-20°S (Rodrigues et al., 2007). Near to the Brazilian coast, because of the obstacle that the continent represents to the winds, the inclination of the coastline in relation to the southeast trade winds, and the variabilities

of the atmospheric pressure on the continent, the variability of this position during the year differs from that of the northern hemisphere, going from the northernmost position during boreal winter to the southernmost position during the boreal spring/summer (Rodrigues et al., 2007).

Together the ITCZ and both zero line of the WSC which represent the variability of the wind regime in both sides of the equator in the TA, and of the local wind forcing are usually used to explain the spatial and temporal variability of the currents and the TA dynamics (Johns et al., 1998; Fonseca et al., 2004; Rodrigues et al., 2007; Urbano et al., 2006, 2008).

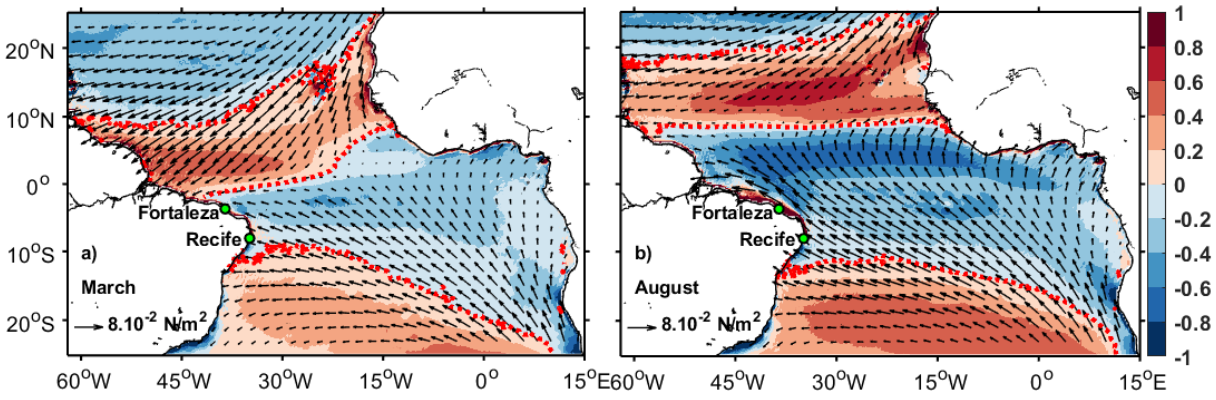

Source: The author (2022).

Figure 2. Monthly climatology (1993-2018) of the wind stress (WS) superimposed on the wind stress curl (WSC) in March (a) and August (b). The colorbar of the WSC is in 10^{-7} N/m^3. The dotted red lines are the zero lines of the WSC, and the ITCZ is the centered one.

2.2 EQUATIONS OF THE OCEAN SURFACE CIRCULATION

In the TA, large-scale anticyclonic wind-driven circulations are centered near 20°-30° latitude and are generated by the water pressure gradients difference in the northern and southern subtropical Atlantic (NA and SA, respectively) and the low-pressure on both sides of their centres as mentioned in the previous sections. The transport of the water mass which is directed to the right of the trade wind and the westerlies directions in the NH and to the left of the wind in the SH creates deformations of the shape of the sea surface topography and generates rises of the SSH in the center of the higher-pressure gyres. Generally, at the near surface of the ocean, the resulting surface current of the movement of waters is directed at an angle of 45° while in the entire water column from the top to the depth of no influence of the winds, the resulting current so-called Ekman transport is directed to an angle of 90° to the wind and is the cause of the higher-pressure gyres (Ekman convergence region).

The gradient of pressure in both side of the Ekman convergence region generates in turn westward and eastward currents in respectively the TA and the SA due to the geostrophic balance between the Coriolis forces and pressure gradients almost always much larger than the other terms of the horizontal momentum balance equations resulting from the application of the Newton's second law of motion to the flowing continuum. The application of this law on an infinitesimal parcel of the ocean in motion is given by:

$$\frac{du}{dt} = -\frac{\left(\frac{\partial p}{\partial x}\right)}{\rho} + \mathrm{fv} + A_h \left(\frac{\partial^2 u}{\partial x^2} + \frac{\partial^2 u}{\partial y^2}\right) + A_v \frac{\partial^2 u}{\partial z^2} \quad (2.2.1)$$

$$\frac{dv}{dt} = -\frac{\left(\frac{\partial p}{\partial y}\right)}{\rho} - \mathrm{fu} + A_h \left(\frac{\partial^2 v}{\partial x^2} + \frac{\partial^2 v}{\partial y^2}\right) + A_v \frac{\partial^2 v}{\partial z^2} \quad (2.2.1)$$

$$\frac{dw}{dt} = -\frac{\left(\frac{\partial p}{\partial z}\right)}{\rho} - g + A_h \left(\frac{\partial^2 w}{\partial x^2} + \frac{\partial^2 w}{\partial y^2}\right) + A_v \frac{\partial^2 w}{\partial z^2} \quad (2.2.3)$$

Where u, v and w are respectively the x-component (west to east direction), y-component (south to north direction) and z-component (bottom to top direction) of the velocity of the particle in a three-dimensional space. p, ρ, f, and g are respectively the pressure, the density of the fluid, the Coriolis parameter and the gravitational acceleration. A_h and A_v are the horizontal and vertical friction coefficients.

From the left to the right, the terms of the equations 2.2.1 and 2.2.2 represent respectively the x-components and the y-components of the acceleration, the pressure gradient force, the Coriolis force and the horizontal and vertical frictions, whereas the terms of the equation 2.2.3 represent the z-component of the acceleration, the pressure gradient force, the gravity and the horizontal and vertical frictions.

So, a steady, linear and non-viscous approximation of the ocean, and considering that the Coriolis force and the pressure gradient force are higher than the other terms as mentioned above, the equations 2.2.1 and 2.2.2 yield to the geostrophic balance:

$$0 = -\frac{\left(\frac{\partial p}{\partial x}\right)}{\rho} + \text{fv} \tag{2.2.4}$$

$$0 = -\frac{\left(\frac{\partial p}{\partial y}\right)}{\rho} - \text{fu} \tag{2.2.5}$$

And the component of the geostrophic current is deduced as follows:

$$u_g = -\frac{\left(\frac{\partial p}{\partial y}\right)}{\rho \text{f}} \tag{2.2.6}$$

$$v_g = \frac{\left(\frac{\partial p}{\partial x}\right)}{\rho \text{f}} \tag{2.2.7}$$

Reaching the WB, the horizontal geostrophic currents intensify and shift northward/southward in the NH/SH because the negative vorticity (relative vorticity) introduced by the lateral and bottom frictions of the western boundary coasts with the particles of water, which is compensated by the gain of positive vorticity due to the latitudinal increase of the Coriolis force (planetary vorticity) to conserve the vorticity balance. The contrary situation happens in the eastern boundary where the current becomes larger and slower when the planetary vorticity decreases with latitude.

Considering the presence of the large geostrophic steady flow in the presence of the Ekman layer, and adding the driving force of the wind to the equations 2.2.4 and 2.2.5 yields to the vorticity equations:

$$0 = -\frac{\left(\frac{\partial p}{\partial x}\right)}{\rho} + \text{fv} + \frac{\left(\frac{\partial \tau_x}{\partial z}\right)}{\rho} \tag{2.2.8}$$

$$0 = -\frac{\left(\frac{\partial p}{\partial y}\right)}{\rho} - \text{fu} + \frac{\left(\frac{\partial \tau_y}{\partial z}\right)}{\rho} \tag{2.2.9}$$

The integration of the equations 2.2.8 and 2.2.9 over Ekman layer from the base of the mixed layer (z=-H) to the surface (z=0, $\tau = \tau_s$) yields to:

$$\int_{-H}^{0} \left(\frac{\partial p}{\partial x}\right) dz = \int_{-H}^{0} f\rho \text{v}\, dz + \int_{-H}^{0} \left(\frac{\partial \tau_x}{\partial z}\right) dz \tag{2.2.10}$$

And

$$\int_{-H}^{0}\left(\frac{\partial p}{\partial y}\right)dz = -\int_{-H}^{0} f\rho \mathrm{u}\, dz \; + \; \int_{-H}^{0}\left(\frac{\partial \tau_y}{\partial z}\right) dz \tag{2.2.11}$$

By definition:

$$\frac{\partial P}{\partial x} = \int_{-H}^{0}\left(\frac{\partial p}{\partial x}\right)dz; \quad \frac{\partial P}{\partial y} = \int_{-H}^{0}\left(\frac{\partial p}{\partial y}\right)dz; \quad \mathrm{M}_x = \int_{-H}^{0} f\rho \mathrm{u(z)}dz; \quad \mathrm{M}_y = \int_{-H}^{0} f\rho \mathrm{v}(z)dz$$

And:

$$\int_{-H}^{0}\frac{\partial \tau_x}{\partial z}dz = \tau_x(0) - \; \tau_x(-H) = \; \tau_s^x \qquad\qquad \int_{-H}^{0}\frac{\partial \tau_y}{\partial z}dz = \tau_y(0) - \; \tau_y(-H) = \; \tau_s^y$$

Therefore, the equation 2.2.10 and 2.2.11 become:

$$\frac{\partial P}{\partial x} = \; fM_y + \; \tau_s^x \tag{2.2.12}$$

$$\frac{\partial P}{\partial y} = \; fM_x + \; \tau_s^y \tag{2.2.13}$$

Applying these equations to the continuity equation:

$$\rho\int_{-H}^{0}\left(\frac{\partial u}{\partial x}dz + \frac{\partial v}{\partial y}dz + \frac{\partial w}{\partial x}dz\right) = 0$$

yields to

$$\frac{\partial M_x}{\partial x} + \frac{\partial M_y}{\partial x} = w(0) - w(-H) = 0 \tag{2.2.14}$$

And the differentiate of the equations 2.2.12 and 2.2.13 with respect to x and y respectively, which are equal bring to a new balance so-called the Sverdrup balance, in which the vorticity input of the wind is compensated by the meridional advection of the planetary vorticity, and is given by the relation:

$$\beta M_y = curl(\tau_s) \tag{2.2.15}$$

Where M_y is the depth-integrated total meridional mass transport and $\beta = (df/dy)_{\phi_0} = 2\Omega \sin \phi_0 / R_T$ is the Rossby parameter. y is the meridional distance from a given latitude ϕ_0, Ω is the angular rotation rate of the earth, and R_T is the Earth's radius

In the western part of the basins near to the continents this balance is no more respected because of the lateral frictions with the continent, the bottom frictions and eddies. In this case the nonlinear terms of the equations 2.2.1 to 2.2.3 count as well as the pressure gradient, the Coriolis force and the wind stress. The entire TA wind regime variability in the regime generates the wind-driven NECC which according to its location can be in Sverdrup balance or not (Garzoli and Katz, 1983, Verdy and Jochum, 2005). West of 32°W, the NECC flow is known to not be in Sverdrup balance while in the eastern side of the basin, this balance is held. Verdy and Jochum (2005) showed that, in the western side of the basin, the contributions of the nonlinear terms of the zonal and meridional advection of the relative vorticity by the mean flow and the eddies are important and need to be considered to close the vorticity budget. This helps to better understand the dynamics in the WB and explains some aspects of the dynamics.

2.3 THE ABSOLUTE DYNAMIC TOPOGRAPHY OF THE OCEAN SURFACE IN THE TROPICAL ATLANTIC

The absolute dynamic topography (ADT) in the ocean show the sea surface height (SSH) relative to the geoïd and explains the geostrophic characters of the currents in the ocean. Its higher and lower values represent the strength of the gradient of pressure between the high pressure (ridge) and low pressure (low) in response to the large-scale wind variability; and its variability are usually coordinated with the vertical movements of the thermocline. The ridge/low shows a character of a deep/shallower thermocline and consequently mirrors the shape of the thermocline (Castellanos et al., 2015).

The ADT variability in the TA can be used to explain the variability of the multiple horizontal surface currents. Its mean state (Figure 3) shows three main areas and its repartition is consistent with the variability of the wind regime. The first area is the western boundary and the visible part of the subtropical gyres which show the highest ADT values (>50 cm). The highest values in the subtropical gyres is explained by the Ekman convergence due to the easterlies trade winds and the westerlies as mentioned in the in the section 2.2 whereas in the western boundary, it is more due to the trade winds blowing westward and pushing water to the west. The second area is the

horizontal band approximately between 3°-6°N with higher values (between 45-55 cm). The higher values in this second area are explained by the accumulation of water due to the northward and southward components of the trade winds, respectively south and north of the equator, and seems to follow the latitudinal movements of the ITCZ (Castellanos et al., 2015). The ridge induced by the accumulation of water is generated by the Ekman divergence in the equatorial region due to the strengthening of the southeast trade winds when crossing the equator, mainly during the second half of the year (Castellanos et al., 2015). And the third area is the eastern boundary in the Gulf of Guinea which show the lowest values (<40 cm) with highest values near the Africa coast where the mouths of Niger and Congo rivers are located.

The Connection between the ridges of the subtropical gyres and the western boundary depicts the connection between the northern branch of the southern subtropical gyre, the western boundary currents, and the southern branch of the northern subtropical gyre in the tropical Atlantic (Schott et al., 2004). In the latitudinal band between 0°-6° of western basin, the positive eastward horizontal gradient should explain the presence of horizontal eastward undercurrents in this band. The low pressure at the equator, and between the second area and the northern subtropical gyre explains the presence of the subtropical cells in the equatorial region and the north/south of the equatorial region (Snowden and Molinari, 2003; Schott et al., 2004; Tuchen et al., 2020). These subtropical cells are formed by the downwelling waters from the subtropical gyre regions or the ridge between 3°-6°N (3°-6°S) which are transported equatorward, upwell in low pressure regions, and are redirected to north (south) in the NH (SH) through the Ekman transport in the surface layers to close the cells.

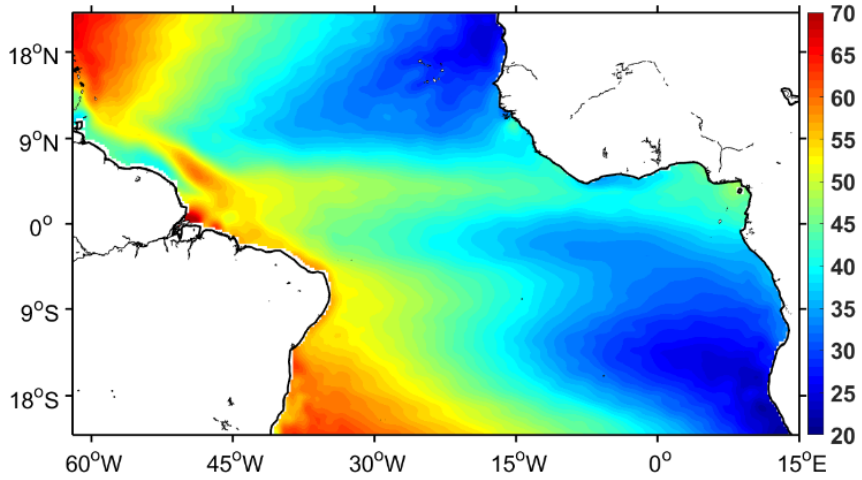

Source: The author (2022).

Figure 3. Annual mean Copernicus Marine Service (CMEMS: https://marine.copernicus.eu/fr) Absolute Dynamic Topography data sets over 1993-2018 period. The values are in centimetre units

2.4 THE SURFACE CURRENTS IN THE TROPICAL ATLANTIC

As mentioned in the introduction, the TA circulation includes several surface currents (upper layer and thermocline layer currents) flowing eastward/westward or northward/southward (Figure 4). The westward currents are the NEC and the three branches of the SEC (sSEC, cSEC and nSEC). The sSEC is weakly visible at the surface (Figure 5) and generally flows south 10°S (Rodrigues et al., 2007). The cSEC and the nSEC flow respectively between 0°-6°S and between 0°-6°N and are strong in the surface mixed layer (Figure 5).

Near to the America coast the sSEC bifurcates at different depth according to its latitudinal position (Rodrigues et al., 2007). In the first 200 m, its bifurcation occurs between 13°-17°S into the surface BC and the undercurrent NBUC, and is associated to the variability of the zero line of the WSC in SH. The upper part of the NBUC is joined by the cSEC between 0°-5°S to become a mixed NBC which flows northward along the Brazilian coast in the upper layer (Figure 5). The NBC is also joined by the nSEC between 2°-4°N and continues flowing northward carrying almost the total AMOC heat.

The retroflection of the NBC (NBCR) occurs between 0°-9°N (Figure 4 and Figure 5), and a large part of its forms a southeastward retroflected NBC (rNBC) which feeds the NECC, the NEUC and the EUC. The other part of the flow is carried by the northward extension of the NBC toward the Caribbean to become later the Guyana current, and by the anticyclonic rings shed during the

retroflection which transfers northward part the NBC waters (John et al., 1998; Garzoli et al., 2004, Aroucha et al., 2020).

The only eastward current in the upper layer is the NECC which flows between 3°-13°N, and its variability depends on the local WSC (Urbano et al., 2006, 2008). It is also partly fed by the NEC (Bourlès et al., 1999a), and enters to the Gulf of Guinea to join the Guinea current (GC). In the thermocline layer, the EUC, the SEUC, and the NEUC also flow eastward (Figure 4). The EUC flows between 2°S and 3°N and is centered at the equator around 100 m-depth whereas the NEUC and the SEUC are both located between 3° and 6° of latitude and are centered around at 4°latitude between 150-200 m-depth (Metcalf et al., 1962; Tsuchiya, 1986; Stramma and Schott, 1999). During boreal spring EUC and the NEUC upwell and connect with each other in the upper thermocline (Urbano et al., 2008; Burmeister et al., 2018). It is also known that, part of the northern waters from the NEC also feeds the EUC in the subsurface (Bourlès et al., 1999).

The variability of the majority of these currents which help to transport northward and redistribute the water masses and heat to the north are associated to the wind variability. Their variability is generally linked to the latitudinal movement of the ITCZ or to wind strength (Johns et al., 1998; Fonseca et al., 2004; Rodrigues et al., 2007; Hormann and Brandt, 2007; Urbano et al., 2006, 2008).

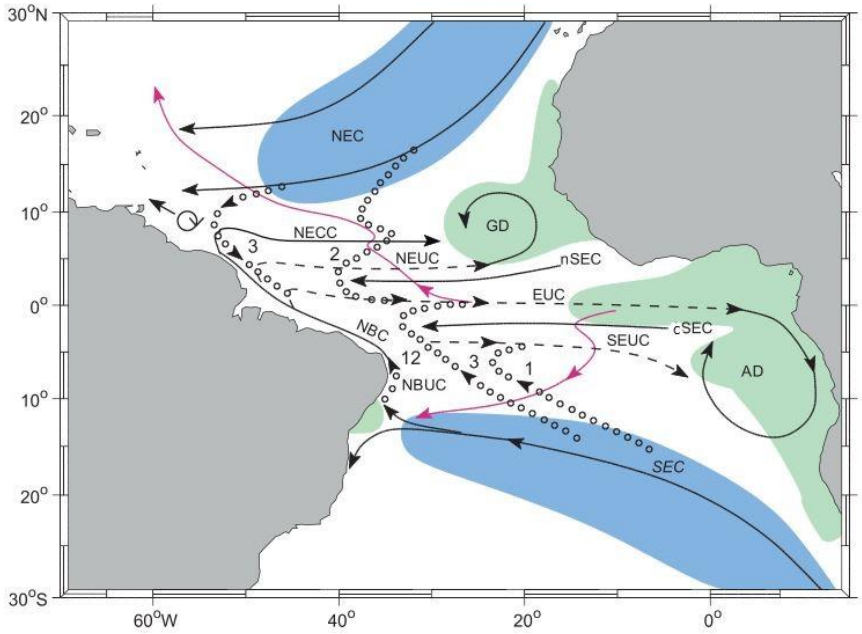

Source: Schott et al. (2004).

Figure 4. Schematic representation of the Atlantic Subtropical Cells (STC) circulation with subduction (blue) and upwelling (green) zones that participate in the STC. Current branches participating in STC flows are NEC = North Equatorial Current, SEC = South Equatorial Current (central and northern branches: cSEC and nSEC), NECC = North Equatorial Countercurrent and EUC = Equatorial Undercurrent; NEUC, SEUC = North and South Equatorial Undercurrent; NBC, NBUC = North Brazil Current and Undercurrent; GD, AD = Guinea and Angola domes. Interior equatorward thermocline pathways dotted, transport estimates marked for interior and west- ern boundary pathways; surface poleward pathways for the central basin (from drifter tracks, after Grodsky and Carton [2002]) marked by thin, magenta line; see text for details.

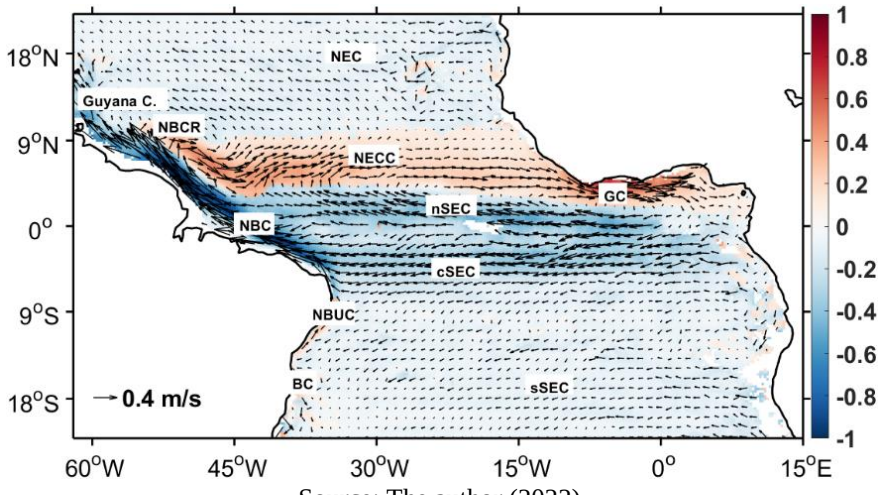

Source: The author (2022).

Figure 5. Annual mean of upper and thermocline layers currents signature from National Oceanic and Atmospheric Administration (NOAA) drifter currents climatology data (1979-2015) at 15 m-depth. Upper layer currents: NEC = North Equatorial Current, SEC = South Equatorial Current (southern, central and northern branches: sSEC, cSEC and nSEC), NECC = North Equatorial Countercurrent, NBC = North Brazil Current, Guyana C. = Guyana Current, GC = Guinea Current, BC = Brazil Current; Thermocline layer current: NBUC = North Brazil Undercurrent. The current's arrows are superimposed on the speed of their speed. The blue (dark red) colors represent the westward (eastward) currents.

2.5 THE MIXED LAYER DEPTH IN THE TROPICAL ATLANTIC

At the interface between the ocean and the atmosphere, there is an oceanic boundary layer (mixed layer) which is in balance with the inferior layer of the atmosphere called “marine atmospheric boundary layer”. Through both layers, the ocean and atmosphere exchanges large amounts of heat, moisture, and momentum, primarily via turbulent transport which homogenizes their thermodynamic parameters (Fairall et al., 1996). In the physical oceanography, there exist two definitions for the oceanic mixed layer. One is the surface layer with a smaller variation of density (ML) while the second is the layer with a smaller variation of the temperature, also called isotherm layer (IL). Different criteria are used to determine these layers depth (MLD and ILD respectively). For example, a criterion of a variation of density $\Delta\sigma$ in the ML corresponding to a certain variation of temperature ΔT in the IL from a chosen reference depth can be used to determine the MLD (de Boyer Montegut et al., 2004). The reference depth is chosen to avoid the strong diurnal cycle that occurs in the first few meters of the ocean. For the larger part of the ocean, the ILD is often deeper than the MLD, and the difference between both so-called the barrier layer (BL) thickness (BLT) can be interesting to understand the exchange of heat between the upper ocean and the deep ocean. The thicker the BL is, the more difficult the exchangesare. Thus, the MLD provides information about the heat content in the upper layers of the ocean and is responsible of the interactions between the ocean and the atmosphere. There are also some regions like the subtropical regions where this difference is negative due to the higher values of the MLD compared to the ILD values (de Boyer Montegut et al., 2004, 2007; Mignot et al., 2007). In these regions, the temperature stratification below the well-mixed layer (ILD) is partially compensated by a stratification in salinity, and the corresponding layer is so-called the salinity compensation layer.

The ILD and MLD have been computed from GLORYS12V1 reanalysis, considering a variation of temperature of $\Delta T=0.5$ from a chosen depth reference of 10 m, and the annual means of the MLD and the difference between both ILD and MLD are sshown in Figure 6. The MDT show similar pattern to the ADT with three main areas: the area connecting the subtropical gyre to the WB the zonal area between 0°-9°N; and the TA eastern boundary. These areas in the WB (eastern boundary) correspond to the area of the higher (lower) values of ADT, and also to the regions where the thermocline is known to be respectively deeper (shallower) (Garzoli and Katz, 1983). In the first two areas, the MLD is respectively higher than 45 m, and between 35-45 m

whereas in the third area, it is lower than 35 m. The highest values are shown near to the subtropical gyres

The difference between the ILD and MLD shows the presence of significant barrier layers in the first two areas, and highest BLT values mainly in WB (higher than 10 m). The eastern boundary of the Gulf of Guinea where the inputs of Niger and Congo rivers are important shows a presence of weaker barrier layer reaching 10 m-tickness. These are consistent with de Boyer Montegut et al. (2007), Mignot et al. (2007), Breugem et al. (2008), and Dossa et al. (2019).

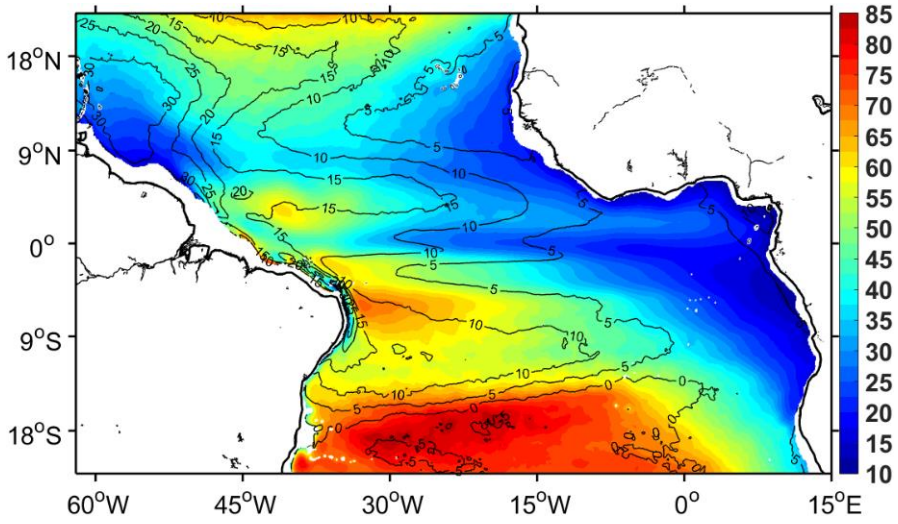

Source: The author (2022).

Figure 6. Annual mean of the density mixed layer depth (MLD) with the contours of the difference between the isotherm layer depth (ILD) and MLD, computed from GLORYS12V1 reanalysis (G12V1) over 1993-2018 period. The reference depth used for the calculations is 10 meters depth as a reference, and the values are in meters

2.6 THE SEA SURFACE TEMPERATURE AND THE SEA SURFACE SALINITY IN THE TROPICAL ATLANTIC

The surface of the ML is characterized by thin limit layer by which the exchanges of heat and mass with atmosphere occur. By this interface the ocean, the ocean receives the solar radiation from the sun, reflects a part and absorbs the other part to warm the upper layer which stores the heat and contributes to the heat budget of the ML. The exchanges of water masses via the evaporation process participates to the establishment of the whole atmospheric process which is part of the water cycle leading to precipitations. This interface is characterized by important thermodynamic properties, mainly the SST and the SSS which are important ocean variables used to the understand the connections between the ocean and the atmosphere. In the TA where the

ocean receives most of the solar radiations and more precipitations, these variables are even more important.

On the global scale, the SST varies strongly with the seasons. In the northern TA, the SST is higher (lower) during the boreal spring and summer (winter and fall) when the NH receives more (less) solar radiation. The opposite case is shown in the SH where the ocean receives more radiation from sun during the boreal fall and winter. The difference of season phases in the two hemispheres due to the inegal repartition of the solar radiation is explained by the earth's polar axis which is tilted about 23°5' with respect to the plane of the earth's orbit around the sun (Watson, 1983). The annual mean (Figure 7) shows higher SSTs on both sides of the equator between 10°S-10°N, and the highest values (> 27°C) near to the continents and in the area of latitudinal displacement of the ITCZ. Lower SSTs are found at the eastern part of the basin, north/south of 10°N/S near to the continent.

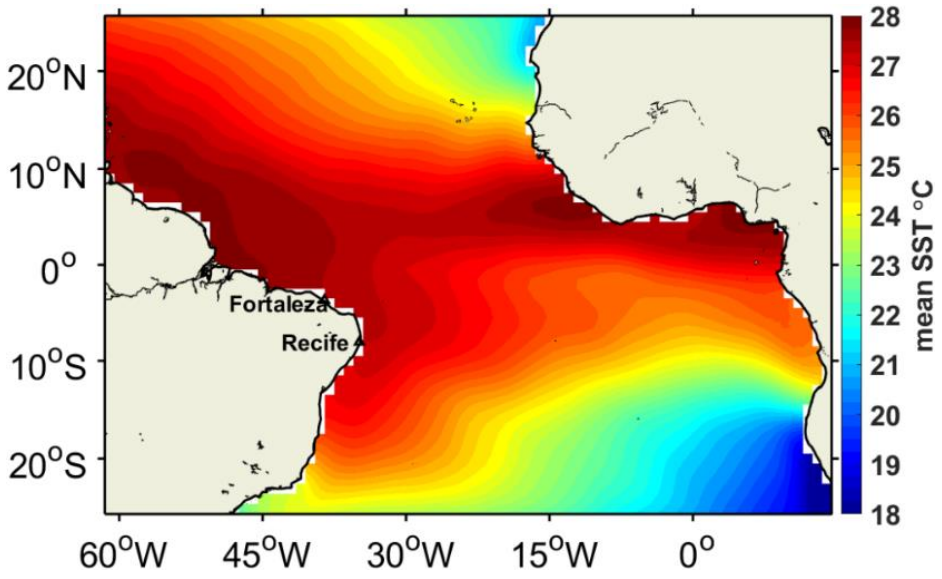

Source: The author (2022).

Figure 7. Annual mean of sea surface temperature from monthly Hadley Centre Sea Ice and Sea Surface temperature data (HadISST: https://www.metoffice.gov.uk/hadobs/hadisst/; Rayner et al., 2003) over 1910-2020 period. Values are in °C.

The interannual variability of the SST (Figure 8) shows generally lower variances in the western boundary and higher variances in the upwelling regions of Senegal-Mauritania and of Benguela, and in the region of the cold tongue so-called Atlantic cold tongue (ACT) in the Gulf of Guinea where the seasonal amplitude of the SST can reach 0.5-0.7°C (Weingartner and Weisberg, 1991). The variance in the ACT region is associated with the wind anomalies in the western basin

which is associated with the anomalies of the thermocline depth in the central/eastern basin (Hormann and Brandt, 2009). The positive/negative easterlies/westerlies anomalies intensify the shear between the surface and subsurface currents, induce the shoaling of the thermocline allowing the subsurface cold water to reach the surface (Marin et al., 2009; Brandt et al., 2011).

The ACT which occurs generally in boreal spring – summer helps the development of the West African Monsoon (WAM) which is driven by the temperature gradient between the African Continent and the South Atlantic Ocean. Its region is included in the AZM box used to understand the influence of the eastern equatorial Atlantic dynamics on the ocean-atmosphere interactions and the TA variability (Zebiak., 1993). More explanation will be done in the section 2.7.

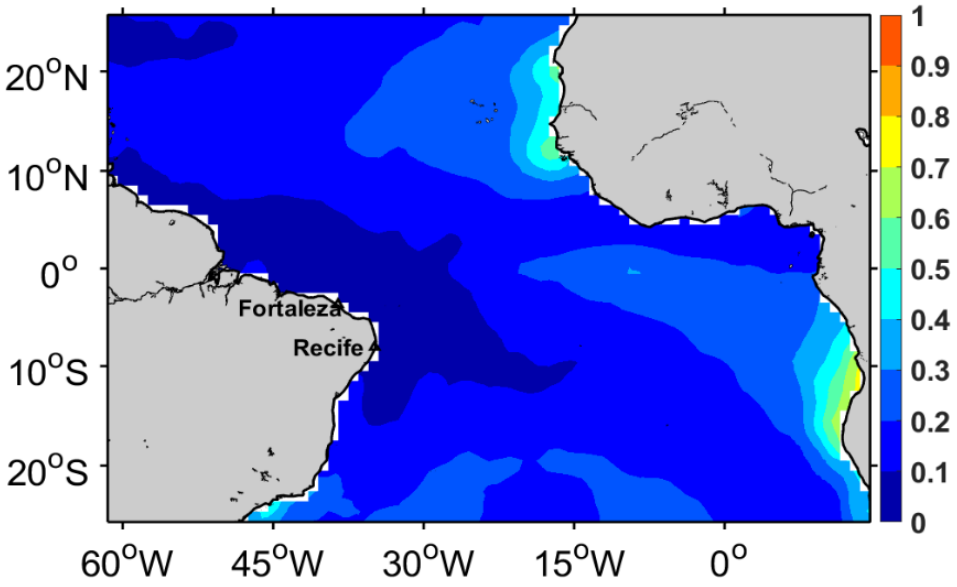

Source: The author (2022).

Figure 8. Variance of the sea surface temperature anomalies from monthly Hadley Centre Sea Ice and Sea Surface temperature data (HadISST: https://www.metoffice.gov.uk/hadobs/hadisst/; Rayner et al., 2003) over 1910-2020 period.

The annual mean of SSS (Figure 9) shows higher values (>36 psu) in the western boundary and the regions near to the subtropical gyres compared to the eastern boundary. The, lowest values occur in the regions surrounding rivers (< 30 psu in the Amazon, Congo, Niger regions), the western Africa regions of coastal upwelling (< 32 psu), and in the NECC region (< 35.5 psu). Salisbury et al. (2011) and Varona et al. (2019) show that, in the WTNA, the SSS is affected seasonally by the Amazon discharges near to the continent, along the NBC route, and in the NECC regions. The latter authors showed the influence of the lower SSS on the MLD which becomes shallower and induced the thick BL in these regions. They also found seasonal changes in the SSS

field which reach approximately 8 psu near the amazon river mouth, and 4 psu in the NECC region. Their findings indicate the influence of the Amazon River inputs on the salinity budget in the WTNA through the NBC/NBCR and NECC currents, especially west of 40°W (Foltz et al., 2015). In addition to the Amazon river influence, Foltz et al. (2015) showed the influence of the rainfall on the seasonal variability of the SSS east of 40°W.

The lowest SSS in the regions surrounding the rivers in Figure 9 explains the shallower ML, and the presence of the thick salinity-induced BL in these regions (Figure 6).

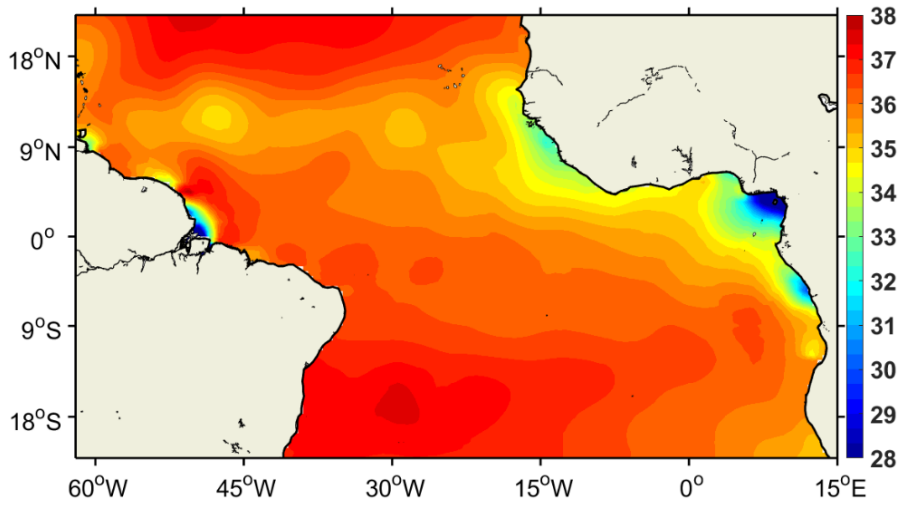

Source: The author (2022).

Figure 9. Annual mean of monthly CORA sea surface salinity (SSS) reanalysis (INSITU_GLO_TS_OA_REP_OBSERVATIONS_013_002_b product) from Copernicus Marine Service (CMEMS: https://marine.copernicus.eu/fr) over 1990-2019 period. Values are in psu.

2.7 THE TROPICAL ATLANTIC CLIMATE MODES

The TA exhibits two dominant climate modes of interannual variability, characterized by strong interannual variabilities of the SST, which are known to influence the regional climate and the precipitations, and are associated to the variability of the currents (Zebiak, 1993; Servain and Merle, 1993; Kushnir et al. 2006; Chang et al., 2006; Hormann and Brandt, 2007; Hormann et al., 2012). The results of the EOF analysis of the monthly SST anomalies from the Hadley Centre Sea Ice and Sea Surface temperature datasets (HadISST: https://www.metoffice.gov.uk/hadobs/hadisst/; Rayner at al., 2003) for 1910-2020 period are shown in Figure 10 and Figure 11 which represent the first two dominant modes of the TA variability, respectively with 32.7% and 24% of the total variance. The box in Figure 10 represents

the region within 20°W to 0°E and 3°S to 3°N so-called ATL3, where the anomalies are usually averaged to compute AZM index (Zebiak, 1993, Hormann et al., 2012). The boxes in Figure 11 represent the two boxes usually used to compute the AMM index by doing the difference between interannual SST anomalies averaged over 5°–25°N, 60°–20°W (northern box) and 20°S–5°N, 30°W–10°E (southern box) (Servain, 1991).

The first climate mode (Figure 10) so-called AZM is similar to the pacific El Niño-Southern Oscillation (ENSO) climate mode, but is weaker compared to the latter due to geometry of the Atlantic basin; and peaks in boreal summer (June-July-August) (Merle, 1980; Keenlyside and Latif, 2007). The dominant driver for its events is the Bjerknes feedback, controlled by the wind anomalies in the west, the SST anomalies within ATL3 and the sea level pressure (SLP) anomalies which influence the thermocline slope (Jouanno et al., 2017). The positive (negative) phases so-called the Atlantic Niño (Atlantic Niña) are associated to positive (negative) Bjerknes feedback which is explained by the relation between the warm (cold) SST in the eastern tropical Atlantic leading to a weaker SST gradient across the basin, the weakening (strengthening) of the trade winds in the western basin, and a shoaling (deepening) of the thermocline due to the Kelvin waves (KWs) propagation, resulting in a weakening (strengthening) of the upwelling in the central equatorial Atlantic. The variability of the AZM which involves ACT anomalies and peaks during the period of the northernmost location of the ITCZ (boreal spring-summer) consequently influences this latter, the intensity of the WAM and also the precipitations in the TA (Okumura and Xie, 2004; Diakhaté et al., 2018; Crespo et al., 2019).

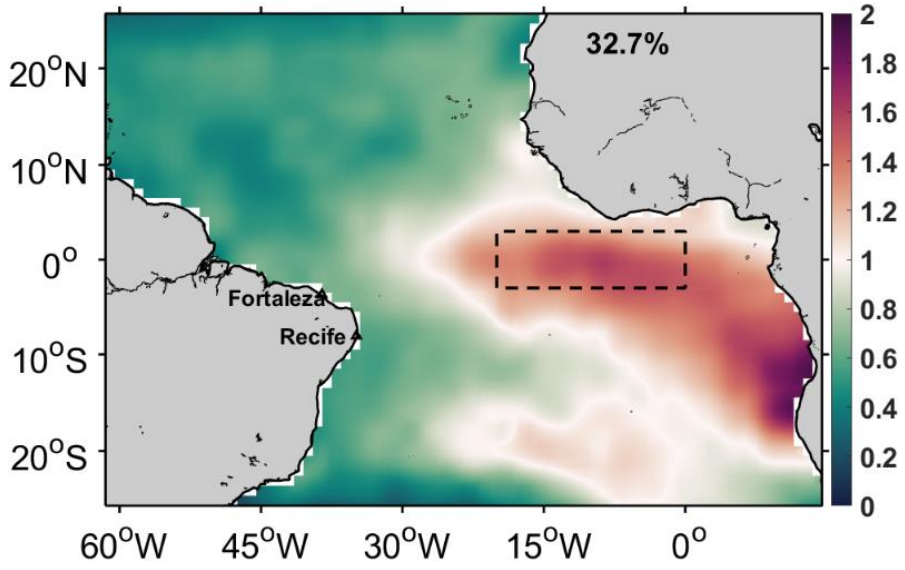

Source: The author (2022).

Figure 10. First EOF mode from monthly Hadley Centre Sea Ice and Sea Surface temperature (HadISST: https://www.metoffice.gov.uk/hadobs/hadisst/; Rayner et al., 2003) over 1910-2020 period: 32.7%. The dashed box is the region within 20°W-0°E and 3°S-3°N so-called ATL3.

The second mode (Figure 11) so-called the AMM is characterized by the cross-equatorial gradient of the SST initiated by the interhemispheric SST/SLP dipole, and is controlled by thermodynamic feedbacks, through cross-equatorial wind stress anomalies (Saravanan and Chang, 2000; Chiang and Vimont, 2004; Cabos et al, 2019). It is more active on longer time scales than the AZM, and peaks during boreal spring (March-April-May). The main mechanism for its onset and growth is the so-called wind-evaporation–SST (WES) feedback which includes also the AZM mechanism during the positive phase (Chang et al., 2000). Its positive phase is represented in Figure 11 by a positive SST anomaly in the NH and a negative SST anomaly in the SH. During its negative phase, the positive and negative SLP anomalies over respectively the NH and the SH led to a strengthening (weakening) of the trade winds in the NH (SH). Because of the wind intensities, the latent heat flux enhances (decreases) in the NH (SH) and then, influences again the SST in the TA, which continues decreasing (increasing) in the NH (SH): this is the negative WES feedback. During this phase, the AMM influences the ITCZ, which shifts southward because of the weakening of the southeast trade winds (Cabos et al., 2019) and influences the precipitations in the northeast of Brazil (Hounsou-Gbo et al., 2015). The TA and Tropical Pacific interannual variabilities are both connected, in particular during the strongest AMM and ENSO events; and the connection between both is modulated by the Atlantic Multidecadal Oscillation (AMO) which involves both the AZM and the AMM (Ham et al., 2013). For instance, when the negative phase

of the AMM is well-established during the boreal spring, the cooling in the northern TA generates a low-level anticyclonic flow over the eastern Pacific, which reduces the wind speed, and leads to SST warming due to the deepening of the thermocline, and to the increase of the convective activity during the following winter. This connection between the northern TA and the Pacific is especially stronger during the positive phase of the AMO. In turn, the positive phase of ENSO in the Pacific during winter generates perturbations of the Hadley circulation which influences the variability of the northern trade wind in the NH (Enfield and Mayer, 1997; Xie, 2004; Xie and Carton, 2004).

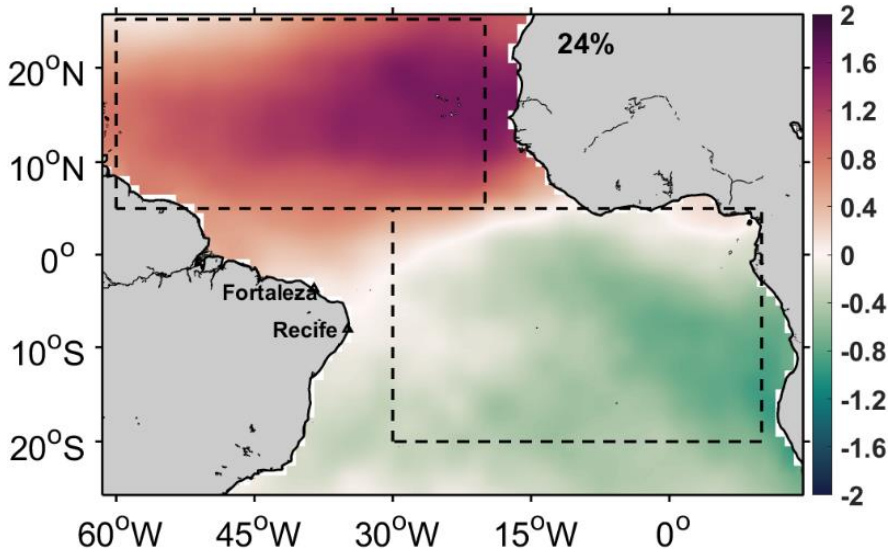

Source: The author (2022).

Figure 11. Second EOF mode from monthly Hadley Centre Sea Ice and Sea Surface temperature (HadISST: https://www.metoffice.gov.uk/hadobs/hadisst/; Rayner et al., 2003) over 1910-2020 period: 24%. The dashed rectangles are the boxes used for the calculation of the AMM index.

The goal of this chapter was to present the main variables of the tropical Atlantic, remind the main equations of the ocean circulation, and to introduce the Atlantic climate modes which will be used later in chapters 4 and 5 to investigate the mechanism associated with the interannual variability of the currents in the WB. The following chapter will be dedicated to the description of the study area, the data and the pre-processing of the data.

3 STUDY AREA, DATA AND ANALYSIS

Since the goal of this thesis is to revisit the WB surface circulation by analyzing all the upper and thermocline layers currents, and the coupling ocean-atmosphere mechanisms which are relevant for its variability, the study area has been chosen from the region of the formation of the NBC to the region after its retroflection, and is extended westward to the 32°W in order to investigate the connections with the nSEC, the NECC and the NEUC, north of the equator, with the EUC in the equatorial region, and with the cSEC and the SEUC south of the equator.

To do so, the Shipboard ADCP (SADCP) data from Prediction and Research Moored Array (PIRATA) program cruises (Bourlès et al., 2008, 2019) deployed by Brazil which is responsible for the maintenance of the buoys of the WB, and 2012 CAMADAS-FINAS cruise are pre-processed and analyzed together with altimetry-derived geostrophic current, ERA5 wind velocity components and the GLORYS12V1 reanalysis to achieve our goals. In order to investigate the spatial variability of the currents, 9 sections crossing the currents have been selected and the cross-section currents are studies.

The goal of this chapter is to present the study area with the nine (09) sections selected and gives the main steps of the processing of the SADCP data performed with CASCADE (Chaîne Automatisée de Suivi des Courantomètres Acoustiques Doppler Embarqués) software. It will present also the data used for this study and which have not been describe in the following chapters.

3.1 STUDY AREA AND SELECTED SECTIONS FOR STUDY

This study focused on the area limited by the latitudes 10°S to 15°N, and the longitudes 25°W to 62°W, and where the currents of interest are the NBC, the cSEC and the nSEC, the southeastward retroflected branch of the NBC (rNBC), the NECC, the EUC, the NEUC and the SEUC (Figure 12). The nine (09) cross-sections of the currents used to analyze the seasonal and the interannual variability of the WB are:

- The oblique section 1 (S1) crossing the NBC at the beginning of its formation; and is the ascendant diagonal of the rectangle area limited by the latitudes 0.6°S to 4.8°S, and the longitudes 33.2°W and 36.8°W;

- The oblique Section 2 (S2) crossing the NBC before the retroflection and the rNBC after the retroflection. This is the ascendant diagonal of the rectangle area limited by the latitudes 3°N to 7.5°S, and the longitudes 45°W and 50.5°W;
- The oblique section 3 (S3) crossing the northward branch of the NBC into the Guyana current. This is the ascendant diagonal of the rectangle area limited by the latitudes 9°N to 12°N, and the longitudes 57°W and 60°W;
- The oblique section 4 (S4) crossing the nSEC and capturing the NBC retroflection participating the rNBC. This is the descendant diagonal of the rectangle area limited by 0°N to 11.2°N, and the longitudes 43°W and 55.2°W;
- The meridional section 5 (S5) crossing the NECC, the NEUC, the nSEC and the zonal component of the rNBC at 42°W;
- The meridional section 6 (S6) crossing the NECC, the NEUC, the EUC, the cSEC and the SEUC at 32°W.
- The meridional section (S38°W) crossing the NECC, the NEUC, the nSEC and the northern part of the EUC at 38°W. This is also the section sampled by the PIRATA-BR ADCP transects used in this thesis;
- And two oblique sections in the equatorial region (Seq1 and Seq2) crossing the NBC and the rNBC. These sections are chosen to investigate the rNBC which reaches the equatorial region and/or the equatorial retroflection of the NBC. They are respectively, the ascendant diagonals of the rectangle areas bounded by 0°-5°N, and 42.5°-47.5°W, and by 2°S-2°N and 40°-44°W.

These different sections also aim to investigate the spatial variability of the currents by analyzing their evolution along their pathway. For the oblique sections S1, S2, S3, S4, Seq1 and Seq2, the analyses have been performed on the cross-section components of the currents while on the meridional sections, the zonal components are considered.

Figure 12 shows the schematic representation of the surface mean currents of the upper and thermocline layers, and the nine (09) sections mentioned above. Fifteen years of SADCP data have been collected at the section S38°W during PIRATA-BR and CAMADAS FINAS III cruises between 2001 to 2018 (See details in chapter 4) and the data have been processed in order to achieve one our objectives which is to reassess GLORYS12V1 reanalysis in the NH. The grey lines near to the south America coasts represents the isobath 300, 1000, 3000 and 4000 meters.

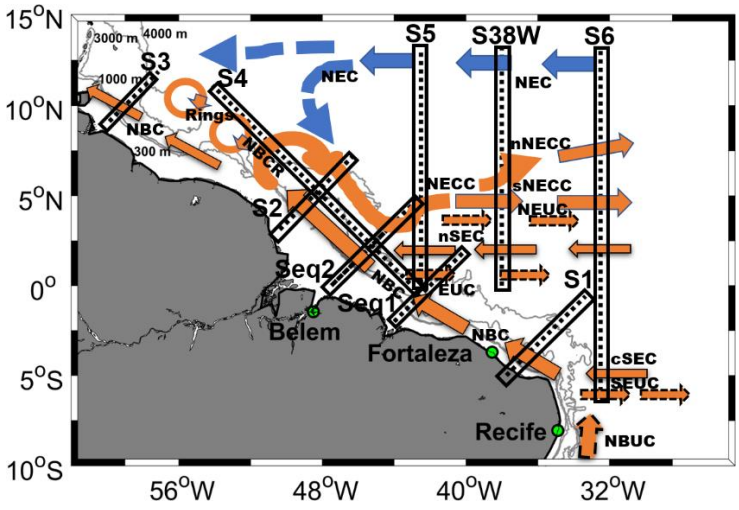

Source: The author (2022).

Figure 12. Study area with the main currents investigated based on Schott et al. (2004), Goes et al. (2005), Urbano et al. (2006; 2008) and Aroucha et al. (2019). The black dashed lines framed by the black rectangles are the sections crossing the currents which are used for the study. The yellow and the blue arrows represent respectively the southern warm waters and the northern cold water transported by the currents. The dashed and the normal arrows represent respectively, the upper and thermocline layers currents. The circles with arrows in the clockwise direction represent the North Brazil Current (NBC) rings. The name of the current branches participating to the western boundary circulation are the same as in Figure 4**.** The nNECC and sNECC are for respectively the northern and the southern branches of the NECC.

3.2 DATA AND ANALYSIS

In this section, the principle of ADCPs measurements will be recall. Then, the post-cruise processing steps with CASCADE and some examples will be given. Some additional data used in this thesis will be also present, and some calculations will be recalled.

3.2.1 Principle of the ADCP measurements

The ADCP is the instrument used to measure how fast the water moves across on entire water column. It usually anchored to a fixed support like a seafloor, a seawall, a bridge, or a canal to measure the current profiles from a fixed position or to a mobile support like a bottom of a ship (so-called ship-mounted ADCP: SADCP) to take constant current measurements during the ship displacement. It is made up of piezoelectric transducers that transmit and receive sound signals (called beams) in the form of pings of sound at a constant frequency into the water, and estimates single velocity components parallel to the beams by using a principle of sound waves called the Doppler effect. At least three transducer beams, inclined from the vertical plan at an angle Θ (called

beam angle) and pointing in different directions are required to estimate the horizontal and vertical water current velocities along all the beams paths, and/or also the error velocity to qualify the data. The ADCP uses the frequency shift between the frequency of the sound waves sent by the ADCP and the frequency of the echoes returning from the sound scatterers in the water (small solid particles, sediments, or plankton) which reflect the sound back to the instruments to estimate the velocity components and the errors. Then, the vertical velocity profiles are divided into uniform segments called depth cells or bins and averaged over the entire cells to reduce the effects of spatial aliasing. The high frequency ADCPs provide more precise data than the low frequency ADCPs which pings travels farther in the water. The accuracy of the data also depends on the type of the ADCP which can be narrowband or broadband. The broadband systems have a greater bandwidth compared to the narrowband system and take advantage of the full signal bandwidth to give broadband ADCPs more information to estimate the velocity. As a result, they reduce largely the variance, and so, the error when compared with the narrowband ADCPs. To obtain the absolute current velocity in earth coordinates (directions north and east), the ADCP need the navigation data available which are required to correct the data from the motions that affect the instrument. Especially two kinds of motion needed to be corrected: the rotation (pitch, roll and heading) and the translation (ship velocity in the case of SADCP).

For the SADCPs of the constructor RDI, a shipboard computer to receive the data, and a global positioning system (GPS) data are required. Generally, the navigation data are provided by an optical gyrocompass, a motion sensor and a GPS system onboard the ship. The conversion of the ADCP beam data to the earth coordinates is performed by using the constructor's software called the vessel-mounted data acquisition system (VmDAS) which generates ensembles of binary files containing averages mono-pings data, and the best navigation data to use during post-cruise processing. The ensembles of files can be averaged with 2 minutes time averages (Short Term Average: STA files) or 5 minutes time averages (Long Term Average: LTA files) (Kermabon et al., 2018). They primarily contain the ship's velocity and the relative velocity of the current to the ship all along the ship trajectory.

The resulting STA and/or the LTA files thus obtained is processed by CASCADE or CODAS software to compute the absolute velocity of the currents.

3.2.2 Processing of PIRATA-BR and CAMADAS FINAS III SADCP data with CASCADE

CASCADE is a matlab software developed by the “Laboratoire d’Océanographie Physique et Spatiale (LOPS)” to process the SADCP data collected along the ship transects and is made operational by the french data center SISMER (Système d’Informations Scientifiques pour la Mer) (Kermabon et al., 2018). For the processing of the ADCP data, we used the CASCADE version 7.0 to qualify and analyze the SADCP data from PIRATA-BR and CAMADAS FINAS III cruises (Figure 13). The details about the cruises are given in the article 1. For all the cruises, the vertical profiling resolution of the SADCPs was nominally 8 m which is the bin size.

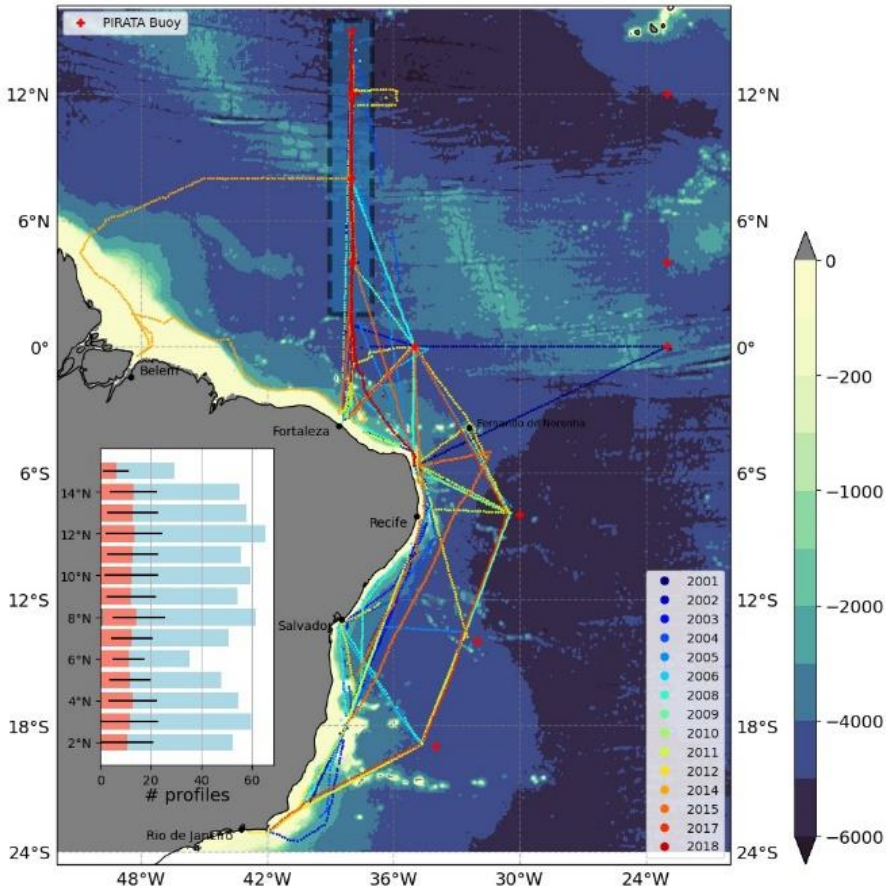

Source: The author (2022).

Figure 13. PIRATA-BR cruises since 2001 and Camadas Finas III (2012) vessel-mounted ADCP sections. A color code is attributed to identify cruise’s routes each year. PIRATA moored location are indicated (red crosses). Underlying bathymetry from the ETOPO2 dataset is shaded. Black dashed rectangle defines the area where ADCP data are considered in this work, along the 38°W section. In addition, for the 15 ADCP legs, the statistics on the number of profiles per degree of latitude are given (the orange and blue bars give the mean and max number of profiles, and the horizontal black bar the standard deviation).

The necessary steps for the processing with CASCADE can be grouped in three main steps

- First, the STA/LTA files conversion into OceanSite standard NETCDF files: the STA/LTA files are concatenated prior to obtain one or several STA/LTA files of several days, before converting. During the conversion, the absolute velocity of the currents is calculated in earth coordinates from the relative velocity of the current and the estimated velocity of the ship which is calculated from the positions and dates of beginning and end of the ensembles;
- Second, the validation and correction of the data: from OceanSite standard NETCDF files obtained, it is required to choose a reference layer (bins) where the data are sure to be good. It is usually advised to considerer the bins between 3-5. Then, if more than 50% of data in this reference layer are qualified not good, all the data are also considered unusable. After this test, if the data are found good to be used, the bathymetry is added to the processing to identify the possible interference with the seafloor in order to eliminate the contaminated data. During our processing, the bathymetry ETOPO 1 which is recommended (temporal resolution of 1 min) has been used. Then, the rotations of the ADCP system are estimated and applied to the new data to realign the velocity components to the ship system; and flags them by defining thresholds of different parameters specific to the ocean region. Table 1 summarize the parameters used in our processing. After, the velocity components are cleaned, and if needed, are corrected from the misalignment and amplitude due to the ship movements. Then, they are smoothed after adding the tide horizontal velocity and transport to the data. The tide model outputs used for our processing is TPX07.2 (Egbert and Erofeeva, 2002), and is available on https://www.tpxo.net/global. The flags 1 to 9 are then applied to the new data, and flag 1 is for the good data that respect all the conditions of Table 1.
- And third, the horizontally and vertically filtering of the current data: in this step, the data flagged 1 are selected and filtered horizontally and vertically to obtained the campaign data. Then, the user is able to create the section and/or station files by re-averaging the filtered absolute current velocity respectively in space and time, and possibly visualizing them with Cascade. (See more details in Kermabon et al., 2018).

Table 1 - Parameters used to flag the currents velocity during the CASCADE processing of the ADCP data of PIRATA-BR and CAMADAS FINAS III

Error threshold of the vertical speed (cm/s)	100
Maximum vertical shear (s^{-1})	0.2
Number of profiles to be considered before and after each profile.	20
Number of deviations from the average	3
Bottom detection	Bathy
V Max (cm/s)	400
Correlation threshold of the ADCP signals	60
Minimum percentage of good ensembles	10

Source: The Author (2022).

In Table 1, the Number of deviations from the average is the number use to check if the absolute velocity can be considered as good at a given position. It is checked by comparing the velocity at the given depth to the median of the 20 profiles before and after at the same depth, multiply by the number of the deviations from the average. The absolute velocity is considered as good when its value is lower than the one calculated. The correlation threshold of the ADCP signals gives information about the ratio transmitted signal/reflected signal. The ratio is lower when the correlation is lower than the threshold (60), and indicates a smaller signal/noise ratio.

3.2.2.1 Example of processed SADCP data obtained from PIRATA-BR XVIII

An example of PIRATA-BR XVIII leg is taken here to show one of the results of processing with CASCADE. In this example, only the section 1 of the cruise transect between 5°S and 15°N which took place between 16/10/2018and 09/11/2018 will be discussed (Figure 14). The data have been collected with a SADCP ocean surveyor working on the narrowband mode and the STA files have been processed. After applying the quality control parameters (Table 1) to the data, the results have been visualized with CASCADE. Figure 15 shows the mean echo intensity (ECI) and the percentage of good data (PGOOD) before the cleaning. The decrease of the ECI with depth indicates the decrease of the signal power with depth. During the processing, the data have been considered as good, when the percentage is higher than 10% for all the cruises. This percentage is

higher where the signal is powerful, and rapidly decrease below 50% after 500 m during 2018 cruise (consistent with the ECI variations). The decrease of the PGOOD locally around 30000 and 63000 ensembles, indicates that the ratio signal/noise is low, possibly due to technical problems which might affect the pings during the corresponding intervals of time, and which is due to the abnormally high ECI to the depth during these periods.

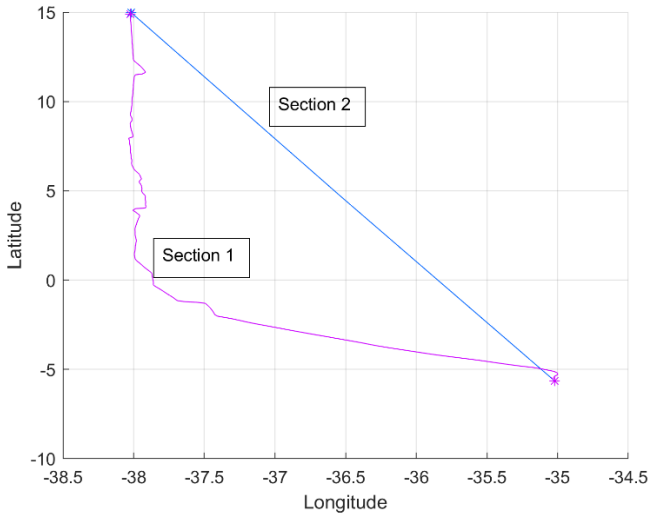

Source: The author (2022).
Figure 14. Sections 1 and 2 of the of the PIRATA-BR VXIII leg between 5°S and 15°N.

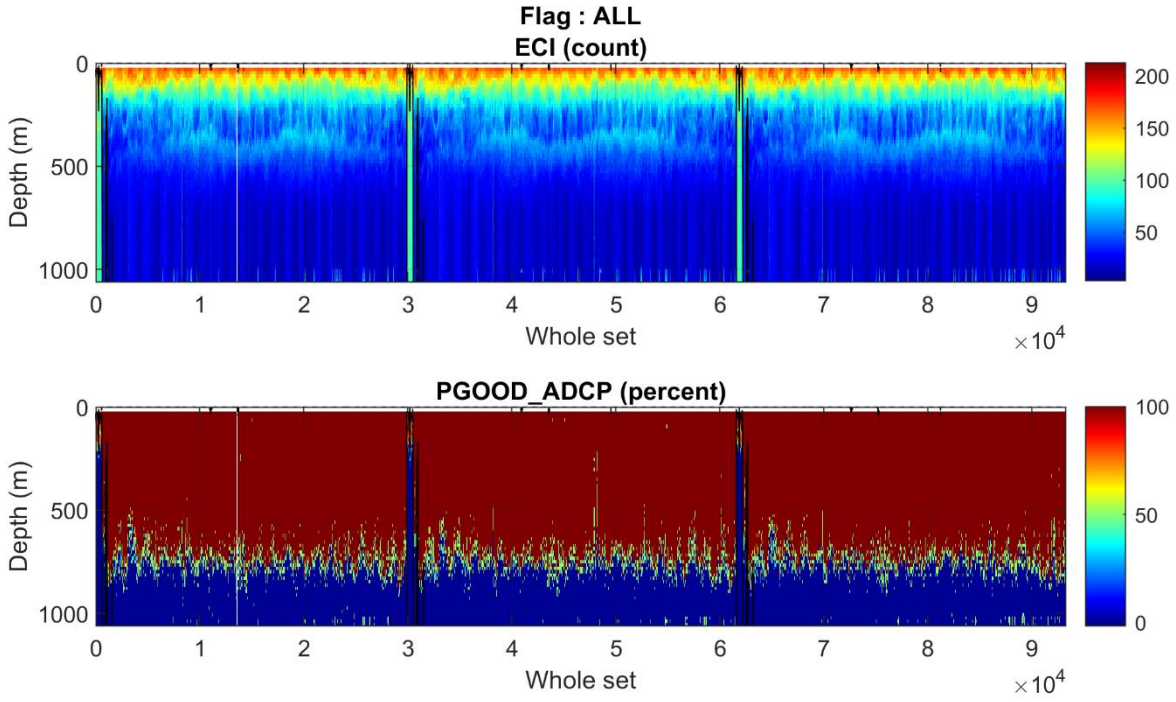

Source: The author (2022).
Figure 15. Mean echo intensity (upper panel) and the percentage of good data (lower panel).

The results during the cleaning process of the data is summarized in Table 2, and only the data with flag 1 are considered to produce the final netcdf file, after correcting the data from the barotropic tide and the navigation errors (misalignment, amplitude and/or pitch); and smoothing horizontally and vertically the data. Then, 15 km average-sections are defined for the 20 minutes averaged files (Figure 14).

Table 2. Flags attributed to PIRATA-BR VXIII data before cleaning.

Flags	Meaning	Percentages
1	Good data	55.17%
2	Doubtful data	13.00%
3	Beyond 30.00 std deviations from the 3 ensembles median value	0.00%
4	Shear > 0.200 s-1	0.00%
5	For error > 1.000 m/s and pgood > 10%	0.00%
6	u, v > 4 m/s	0.00%
7	No data	31.84%
8	Data under bottom	0.00%
9	Invalid data between 2 date	0.00%

Source: The Author (2022).

Figure 16 shows the vector plots of 15 km average-section velocities averaged of the section 1 (Figure 15) from 30 to 94 m depth (depth), and from 94 to 206 m depth (right). Interesting features of the currents are shown in both layers. A strong eastward current is shown on the 30-94 m depth average between 3°N-6°N. It corresponds to the NECC (Urbano et al., 2006, 2008) and is strongly attenuated below 100 m. Another eastward flow is visible between 0°-2°S and is stronger on the 94-206 m average. This current could be the EUC or a recirculation of the SEC which is known to feed the SEUC (Dossa et al., 2020) since it is not centered at the equator. A very weak eastward flow is also shown north of 6°N, around 9°N and can be identified as the northern branch of the NECC which is described by Urbano et al. (2008) as weak flow of the NECC migrating northward. Two westward flow are also shown: one between 0°-3°N which can be identified as the nSEC, and the second, between 2°S-4°S which can be identified as the cSEC. Both currents seem to be stronger within 94-206 m depth. The vertical structure of the currents plotted with CASCADE (Figure 17) gives additional details about the currents on the section 1. The maximum core velocity

of the NECC is shown in the first 100 m depth with a value higher than 100 cm/s while the maximum core velocity of other currents is below 100 m depth.

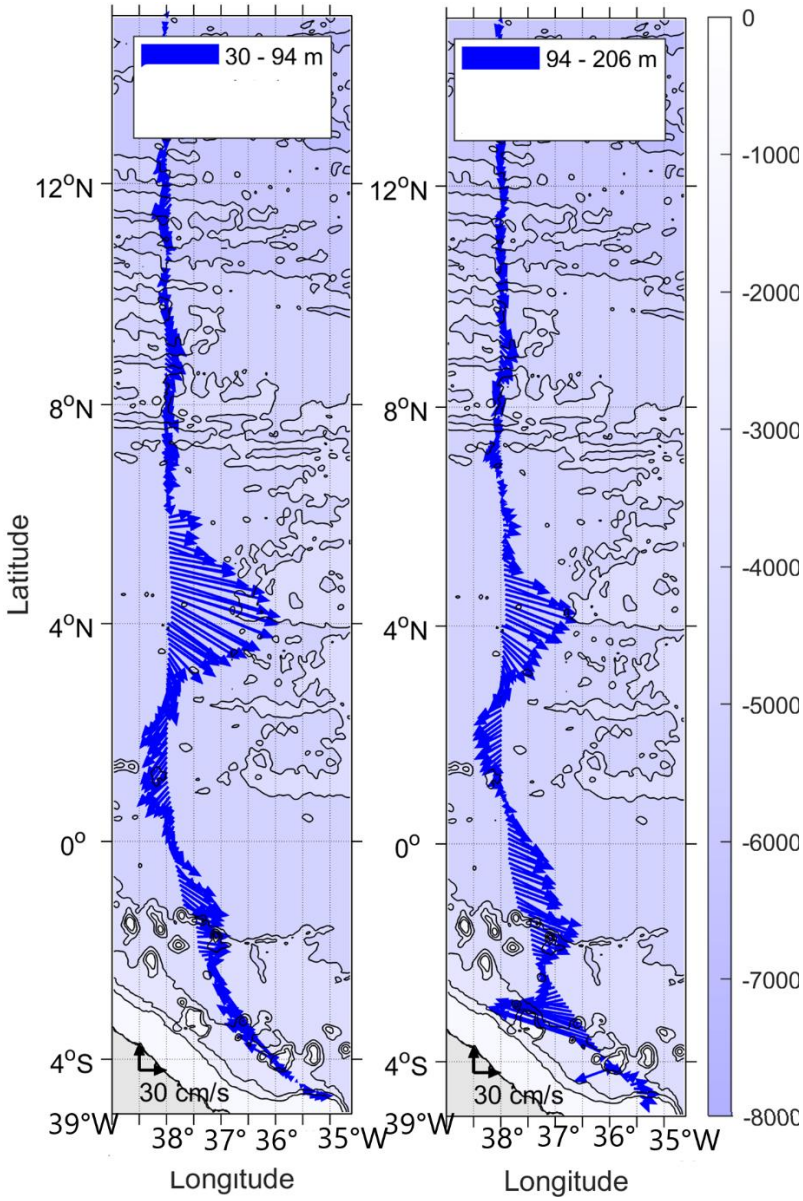

Source: The author (2022).

Figure 16. Vector plots of 15 km average horizontal currents along the section 1 of the selected transect of PIRATA-BR VIII cruise's averaged from 30 to 98 m depth (left), and from 94 to 206 m depth (right) superimposed on the bathymetry ETOPO1 of the area. The arrows are displayed every 1 data point.

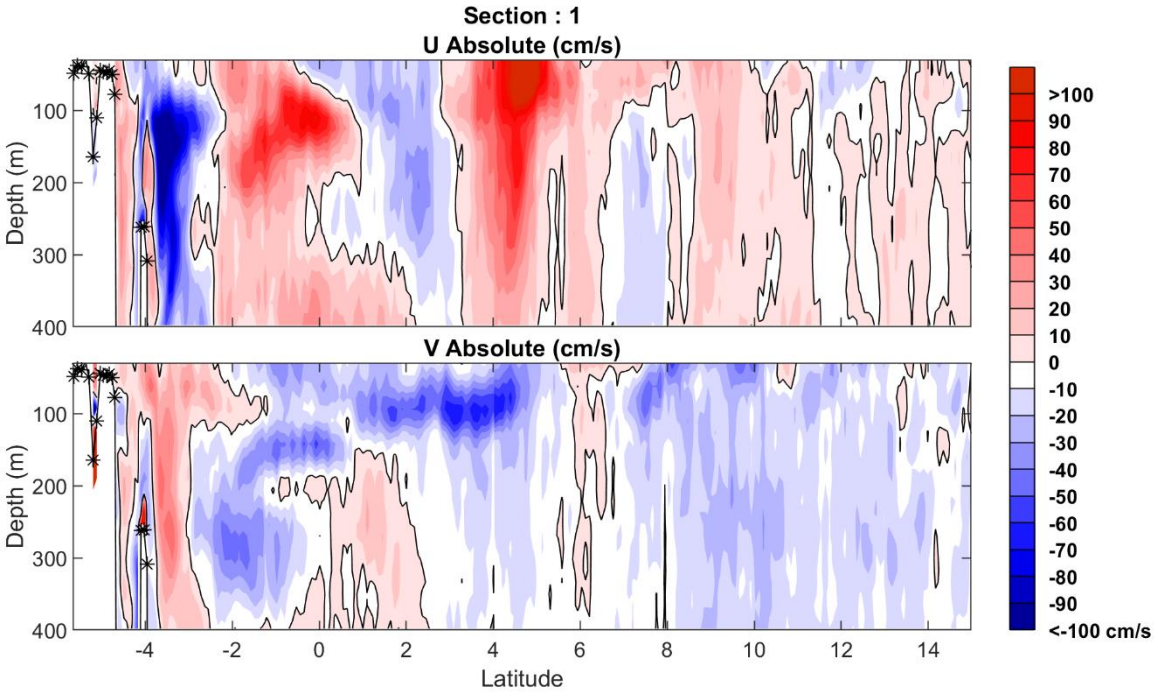

Source: The author (2022).

Figure 17. Vertical distribution of the zonal and meridional currents (in cm/s) function of latitude along the section 1 of the selected leg of PIRATA-BR VIII cruise.

3.2.2.2 Difficulties during the processing of the data and some recommendations

Some difficulties have been encountered during the processing of the SADCP data. They are mostly due to the errors during data recording/collection and are different from a cruise to another. The main issues are listed in Table 3 for the future cruises planification's.

Table 3. Summary of the challenges during the ADCP data processing for the PIRATA-BR cruises held between 2001 and 2018

Cruises	Year	Type of SADCP (kHz)	Difficulties
PIRATA-BR XVIII	2018	OS75	• Noise problem
PIRATA-BR XVII	2017	OS75	• Only STA for NB available • Noise problem • Low range at some locations
PIRATA-BR XVI	2015	OS75	• Both BB and NB files in the same files • Problem with BB files • NB files ok
PIRATA-BR XV	2014	OS75	• Big calibration problem • Very poor range • Lot of data gaps
CAMADAS FINAS III	2012	OS75	• Low range • Lot of acquisition gaps
PIRATA-BR XIII	2011	OS75	• Good range • Lot of acquisition gaps
PIRATA-BR XII	2010	BB75	• Problem with beam 4 • Some non-chronological GPS data
PIRATA-BR XI	2009	BB75	• Very low range
PIRATA-BR X	2008	BB75	• Heading problems • Very low range
PIRATA-BR IX	2006	BB75	• Heading problems • Low range
PIRATA-BR VIII	2005	BB75	• Very low range
PIRATA-BR VII	2004	BB75	• Some LTA files corrupted • Some non-chronological GPS data • Low signal power • Poor range
PIRATA-BR VI	2003	BB75	• Some LTA files corrupted • Some non-chronological GPS time • Big data gaps
PIRATA-BR V	2002	BB75	• Some LTA files corrupted • Lot of bad data • Unrealistic barotropic U or V
PIRATA BR IV	2001	BB75	• Lot of bad data • Barotropic unrealistic U or V • Poor range

Source: The Author (2022).

To avoid the problems encountered during the processing, and contribute to the efforts of the scientific community of Brazil to provide good ocean current data, some recommendations need to be implemented. First, it will be good to establish a policy for handling and storing the data which will be recorded during all the cruises. Before every cruise, it will be required to ensure that, the ADCP hardware and software, and all the ancillary equipment for use with the ADCP such as the

GPS are working properly and are configured consistent with the policies established. Second, the team onboard of the research vessel for the measurements should be aware of all the guidelines and the best practices for the recording of the data. And third, for a permanent availability of all cruise measurement files, we suggest to have a permanent storage location for archival and backup of the field computer data to avoid losses which have been noticed over the years for some cruises.

3.2.2.3 Data archiving and data access

The processed SADCP datasets from the 15 years of PIRATA-BR and CAMADAS FINAS III cruises were archived in netcdf files and made available on SEANOE (Sea Scientific Open Data Edition) data repository for open access. The access to the netcdf files can be found respectively on https://doi.org/10.17882/80771 and https://doi.org/10.17882/80828.

3.2.3 Main datasets used for the study

To pursue this study, data from different source have been used. The climatology of the near-surface currents from drifters and the 38°W section of PIRATA-BR cruises SADCP current data processed with CASCADE have been used to compare with G12V1 currents reanalysis respectively in the WTNA and at 38°W; and this latter have been used to investigate the variability of the NECC at 38°W over 1993-2018 period. Then, the altimetry-satellite geostrophic currents were also used to study the variability of the surface currents of the WTA and pursue later with the 4D G12V1 reanalysis to investigate the vertical structure and the volume transport of the currents.

During the investigations, the wind and SST data were also used. The wind data helped to investigate the influence of the large-scale wind on the variability of the WTA while the SST data allowed to compute the ACM indexes in order to find the possible relationship between the ACM and the currents. The SSS data have been also used to show the spread of the low salinity water into the NECC. More details about all the data is given in the Chapter 4 and 5.

3.2.4 Supplementary data

Supplementary data were also used to do some investigation prior to the study. The salinity and the temperature profiles from G12V1 product were used to compute the MLD and the BLT in the WTA. The results of the spatial variability were similar to the previous studies (eg. de Boyer Montegut et al., 2004; 2007; Mignot at al., 2007; Araujo et al., 2011; Assunção et al., 2020) and

were in good agreement with the variability of the ADT in the study area (see sections 2.5 and 2.6). This give more credit to G12V1 to be used.

The more recent Hadley Centre Sea Ice and SST dataset (HadISST), version 1.1 from Met Office Hadley Centre for Climate Prediction and Research (Rayner et al. 2003) has been also used. The monthly data are available on https://www.metoffice.gov.uk/hadobs/hadisst/ over 1870-2020 with a spatial resolution of 1°. The EOF analysis have been performed on the HadISST SST over 1910-2020 period to evidence the two dominant modes of the TA (see section 2.7) and compare their principal components to the indexes calculated by using the boxes mentioned in section 2.7. The correlation between the AMM principal component and the SST anomalies difference between the northern box and the southern box usually used to calculate the AMM index (Servain, 1991) gives a coefficient of 0.91. The correlation between the principal component of the AZM and the ATL3 index (Zebiak, 1993) gives a coefficient of 0.84. These results are satisfactory but show that the ACM indexes using the SST anomalies in their boxes can be biased. The differences between the principal components and the indexes calculated considering the boxes can be due to the numerical errors. However, the comparison of the time series over 1993-2020 period (Figure 18) shows the same strong events described in the literature (Foltz and McPhaden, 2006; Hormann and Brandt, 2009; Marin et al., 2009) and allows us to considerer the SST anomalies in the AMM and AZM boxes to calculate their indexes for the rest of our study. This consideration is also motivated by the previous studies (e.g., Hormann et al., 2012) which proceed in the same way in order to make a good comparison with these latter. Over the 2017-2020 period, the AZM/AMM shows strong positive/negative event in 2019/2018-20192018-2019. The end of 2019 witnesses two strong opposite events of AMM and AZM like in 1997, 2005 and 2008 which has been mentioned in the literature. More attention might be given to these events in future studies to understand their relationship with the regional climate and circulation.

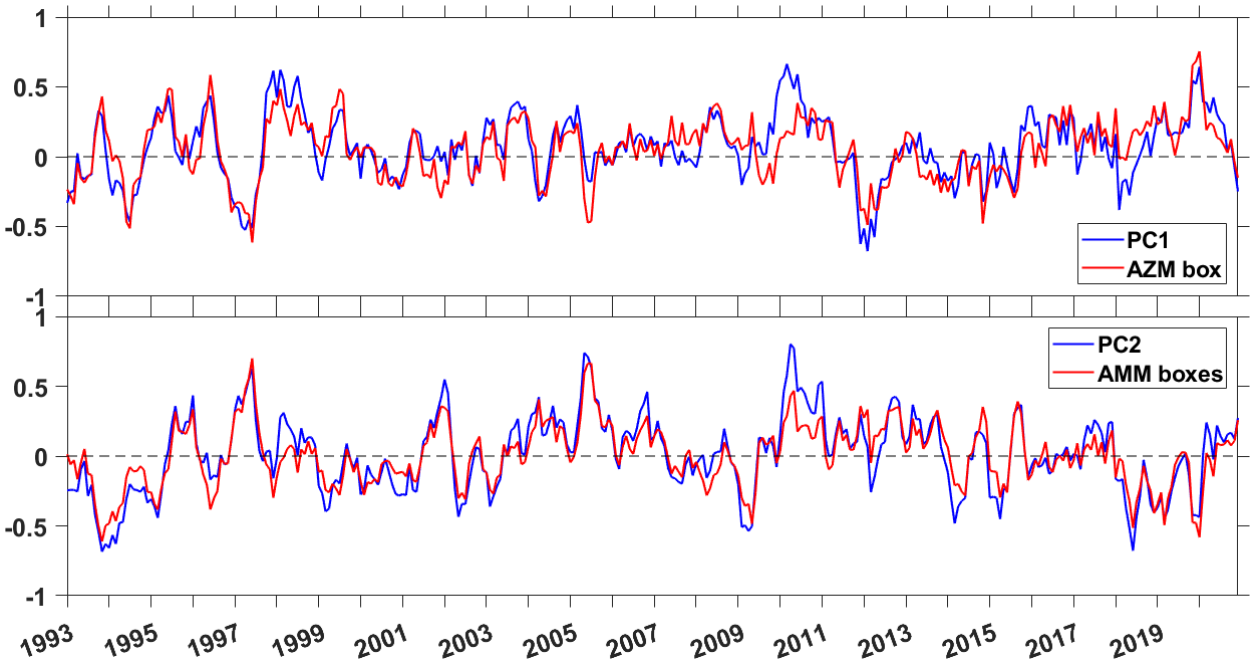

Source: The author (2022).

Figure 18. Comparison between the times series of the principal component of the AZM and the SST anomalies averaged in the ATL3 box (top panel), and the principal component of the AMM and the difference between the averages of the SST anomalies in the northern and the southern boxes of the AMM (bottom panel). The times series are normalized with maximum values of the absolute values of each time series over 1910-2020 period. The principal components are in blue color, and the indexes calculated with the AZM and AMM boxes are in red color.

3.2.5 Estimation of the water volume transport

To estimate the volume transport in our study, the vertical profiles of the currents are interpolated each one meter, and then, the transport is calculated by integrating the velocity over the depth and the width of the positive current (northward or eastward) or negative current (southward or westward) following Burmeister et al. (2019):

$$T = \int_{Di}^{Df} \int_{Zs}^{Z} U_f . d\,x . dz \tag{3.1}$$

Where U_f is the velocity of the flow; x is the latitude, converted into meters; and z is the depth of the water column, also in meters. Di and Df are respectively the lower and the higher latitude of U_f; and Zs and Z are respectively the reference depth at the surface, and the depth limit for calculating of the transport.

For a better estimation of the volume transport in our study, it has been determined through the vertical section perpendicular to the current fields.

All the data and analyses described above will help to perform our investigations. In the following chapters, the main datasets will be used to revisit the spatial variability of the WB currents branches at the seasonal and interannual timescales. The variabilities of the circulation will be investigated in relation to the large-scale wind variability in the TA and the ACM.

4 EVALUATION OF GLORYS12V1 REANALYSIS AND STUDY OF THE SEASONAL AND INTERANNUAL VARIABILITY OF THE NORTH EQUATORIAL COUNTERCURRENT AT 38°W

In this chapter, we are going to validate the monthly estimates of G12V1 currents data by comparing them to the near-surface drifter currents in the whole WTA to assess it at the near-surface. To have a closer look of the capability of G12V1 to reproduce the two-core structure of the NECC which is the subject of investigation of this chapter, we are also going to compare the daily G12V1 current velocity to the SADCP current velocity available at 38°W between 2°-15°N. And after the validation, the monthly estimates of G12V1 currents are going to be used to investigate the interannual variability of the NECC. The following paper 1 carried out the whole study.

Paper 1: Variability of the Atlantic Ocean North Equatorial Countercurrent from 15 years of ADCP Observations and GLORYS12V1 Reanalysis

Djoirka M. Dimoune[1†], Fabrice Hernandez[1,2*], and Moacyr Araujo[1,3‡]

[1]Laboratório de Oceanografia Física Estuarina e Costeira (LOFEC), Departamento de Oceanografia da Universidade Federal de Pernambuco (UFPE).

[2]LEGOS, Université de Toulouse, CNES, CNRS, IRD, UPS (Toulouse), France

[3]Brazilian Research Network on Global Climate Change (Rede CLIMA).

Corresponding author: Dimoune Djoirka Minto (pmintodimoune@gmail.com)

† Departamento de Oceanografia da Universidade Federal de Pernambuco (UFPE), Cidade Universitária, Avenida Arquitetura s/n, 50740-550 Recife, PE, Brazil.

* LEGOS, 18 avenue Edouard Belin, 31400 France.

‡ (Rede CLIMA), Av. dos Astronautas, 1758, 01227-010 São José dos Campos, SP, Brazil.

Key Points:

- The GLORYS12V1 reanalysis is validated by the near-surface drifter current and the ADCP data for the North Equatorial Countercurrent study.
- The seasonal changes in the wind stress curl lead to the North Equatorial Counter Current branches transport with 1- and 2-month delay.
- The North Equatorial Countercurrent branches interannual variability (transport/location) is associated to the tropical Atlantic climate Modes/migration of the Intertropical Convergence Zone.

Prepared to be submitted to JGR-Oceans:

Abstract

The North Equatorial Countercurrent (NECC) contributes to the Atlantic Meridional Overturning Circulation by redistributing warmer tropical Atlantic surface waters toward the north and east of the basin, affecting the Sea Surface Temperature (SST) pattern, which, in turn, affects ocean-atmosphere interactions, regional precipitations and the climate. Its structure and variabilities are analyzed using 15 years of velocity data from shipboard acoustic Doppler current profilers at 38°W, from near-surface drifters currents, and from GLORYS12V1 reanalysis. The NECC characteristics from GLORYS12V1 are in good agreement with the other dataset used and are further used to revisit the seasonal and interannual variability from 1993–2018. The NECC is characterized by two branches from July to January, when a second core stand out from the southern branch (sNECC), becomes a northern branch (nNECC) and shifts northward. The nNECC migrates northward following the Intertropical Convergence Zone (ITCZ) seasonal migration with a three-month delay, and then, under the influence of the wind stress. It vanishes in February/March at approximately 11°N. From December to May, the sNECC moves from its 4–6°N position toward 7–9°N and decays, influenced by the strengthening of the Northeast trade winds. The seasonal cycle of both branches transport (1.7 to 24.5 Sv from May to October) is influenced by the wind

stress curl strength with 2-month delay. The NECC transport interannual variations are associated to the tropical Atlantic climate modes: the positive transport anomalies are associated with the opposite phases of the meridional and zonal modes, while the negative anomalies are associated with the same phases of both modes or a meridional mode phase with a weak zonal mode phase.

Keywords:

Tropical Atlantic, Western boundary, NECC, ITCZ, Atlantic climate modes, Observations, Ocean Reanalysis

Plain Language Summary

The North Equatorial Countercurrent (NECC) lies between 3-12°N across the tropical Atlantic, and is essentially driven by trade winds, transporting warm and anomalously saline waters to the east. It is observed during PIRATA cruises at 38°W and its variations since 1993 can be studied by GLORYS12V1 numerical simulation representing ocean circulation. In addition to in-situ observations, the realism of GLORYS12V1 currents allows a complementary view. The NECC seasonal cycle is directly influenced by the northeast and southeast trade winds seasonal regimes. The southern NECC branch starts the cycle in June at approximately 5°N and grows, generating a second core at its northern flank that forms the northern NECC branch during July-August. This branch migrates northward and vanishes after January at approximately 11°N. From December to May, the NECC moves toward 7–9°N, decaying. The NECC system changes over the years in relation to the climate modes which affect the sea surface temperature anomalies in the tropical Atlantic. Over a period of 25 years, we find two main scenarios linking the NECC with these modes: a more intense southern NECC branch is associated with both zonal and meridional modes, while the weaker is associated with the same phases of both modes.

1. Introduction

The Western Tropical North Atlantic Ocean (WTNA) experiences a complex circulation (represented in Figure 1) resulting from direct interactions with the atmosphere and interhemispheric heat, salt and water mass exchanges over the entire Atlantic basin, which are linked to the global circulation (Bourlès et al., 1999a, b; Stramma and Schott, 1999; Urbano et al.,

2008). Wind-driven subtropical gyre circulations from the south and north Atlantic basins feed the western boundary currents in the tropics. Along the Brazilian shelf, the North Brazil Under Current (NBUC) and the North Brazil Current (NBC) transport northward the warmest and most saline waters of the return branch of the Atlantic Meridional Overturning Circulation (AMOC). Between 5°N and 8°N, the NBC undergoes a retroflection (hereafter referred to as the NBCR) to the east that partly feeds in the upper layer, the North Equatorial Countercurrent (NECC) which is the strongest eastward geostrophic current in the area (Bourlès et al., 1999b; Urbano et al., 2006, 2008). The NECC flows across the entire tropical Atlantic to connect with the Guinea Current at 2–4°N (Lumpkin and Garzoli, 2005). It transports toward the eastern side of the tropical Atlantic basin a large part of the heat and salt anomalies (Philander and Pacanowski, 1986). As shown by Schouten et al. (2005), Stramma et al. (2012) or Castellanos et al. (2015), the NECC also transports oxygen-rich waters. Because of its strength and its width, the NECC plays a key role in the variability of the regional climate precipitation due to the amount of heat it spreads eastward of the WTNA basin which participates to enhance evaporation over warmer surface waters (Lindzen and Nigam, 1987). Its path is associated with a zonal band of strong variability of the sea surface salinity (SSS) (Figure 1), which is explained both by evaporation and precipitation. The latter is linked to the spatial variability of the Intertropical Convergence Zone (ITCZ) from spring to fall while the transport of fresher Amazon waters toward the center of the basin which is maximum during the same period of the year strongly affects the variability of the SSS (Masson and Delecluse, 2001, Coles et al., 2013; Varona et al., 2019).

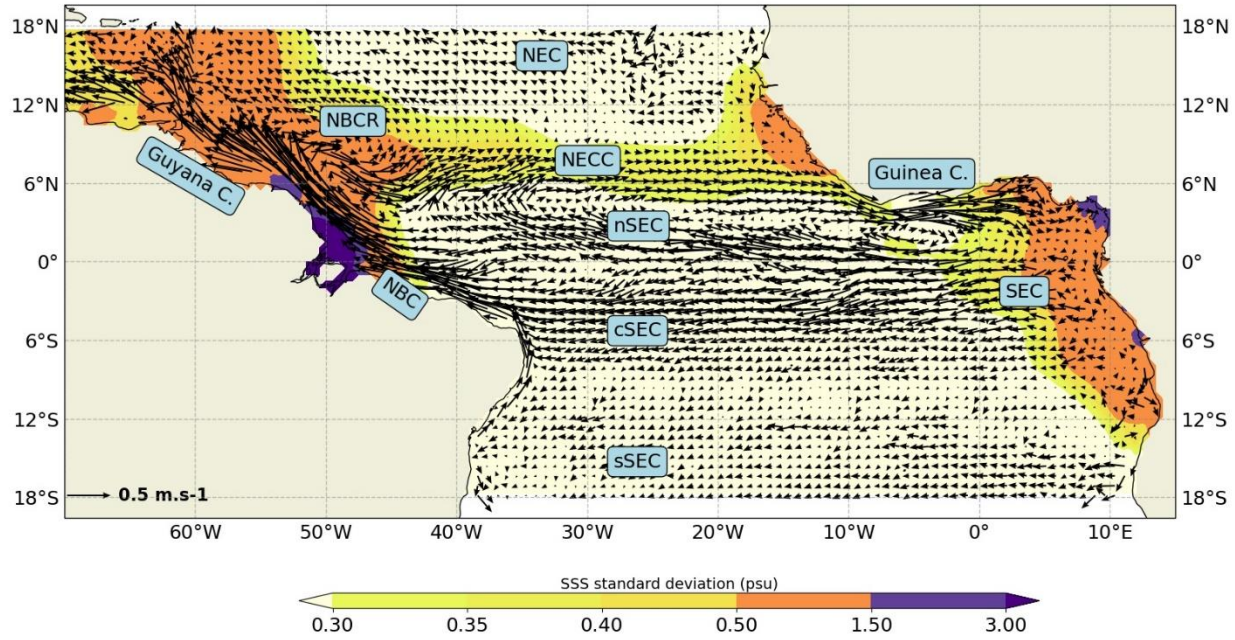

Figure 1. Surface currents from the AOML annual drifter-derived climatology in the tropical Atlantic (units m/s). The standard deviation of the SSS product INSITU_GLO_TS_OA_REP_OBSERVATIONS_013_002_b from CMEMS over 1993-2018 period is superimposed (units psu) with the main currents discussed in the text, which are highlighted

The NECC dynamical explanation and variability have been studied over the last decades using satellite altimetry, hydrographic, acoustic Doppler current profilers (ADCP) data, and model simulations. Garzoli and Katz (1983), using hydrographic data, found the NECC lying between 3°-10°N, and showed the primary influence of seasonal changes in the wind stress curl (WSC) on the underlying thermocline gradient in the area of NECC with a one-two month lag. In other words, the Sverdrup dynamics drives the NECC eastward flow in the central tropical Atlantic and explain its weakening or reversal flow during boreal spring. The NECC exhibits a strong seasonal cycle associated the variability of the wind regimes (Garzoli and Katz, 1983), and is also part of the equatorial gyre. It was shown that its core shifts from 4–6°N (boreal spring) to 6–8°N (boreal summer/fall) following the migration of the ITCZ (Garzoli and Richardson, 1989; Garzoli, 1992). Richardson and Reverdin (1987) found that it reaches a maximum flow in summer, when the ITCZ reaches its northernmost position. It has been found that, along its path, the input of vorticity by the wind is not the only mechanism which influences the NECC's variability. Verdy and Jochum (2005) using a primitive equation ocean model over the tropical Atlantic showed the nonlinear term effects due to the mean flow and the eddy field in the NECC vorticity balance west of 32°W. The

barotropic instability due the shear between the northern branch of the westward South Equatorial Current (nSEC: Figure 1), the southern flank of the NECC are a source of eddy kinematic energy in the central and western tropical Atlantic which is linked to the generation and propagation westward of the tropical instability waves, predominantly in the second half of the year von Schuckmann et al. 2008; Jochum et al., 2004).

Fonseca et al. (2004) studying the NECC's variability west of the 32°W showed its mean positions approximately at 6°N. They found a NECC confined between 3°-10°N, with a semiannual cycle of its position which shows a northernmost location in February and August, associated with northward migrations from June to August and then from December to February. In contrast, they found an annual cycle of for NECC transport with a maximum transport of 12 Sv (Sverdrup) in November. They suggest that the NECC transport in the WTNA is remotely influenced by the WSC strength in the central/eastern part of the basin. This strength results from the difference between the positive-negative WSCs located north and south of the ITCZ, with a peak in August and a 1–3 months lag with the NECC maximum transport. This confirms the hypothesis of delayed Rossby waves propagating from the eastern side and modifying the thermocline gradients in the WTNA (e.g., Garzoli and Katz, 1983; Tuchen et al., 2020). Urbano et al. (2006) confirmed the influence of the nonlinear terms in the vorticity balance at 35°W and also found the influence of the Rossby waves propagation on the NECC transport. More interestingly, when analyzing the shape of the NECC during the year in relation to the wind stress variability, the authors confirmed a two-core structure of the NECC previously mentioned by Schott and Boning (1991) and Didden and Schott (1992). The interpreted the presence of the northern second core during the second half of the year by the width of the convergence zone of the wind due to the migration of the ITCZ. The demonstrated that, both cores are forced by the wind stress second meridional derivative (Urbano et al., 2006). Using the first 6 years of the ship-mounted ADCP (SADCP) of the Prediction and Research mooring Array in the Tropical Atlantic program (PIRATA) cruises along the 38°W transect (Bourlès et al., 2008) and the near-surface drifter current velocities, Urbano et al. (2008) confirmed the presence of a two core of the NECC which separate later to become two branches (sNECC and nNECC for the southern and northern core, respectively). The two-core structure of the NECC appears during the second half of the year and has been shown to be driven by the ITCZ with a 3-month delay. The authors concluded that both cores of the NECC are driven by the WSC which has two lines of zero curl: The ITCZ and the secondary zero line of the WSC north of the

ITCZ. They didn't investigate the variability of the transports associated with both cores, but found that from boreal spring to summer, the subsurface North Equatorial UnderCurrent (NEUC) located south of 5°N in the upper thermocline usually shifts northward when surfacing, and merges vertically with the NECC's southern branch (sNECC) which is stronger during boreal summer.

The interannual variability of the NECC has been less discussed in the WTNA. Fonseca et al. (2004) who analyzed 8 year of hydrographic and satellite altimetry data, have mentioned relevant interannual changes of the NECC's position and transport. They also investigated these changes in relation to the wind variability, but could not find any robust relationship. More recently, the relationship between the NECC system interannual variability and the tropical Atlantic climate modes has been studied by Hormann et al. (2012) using 17 years of geostrophic currents and drifter trajectories. They found a relationship between the NECC's interannual changes and the Atlantic climate modes (ACM) through a response of changes in the wind patterns: the northward shift of the NECC's core was associated with the warm phase of the Atlantic Meridional Mode (AMM) phased in boreal spring, whereas the NECC intensity was associated with the cold phase of the Atlantic Zonal Mode (AZM), phased in boreal summer. These two modes are the two dominant interannual modes in the tropical Atlantic that also influence regional climate and rainfall anomalies over northeastern Brazil, the surrounding regions of the Gulf of Guinea and the Sahel (Cabos et al., 2019). In terms of mechanisms, the authors suggest that seasonal forcings and corresponding NECC responses also prevail for interannual extreme events. The southern flank of the NECC is influenced by equatorial wind anomalies, while interannual variation in Rossby waves generated in the northeast tropical Atlantic by wind curl anomalies tends to influence the northwestward displacement of the NECC system (Hormann et al., 2012).

Currently, global ocean reanalysis GLORYS products provide a consistent description of ocean circulation at the mesoscale over long periods. These numerical simulations offer reasonable reliability due to the improvement of ocean models, reduction of errors in atmospheric forcings, and the intensive use of sophisticated assimilation techniques that profit from the increasing number of ocean observations every year (e.g., Storto et al., 2019). The recent GLORYS12 reanalysis which has been released by the Copernicus Marine Environment Monitoring Service (CMEMS) has been extensively evaluated (Lellouche et al., 2021). It has been used in the South Atlantic Ocean to study the large and mesoscale dynamics of western boundary currents and has been found better compared to several kinds of observations from synoptic to longer time scales

(Artana et al., 2018, 2019; Poli et al., 2020). Hence, the GLORYS12V1 reanalysis (hereafter G12V1) has been chosen to be compared to 15 years of vessel-mounted acoustic Doppler current profilers (SADCP) data at 38°W and drifters' monthly climatology to validate its use and to use it for the investigation of the seasonal and interannual variability of the NECC.

The purpose of this study is to study the variability of the two core/branches structure of the NECC (transport, velocity field) which is less discussed in the literature. This will be done by using G12V1 reanalysis over 1993-2018 period to investigate the seasonal and interannual variability of its characteristics at 38°W after validation. During the study, we will be looking for the relationship between the variability of the NECC, the variability of the wind and the ACM. This work is presented in four parts. First, the data (ADCP section, drifter climatology, G12V1 reanalysis and ERA-5 wind) are described. Next, the circulation in the WTNA is discussed, comparing drifter-derived current climatology to the general patterns from the G12V1 reanalysis and the vertical profiles of the zonal velocity of the currents from the SADCP at 38°W to the G12V1 daily estimates. Section 4 is devoted to reassessing the NECC seasonal and interannual variability taking advantage of the longer period of G12V1 data. Finally, the results are discussed before presenting a conclusion. As a reminder, in this work we use the boreal seasons definition referring to the Northern Hemisphere.

2. **Data and Processing**

2.1. ADCP data processing

Since 2001, 15 SADCP surveys have been performed onboard Brazilian research vessels in the vicinity of the 38°W section. First, the data were obtained by Brazilian cruises servicing the PIRATA moored buoy program yearly. Until 2016, Research/Vessel (R/V) Antares equipped with an Ocean Surveyor 75 kHz ADCP system was used. Then, the brand-new R/V Vital de Oliveira took over, equipped with two Ocean Surveyor ADCPs, working at 75 kHz. To complete our dataset, we use ADCP profiles obtained during the Camada Finas III experiment, which occurred 9–31 October 2012 with the research vessel NHo. Cruzeiro do Sul - H38 (DHN/Brazilian Navy), equipped with a Teledyne RD Ocean Surveyor ADCP working at 75 kHz. All these SADCPs used Vessel-mounted Data Acquisition System software (VmDAS) to collect vertical profiles data along the ship route. These measurements (ship velocity and currents velocity relative to the ship) are averaged over 2 minutes (STA: short-term averaged files) and 5 minutes (LTA: long-term averaged

files) onboard. For this study, ADCP data from every cruise along the repeated section at 38°W from 2°N to 15°N are selected, even if the Camadas Finas III cruise only sampled this section from 2°N to 8°N. Table 1 summarizes the different durations of sections considered, the seasons during which data were collected, and other information about the cruises.

Under good sea-state conditions, the 75 kHz SADCP data can provide reliable upper ocean velocity profiles down to 600 m depth. It can be reduced to less than 100-m depth in the case of bad sea-state conditions, associated most of the time with intensified trade winds and larger waves. In this case, the ship stability along its route is reduced and the acoustic signal penetration is unable to reach the deepest layers (Urbano et al., 2008). During the 2014 cruise, the maximum depth reached was less than 100 m. The acoustic downward ping was processed in 8-m length bin vertical resolution. Near the surface, velocity profiles are considered reliable from a defined depth downward, between the bin 3 and bin 5.

Table 1. Name and characteristics of PIRATA-BR and Camadas Finas III cruises at the section 38°W: cruise, year, latitudinal coverage, duration of the section, and research vessel.

Cruise	Year	Latitud. coverage	Duration of the section	Boreal season	Research Vessel
PIRATA BR XVIII	2018	2°N-15°N	19–26 October	Fall	Vital de Oliveira
PIRATA BR XVII	2017	2°N-15°N	14–22 November	Fall	Vital de Oliveira
PIRATA BR XVI	2015	2°N-15°N	27 October to 03 November	Fall	Antares
PIRATA BR XV	2014	2°N-15°N	23–28 July	Summer	Antares
Camadas Finas III	2012	2°N-8°N	27–31 October	Fall	Cruzeiro do Sul
PIRATA BR XIII	2011	2°N-15°N	23 August to 13 September	Summer	Antares
PIRATA BR XII	2010	2°N-15°N	24–30 July	Summer	Antares
PIRATA BR XI	2009	2°N-15°N	26–31 March	Spring	Antares
PIRATA BR X	2008	2°N-15°N	02–08 April	Spring	Antares
PIRATA BR IX	2006	2°N-15°N	01–07 December	Fall	Antares
PIRATA BR VIII	2005	2°N-15°N	14–19 July	Summer	Antares
PIRATA BR VII	2004	2°N-15°N	27–31 July	Summer	Antares
PIRATA VI	2003	2°N-15°N	17–31 July	Summer	Antares
PIRATA BR V	2002	2°N-15°N	05–12 April	Spring	Antares
PIRATA BR IV	2001	2°N-15°N	09–15 April	Spring	Antares

The ADCP STA files were processed and calibrated using CASCADE (Chaîne Automatisée de Suivi des Courantomètres Acoustiques Doppler Embarqués) software, developed at Ifremer Laboratoire de Physique de Océans (LPO, Brest, France) (Kermabon et al., 2018). Each individual vertical profile was considered reliable if over 50 percent of the values between bins 3 and 5 were good. ETOPO/GEBCO bathymetry along the ship route is used to discard bins contaminated by seafloor interference. The absolute current velocity along the vertical profile is computed using the

standard shipboard gyroscopic compass heading and navigation from the Global Positioning System (GPS). Then, the data were flagged using a threshold of the vertical speed to 100 cm/s; the vertical shear to 0.2 s^{-1}; the maximum current speed to 400 cm/s; a discrepancy to the averaged surrounding pings less than 3 standard deviation; a threshold ratio signal/noise value larger than 60; and the profile is kept if more than 10% of the bins are not erroneous (see Kermabon et al., 2018). If needed, the misalignment and amplitude error detected have been corrected. The data are also corrected from barotropic tide using the model TPOX9 (Egbert and Erofeeva, 2002). Once validated, the 2-minute vertical profiles are low-pass filtered over 20 minutes at each depth. Finally, along the ship route, the vertical section is resampled every 15 km horizontally to provide a series of reprocessed profiles for each ADCP leg used in this study (Araujo et al., 2021a, 2021b). This dataset provides a unique opportunity for a close look at the two branches structure of the NECC along 38°W, between 2°N and 15°N, and are used to validate G12V1 for the study of the time variability of structures throughout the year and from year to year.

2.2. GLORYS12V1 global ocean reanalysis

The G12V1 reanalysis, described extensively by Lellouche et al. (2021), provides a 3D description of the ocean circulation at the mesoscale in the WTNA. Global ocean numerical simulations offer a self-consistent representation of the circulation from the surface to the bottom, anywhere in the world ocean, and in a continuous timeline. The Mercator Océan G12V1 reanalysis delivered by the CMEMS (https://marine.copernicus.eu/) covers the period from 1993–2018, with a 1/12° horizontal resolution. In summary, it is based on the 1/12° global operational system of the Mercator Océan (Lellouche et al., 2018). This reanalysis uses the NEMO3.1 ocean/sea-ice general circulation model (Madec, 2008), with the ORCA12 global configuration developed by the DRAKKAR consortium (Barnier et al., 2014) with 50 vertical levels. It is forced at the surface by the ECMWF ERA-Interim reanalysis after some specific corrections. Throughout the simulation, data assimilation is performed using a reduced-order Kalman filter with a 3D multivariate modal decomposition of the background error, which includes an adaptive-error estimate and a localization algorithm. CMEMS along-track altimeter data (sea level anomaly – SLA), satellite sea surface temperature (SST), and sea ice concentration are assimilated together with in situ temperature and salinity (T/S) vertical profiles from the CORA database (Cabanes et al., 2013). Moreover, a 3D-VAR scheme provides a correction for the slowly evolving large-scale biases in

temperature and salinity. The simulation is initialized using the T/S conditions derived from the EN4.2.0 database (Good et al., 2013). The G12V1 overall reliability is addressed by Lellouche et al. (2021) and the CMEMS QuID Report (Drévillon et al., 2018), which show a significant reduction in T/S bias thanks to the availability of Argo data in 2001 and is associated with a faithful reproduction of the mean sea level. They exhibit a better representation of the AMOC transport than previous estimations, with meridional heat transports consistent with known values. Their Eddy Kinetic Energy (EKE) comparison with independent products (Figure 10 in Lellouche et al., 2021) also shows a better reproduction of mesoscale activities over the global ocean western boundaries. Therefore, G12V1 appears interesting for upcoming studies in the WTNA.

In the present work, the G12V1 official product GLOBAL_MULTIYEAR_PHY_001_030 (DOI: https://doi.org/10.48670/moi-00021) which includes both the daily and monthly mean files of ocean variables is used. The daily horizontal velocity is interpolated under the ADCP section at 38°W every 15 km to match the ADCP, and both re-gridded vertically every meter in order to be able to find the core position in both products and compare them. Then, G12V1 monthly estimates over the tropical Atlantic are downloaded for our seasonal and interannual analysis of the NECC.

2.3. Other datasets

The drifter-derived climatology of near-surface currents based on surface drifter trajectories from the Global Drifters Program (GDP) between 1979 and 2015 is used. It was produced by the Atlantic Oceanographic and Meteorological Laboratory of the National Oceanic and Atmospheric Administration (AOML/NOAA, http://www.aoml.noaa.gov/phod/dac/index.php) (more details can be seen in Laurindo et al., 2017). From the 12 months of this climatology data, we extracted the tropical Atlantic area between 15°S-15°N and 25–70°W to compare with our estimation of the G12V1 monthly climatology results.

The ERA5 product provides surface wind information produced recently by the European Centre for Medium-Range Weather Forecasts (ECMWF, http://www.ecmwf.int) from January 1950 to near real time (NRT) and distributed by the Copernicus Climate Change Service (C3S). ERA5 combines a large amount of information into global estimates using advanced modeling and a 4-dimensional variational analysis with a 12-hour analysis window (details at https://confluence.ecmwf.int/display/CKB/ERA5+data+documentation). Ten-meter height monthly zonal and meridional component wind velocity fields with a spatial resolution of 31 km

(0.28125 degrees) from 1993 to 2018 were used in this work. From these data, we compute the wind stress and its curl using empirical formulations (Large and Pound,1981; Gill, 1982; and Trenberth et al., 1990) and following NRSC (2013). Then, we derive the WSC strength in the tropical Atlantic following Fonseca et al. (2004) to measure the influence of the wind regimes east of 30°W on the NECC system at 38°W. Finally, the ITCZ position and the secondary zero line of WSC are estimated as the latitude where the absolute value of the wind stress meridional component is minimum (Servain et al., 1985) and are located between two WSCs of opposite signs.

The National Oceanic and Atmospheric Administration (NOAA) produces a weekly SST global product on a 0.25° grid using the optimum interpolation (OI) analysis method: NOAA OI SST v2. This analysis uses in situ and bias-corrected satellite SSTs. Technical details are given by Reynolds et al. (2002). From this weekly dataset, monthly global SST averages are also produced (available at https://www.esrl.noaa.gov/psd/data/gridded/data.noaa.oisst.v2.html). We considered this monthly dataset from 1993 to 2018 over the tropical Atlantic.

From the CMEMS, the monthly SSS gridded data are also downloaded from 1993–2018 in the tropical Atlantic (product name INSITU_GLO_TS_OA_REP_OBSERVATIONS_013_002_b). The grid was produced by the ISAS objective mapping tool on a 0.5° grid (Gaillard et al., 2016) using in situ temperature and salinity edited and corrected by the Coriolis data Center.

3. Circulation patterns from drifters, G12V1 reanalysis and ADCP sections

3.1. The Western Tropical Atlantic general circulation from drifters and G12V1 reanalysis

The general circulation is reviewed in the introduction and illustrated using the AOML surface drifter annual climatology (Figure 1). A complementary view can be obtained through the G12V1 reanalysis time average surface current field. Indeed, through assimilation of T/S profiles, satellite altimetry and radiometric products, G12V1 is constrained by a large number of observations available in the tropical Atlantic. Its global validation shows its overall reliability, with the large-scale circulation correctly represented (Drévillon et al., 2018; Lellouche et al., 2021). In particular, Lellouche et al. (2021) compare global G12V1 currents against non-assimilated drifter individual trajectories, providing 15 m-depth currents, and they show strong agreements on

mean zonal currents. Hence, the common analysis with AOML climatology offers new insights into WTNA seasonal variability.

The AOML drifter-derived surface current monthly climatology provides a detailed representation of the seasonal pattern of the near-surface circulation (figure not shown). Equivalent climatology data can be obtained by averaging the G12V1 numerical simulation. By this construction, the time average estimates from the G21V1 reanalysis are statistically more temporally and spatially consistent than the time average estimates from the AOML product, which depend on the distribution in space and time of the drifter trajectories. The AOML mean surface current estimate in a given location will be more accurate as the number of drifter samples is higher and regularly distributed over time. Moreover, the interpolation techniques used to build gridded products from observations usually do not guarantee dynamical continuity and conservation properties of the flow in the ways an ocean model would. On the other hand, the ocean reanalysis accuracy depends on model errors, effectiveness of the assimilation techniques, and density and availability of observations to guarantee the expected accuracy (Lellouche et al., 2021). This is the reason why we propose here to commonly analyze the AOML and G12V1 circulation climatological cycles prior to any further analysis. This is also a way to demonstrate the strengths and weaknesses of the G12V1 large-scale surface circulation in the WTA.

The G12V1 monthly mean currents from 1993 to 2018 are first averaged over the 5–15-m depth layer to correspond to the AOML surface current estimates from the SVP drifter trajectories. Then, the annual mean and the 12-month climatology means are produced, with a focus on the 15°S-15°N, 70°W-25°W region. Due to the denser resolution of the G12V1 grid (1/12° versus ¼° for AOML), the nearest grid points between each grid are selected. Although averaging periods in the two products are not identical (the AOML product gathers drifter data over 1979–2015), the annual mean comparison between AOML and G12V1 (figure not shown) indicates a satisfactory match between positions of the NBC and NBCR, the nSEC, the cSEC and the NECC. The NBCR and NECC connection is shown between 3–10°N in both products, as in Fonseca et al. (2004). The NECC annual mean signature presents a meandering pattern between 42°W and 44°W, as was also mentioned by Garzoli and Richardson (1989) and Garzoli (1992). Figure 2 shows the NBCR and NECC systems weaker (May) and stronger (October) climatological patterns. In October, the sNECC is fully developed, bifurcates and extends toward the north into the nNECC, which is also partially fed by an eastward flow coming from the NBCR.

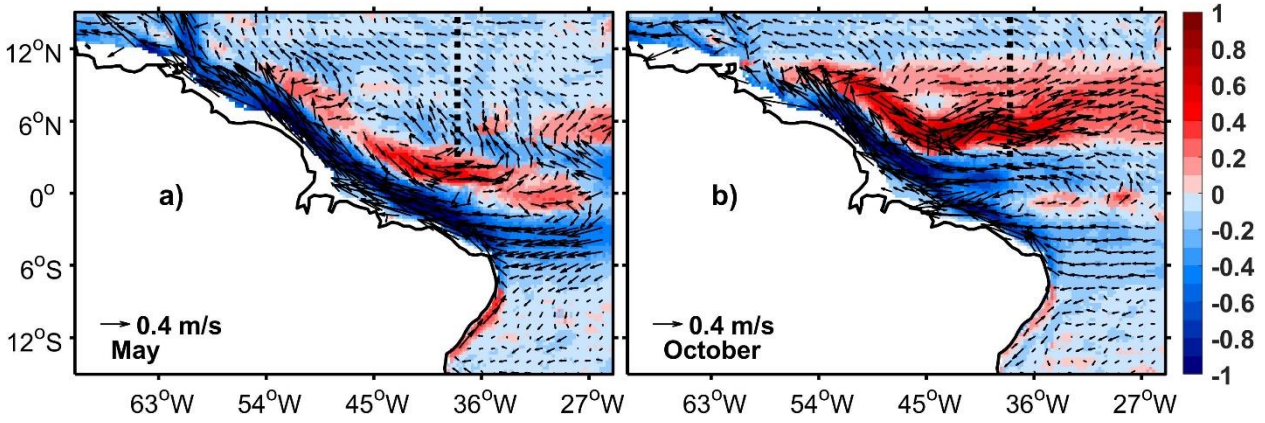

Figure 2. Monthly climatology of the AOML current during May (a) and October (b). Shading corresponds to their speed (colorbar in m/s). Red (blue) color for eastward (westward) flows. The dashed black line represents the section at 38°W.

From the two annual mean products, maps of the speed ratio (AOML divided by G12V1) and velocity relative angle between AOML and G12V1 are computed (Figure 3).

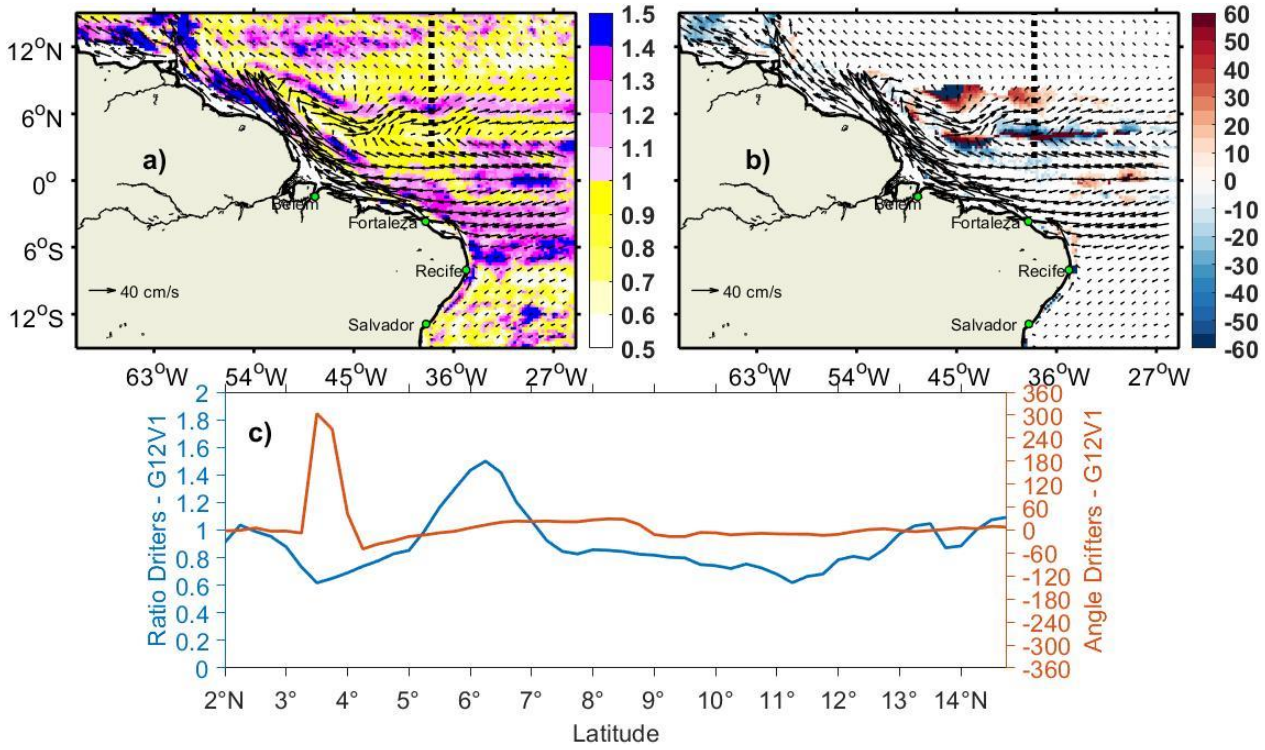

Figure 3. G12V1 annual mean circulation superimposed on a) the ratio of the speed between AOML and G12V1, and on b) the angle difference between AOML and G12V1 in 15°S-15°N, 70°W-25°W. c) The speed ratio and the angle difference for the 38°W section from 2°N to 15°N. This section is indicated by the black dashed lines on a) and b).

On average, over the given area, the speed ratio is 0.98 (varying between 0.6 and 1.5). Along the main currents (the nSEC, cSEC, NBC, NBCR, and NECC in the 4.5–7.4°N band), the AOML speed is higher (ratio larger than 1.), but with the signature of G12V1 being higher at the nSEC location between 36°W and 45°W, and parts of NECC location (yellow band at the edge of purple color in Figure3a). This demonstrates a relative lateral shift of these currents between the two products. The relative angle values (Figure 3b) are on average below 20°, but they are higher along the edge of the NECC's path with higher G12V1 signature. The lateral shift of the currents of the two products is confirmed by differences at 38°W, where a larger angle difference appears at approximately 3.5°N, and the ratio is lower (slightly lower) than that between 5.1–7.1°N (the mean ratio) (Figure 3c). The NECC's meandering movement in the annual climatology does not exactly match in either product. Their differences also witness AOML possible errors in the region where the ratio and angles are not uniform. As already mentioned, uneven drifter distribution in time and space hampers the ability of the interpolation scheme, whatever its quality, to produce reliable surface velocity estimates on the grid. Figure 1 of Laurindo et al. (2017) shows that the WTNA is a region not well sampled by drifters, and larger errors can be expected in this area with AOML climatology results. For the same reasons, the coastal areas where fewer drifters are advected may also present higher error levels. This might explain the large ratio along the inner shelf flank of the NBC. Moreover, regions of high kinetic energy associated with stronger eddy activity or stronger mean currents might not be sufficiently sampled over time by the drifters and may bring some aliased estimates of the mean surface currents. This can also be the case on the southern flank of the NECC.

In the vicinity of the NECC at 38°W, the G12V1 and AOML climatological cycles show some differences in the amplitude of the currents (Figure 4). As mentioned above, the relative accuracy of the G12V1 and AOML circulation seasonal cycles is difficult to infer due to their specific drawbacks. However, their differences indicate where our results need to be further analyzed. In May, both products show a westward flow north of 3°N at the location of the average position of the NECC. An eastward flow is shown south of 3°N, extending northward to become the sNECC in June. It is weaker and less extended to the north in G12V1 compared to AOML. The sNECC grows and migrates northward from June to November in both climatologies, although its main position in November/December is shifted southward by approximately 1° latitude in G12V1. In August-September, the sNECC exhibits a two core/branch structure in both products, with the

northern branch disappearing at the end of the year. From December to April, the nSEC strengthens in both climatologies, extending northward, and the sNECC migrates again northward, weakening until reaching ~8°N and then vanishing.

The differences between G12V1 and AOML climatological cycle estimates from September to January might be caused by various factors. First, the two climatologies are computed over different periods (1979–2015 versus 1993–2018), which may create some biases. Second, as mentioned above, the NECC mean location and shape from drifters might be mispositioned due to higher variability, with growing errors at the NECC's flank. Third, differences between AOML and G12V1 intensity and position of the NECC could be caused by differences in their Ekman component at 38°W. The processing aimed at removing direct wind entrainment of the drifters (slip effect) might have biased the Ekman component of the AOML surface currents compared to G12V1 upper dynamics mixing and direct response to wind forcing. Ekman currents at 38°W are westward or northwestward, dominated by northeasterly trade winds from December to May between 4–8°N (see Figure 9a below), that is, in the opposite direction of the NECC. Finally, the G12V1 dynamics at the surface and the model approximation tend to produce currents weaker than reality: ocean atmosphere coupling is still lacking from fine scale effects of waves, high frequency mixing in the upper layer, and atmospheric feedbacks in the marine boundary layer not reproduced in the atmospheric forcing (Lellouche et al., 2021). However, Figure 4 provides confidence that G12V1 would be useful for further study of the NECC's branch variability at different scales.

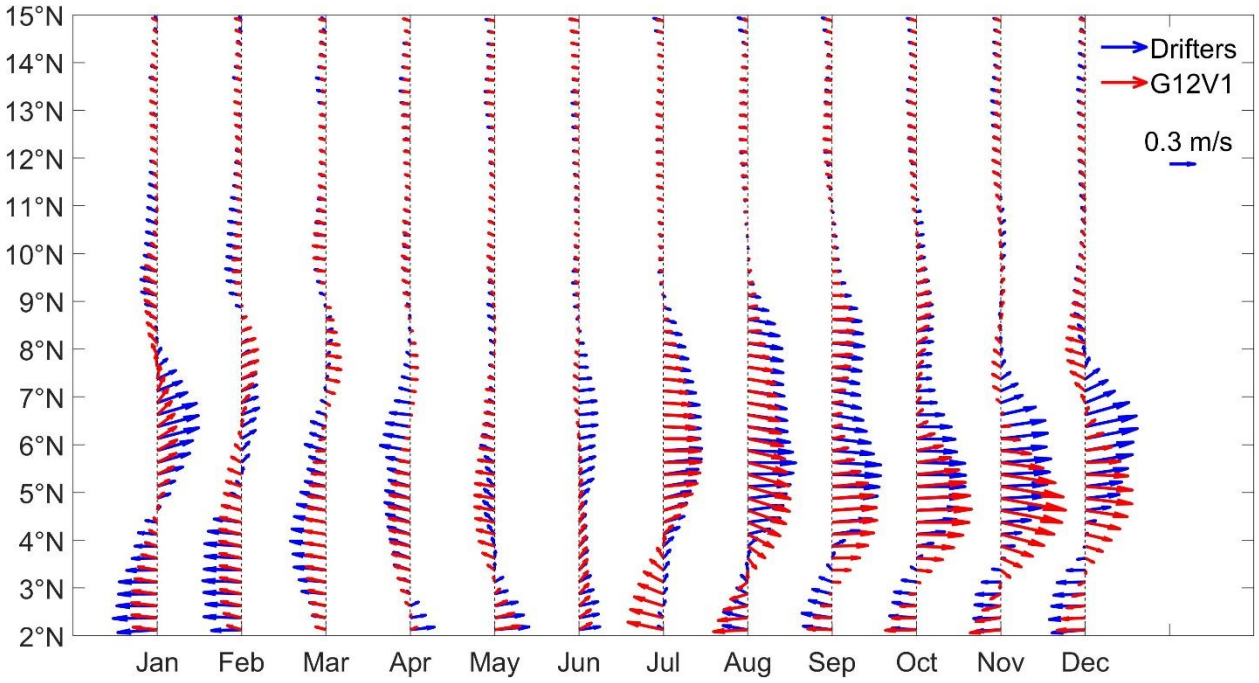

Figure 4. Hovmöller diagram of surface currents at 38°W from AOML drifter-derived surface climatology (blue) and G12V1 monthly climatology (red).

.

3.2. The circulation at 38°W from ADCP and G12V1 sections

The fifteen ADCP sections obtained during various cruises and periods of the year between 2001 and 2018 allow us to analyze the synoptic situations of the NECC system at 38°W. In addition, between 2–15°N, the intersected currents occurring at that particular moment, their extension and intensity are identified (Figures S1 and S2 of the supplementary material). To equally represent all the sections, the 2018 section distribution is taken as a reference, and then the others are interpolated and resampled to a similar horizontal 15-km spacing resolution. Then, the currents are linearly interpolated to a depth of 1 m, and depths from 30 m to more than 200 m are considered for the NECC study due to the limitation of ADCP measurements near the surface. Similarly, fifteen G12V1 vertical sections are obtained by sampling the reanalysis daily currents at the date and position of the ADCP measurements. The eastward NECC branches are determined by averaging the currents between 30–100 m (Figure 5) and finding the positive local maxima. The presence of the two branches was determined by identifying the two highest local maximum values separated by the lowest local minimum (case of July 2005, December 2006, November 2015 and 2017, and October 2018). These two branches are commonly shown in the current sections by a two-feet structure of the NECC in depth (Figure S2 of the supplementary material). The position

of each maximum represents the position of each core and is used to find in the current section the maximum core velocity (Vcmax) and its corresponding depth. These core positions are assumed to be confined between 3.5°-11°N (Figure 5), considering that the southern edge of the NECC reaches no further south than 3°N and that the eastward flow beyond 11°N is weak (Urbano et al., 2008). For the unique branch (sNECC), only one maximum is found. The latitudinal coverage of the branches is determined by the positions of the southern and northern edges of each eastward (positive) velocity (as illustrated below by the green and purple lines in the Figure 6 top panel). The limit between the southern and northern branches is determined by finding the position the lowest local minimum between the two highest local maxima. This local minimum is positive (negative) when the two branches are not yet separated (are seaparated).

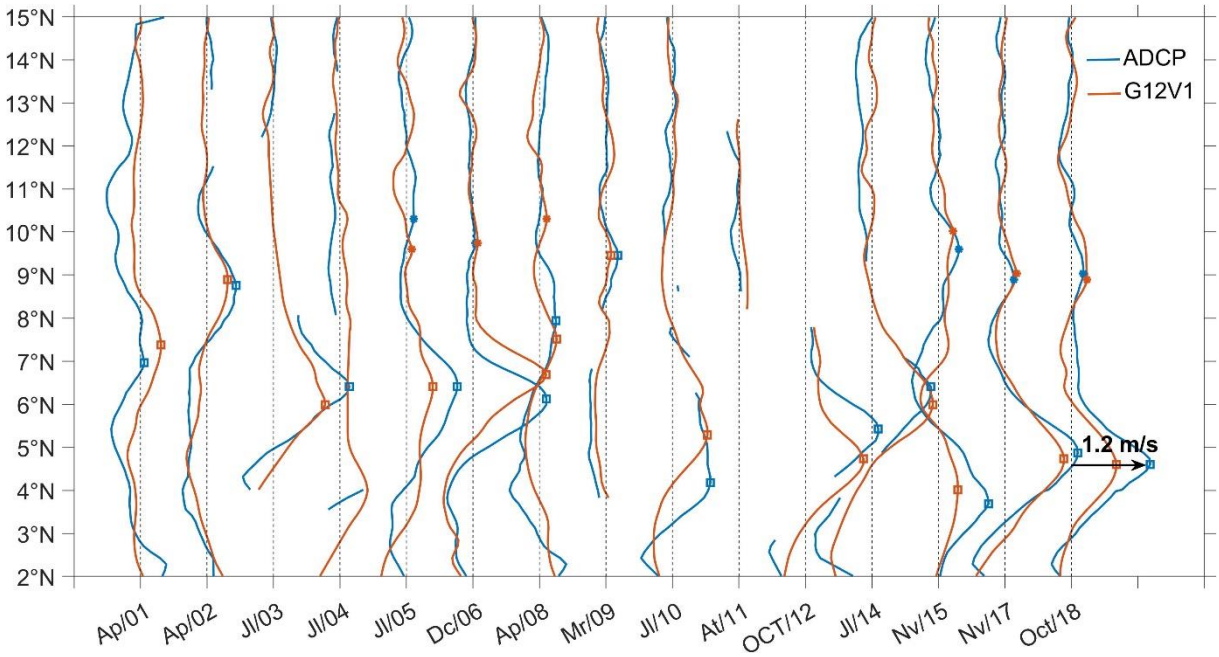

Figure 5. Upper layer currents at 38°W, averaged between 30–100-m depth. The blue (orange) lines represent the integration from ADCP (G12V1) sections. The squares (asterisks) represent the positions of the sNECC (nNECC) cores. Eastward (westward) currents are on the right (left) of the vertical dashed lines.

The ADCP sections show similarities over years during the same periods, but some sections offer very poor sampling (2003, 2004, 2009, 2010, 2011 and 2012, as seen in Figure 5 and in Figures S1 and S2 of the supplementary material). Considering our focus on the seasonal patterns, sections over the same seasons were averaged to provide three synthetic sections (Figure 6) for March-April (March 2009, April 2008, April 2002, and April 2001), July-September (July 2014,

2010, 2005, 2004, 2003 and September 2011), and October-November-December (October 2018, 2012, and November 2017 and 2015).

The NECC (defined by the eastward flow onFigure 5) is visible in every section, with a pronounced seasonal pattern. Its flow is weaker during spring and stronger during the second half of the year (Figure 6) when it exhibits a second core, which later becomes the nNECC branch. The NECC lies between 3°N and 11°N, with the sNECC and nNECC flowing between 3°N and 10°N and 8°N and 11°N, respectively, and separated by a westward flow in fall. From July to December, the NECC becomes increasingly stronger and larger with two nonseparated branches, and later, two separated branches which occur in late fall. The maximum sNECC Vcmax of 1 m/s is found in July-September, when it is deepest (56-m depth at 6.4°N), while the minimum of 0.2 m/s is found in March-April, when it is shallower (36-m depth at 8.1°N) (Figure 6 and Figure 7). In October-November-December, the nNECC Vcmax is approximately 0.2 m/s at 36-m depth (at 9.2°N). There is no signature of the nNECC in March-April and July-September. In the individual sections (Figures S1 and S2 of the supplementary material), a sNECC Vcmax of 1.2 m/s is found in July 2003, December 2006, October 2012 and 2018, and November 2017 at 6.4°N (51-m depth), 6.1°N (51-m depth), 5.4°N (44-m depth), 4.6°N (61-m depth) and 4.9°N (61-m depth), respectively. A nNECC Vcmax of 0.3 m/s was found in November 2015 at 9.6°N (35-m depth).

The NECC shows the highest/lowest transport between 30 and 150/200-m depth in the second half of the year (18.9/21.1 Sv)/March-April (2/2.23 Sv). Among the individual sections, the maximum/minimum transport occurred in October 2018/April 2001 (26.4/~1 Sv between 30–200-m depth) (Figure not shown).

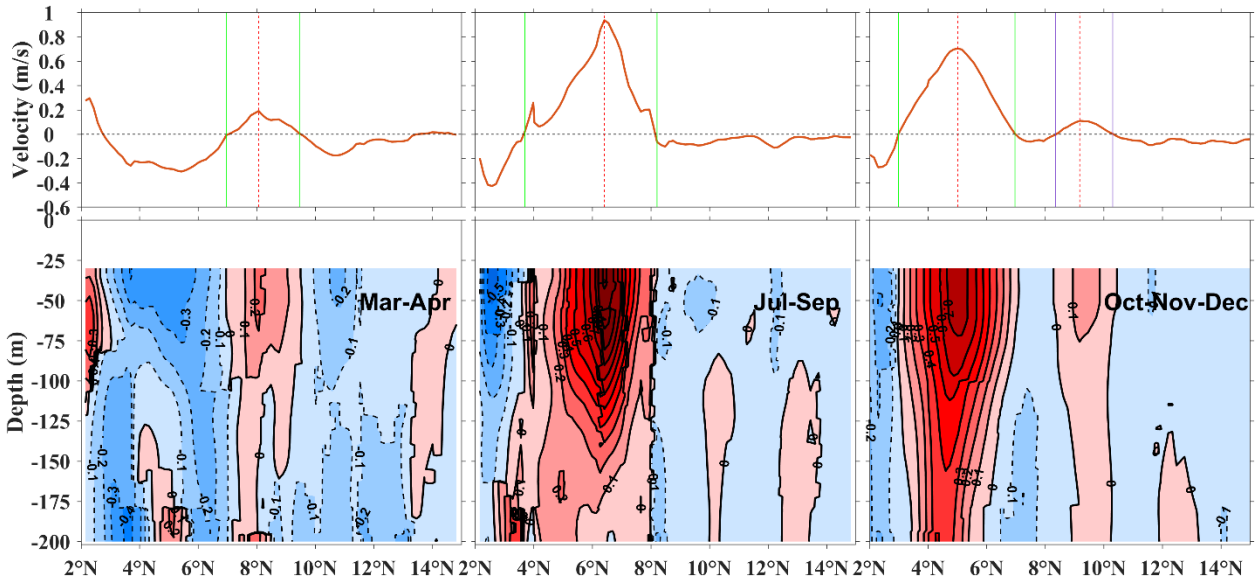

Figure 6. Synthetic averaged ADCP vertical section of zonal velocity (m/s) between 2°N and 15°N at 38°W during March-April (left column), July-September (middle column), and October-November-December (right column). Red and blue shading indicate the eastward (positive) and westward (negative) velocities (0.1 m/s contours), respectively. The 30–100-m depth velocity average of each synthetic section is plotted on the top panel (red line). The vertical green (purple) solid lines define the southern and northern limits of the sNECC (nNECC). The red dashed lines represent the positions of the cores.

Figure 6 also shows the presence of an eastward flow identified as the surfacing EUC by Urbano et al. (2008), and which is found south of 2°N during March-April. At depth, during the same period, a weak NEUC signature appears below 125-m depth, between 4°-6°N. During the second half of the year, it grows, surfaces, and merges with the sNECC. The nSEC is most extended and relatively weaker in March-April (0.3 m/s), while it is less extended but stronger (0.5 m/s) during July-September.

Synthetic sections in March-April, July-September, and October-November-December are computed from the fifteen G12V1 synoptic sections, similar to the ADCP data. The synthetic averages are a way to eliminate in the daily G12V1 product potential synoptic scale inaccuracies when comparing with the ADCP sections. Note that the G12V1 reanalysis is forced by 3-h ERA-Interim atmospheric fields, which guarantee a representation of the circulation and its turbulence with typical ~20 km and one day, space and time scales. However, on a daily basis, differences can appear with the ADCP observed currents. Differences first inform on the ability of such reanalysis to provide realistic synoptic regimes and infer the skill in representing the various features composing this synoptic mesoscale circulation. We already know the limitations in operational

oceanography to represent such scales unlike the seasonal and longer timescales (e.g., Lellouche et al., 2018, 2021; Davidson et al., 2019). So, the ability to reproduce the synthetic ADCP sections will give more credit to G12V1 product which might complete the gappy ADCP sections and offer a complementary representation of the vertical circulation at 38°W and elsewhere.

From the ADCP and G12V1 synthetic seasonal sections, the NECC system characteristics are compared in Figure 7. Figure 7a shows the latitudinal extension of the two branches from G12V1 and ADCP estimates. G12V1 matches the two-branch pattern observed by the ADCP profiles, but shows slightly larger branches. The NECC branches are located between 3–11°N for both products, and the sNECC is located more north in March-April than in the second part of the year. The highest/lowest sNECC extension difference of 1.4°/0.7° latitude occurs in the July-September/March-April period, while the nNECC extension difference in October-November-December is 0.5° latitude. The sNECC/nNECC core Vcmax values from the ADCP and G12V1 synthetic sections (Figure 7b) show larger/slightly lower ADCP Vcmax (38% and 6% on average for sNECC and nNECC, respectively). Both products show more intense cores during the second part of the year. G12V1 does not reproduce well the depth variability (Figure 7b). It exhibits deeper sNECC cores in October-November-December and March-April (47 m) when the ADCP estimates are still shallower (~34 m in March-April). However, the depth values are consistent in July-September (38 m for both). The G12V1 and ADCP nNECC Vcmax values are similar, but G12V1 Vcmax is slightly deeper. The overall image is an under/overestimation of the sNECC intensity/depth by G12V1 and a slightly deeper nNECC core position. For the first time, the NECC total transport was estimated beyond 7.5°N with ADCP data. As mentioned above, the maximum/minimum sNECC transport between 30 and 150-m depth occurs here in the July-September/March-April period (18.9/2 Sv) (Figure 7c). Overall, G12V1 transport reproduces the same variability but underestimates sNECC transport in the second part of the year, even if nNECC transport is added. In summary, G12V1 reproduces the overall NECC structure, but in some years, it fails to represent their shape on particular days (figure not shown).

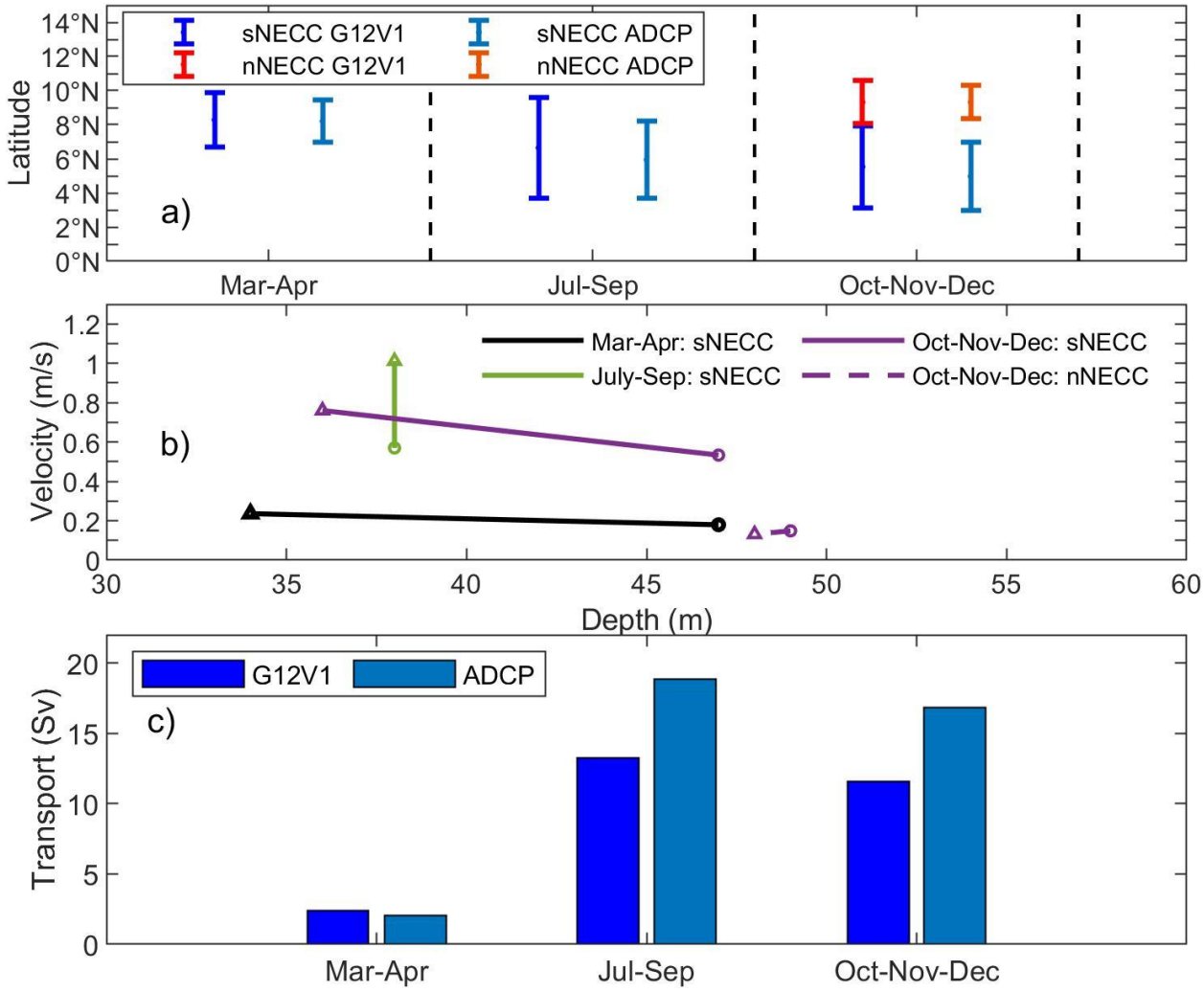

Figure 7. NECC's characteristics compared between G12V1 and ADCP vertical sections for the period of time March-April, July-September, and October-November-December: a) latitudinal coverage of NECC branches from ADCP and G12V1; b): depths and maximum velocity of the southern and northern branches of the NECC, and c) the zonal transport (in Sverdrup) computed for each 38°W section between 30 and 150-m depth for the ADCP and G12V1. Colors in b) are associated with each averaged period of time; the solid lines represent the sNECC, and the dashed lines represent the nNECC. The circles and triangles represent the G12V1 and ADCP values, respectively.

This analysis of the circulation represented by the global G12V1 1/12° ocean reanalysis, in comparison to the AOML climatology and vertical ADCP sections, shows that G12V1 offers reliable representation of the seasonal and larger scales. The ADCP data allowed us to precisely characterize the NECC structures during fifteen years and describe the associated NECC's specific fine scales. These synoptic situations are not anomalous regarding the known general NECC seasonal pattern. The G12V1 synthetic sections reproduce the overall NECC structure, but show that, there are still some improvements to be made at the fine scales. This gives us some hints at

the upper skill limits of G12V1 in modelling the NECC synoptic scales. Such limitations of state-of-the-art global ocean modelling are identified by the community, with many propositions for future improvements (e.g., Lellouche et al., 2021; Fox-Kemper et al., 2019), which does not prevent us from using G12V1 monthly estimates to further analyze the seasonal and interannual variability of the NECC.

4. Analysis of the NECC variability at 38°w using the GLORYS12V1 reanalysis

4.1. Seasonal variability of the NECC and the relationship between its transport and the wind stress curl at 38°W

To investigate the temporal and spatial variability of the NECC, the G12V1 monthly climatology is computed over the 1993–2018 period along the 38°W section (Figure 8). This climatology provides a more detailed view and confirms the description of the NECC's seasonal structures observed with ADCP data. The NECC flows between 3–12°N during the year, separated into two branches from September to December. The sNECC (nNECC) extends from 3–9.2°N (7.3–11.6°N), with its core position on average at 6.1°N±0.1° (9.7°N±0.1°) and a mean depth of 50.2±0.9 m (47±1.9 m). In parallel, from the ERA5 monthly estimates of WSC, WSC strength, ITCZ, and the secondary zero line of WSC at 38°W (see Section 2.3 above) monthly climatologies are computed.

The NECC annual cycle can be considered to start in June when the new sNECC grows at the surface and migrates northward (Figure 8 and Figure 9a). In July, it starts presenting an independent vertical extension at 8–9°N, considered the second eastward flow foot, with a small second velocity core at its northern side, which becomes a well-established nNECC core and a branch vertically extended to depth in August-September. It migrates northward, weakens, and completely separates from the sNECC in November. The nNECC appears under the influence of the ITCZ northward migration with a 3-month lag (Figure 9a). The NBCR principally feeds the sNECC branch and partially feeds the growing nNECC at the surface, as depicted in Section 3.1 (Figure 2). After the separation of the two branches, the entire NECC system starts a northward migration from December to May of the next year. The nNECC weakens during this northward migration to almost vanish at approximately 11°N in March. The sNECC core migrates northward from June to July when the northern core is forming, and then returns to its initial location at

approximately 5°N (Figure 9a). It starts another northward migration after October-November when a secondary zero line of the WSC appears between 10°-12°N until May.

From December to May, on the southern flank of the NECC, the nSEC also shifts northward and expands with its maximum intensity in April-May (Figure 8 and Figure 9a). At 50-m depth, Figure 10a shows that in April the sNECC bifurcates southward at approximately 36°W, loops clockwise, and generates a westward flow (observed at 38°W between 3–6°N) that merges vertically with the nSEC at the surface. Then, the resulting westward flow reaches the shelf and the dynamical outer boundary of the NBC at approximately 45°W and bifurcates again south-eastward and strengthens the northern side of the EUC. The EUC is shallower and exhibits maximum transport during this period of the year (Hormann and Brandt, 2007). Figure10b shows that the EUC flow might be associated at the surface with the current directly coming from the NBCR. This creates a large eastward flow extending with the EUC from the equator to 3°N from April to June. At depth, Figure 8 shows in May that this eastward flow connects with the upper part of the NEUC at approximately 75-m depth. The NEUC lies between 4–7°N and presents a maximum core intensity of 0.3 m/s at approximately 155-m depth in June. Additionally, in June, the shallower NEUC combines with the above-mentioned eastward flow to contribute to sNECC development at the surface. East of 35°W, Figure 10b shows another NECC onset phase, formed by a central branch, which is fed by the clockwise recirculation of the nSEC during this month. This is also shown in Figure 2.

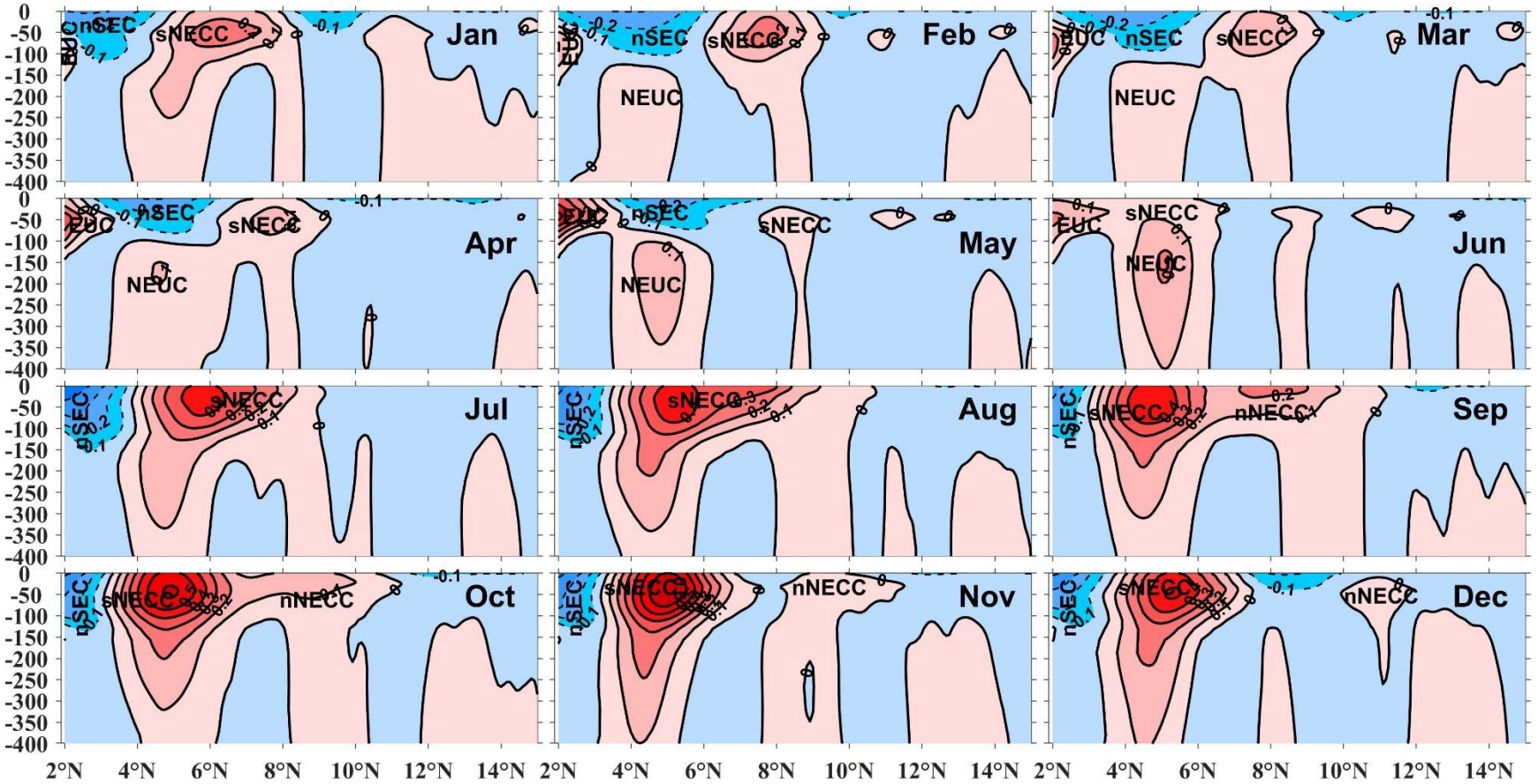

Figure 8. monthly climatology of zonal currents at 38°W between 2–15°N. Red and blue colors represent the eastward (positive) and westward (negative) velocities, respectively. The contour solid (dashed) lines represent each 0.1 m/s current velocity greater (less) than zero or equal to zero.

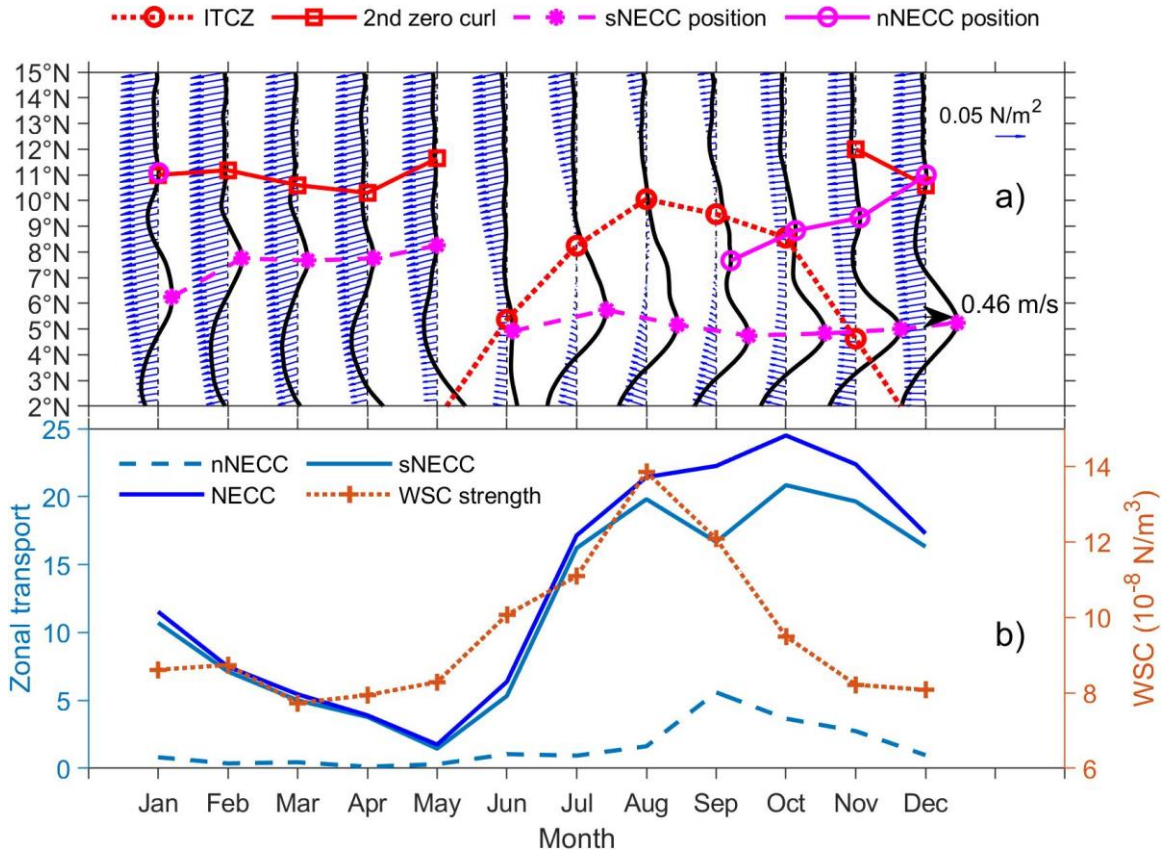

Figure 9. a): Hovmöller diagram of 0–100 m vertically averaged currents from G12V1 monthly climatology at 38°W (thick black lines). Black vertical thin dashed lines correspond to the zero-line reference of currents each month and indicate whether currents are negative/positive (westward/eastward). The wind stress influence on currents is given by the ERA5 monthly wind stress at 38°W (blue arrows). ITCZ latitudinal position at 38°W given by the red dotted line with a square. The secondary zero line of the wind stress curl at 38°W is indicated by thick red lines and circles. The magenta tick line/dashed line represents the evolution of the nNECC/sNECC core location throughout the year. b): Annual cycle of the G12V1 NECC transport between 0 and 150-m depth at 38°W (blue, in Sverdrup) as the sum of the sNECC (light blue thick line) and nNECC transport (light blue dashed line); ERA5 wind stress curl strength in the central tropical Atlantic (orange dotted line in N/m^3).

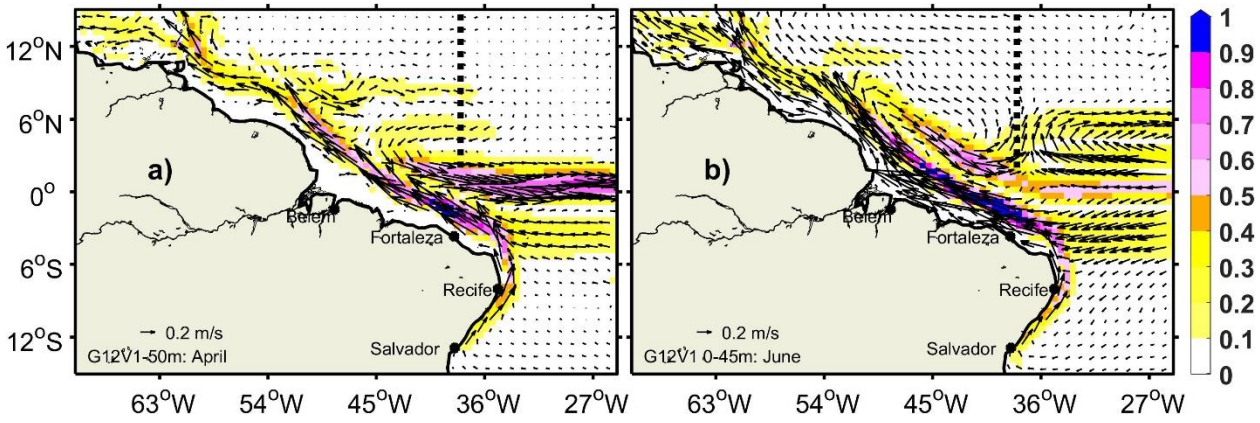

Figure 10. a) G12V1 velocity climatology in April at 50-m depth. b) G12V1 averaged velocity from the surface to 45-m depth in June. The currents are superimposed on the absolute value of their speed (shaded). The black line indicates the section at 38°W between 2–15°N.

The NECC transport annual cycle in the first 150-m depth is summarized in Figure 9b. The transport integrated from the surface to 150-m depth is used in the rest of this study as the upper thermocline transport in the WTNA, where the influence of the winds is significant (Urbano et al., 2006). The transports associated to the sNECC and the nNECC cores grow from June to August-October. From January to July, the nNECC transport is very weak (<1 Sv) and increases rapidly to a maximum of ~5.6 Sv in September. The sNECC contributes more to the total NECC transport and its maximum transport (~20.8 Sv) occurs in October. A larger part of the sNECC go for the nNECC in September and the sNECC transport slows down before to increase again in October, probably because of the the NBCR contribution. The decrease of the nNECC after September is due to the westward recirculation of the nNECC under the influence of the Ekman transport due to the strengthening of the Northeast trade winds. The total NECC integrated transports grows from 1.7 Sv in May to 24.5 Sv in October, which appears two months after the WSC strength maximum which occurs in August in the eastern tropical Atlantic.

4.2. Interannual variability of the NECC and its relationship with the Atlantic modes at 38°W

The first 15-m depth averaged velocity and seasonal anomalies from G12V1 monthly estimates across the 38°W section from 1993 to 2018 (Figure S3 of the supplementary material) show year-to-year variations in NECC structures and connections between the sNECC of the previous year and the new nNECC of the following year. To investigate the spatial variability of the NECC system over the years, its characteristics have been analyzed. Their interannual

variability have been studied in relation to the ocean-atmosphere interactions, which are particularly relevant in the WTA (Foltz et al., 2003, 2012; Hounsou-Gbo et al., 2016).

To do so, four parameters are analyzed. First, the Atlantic zonal mode index (AZM) is based on NOAA OI SST monthly anomalies in the ATL3 box, defining warm events so-called "Atlantic Niño" (Zebiak, 1993). Second, the Atlantic meridional mode index (AMM) discussed by, e.g., Servain (1991), Carton et al. (1996), and Foltz et al. (2012), was computed here using the NOAA OI SST anomalies over the tropical North Atlantic (TNA) and tropical South Atlantic (TSA) boxes as defined by Enfield et al. (1999). AMM's positive/negative phases are associated with opposite warm/cold events in the TNA/TSA and anomalous northward/southward latitudinal shifts of the ITCZ (Cabos et al., 2019). Third, the monthly ITCZ position seasonal anomalies at 38°W were computed as described in Section 2 (hereafter ITCZ index). Fourth, the G12V1 monthly anomalies of the NECC (sNECC and nNECC) transport/core velocity/depth /location, considering the upper 150 m at 38°W. As mentioned by Hormann et al. (2012), the time series of the AMM and AZM indices are found to be significantly anti-correlated (-0.50), with particular years of opposite events described in the literature: 1997, 2005 and 2008 (Foltz and McPhaden, 2006; Marin et al., 2009; Hormann et al., 2012). This is also the case with the ITCZ index, for which we found positive/negative correlations with the AMM/AZM index (0.65/-0.5).

To analyse the year-to-year variations in the total transport, a low-pass 24-month Loess filter (Cleveland and Devlin, 1988) is applied to the seasonal anomaly time series to remove the remaining high-frequency variations (Figure 11) after a wavelet analysis have been performed to find the common cutoff frequency (Figure not shown). In parallel, to identify when the maximum interannual variability occurs within each year, the monthly time series of the seasonal anomalies are smoothed using a three-month running mean to generate a time series of anomalies from 1993 to 2018 every month (hereafter called "3-month anomalies": figures not shown). In our analysis below, links between the parameters mentioned above are inferred using correlation analysis, where the 95% confidence level significance was verified prior to any discussion.

The 3-month ITCZ anomalies correlations with the AMM index are larger (0.8) during the March-June and Oct-Dec (0.7) periods, with a one-month delay, as already documented (e.g., Cabos et al., 2019). These periods correspond to the start of the ITCZ northward (southward) migration from its southernmost (northernmost) position in austral (boreal) summer. The 3-month ITCZ anomalies index indicates anti-correlation (-0.65) with the AZM index only for the April-

June period, with a one-month delay when the ITCZ migrates from its southern to northern bounds. Correlations between the meridional component of the wind stress interannual anomalies at the mean position of the NECC (6°N/38°W) and the AZM indices (Figure not shown) were calculated and are found smaller. However, negative correlations (-0.5 to -0.6) were observed for the 3-month anomalies during the January-June period. In other words, during the positive (negative) phase of AZM, the Northeast trade winds weaken (strengthen) and the Southeast trade winds strengthen (weaken). This is also in agreement with the known negative impact of the positive AZM phase on trade winds in the WTNA (Cabos et al., 2019).

To understand the ACM influence on the interannual variability of the NECC system, we first analyze at this timescale the relationship between the NECC's branch characteristics (transport, location, Vcmax intensity and depth). Figure 11 illustrates the filtered time series of these characteristics together with the climate mode indexes. Figure 11a shows an obvious relationship between sNECC transport and its core velocity at the interannual timescale as it was found for the seasonal timescale. Correlations of the 3-month anomalies computed over 1993–2018 are larger than 0.85 for most seasons, except from May to July, when a new sNECC branch starts. In contrast, there is no obvious correlation between the filtered sNECC transport and its core depth. However, 3-month anomalies show a correlation (0.6) in September, with a one-month delay: when the sNECC is well established, its core depth seems related to its transport in the previous month. The sNECC core location and transport in November show anti correlations (-0.6) and a 2-month delay. When the transport is higher, the sNECC northward migration might be shorter. The sNECC transport from December to April is anticorrelated (-0.5 to -0.6) with the AZM index with zero/one-month delay, while in June and July, it appears anticorrelated (-0.65) with the AZM index in February-April. This suggests that positive (negative) anomalies of sNECC might be associated with negative (positive) phases of the AZM. The relationship between the filtered sNECC core velocity/transport time series and the AZM index confirms this latter (Figure 11a-b). Negative (positive) phases of AZM are associated with positive/decreasing (negative/increasing) anomalies of the sNECC Vcmax/transport. Conversely, the 3-month anomalies suggest relationships with AMM index between April and May with a one-month delay (correlations higher than 0.5), which is consistent with the peaks of low-pass 24-month filtered time series of the sNECC Vcmax/transport or total NECC transport and of AMM index in Figure 11a-b, in 1994, 1997, 2001, 2004, 2009, 2012, 2014, 2015, 2017 and 2018. For this period (April-May), correlations are also

significant with the ITCZ location (0.5–0.7). In other words, during AMM positive (negative) phases in spring, when the ITCZ northward (southward) shift is more pronounced with a south-easterly winds tendency, the sNECC might have a larger (lower) transport. To a lesser extent, the opposite pattern appears for the sNECC core location in the second half of the year. Negative correlations about -0.5 were found between the sNECC core location, the AMM and ITCZ indices, and suggest that during warm AMM events and ITCZ further-north-than-normal positions, the sNECC branch from November to January might be shifted southward.

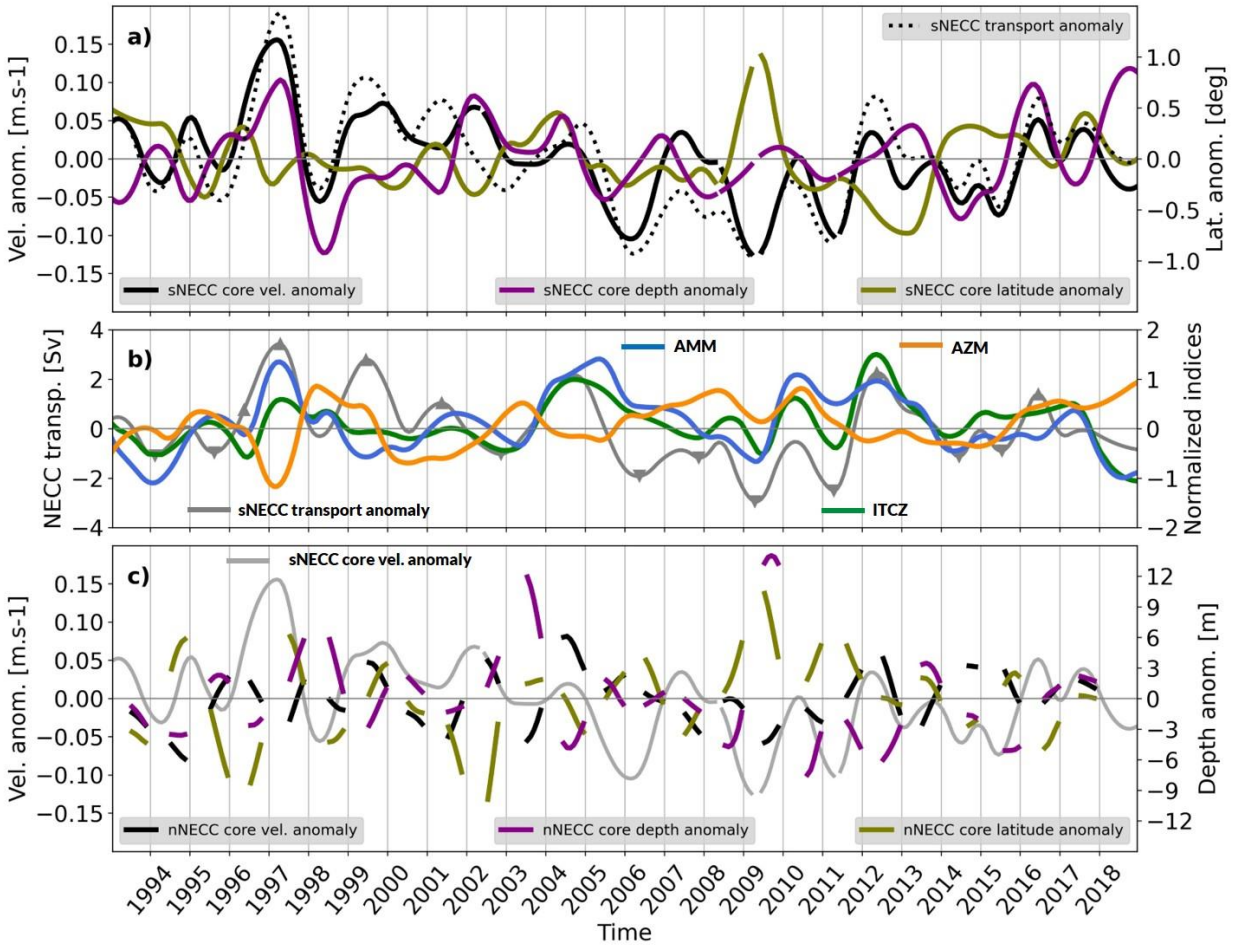

Figure 11. Low-pass filtered time series: a) sNECC interannual anomalies of core velocity (black, units in m/s: scale on the left axis), core depth (dark magenta, units in meters: same scale as the right axis of Figure c) below), core location (olive, units in degrees, scale on the right axis) and sNECC transport anomalies (dotted black line, units in Sv: same scale as the left axis of Figure b) below); b) AMM (blue solid line), AZM (yellow solid line), ITCZ location (green solid line) normalized (scale on the right axis), and sNECC transport anomalies (gray line, units in Sv: scale on the left axis) with marked anomalous years (triangle); and c) nNECC interannual anomalies of core velocity (black, units in m/s: scale on the left axis), core depth (dark magenta, units in meters: same scale as the right axis), core location (olive, units in degrees, same scale as the right axis of Figure a) above), and sNECC core velocity anomalies (light gray thin solid, in m/s: scale on the left axis, and plotted in black above in Figure a)).

The correlations of the 3-months anomalies of the nNECC transport and Vcmax were also found significant (0.6), and the correlations exceed 0.7 from October to December during the nNECC northward migration and decay (figures not shown). Regarding the relationship between the nNECC transport, its core location and depth, significant correlations were found between the transport and the core location only in August-September (anticorrelation of -0.5), and between the transport and the depth only in July-August (correlation of 0.5). This suggests that the higher

transports at these periods might be associated to the southernmost and deeper nNECC core. No evidence of the AZM influence on the interannual changes in the nNECC branch characteristics were found (Figure 11b-c). However, the 3-months anomalies show significant correlations between the nNECC transport/Vcmax intensity in November-December and the AMM index in August-October (~0.5), and the ITCZ location with a one-month delay (~0.6). It suggests that the positive (negative) anomalies of the nNECC Vcmax/transport might be associated with positive (negative) phases of the AMM and the northermost (southernmost) location of the ITCZ in some particular periods. This is also consistent with most association of the positive/negative filtered times series of the nNECC core and AMM in Figure 11b-c. Regarding the nNECC core location, the 3-months anomalies show significant correlation in October-November with the ITCZ location (0.55), with a one-two month delay. The correlations between ITCZ location in February-March and the nNECC core depth in July-August were found significant (-0.6). In other words, the northermost location of the ITCZ in boreal spring might be associated with the shallower nNECC core in July-August, while in boreal summer, it might be associated with the northernmost location of the nNECC core in October-November. This is consistent with most the the scenarios concerning the ITCZ, the nNECC core depth and the nNECC core latitude in Figure 11b-c.

The correlations between the 3-months anomalies of the nNECC and sNECC core characteristics shows only a significant correlation between the nNECC core location from October-November and the sNECC Vcmax intensity in September (-0.5). This shows that, the intensity (stronger/weaker) of sNECC might be associated to the location (southernmost/northernmost) of the nNECC during fall.

5. Discussion

Comparisons of G12V1 seasonal circulation in the WTNA with the NOAA drifter derived surface velocity climatology exhibits strong similarities and gives validity to the overall quality of the regional circulation pattern depicted by G12V1. Moreover, comparisons with the ADCP three synthetic seasonal sections at 38°W indicate that G12V1 can reasonably reproduce the strength and the location of the main cores of the NECC branches, and can be used to study the currents in WTA at the seasonal and longer timescales.

The NECC at 38°W shows a strong seasonal cycle with two-core structure well pronounced the second half of the year. Its seasonal cycle appears to start in June at approximately 4–6°N

(Figure 8) when the NEUC surfaces. From June, the NECC grows under the influence of the WSC strength and display another core north of 7°N in July-August which generates a northern branch. During the NECC evolution, it undergoes northward/southward migrations under the influence of the trade winds (Figure 9). In agreement with the findings of Fonseca et al. (2004) and Urbano et al. (2008), the NECC system was found to present two northward migration periods. We found here that, the first period from June to July-August corresponds to the start and growth of the NECC southern branch (sNECC). It also corresponds to the formation and the northward migration of the northern core/branch (nNECC) in conjunction with the ITCZ northward migration with a three-month time lag (Figure 9). After July-August to November, the sNECC returns southward to its initial location where its core is found approximately at 5°N, and undergoes the second northward migration from December to May while the nNECC is still migrating northward in conjunction with the secondary zero of the WSC this time. Urbano et al. (2008) also mentioned the presence of the second zero line of WSC during the northward migration of the NECC system. In this study, we found that this second migration is more specifically due to the strengthening of the Northeast trade winds, which consequently induces this secondary WSC zero line (Figure 9a). In addition, this wind strengthening, visible in Figure 9a, induces an important north-westward Ekman current component in the upper layer, which weakens and deviates the surface sNECC (nNECC) core northward, from approximately 5°N to approximately 9°N (north of 11°N). This migration is also in conjunction with the northward extension of the nSEC at the surface. In June-July, the very weak sNECC of the previous year which flows between 8–10°N is finally absorbed by the northern flank of the new sNECC to allow another NECC cycle. The northern flank of the new NECC will form later the new nNECC, which separates and migrates northward after August.

The WTA upper layer (0 to 100-m depth average) seasonal variability from G12V1 (Figure 12) highlights in this study the importance of the NBCR, which feeds and strengthens the sNECC, especially in the second half of the year. It explains the higher sNECC transport of October, while the nNECC reaches its maximum transport in September, and is partly fed by the northern flank of the NBCR (Figure 9). The influence of the NBCR on the sNECC strength is more important west than east of 32°W certainly because of the nonlinear terms due to the eddy interactions and the mean flow which contribute to the vorticity balance west of 32°W (Verdy and Jochum, 2005). In the first half of the year, the NBCR-NECC system migrates northward and becomes weaker during the spring (Figure 12). During this period, a cyclonic circulation appears between 3–7°N/34–44°W

dampens the input of NBCR waters to the NECC, which is only shown east of 32°W due to the recirculation of the nSEC eastward already mentioned. Figure 12 also shows that, west of 32°W, there is the presence of a weak eastward flow between 8°-10°N, known as the migrated sNECC in spring, in the upper 0-100 m depth.

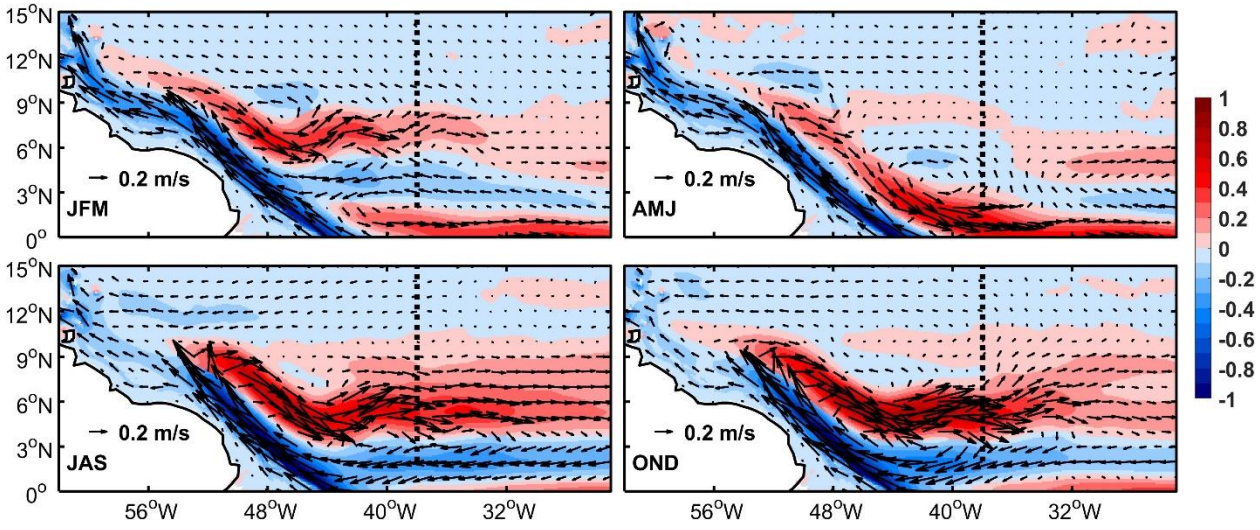

Figure 12. G12V1 upper layer currents (0 to 100-m depth average) seasonal variability in the WTNA. Shading corresponds to the current speed (colorbar in m/s). Red (blue) color for eastward (westward) flows. The dashed black line represents the section at 38°W. JFM, AMJ, JAS, and OND represent January-February-March, April-May-June, July-August-September, and October-November-December seasons, respectively.

The sNECC core mean position was found at 6.1±0.1°N, consistent with estimations at 6°N by Hormann et al. (2012) and Fonseca et al. (2004). Its core maximum velocity of 0.7 m/s is found in November at approximately 5°N (Figure 8). Seasonally, the two northernmost (southernmost) positions of the sNECC occur in May and July (June and September-November) at approximately 8.3°N and 5.8°N (4.9°N), respectively (Figure 9a). Fonseca et al. (2004) used satellite altimetry, considering the NECC as a unique branch (the sNECC in this study), and found two southernmost (northernmost) positions in June and December, approximately 4°N and 5°N, respectively (in February and in August, both at approximately 7°N). The differences with ours finding might be caused by the lack of precision of geostrophic surface current signatures estimated from satellite altimetry maps, associated with the limitation of their method to deduce the structure of the current cores at depth. In our study, we found the presence of the nNECC core, which is well marked in

September at approximately 7.3°N, and then develops and migrates northward at approximately 10.4°N in November-December.

Contrary to previous studies (Schott et al., 1998; Bourlès et al., 1999; Fonseca et al., 2004; Urbano et al., 2006), which stipulate that in spring the NECC becomes a westward flow, G12V1 results show a presence of a weak sNECC between 7°-11°N, which allows a development of a cyclonic circulation formed at its northern flank by an eastward flow occupying the latitudes from 2° to 7°N (Figure 12). Consequently, the negative transport found in the litterature between 3°N to 7.5°N during spring might be due to the contribution of this eastward flow, which should be fed by the southwestward recirculatinon flow of the sNECC (Figure 10a) and the nSEC from the east (Figure 12). During the NECC seasonal cycle, the Vcmax intensity and its depth are associated (figure not shown). From July to November, the sNECC Vcmax intensity increases, and its core deepens. The deepening of the sNECC core is consistent with the deepening the thermocline found by Garzoli and Katz (1983) in the NECC region with 1-2 months delay over the WSC strength, and the delay was found corresponding to the travel time of Rossby waves from Africa coast to the NECC region (Fonseca et al., 2004; Urbano et al., 2006). The seasonal cycle of the total transport (sNECC and nNECC) in the first 150-m depth follows the WSC strength east of 30°W with 2-month lag (Figure 9b). The delay is consistent with Garzoli and Katz (1983) and Fonseca et al. (2004) and confirms the possible influence of Rossby waves in the NECC region. The difference of one month between the nNECC and the total transport shows the higher contribution of the sNECC, and can be explained by the reversal phase of 180° found by Garzoli and Katz (1983) between the the sNECC region and the nNECC region, and which may suggest a major influence of the WSC strength in the southern region of the NECC compared to its northern region.

The relationship between the sNECC and the nNECC characteristics and the Atlantic climate modes described in section 4.2 shows relationships between the sNECC transport and both the AMM and AZM phases occurring during differents period of the year, and between the nNECC core location and the ITCZ. The relationship of the AMM with the sNECC transport occurs only when the AMM phases peak in April-May and is associated with a transport anomaly of June while this transport anomaly from December to April/June-July is associated to the AZM of the same period/AZM of February-April. Two important air-sea feedback mechanisms can be used to explain both relationships. First, the relationship with AMM shows the influence of the trade winds anomalies in April-May on the interannual variability of the sNECC transport in June. The positive

anomalies of the sNECC transport associated with AMM positive phases and a northward shift of the ITCZ show the influence of the weakening/strengthening of the northeast/southeast trade winds on the higher values of the sNECC transport and vice-versa according to Xie (2004) and Cabos et al. (2019). Second, the relationship between the negative anomalies of the sNECC transport and the positive (negative) and/or decreasing (increasing) AZM phases in December -April or February-April shows the influence of the positive (negative) westerly wind anomalies on the lower (higher) values of the sNECC transport in December-April or June-July. From the 24-month low-pass filtered time series, the occurrence of sNECC transport anomalies shows two important scenarios for the significant anomalies (higher than 0.6 times the standard deviation). First, the positive sNECC transport anomalies are associated to the opposite phases of AMM and AZM (e.g., 1997, 1999, 2001, 2004-2005, 2012, 2016). And second, the negative sNECC transport anomalies are associated with the same phases of AMM and AZM (e.g., 1995, 2006, 2011 and 2015) or an AMM phase with a weak AZM phase (e.g., 2009) (Figure 11a-b).

Hormann et al. (2012), using complex empirical orthogonal function analyses, found that the NECC's intensity was associated with the AZM, while its latitudinal shift was related to the AMM. In our study, we couldn't find any evidence of the latitudinal shift of the sNECC related to the AMM. However, we found a relationship between the sNECC transport and the AZM as mentioned above, and a relationship between the nNECC core location/depth in July-August/October-November and the ITCZ in boreal spring/summer. This shows that, the interannual variability of the NECC system, considering the two-core structure can be more challenging and more complex.

6. Summary and conclusion

The ADCP surveys, the near-surface drifter currents climatology and the G12V1 reanalysis from 1993–2018 allow us to study the two-core structure of the NECC along 38°W, from 2°N to 15°N; and to complement the knowledge about the seasonal and the interannual variability of the two-branch pattern associated to its two cores, which is less documented in the literature. The NECC characteristics (volume transport, maximum core velocity, location and depth) are revisted with G12V1 reanalysis after a validation process.

The G12V1 monthly estimates allowed to characterize the seasonal and interannual variability of the two branches of the NECC (sNECC and nNECC) and their transport at 38°W. The monthly climatology of the vertical distribution of the NECC shows a seasonal cycle which

starts in June by the sNECC branch that grows, extends northward and forms a northern core in July-August. This core grows while shifting northward until it separates in November to form a separated nNECC branch that vanishes after December. This period represents the first part of the NECC migration cycle, and is driven by the WSC pattern over the basin and the associated ITCZ migrations. During this period, the sNECC core location is about 5°N and starts another northward migration from December to May under the influence of an important northward Ekman transport associated with the strengthening of the Northeast Trade Winds. The volume transport associated with both branches are found to be approximately in Sverdrup balance, with a 2-month delay for the sNECC and 1-month delay for the nNECC. The total volume transport follows an annual cycle influenced by the WSC strength over the basin with a two-month delay, corresponding to the travel time of Rossby wave propagation from the eastern basin to the NECC region.

The analysis of the interannual variability of the two-core structure with respect to the Atlantic climatic modes comes to complement the study initiated by Hormann et al. (2012) and shows that, the interannual variability of the two-core structure is more complex. For the first time, the interannual variability of the transport, the core intensity, location and depth associated to the two branches of the NECC have been investigated. Based on correlation analysis between these different characteristics of the NECC and the tropical Atlantic climate modes, it has been found a relationship between the sNECC transport and both the Atlantic meridional and zonal modes (respectively AMM and AZM) over different periods of the year. Any significant correlation was found between the interannual anomalies of the nNECC transport and the climate modes. However, it has been found that, its core location and depth are associated to the migration of the ITCZ respectively, in October-November and July-August.

This work about the characterization of the variability in NECC branches opens the door for further investigations on their contribution to the overall tropical Atlantic circulation, both at the western boundary and over the entire basin. Our results also validate the G12V1 reanalysis for future uses in the tropical Atlantic studies, and give leads to consider in the NECC investigations. However, ocean observations are crucial, and the programs such as PIRATA are key in the tropical Atlantic to maintain the capability to precisely characterize the ocean circulation, further improve the numerical models by ingesting observations into simulations and continue increasing their realism.

Author contribution

Djoirka M. Dimoune performed the ADCP and GLORYS2V1 analyses as part of his PhD thesis research. Fabrice Hernandez contributed to these tasks and performed complementary analyses. Fabrice Hernandez and Moacyr Araujo provided overall supervision of this study.

Acknowledgments and data

We are grateful to PIRATA Brazil for providing the ADCP data. Preprocessed Camadas Finas III ADCP data were provided by Pr. Alex Costa. We particularly thank Gerard Eldin for his advice in processing the ADCP data and Jean-Michel Lellouche, Marie Drévillon, Charly Régnier and Romain Bourdallé-Badie from Mercator Océan International for exchanges on the GLORYS12V1 reanalysis. Through the revision of this article, the two anonymous reviewers provided numerous advice that allowed us to improve the manuscript, and we are thankful for their help. We are also grateful to the CMEMS and the ECMWF who made available the ocean reanalysis and the mean wind fields, respectively; and the NOAA who provided the SST products and the near-surface currents data from drifters for this work. We are also thankful to CAPES Foundation. Fabrice Hernandez supervised this work as part of the TAPIOCA Laboratoire Mixte International funded by IRD and CAPES/MEC in Brazil. Moacyr Araujo thanks the support of the Brazilian Research Network on Global Climate Change FINEP/Rede CLIMA (grants 01.13.0353-00). This work has been supported by the French LEFE/GMMC funded project Merca2Recife (42-DS-GMMC-MERCA2RECIFE – REF. CNRS N° 197932) and represents a contribution to the INCT AmbTropic, the Brazilian National Institute of Science and Technology for Tropical Marine Environments, CNPq/FAPESB (grants 565054/2010-4 and 8936/2011 and 465634/2014-1), and to the TRIATLAS project, which has received funding from the European Union's Horizon 2020 research and innovation program under grant agreement No 817578. The PIRATA and Camadas Finas III ADCP data are made available in netcdf files on Sea Scientific Open Data Edition (SEANOE) repository, on respective links: https://doi.org/10.17882/80771 and https://doi.org/10.17882/80828.

References

Araujo, M., Noriega C., Hounsou-Gbo, G. A., Veleda, D., Araujo, J., Bruto, L., et al. (2017). A Synoptic Assessment of the Amazon River-Ocean Continuum during Boreal Autumn: From

Physics to Plankton Communities and Carbon Flux. *Frontiers in Microbiology*. doi: 10.3389/fmicb.2017.01358.

Araujo, M., Dimoune, D. M., Trotte-Duhá, J., Nobre, P., Rodrigues, R., Cotrim, L., et al. (2021). Brazilian PIRATA cruises: S-ADCP data. *SEANOE*. https://doi.org/10.17882/80771

Araujo, M., Dimoune, D. M., Noriega, C., Hounsou-Gbo, G. A., Veleda, D., Araujo, J., et al. (2021). Camadas Finas III - BR cruise: S-ADCP data. *SEANOE*. https://doi.org/10.17882/80828

Aroucha, L. C., Veleda, D., Lopes, F. S., Tyaquiçã, P., Lefèvre, N., & Araujo, M. (2020). Intra- and Inter-annual variability of NBC rings using AMEDA algorithm: observations from 1993 to 2016. *Journal of Geophysical Research: Oceans*. doi:10.1029/2019jc015921

Artana, C., Lellouche, J.-M., Sennéchael, N., & Provost, C. (2018). The Open-Ocean Side of the Malvinas Current in Argo Floats and 24 Years of Mercator Ocean High-Resolution (1/12) Physical Reanalysis. *Journal of Geophysical Research: Oceans*, 123(11), 8489–8507. doi:10.1029/2018jc014528.

Artana, C., Provost, C., Lellouche, J., Rio, M., Ferrari, R., & Sennéchael, N. (2019). The Malvinas Current at the Confluence With the Brazil Current: Inferences From 25 Years of Mercator Ocean reanalysis. *Journal of Geophysical Research: Oceans*. doi:10.1029/2019jc015289.

Barnier B., Blaker A.T., Biatosch A., Böning C.W., Coward A., Deshayes J., et al. (2014). DRAKKAR: developing high resolution ocean components for European Earth system models. CLIVAR Exchange, 65 - 19(2), 18-21. Open Access version : https://archimer.ifremer.fr/doc/00326/43698/

Bourlès, B., Gouriou, Y., & Chuchla, R. (1999). On the circulation in the upper layer of the western equatorial Atlantic. *Journal of Geophysical Research: Oceans*, 104 (C9), 21151-21170. doi: 10.1029/1999jc900058.

Bourlès, B., Lumpkin, R., McPhaden, M. J., Hernandez, F., Nobre, P., Campos, E., et al. (2008). The PIRATA program: History, Acomplishments, and Future Directions. *Bulletin of the American Meteorological Society* , 89 (8), 1111-1125. doi: 10.1175/2008BAMS2462.1.

Bourlès, B., Araujo, M., McPhaden, M. J., Brandt, P., Foltz, G. R., Lumpkin, R., et al. (2019). PIRATA: A Sustained Observing System for Tropical Atlantic Climate Research and Forecasting. *Earth and Space Science*. doi: 10.1029/2018EA000428.

Cabanes, C., Grouazel, A., von Schuckmann, K., Hamon, M., Turpin, V., Coatanoan, C., et al. (2013). The CORA dataset: validation and diagnostics of in-situ ocean temperature and salinity measurements. *Ocean Science*, 9 (1), 1-18. doi: 10.5194/os-9-1-2013.

Cabos, W., de la Vara, A., & Koseki, S. (2019). Tropical Atlantic Variability: Observations and Modeling. *Atmosphere*, 10 (9), 502.

Carton, J. A., Cao X., Giese, B. S., & Silva, A. M. D. (1996). Decadal and Interannual SST Variability in the Tropical Atlantic Ocean. Journal of *Physical Oceanography*, 26 (7), 1165-1175. doi: 10.1175/1520-0485(1996)026<1165:Daisvi>2.0.Co;2.

Castellanos, P., Pelegrí, J. L., Campos, E. J. D., Rosell-Fieschi, M., & Gasser, M. (2015). Response of the surface tropical Atlantic Ocean to wind forcing. *Progress in Oceanography*, 134271-292. doi: 10.1016/j.pocean.2015.02.005.

Chang, P., Yamagata, T., Schopf, P., Behera, S. K., Carton, J., Kessler, W. S., et al. (2006). Climate Fluctuations of Tropical Coupled Systems—The Role of Ocean Dynamics. *Journal of Climate*, 19 (20), 5122-5174. doi: 10.1175/jcli3903.1.

Cleveland, W. S., & Devlin, S. J. (1988). Locally Weighted Regression: An Approach to Regression Analysis by Local Fitting. *Journal of the American Statistical Association*, 83 (403), 596-610. doi: 10.1080/01621459.1988.10478639.

Coles, V. J., Brooks, M. T., Hopkins, J., Stukel, M. R., Yager, P. L., & Hood, R. R. (2013). The pathways and properties of the Amazon River Plume in the tropical North Atlantic Ocean. *Journal of Geophysical Research: Oceans*, 118 (12), 6894-6913. doi: 10.1002/2013jc008981.

Davidson, F., Alvera-Azcárate, A., Barth, A., Brassington, G. B., Chassignet, E. P., Clementi, E., et al. (2019). Synergies in Operational Oceanography: The Intrinsic Need for Sustained Ocean Observations. *Frontiers in Marine Science*, 6450. doi: 10.3389/fmars.2019.00450.

Didden, N., & Schott, F. (1992). Seasonal variations in the western tropical Atlantic: Surface circulation from Geosat altimetry and WOCE model results. *Journal of Geophysical Research: Oceans*, 97 (C3), 3529-3541. doi: 10.1029/91jc02860.

Drévillon, M., Régnier, C., Lellouche, J.-M., Garric, G., Bricaud, C., & Hernandez, O. (2018). QUALITY INFORMATION DOCUMENT For Global Ocean Reanalysis Products GLOBAL-REANALYSIS-PHY-001-030 v1.2. (CMEMS-GLO-QUID-001-030), ed. by Mercator Ocean International, pub. by C. M. E. M. Service, 48 pp pp. [Available at http://marine.copernicus.eu/documents/QUID/CMEMS-GLO-QUID-001-030.pdf.]

Egbert, G. D., & Erofeeva, S. Y. (2002). Efficient inverse modeling of barotropic ocean tides. *Journal of Atmospheric and Oceanic technology*, *19*(2), 183-204. Doi: doi: 10.1175/1520-0426(2002)019<0183:EIMOBO>2.0.CO;2

Enfield, D. B., Mestas-Nuñez, A. M., Mayer, D. A., & Cid-Serrano, L. (1999). How ubiquitous is the dipole relationship in tropical Atlantic sea surface temperatures? *Journal of Geophysical Research: Oceans*, 104 (C4), 7841-7848. doi: 10.1029/1998jc900109.

Foltz, G. R., Semyon, A. G., & Carton, J. A. (2003). Seasonal mixed layer heat budget of the tropical Atlantic Ocean. *Journal of Geophysical Research*, 108(C5). doi:10.1029/2002jc001584.

Foltz, G. R., & McPhaden, M. J. (2006). The Role of Oceanic Heat Advection in the Evolution of Tropical North and South Atlantic SST Anomalies*. *Journal of Climate*, 19(23), 6122–6138. doi:10.1175/jcli3961.

Foltz, G. R., McPhaden, M. J., & Lumpkin, R. (2012). A Strong Atlantic Meridional Mode Event in 2009: The Role of Mixed Layer Dynamics. *Journal of Climate*, 25 (1), 363-380. doi: 10.1175/JCLI-D-11-00150.1.

Fonseca, C. A., Goni, G. J., Johns, W. E., & Campos, E. J. D. (2004). Investigation of the North Brazil Current retroflection and North Equatorial Countercurrent variability. *Geophysical Research Letters,* 31 (21). doi: 10.1029/2004gl020054.

Fox-Kemper, B., Adcroft, A., Böning, C. W., Chassignet, E. P., Curchitser, E., Danabasoglu, G., et al. (2019). Challenges and Prospects in Ocean Circulation Models. *Frontiers in Marine Science,* 6 (65). doi: 10.3389/fmars.2019.00065.

Gaillard, F., Reynaud, T., Thierry, V., Kolodziejczyk, N., & von Schuckmann, K. (2016). In Situ–Based Reanalysis of the Global Ocean Temperature and Salinity with ISAS: Variability of the Heat Content and Steric Height. *Journal of Climate,* 29 (4), 1305-1323. doi: 10.1175/jcli-d-15-0028.1.

Garzoli, S. L., & Katz, E. J. (1983). The Forced Annual Reversal of the Atlantic North Equatorial Countercurrent. *Journal of Physical Oceanography,* 13 (11), 2082-2090. doi: 10.1175/1520-0485(1983)013<2082:Tfarot>2.0.Co;2.

Garzoli, S., & Richardson, P. L. (1989). Low-frequency meandering of the Atlantic North Equatorial Countercurrent. *Journal of Geophysical Research: Oceans,* 94 (C2), 2079-2090. doi: 10.1029/JC094iC02p02079.

Garzoli, S. L. (1992). The Atlantic North Equatorial Countercurrent: Models and observations. *Journal of Geophysical Research: Oceans,* 97 (C11), 17931-17946. doi: 10.1029/92jc01363.

Garzoli, S. L., Ffield, A., Johns, W. E., & Yao, Q. (2004). North Brazil Current retroflection and *transports. Journal of Geophysical Research: Oceans,* 109 (C1). doi: 10.1029/2003jc001775.

Gill, A. E. (1982). "Atmosphere-Ocean Dynamics", Academy Press, Vol. 30.

Goni, G. J., & Johns, W. E. (2001). A census of North Brazil Current Rings observed from TOPEX/POSEIDON altimetry: 1992–1998. *Geophysical Research Letters,* 28 (1), 1-4. doi: 10.1029/2000gl011717.

Good, S. A., Martin, M. J., & Rayner, N. A. (2013). EN4: Quality controlled ocean temperature and salinity profiles and monthly objective analyses with uncertainty estimates. *Journal of Geophysical Research: Oceans,* 118 (12), 6704-6716. doi: 10.1002/2013jc009067.

Hormann, V., & Brandt, P. (2007). Atlantic Equatorial Undercurrent and associated cold tongue variability. *Journal of Geophysical Research: Oceans,* 112 (C6). doi: 10.1029/2006jc003931.

Hormann, V., Lumpkin, R., & Foltz, G. R. (2012). Interannual North Equatorial Countercurrent variability and its relation to tropical Atlantic climate modes. *Journal of Geophysical Research: Oceans,* 117 (C4). doi: 10.1029/2011jc007697.

Hounsou-Gbo G. A., Servain, J, Araujo, M, Martins, E. S., Bourlès, B. & Canaix, G. (2016). Oceanic Indices for Forecasting Seasonal Rainfall over the Northern Part of Brazilian Northeast. *American Journal of Climate Change,* 5: 261-274.

Jochum, M., & Malanotte-Rizzoli, P. (2003). On the generation of North Brazil Current rings. *Journal of Marine Research,* 61, 147- 173.

Jochum, M., Malanotte-Rizzoli, P., & Busalacchi, A. (2004). Tropical instability waves in the Atlantic Ocean. *Ocean Modelling,* 7(1-2), 145–163. doi:10.1016/s1463-5003(03)00042-8

Johns, W. E., Lee, T. N., Schott, F. A., Zantopp, R. J., & Evans, R. H. (1990). The North Brazil Current retroflection: Seasonal structure and eddy variability. *Journal of Geophysical Research*, 95(C12), 22103. doi:10.1029/jc095ic12p22103

Johns, W. E., Lee, T. N., Beardsley, R. C., Candela, J., Limeburner, R., & Castro, B. (1998). Annual Cycle and Variability of the North Brazil Current. *Journal of Physical Oceanography*, 28(1), 103–128. doi:10.1175/1520-0485(1998)028<0103:acavot>

Kermabon, C., Lherminier, P., Le bot, P., & Gaillard, F. (2018). Chaine Automatisée de Suivi des Courantomètres Acoustiques Doppler Embarqués. CASCADE V7.2: Logiciel de validation et de visualisation des mesures ADCP de coque. Documentation utilisateur et maintenance. (ODE/LOPS 18), edited by Ifremer, Brest, France, 115 pp. [Available at ftp://ftp.ifremer.fr/ifremer/lpo_permanents/cascade/CASCADE_V72_V2.pdf.]

Large, W. G. & Pond. S. (1981), Open Ocean Measurements in Moderate to Strong Winds. *Journal of Physical Oceanography*, Vol. 11, pp. 324 - 336.

Laurindo, L. C., Mariano, A. J., & Lumpkin, R. (2017). An improved near-surface velocity climatology for the global ocean from drifter observations. *Deep Sea Research Part I: Oceanographic Research Papers*, 12473-92. doi: 10.1016/j.dsr.2017.04.009.

Lellouche, J.-M., Greiner, E., Le Galloudec, O., Garric, G., Regnier, C., Drevillon, M., et al. (2018). Recent updates to the Copernicus Marine Service global ocean monitoring and forecasting real-time 1⁄12° high-resolution system. *Ocean Science*, 14 (5), 1093-1126. doi: 10.5194/os-14-1093-2018.

Lellouche, J.-M., Greiner, E., Bourdallé-Badie, R., Garric, G., Melet, A., Drévillon, M., et al. (2021). The Copernicus Global 1/12° Oceanic and Sea Ice GLORYS12 Reanalysis. *Frontiers in Earth Science*, 9 (585). doi: 10.3389/feart.2021.698876.

Lindzen, R. S. and Nigam, S. (1987). On the role of sea surface temperature gradients in forcing low-level winds and convergence in the tropics. *Journal of The Atmosphere Sciences*, 44, 2418-2436.

Lumpkin, R., & Garzoli, S. L. (2005). Near-surface circulation in the Tropical Atlantic Ocean. *Deep Sea Research Part I: Oceanographic Research Papers*, 52 (3), 495-518. doi: 10.1016/j.dsr.2004.09.001.

Madec, G. (2008): NEMO ocean engine - Version 3.1. Note du Pôle de modélisation, (27), edited by Institut Pierre-Simon Laplace (IPSL), Paris, France1288-1619, 201 pp

Marin, F., Caniaux, G., Bourlès B., Giordani, H., Gouriou, Y., & Key, E. (2009). Why were sea surface temperatures so different in the eastern equatorial Atlantic in June 2005 and 2006? *Journal of Physical Oceanography*, 39, 1416–1431, doi:10.1175/2008JPO4030.1.

Masson, S., & Delecluse, P. (2001). Influence of the Amazon River runoff on the tropical Atlantic. *Physics and Chemistry of the Earth, Part B: Hydrology, Oceans and Atmosphere*, 26(2), 137-142.

NRSC (2013). "OSCAT Wind stress and Wind stress curl products", Ocean Sciences Group, Earth and Climate Science Area, Hyderabad, India.

Philander, S. G. H., & Pacanowski, R. C. (1986). The mass and heat budget in a model of the tropical Atlantic Ocean. *Journal of Geophysical Research: Oceans*, 91 (C12), 14212-14220. doi: 10.1029/JC091iC12p14212.

Poli, L., Artana, C., Provost, C., Sirven, J., Sennéchael, N., Cuypers, Y., & Lellouche, J. (2020). Anatomy of subinertial waves along the Patagonian shelf break in a 1/12° global operational model. *Journal of Geophysical Research: Oceans*. doi:10.1029/2020jc016549.

Reynolds, R. W., Rayner, N. A., Smith, T. M., Stokes, D. C., & Wang, W. (2002). An Improved In Situ and Satellite SST Analysis for Climate. *Journal of Climate*, 15 (13), 1609-1625. doi: 10.1175/1520-0442(2002)015<1609:Aiisas>2.0.Co;2.

Richardson, P. L., & Walsh, D. (1986). Mapping climatological seasonal variations of surface currents in the tropical Atlantic using ship drifts. *Journal of Geophysical Research: Oceans*, 91 (C9), 10537-10550. doi: 10.1029/JC091iC09p10537.

Richardson, P. L., & Reverdin, G. (1987). Seasonal cycle of velocity in the Atlantic North Equatorial Countercurrent as measured by surface drifters, current meters, and ship drifts. *Journal of Geophysical Research: Oceans*, 92 (C4), 3691-3708. doi: 10.1029/JC092iC04p03691.

Schott, F. A., & Böning C. W. (1991). The WOCE model in the western equatorial Atlantic: Upper layer circulation. *Journal of Geophysical Research: Oceans*, 96 (C4), 6993-7004. doi: 10.1029/90jc02683.

Schott, F. A., Fischer, J., & Stramma, L. (1998). Transports and pathways of the upper-layer circulation in the western tropical Atlantic. *Journal of Physical Oceanography*, 28 (10), 1904-1928. doi: 10.1175/1520-0485(1998)028<1904:tapotu>2.0.co;2.

Schouten, M. W., Matano, R. P., & Strub, T. P. (2005). A description of the seasonal cycle of the equatorial Atlantic from altimeter data. *Deep Sea Research Partt I: Oceanographic Research Papers*, 52 (3), 477-493. doi: 10.1016/j.dsr.2004.10.007.

Servain, J., Picaut, J., & Busalacchi, A. J. (1985). Chapter 16 Interannual and Seasonal Variability of the Tropical Atlantic ocean depicted by Sixteen years of Sea-Surface Temperature and wind stress. *Elsevier Oceanography Series*, 211–237. doi:10.1016/s0422-9894(08)70712-8.

Servain, J. (1991). Simple climatic indices for the tropical Atlantic Ocean and some applications. *Journal of Geophysical Research: Oceans*, 96 (C8), 15137-15146. doi: 10.1029/91jc01046.

Storto, A., Alvera-Azcárate, A., Balmaseda, A., Barth, A., Chevallier, M., Counillon, F., et al. (2019). Ocean reanalyses: Recent advances and unsolved challenges. *Frontiers in Marine Science*, 6418. doi: 10.3389/fmars.2019.00418.

Stramma, L., & Schott, F. A. (1999). The mean flow field of the tropical Atlantic Ocean. *Deep Sea Research Part II: Tropical Studies in Oceanography*, 46 (1-2), 279-303. doi: 10.1016/s0967-0645(98)00109-x.

Stramma, L., S. Schmidtko, J. Luo, J. Hoolihan, M. Visbeck, D. Wallace, P. et al. (2012). Expansion of oxygen minimum zones may reduce available habitat for tropical pelagic fishes. *Nature Climate Change*, 2, 33-37, doi:10.1038/nclimate1304.

Trenberth, K.E., Large, W. G., & Olson, J. G. (1990). The Mean Annual Cycle in Global Ocean Wind Stress. *Journal of Physical Oceanography*, Vol. 20, pp. 1742-1760.

Urbano, D. F., Jochum, M., & da Silveira, I. C. A. (2006). Rediscovering the second core of the Atlantic NECC. *Ocean Modelling*, 12 (1), 1-15. doi: 10.1016/j.ocemod.2005.04.003.

Urbano, D. F., De Almeida, R. A. F., & Nobre, P. (2008). Equatorial Undercurrent and North Equatorial Countercurrent at 38°W: A new perspective from direct velocity data. *Journal of Geophysical Research: Oceans*, 113 (C4). doi: 10.1029/2007jc004215.

Varona, H. L., Veleda, D., Silva, M., Cintra, M., & Araujo, M. (2019). Amazon River plume influence on Western Tropical Atlantic dynamic variability. *Dynamics of Atmospheres and Oceans*, (85) 1-15. doi: 10.1016/j.dynatmoce.2018.10.002.

Verdy, A., & Jochum, M. (2005). A note on the validity of the Sverdrup balance in the Atlantic North Equatorial Countercurrent. *Deep Sea Research Part I : Oceanographic Research Papers*, 52 (1), 179-188. doi: 10.1016/j.dsr.2004.05.014.

von Schuckmann, K., Brandt, P. & Eden, C. (2008). Generation of tropical instability waves in the Atlantic Ocean, *Journal of Geophysical Research*, 113, (C8), doi:10.1029/2007JC004712.

Zebiak, S. E. (1993). Air–Sea Interaction in the Equatorial Atlantic Region. *Journal of Climate*, 6 (8), 1567-1586. doi: 10.1175/1520-0442(1993)006<1567:Aiitea>2.0.Co;2.

SUPPLEMENTARY MATERIAL

The goal of the supplementary material is to detail and complete some results mentioned in the paper. In the first part, we show the vertical structures of the individual ADCP sections. Then, in the second part, we show the variability of the near-surface zonal velocity from G12V1 reanalysis over the 1993-2018 period.

1. Vertical distribution of the zonal velocity of PIRATA-BR SADCP sections at 38°W between 2°- 15°N

Four main currents appear during the ADCP cruises at 38°W: part of the EUC and the NEUC, the nSEC and the NECC with its two branches during the second half of the year.

The EUC appears more extensive to the north during Spring (Figure S1) than the rest of the year (Figure S2). In April 2008 (Figure S1b) it is most extended (toward 4°N) with a 0.6 m/s core at approximately 2.5°N/85 m depth. North of the EUC, it appears a westward current identified as the nSEC in the upper layer (Figures S1 and S2). During spring, the nSEC is wider and weaker (Figure S1) while it is stronger and less extended during the second half of the year (Figure S2). The strongest nSEC among the 15 ADCP sections (0.9 m/s) occurs in July 2014 approximately at 2.5°N/35 m depth (Figure S2d). Below 100 m depth, the eastward NEUC lies between 3-6°N. It is separated from the NECC during spring (Figure S1c-d) and is connected to the southern branch (sNECC) during the second half of the year. The NEUC-NECC connections are visible in 2003, 2005, 2010, 2017 and 2018 (Figure S2 k, i, g, b, a, respectively) and the highest core velocity of the NEUC (0.4 m/s) appears in July 2010 underneath the NECC, between 3.5°N and 4.5°N, at approximately 180 m depth.

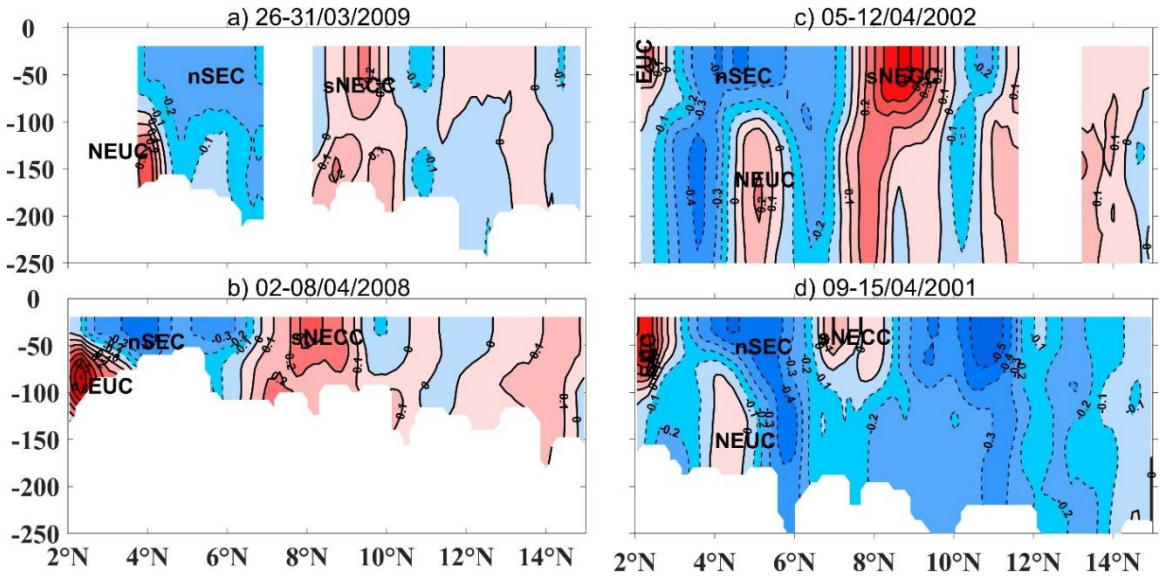

Figure S1. Zonal ADCP velocity (m/s) from 2°N to 15°N at section 38°W during Spring: a) March 2009, b) April 2008, c) April 2002, d) April 2001. Red and blue areas represent respectively the eastward (positive) and the westward (negative) velocities with contours each 0.1 m/s. The dashed contours are for the westward (negative) velocities.

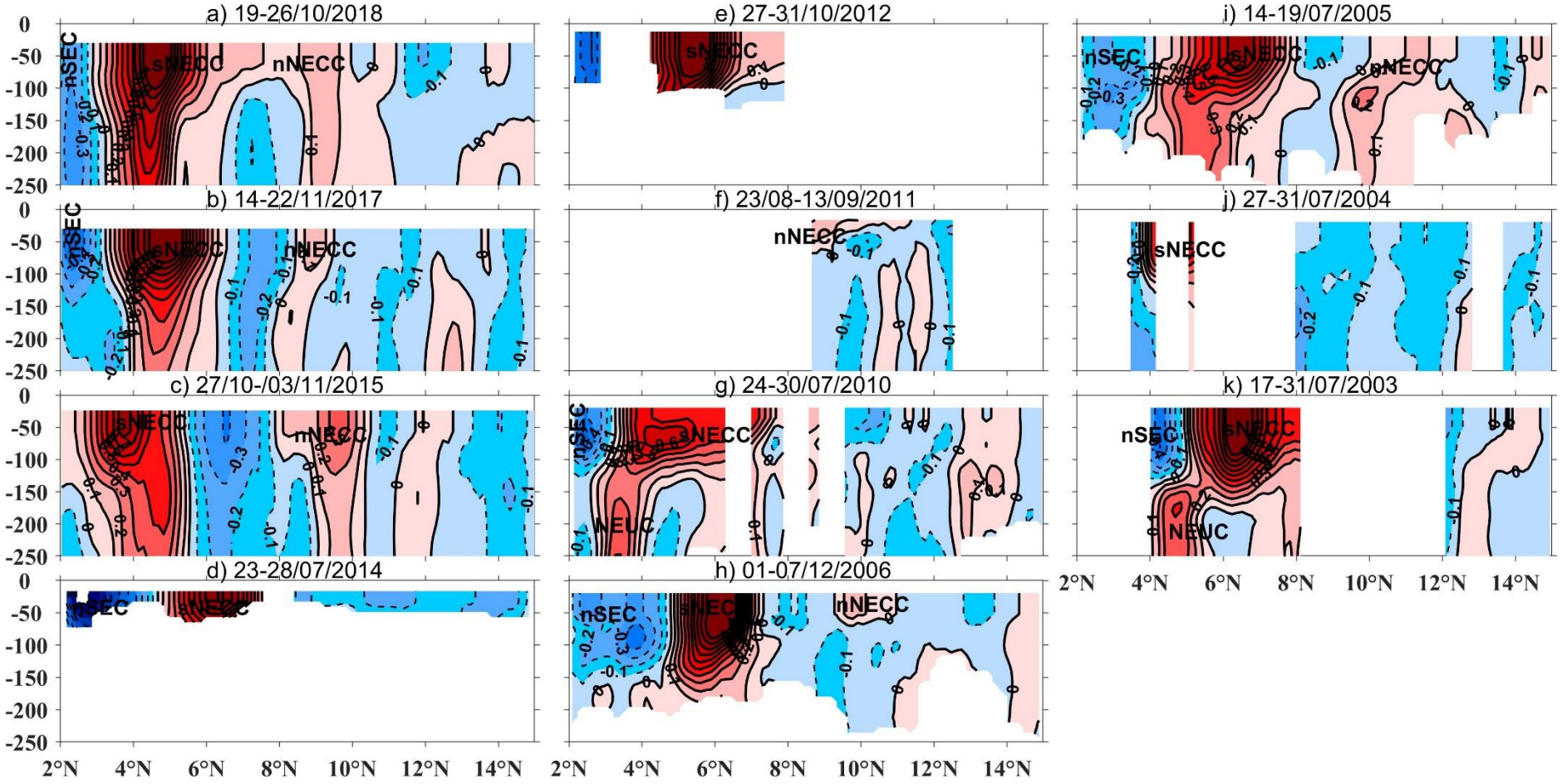

Figure S2. Zonal ADCP velocity (m/s) from 2°N to 15°N at section 38°W during the second half of the year: a) October 2018; b) November 2017; c) October-November 2015; d) July 2014; e) October 2012; f) August-September 2011; h) December 2006; i) July 2005; j) July 2004; and k) July 2003. Red and blue areas represent respectively the eastward (positive) and the westward (negative) velocities with contours each 0.1 m/s. The dashed contours are for the westward (negative) velocities.

2. GLORYS12V1 near-surface zonal velocity at 38°W for 1993-2018 period

From G12V1 monthly estimates across the 38°W section, the first 15m-depth averaged velocities are computed over 1993-2018 period (Figure S3a), as well as their anomalies relative to the seasonal climatology (Figure S3b). For the sake of clarity, anomalies are plotted only where the NECC is observed (eastward positive values in Figure S3a). These Hovmoller diagrams show a significative year-to-year variability of the current. The NECC mean location about 6.1°N is plotted (dashed line in Figure S3). Around this latitude, the NECC is stronger during the second half of the years 1993, 1994, 2000, 2007, 2011, 2013, 2014, and 2017. The sNECC appears every year south of this mean latitude, with approximately equal occurrence of positive/negative anomalies over years. The two-core structure is visible the second half of the year, with interannual variations. There is no evidence of nNECC remnant pattern from one year to the other, although in 1995, 1999-00 and 2012-13, north of 10°N, the anomalies exhibit stronger nNECC branches extending northward. In contrast, south of 10°N, at the end of the previous year the sNECC branch undergoes a northward migration that can be visible until the summer of the next year and connects later with the new sNECC of the following year.

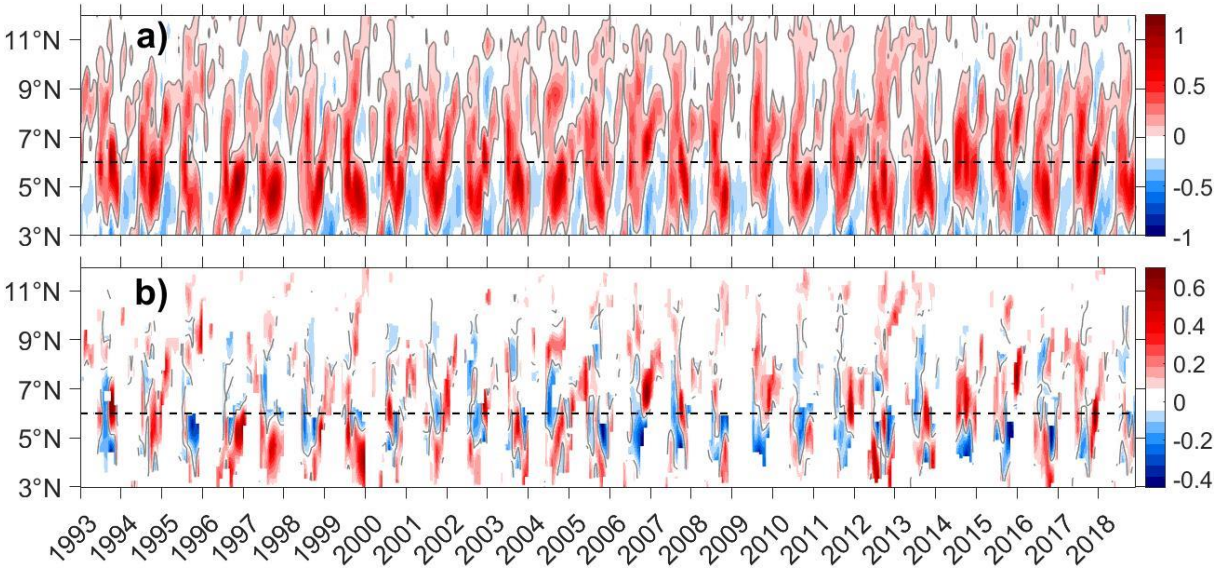

Figure S3. Hovmöller diagram of: a) the zonal velocity averaged between 0-15m at 38°W, and b) its corresponding seasonal anomalies over the years. The horizontal dashed line represents the NECC's mean location. The zero contours velocity are plotted in grey lines.

To conclude this chapter, we compared the daily G12V1 current velocity to the ADCP data available at 38°W and showed that, the reanalysis can reproduce the two-core structure of the NECC, and can be considered for a better understanding of this structure. We also compared the monthly climatology of G12V1 to the near-surface drifter currents velocity climatology in the WTA to show the similarities between both products. Overall, the results were conclusive and motivate the idea to study the seasonal and the interannual variability of the NECC at 38°W which have been presented in the chapter. The goal of these investigations was also to validate G12V1 product in the WNTA, and use it in the chapter 6 to investigate the seasonal variability of the vertical structure of the currents crossing the different sections chosen and their transports (Figure 1 of Chapter 3).

The following chapter is dedicated to the investigation of the seasonal and interannual variability of WB currents using the gridded altimetry-derived geostrophic currents.

5 STUDY OF THE SURFACE CIRCULATION OF THE WESTERN TROPICAL ATLANTIC USING ALTIMETRY-DERIVED GEOSTROPHIC CURRENTS OVER THE 1993-2017 PERIOD

The goal of this chapter is to use cross-sections of the currents described in the section 3.1 to investigate the seasonal and interannual variability of all the surface currents, which influence the dynamics of the WTA. The gridded altimetry-derived currents are used together with the wind data over the 1993-2017 period to achieve our goal and pursue later this study in the chapter 6 by using G12V1 current to analyze the vertical structure of the currents and their transport variability. The whole study is carried out in the research article below.

Paper 2: Revisiting the tropical Atlantic western boundary circulation from a 25-year time series of satellite altimetry data

Djoirka M. Dimoune[1], Florence Birol[2], Fabrice Hernandez[1,2], Fabien Léger[2], Moacyr Araujo[1,3]

[1]Laboratorio de Oceanografia Física Estuarina e Costeira (LOFEC), Departamento de Oceanografia da Universidade Federal de Pernambuco (UFPE), Cidade Universitária, Avenida Arquitetura s/n, 50740-550 Recife, PE, Brazil

[2]LEGOS, Université de Toulouse, CNES, CNRS, IRD, 18 avenue Edouard Belin, 31400, France

[3]Brazilian Research Network on Global Climate Change (Rede CLIMA), Av. dos Astronautas, 1758, 01227-010 São José dos Campos, SP, Brazil

Correspondance to: Dimoune Djoirka Minto (pmintodimoune@gmail.com)

Prepared to be submitted to Remote Sensing:

Abstract: Altimetry-geostrophic currents data over the 1998-2017 period are used to investigate the upper layer circulation in the western tropical Atlantic. Based on six sections

chosen to cross the different current branches, we investigate their respective variability at both seasonal and interannual time-scales. Concerning the seasonal variability, our results show the central branch of the South Equatorial Current (SEC), the North Brazil Current (NBC) south of the equator, its continuity toward the Caribbean, and the northern branch of the SEC at 42°W, which follow similar annual cycles with maxima/minima during boreal winter-spring/October-November. The NBC branch located north of the equator before the retroflection, its retroflected branch (rNBC) and the North Equatorial Countercurrent (NECC) also follow similar annual cycles, but with maxima/minima during boreal fall/in May. The annual cycle of northern branches of the SEC west of 42°W and at 32°W is different from the first two groups by showing maxima in July-August. An equatorial eastward current has been observed between 0°-2°N, west of 42°W and is identified as the equatorial extension of the rNBC at the surface. It participates to a large cyclonic circulation during boreal spring between 0°-6°N and 35°-45°W. The NECC shows two-core structures during the second half of the year when the NBC presents 2 retroflection regions. Its 2 cores/branches are influenced by the wind stress curl seasonal changes. The NBC interannual variability shows two opposite scenarios related to the tropical Atlantic meridional mode (AMM) phases, depending on which side of the equator the NBC is. The NECC and nSEC interannual variability (strength and/or latitudinal shift) at 42°W are also associated with the AMM phases while they are associated to the zonal mode phases at 32°W.

Keywords: tropical Atlantic, western boundary circulation, altimetry-derived currents, seasonal and interannual variability, wind stress curl, climate modes.

1. Introduction

The energetic Western Tropical Atlantic (WTA) boundary surface circulation is known to play a key role in the transport of heat, salt and water mass from the southern to the northern hemispheres of the Atlantic Ocean, and corresponds to the return branch of the thermohaline Atlantic Meridional Overturning Circulation (AMOC), influenced by the wind (Schmitz and McCartney, 1993; Schott et al., 2004; Rodrigues et al., 2007). A regional scheme of the surface currents in the study area is proposed in Figure 1, and is derived from a global analysis of the different works mentioned below.

From 5°S to 15°N, the surface boundary circulation is formed by the North Brazil Current (NBC) flowing northward along the South American shelf. It carries tropical waters originating

from the South Atlantic subtropical gyre and contributes to interhemispheric water transport (Johns et al., 1990; 1998; Peterson and Stramma, 1991; Stramma and England, 1999; Fratantoni et al., 2000; Silva et al., 2009; Zheng and Giese, 2009, Garzoli and Matano, 2011). The NBC has its origin near 5°S, with two sources: the central branch of the westward South Equatorial Current (cSEC); and the along-shelf equatorward North Brazil Undercurrent (NBUC) which surfaces around 5-6°S (Schott et al., 1998, Dossa et al., 2020). The latter advects warm waters from the South Equatorial Current (SEC) through its southern branch (Schott et al., 1995). Further north, around 5°N, the NBC is also fed by the northern branch of the SEC (nSEC) (Goes et al., 2005). Then, between 5°-9°N and 45-50°W, a large part of the NBC retroflects to form a southeastward retroflected branch (called hereinafter rNBC). Between 3°N and 8°N, this branch first feeds at the surface the eastward North Equatorial Countercurrent (NECC) throughout the year, except during the boreal spring. At this time, the NECC is fed only by the North Equatorial current (NEC) (Bourlès et al., 1999a; Goes et al., 2005). The NECC flows eastward between 2°N and 12°N, and crosses the tropical Atlantic (Didden and Schott, 1992; Ffield, 2005; Urbano et al., 2008; Araujo et al., 2017). During the second half of the year, the NECC shows two cores that eventually separate into a southern and a northern branch (sNECC and nNECC: Urbano et al., 2006; 2008).

At depth, around 3-8°N, Cochrane et al. (1979) and Schott et al. (2004) suggested that, part of the subsurface component of the rNBC feeds the eastward North Equatorial UnderCurrent (NEUC) located around 5°N. Then, the rest of the rNBC that flows southeastward feeds between 3°N and 2°S, the subsurface eastward Equatorial UnderCurrent (EUC) (Hisard and Hénin, 1987; Bourlès et al., 1999b; Hazeleger et al., 2003; Hazeleger et de Vries, 2003; Schott et al., 1995; 2004). North of 10°N, the part of the NBC which has not retroflected, forms the Guyana Current flowing along the Guyana coast. The latter is also fed seasonally by the NEC (Johns et al., 1998) and finally flows toward the Caribbean Sea (Stramma and Schott, 1999; Garzoli et al., 2003).

The WTA upper boundary circulation is wind-driven. In the vorticity equation, the terms that dominate localy are the Ekman pumping and the divergence of the geostrophic currents (Garzoli and Katz, 1983; Urbano et al., 2006). The region is also known to be influenced by large mesoscale activities due to the barotropic instabilities of the currents (Aguedjou et al., 2019; Aroucha et al., 2020). Previous studies of Garzoli and Katz (1983), Jochum and Malanotte-Rizzoli (2003) and Verdy and Jochum (2005) about the WTA boundary circulation and the NECC indicate that, west of 32°W, the Sverdrup balance is no more respected, and the

advection terms of the relative vorticity due to the eddies and the mean flow also play a significant role. North of the equator, the region is characterized by strong seasonal variability of the wind. The Trade Winds variations influence the currents system formed by the NBC, the NBCR, the rNBC and the NECC. In particular the NBCR location, the NBC transport and the NECC position/transport respond to the seasonal changes in the wind regimes (Johns et al., 1990; 1998; Garzoli et al., 2003; 2004; Urbano et al., 2006; 2008). This wind influence appears through the latitudinal changes of the currents in conjounction with the Intertropical Convergence Zone (ITCZ) location. The variability of the currents strength appears as a regional response of the wind stress curl (WSC) distribution and the WSC strength over the basin (Johns et al., 1998; Fonseca et al., 2004; Garzoli et al., 2004, Urbano et al., 2006; 2008). In the equatorial region, the EUC seasonal variability is first associated to the basin scale zonal pressure gradient (ZPG), and also to the seasonal cycle of the local wind forcing (Hisard and Hénin, 1987; Provost et al., 2004; Brandt et al., 2006; Hormann and Brandt, 2007; Brandt et al., 2016).

The interannual variability of the WTA boundary currents has been less investigated because of the lack of long-term data in this area. Nevertheless, Fonseca et al. (2004), using a combination of 8 years period altimetry and hydrographic data from 1993 to 2000, investigated the influence of the wind on both the NBCR and the NECC variability. They did not find any direct relationship between the wind parameters and the currents variability. Hormann et al. (2012), used the surface velocity data from drifters from 1993 to 2009 and found a relationship between the NECC intensity/location and the tropical Atlantic climate modes (ACM), represented by positive and negative phases of the Atlantic zonal mode (AZM) and the Atlantic meridional mode (AMM) (Cabos et al., 2019). In the equatorial Atlantic, Hormann and Brandt (2007) also exhibit such relationship, using a high-resolution ocean general circulation model, observations and sea surface temperature (SST) anomalies in the Atlantic cold tongue region. They confirmed the previous findings of Goes and Wainer (2003) concerning the link between the interannual variability of the wind and the ACM impacting the strength of the tropical Atlantic circulation by showing that, the EUC transport is affected by the cold and warm events of the AZM (the so called “Atlantic Niño / Niña”).

In this study, we propose to revisit the scheme of the WTA boundary circulation using a 25-year time series of gridded altimeter-derived geostrophic currents. This dataset is longer than the one used by Fonseca et al. (2004) and allows to provide a more robust description of the current branches described above, as well as of their seasonal and interannual variations.

The data also allows to infer regional relationship among these currents. The paper is organized as follow: in section 2, the data and methods used are presented. Section 3 brings some general characteristics of the current variability in the study area. In the fourth section we analyze and discuss the seasonal and spatial variabilities of the surface geostrophic currents, and propose an updated seasonal map of the WTA surface circulation. The interannual variability of the circulation is analyzed in section 5. Section 6 is devoted to a general discussion, and section 7 offers a summary and some perspectives.

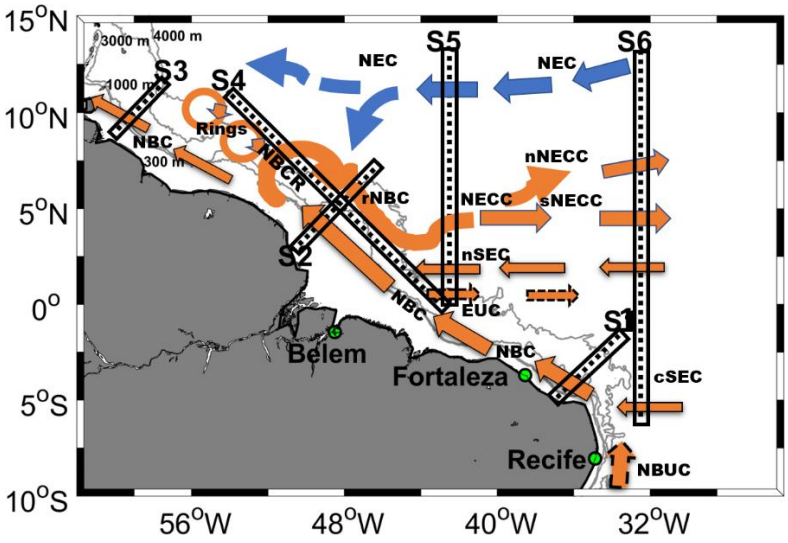

Figure 1. Schematic view of the northwest boundary surface circulation in the tropical Atlantic based on Schott et al. (2004), Goes et al. (2005), Urbano et al. (2006; 2008) and Aroucha et al. (2019); and the distribution of the cross-section of the currents chosen in the area of study: S1, S2, S3, S4, S5 and S6. Solid and dashed arrows are the upper and the thermocline layers currents, respectively. The blue and yellow colors of the arrows show connections respectively with the northern and southern hemisphere waters. From south to north, the currents shown are the North Brazil Undercurrent (NBUC), the central and northern branches of the South Equatorial Current (cSEC and nSEC, respectively), the North Brazil Current, its retroflection and its retroflected branch (NBC, NBCR and rNBC, respectively), the Equatorial Undercurrent (EUC), the North Equatorial Countercurrent (NECC) and its southern and northern branches (sNECC and nNECC, respectively), and the North Equatorial Current (NEC). The 300 m, 1000 m, 3000 m and 4000 m isobaths (grey lines) are from ETOPO2v1 global gridded database.

2. Data and methods

2.1. Altimeter-derived geostrophic currents

From along-track altimetry sea surface height measurements of all available satellite missions, the Copernicus Marine Environment Monitoring Service (CMEMS) produces daily maps of ocean dynamic topography and derives gridded geostrophic surface currents. Here, we use the SEALEVEL_GLO_PHY_L4_REP_OBSERVATIONS_008_047 product (https://resources.marine.copernicus.eu/) from January 1993 to December 2017. Daily maps of dynamic topography are estimated by optimal interpolation on 0.25° × 0.25° global grid (details

can be found in Pujol et al., 2016), and the geostrophic currents are computed using the 9-points stencil width methodology (Arbic et al., 2012) for latitudes outside the equatorial band (Equator +/-5°), and the β-plane approximation (Lagerloef et al., 1999) in the equatorial band.

For the present work, which focus on the seasonal and interannual variability, the daily gridded velocity fields have been averaged on a monthly basis after currents with high variability certainly due to the noise have been removed in the Amazon region. We have then defined 6 sections, which cross perpendicularly at least one of the current veins observed in Figure 1. For each section, the original zonal and meridional surface velocity components have been rotated in order to derive the along-section and cross-section velocity components. In this study, we considered only the cross-section component.

2.2. GEKCO Ekman currents from LEGOS

We also used for this study the daily estimates of zonal and meridional components of the wind-driven currents (Ekman currents) from the GEKCO product (Geostrophic and Ekman Current Observatory), made available by LEGOS (Laboratoire d'Etudes en Géophysique et Océanographie Spatiale). The data were calculated using the standard Ekman formulation, and the estimates have been improved in the equatorial region, considering the singularity of the equator. Then, they were validated with independent observations from both Lagragian and Eulerienne perspectives (Sudre et al., 2013). For this work, the daily estimates have been monthly averaged over the period 1993-2017. The horizonal spatial resolution is 0.25° as for the geostrophic currents, described above.

2.3. ERA5 wind velocity fields

Monthly wind velocity fields data from the ERA5 atmospheric reanalysis produced by the European Centre for Medium-Range Weather Forecasts (ECMWF, http://www.ecmwf.int) are used in order to evaluate the influence of the remote winds on the WTA ocean circulation. Monthly gridded maps are downloaded from the Copernicus Climate Change data server over the January 1993 - December 2017 period. We used the wind velocity data to calculate the wind stress field.

The zonal and meridional components of the wind stress, ζ_x and ζ_y are calculated using empirical formulations (Large and Pound; 1981: Gill, 1982; Trenberth et al., 1990) following NRSC (2013):

$$\zeta_x=\rho_{air}C_DW*U \quad \text{and} \quad \zeta_y=\rho_{air}C_DW*V \qquad 5.2.3.1$$

where U/V represent the zonal/meridional wind velocity components; W, the wind speed; ρ_{air}, the air density (1.2 kg/m^2); C_D, the drag coefficient at the ocean surface, calculated according to Large and Pound (1981).

The wind stress curl (WSC) is then deduced from the wind stress following Gill (1982):

$$Curl(\zeta) = \frac{\partial \zeta y}{\partial x} - \frac{d\zeta x}{dy} \qquad 5.2.3.2$$

From the WSC values, we found the ITCZ location (~zero values location), the minimum/maximum negative/positive values, and the WSC strength (sum of the absolute minimum negative value and absolute maximum positive value) in the tropical Atlantic, by zonally averaging each parameter over the region covering 6°S -16°N, and 30°W-0°W, following Fonseca et al. (2004).

2.4. Sea Surface temperature (SST) OI v2 from NOAA

Monthly estimates of SST OI v2 product from the NOAA are also used in order to compute the Atlantic climate mode indexes and evaluate their possible relationship with the interannual changes observed in the WTA boundary circulation. The global gridded product, with a 0.25° spatial resolution (detailed in Reynolds et al. 2002) is downloaded from a NOAA repository (https://www.esrl.noaa.gov/psd/data/gridded/data.noaa.oisst.v2.html). The AZM index is calculated considering the SST anomalies (SSTA) relative to the 1993-2017 monthly climatology in the ATL3 region bounded by 3°S-3°N/20°W-0°E (Zebiak, 1993, Hormann et al., 2012). The AMM index is also based on SSTA relative to the 1993-2017 monthly climatology, and calculated as the difference between the spatial average SSTA in the box 5°N-25°N/60°W-20°W and the spatial average SSTA in the box 20°S-5°N/30°W-10°E (Servain, 1991; Hormann et al., 2012).

3. General characteristics and variability of the circulation in the west tropical Atlantic

The mean WTA surface geostrophic circulation is first derived by averaging the daily gridded maps derived from altimetry over 1993-2017 (Figure 2a). Three key transition areas of currents are shown from south/east to north/west:

1) The transition area for the NBC formation around 5°S: the westward cSEC flowing zonally north of 6°S (mean value of ~0.3m/s) encounters the surfacing along-shelf equatorward NBUC to generate the NBC-NBUC current system around 34°-36°W. The

signature of this latter at the surface (so-called NBC) changes amplitude along its northward along-shelf course. From approximately 0.8 m/s between 3°-4°S, it slows down near the equator, then intensifies again north of 3°N. Its continuity along the Guyana coast exhibits weaker mean velocities of ~0.3 m/s.

2) The transition area of the NBC retroflection between 5°-8°N and 48°-52°W: in this area, the NBC undergoes an eastward recirculation, which feeds a southeastward vein of current so-called the NBC retroflected branch (rNBC). The rNBC reaches annual mean velocities of ~0.6 m/s.
3) This transition area located between 3°-6°N and 42°-46°W: it represents the region where the rNBC meanders with an annual mean velocity of 0.5m/s to partly feed the surface eastward NECC which decays along its course. This area is located in the region of high variability of the wind (Figure not shown).

In addition, the currents flowing in the three key areas, the mean circulation is formed in the equatorial region by the westward nSEC flowing between 2°-6°N, and stronger at the eastern part of the basin (mean velocity larger than 0.3 m/s).

The mean power spectral density of the daily geostrophic current time series (Figure not shown) helped to detect the dominant components of the WTA current variations. It shows the presence of three main variability regimes: an intraseasonal variability with energy peaks at periods less than 120 days; a seasonal variability, with peaks at periods between 120-600 days; and a weak interannual variability, with peaks at periods larger than 600 days. The filtered time series with the different cut-off frequencies allowed to isolate each of this current variability component and compute the ratio between the standard deviation of each filtered current field and of the total current field. The resulting maps (Figure 2b-d) show the relative importance of each component with regard to the total variance, as a function of the location. We observe the predominance of the seasonal scales in the whole WTA (overall ratio of 0.44), with the highest values (0.48) in the NBC region along the shelf, and between 0°-2°S east of 36°W. Intraseasonal fluctuations are also important in the same areas (with largest ratio of 0.44) while the interannual variability is only noticeable north/east of 4°N/40°W, where the NECC is located, with values representing less than 0.2 of the total variance (consistent with Richardson and Walsh, 1986).

In the rest of the study, we focused on the seasonal and interannual timescales to avoid the incertainties due to the estimation errors from the satellite near to the coast at the smaller timescales

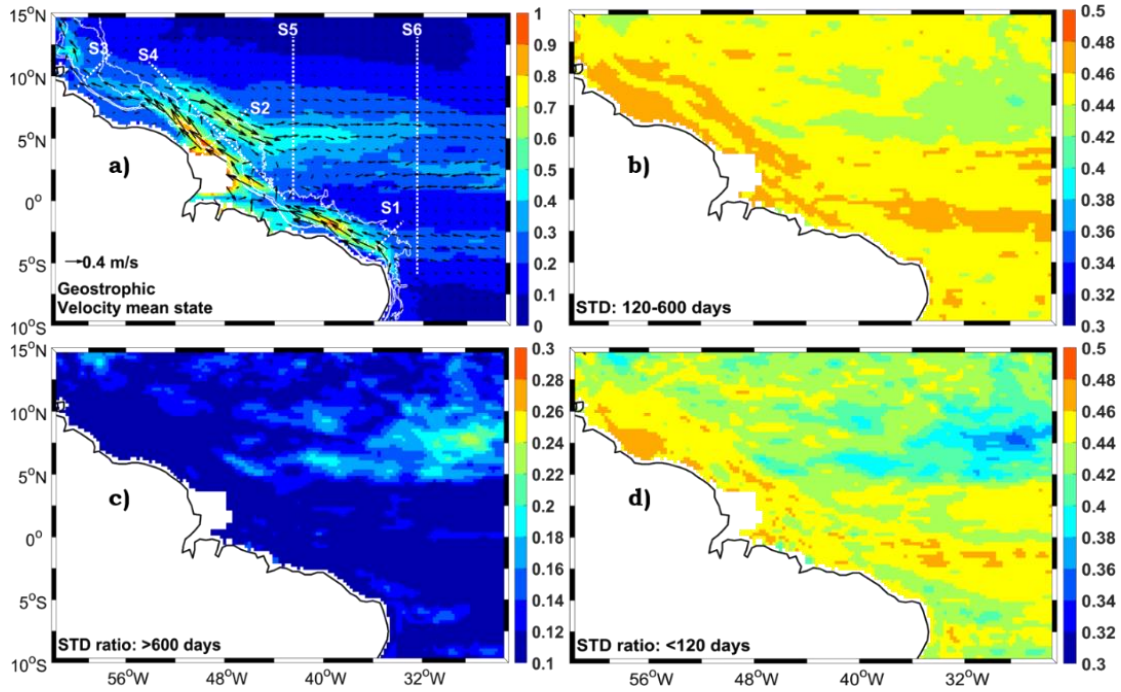

Figure 2. a) Mean state of the geostrophic currents superimposed on the absolute values of their speed (colorbar in m/s) in the study area from 1993 to 2017; **b), c)** and **d)** ratios of standard deviations of the currents for the signals between 120 and 600 days, more than 600 days and less than 120days, respectively. The white dashed lines S1, S2, S3, S4, S5, S6 in a) represent the cross-sections of the currents. The solid white lines in a) are the 300 m, 1000 m, 3000 m and 4000 m isobaths.

For the seasonal and interannual study, we first monthly averaged the daily geostrophic currents and extracted the cross-section geostrophic velocities along the six sections defined above (Figure 1). The velocities are then 4-months low-pass filtered in order to remove most of the intraseasonal variability. The time-space diagrams (also called Hovmöller diagrams) along these six sections (Figure 3) show the complexity of the surface circulation in the WTA and large changes in both time and space with respect to the different current branches. The seasonal and interannual fluctuations of the currents mentioned above are clearly visible across these sections. For each section, the time-average current values are computed (left-side plots in Figure 3), highlighting the mean spatial extension of the current veins crossing the corresponding section. Note that in addition to the main currents in Figure 1, between 1.5°S-2°N, the sections 4 to 6 show an eastward current, located where the EUC could appear. At 44°W, Bourlès et al. (1999b) have also noticed the presence of a surface eastward flow above the EUC, which was identified to be different than the EUC. So, in order to investigate this point, we chose to name it X, hereinafter before to try investigating its presence at the surface.

Table 1 summarizes the current width computed along the different sections. Note first that the positive direction convention has been chosen across the sections as follows: northward NBC in sections 1 to 3; eastward NBCR in section 4; eastward NECC in sections 5 and 6, and

eastward X flows in sections 4 to 6. Hence, the signatures of the rNBC on the section 2, the nSEC (sections 4 to 6) and the cSEC (section 6) are considered as negative. From Table 1, we observe that the NBC becomes narrower from the section 1 to the section 2, before the retroflection. The retroflection zone (section S4, Figure 3S4) extends from 3.7°N to 10.5°N, in agreement with Fonseca et al., (2004) who found the northernmost position of the NBCR around 11°N. North of the retroflection, the NBC continuity along the Guyana coast is weaker, but broader relatively to the section 2 (NBC2 and NBC3 in Figure 3). From section 6 to 4, the nSEC signature changes. It is latitudinally more extended at 32°W (nSEC6), then narrows at 42°W (nSEC5), and widens again closer to the shelf at 44°W (nSEC4) (respectively 550, 67 and 190 km in Table 1). The NECC extension also varies from 32°W to 42°W, and is located further north and wider on the east, with mean width extending from 860 km (NECC5) to 920 km (NECC6).

Table 1. Latitudinal coverage of the different sections current branches: NBC1, NBC2 and NBC3 are respectively the North Brazil Current on the section 1, 2 and 3; NECC5 and NECC6 are respectively the North Equatorial Countercurrent on the section 5 and 6; nSEC4, nSEC5 and nSEC6 are respectively the northern branch of the South Equatorial Current (SEC) on the sections 4, 5 and 6; cSEC6 is the central branch of the SEC on the section 6; and X4, X5 and X6 are the equatorial eastward flow X on respectively on the sections 4, 5 and 6.

Current of the sections	Latitudinal coverage	Extension of the currents (km)
NBC1	1.3°S-4.6°S	~520
NBC2	3.6°N-5°N	~220
rNBC2	5°N-7.4°N	~380
NBC3	9.1°N-11.9°N	~440
NBCR4	3.7°N-10.5°N	~760
nSEC4	2°N-3.7°N	~190
X4	1.2°N-2°N	~120
NECC5	2.4°N-10.1°N	~860
nSEC5	1.7°N-2.3°N	~70
X5	0°N-1.7°N	~190
NECC6	4.1°N-12.4°N	~920
nSEC6	0°N-4.1°N	~550
X6	0°S-1.4°S	~110
cSEC6	1.4°S-5.9°S	~500

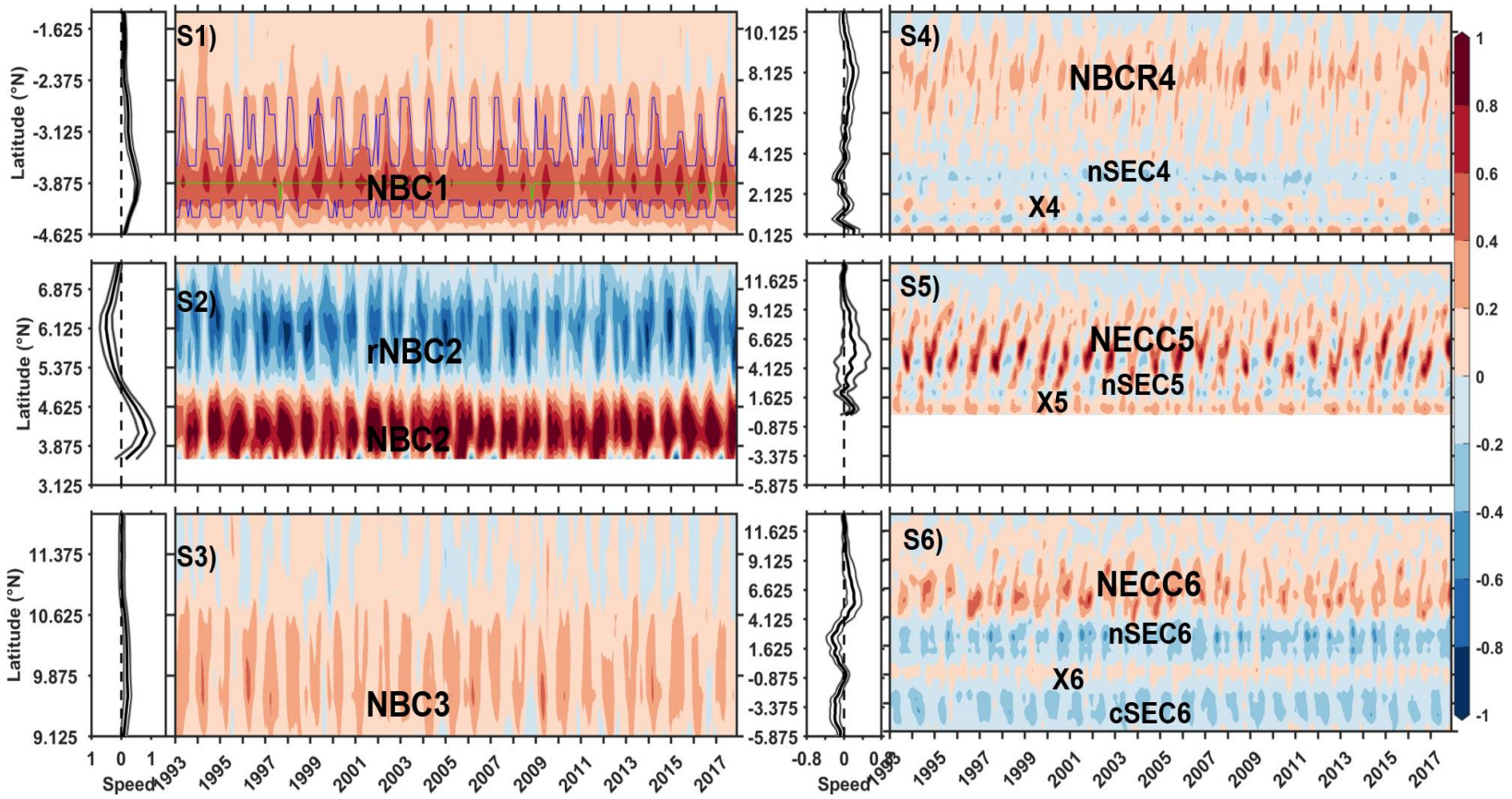

Figure 3. Hovmoller diagrams (1993-2017) of the cross-currents (m/s) for: **S1)** the cross-section 1, **S2)** the cross-section 2, **S3)** the cross-section 3, **S4)** the cross-section 4, **S5)** the cross-section 5, and **S6)** the cross-section 6. The boxes before each diagram are the time averages of the cross-currents framed by their standard deviations at each point. The red (blue) colors show the northward/eastward (southward/westward) directions of the cross-currents: North Brazil current (NBC), its retroflected branch (rNBC) and the retroflection signature at the limit between the NBC and the rNBC (NBCR); North Equatorial Countercurrent (NECC); the equatorial surface eastward flow named X; the northern and the central branches of the South Equatorial Current (nSEC and cSEC, respectively). The numbers next to the acronym of the currents represents the number of the cross-sections. The blue lines (green line) in S1) frame the velocities higher than the half of the maximum velocity (maximum velocity) over 1993-2018 period.

In order to further investigate the variations of the geostrophic current intensity at the different time scales, the maximum velocity value of each current vein identified in Table 1 have been found for each month (corresponds to the current core and called Vmax hereafter: see Figure 3, green line on S1). Then the corresponding current vein width is estimated considering the portion of the section where the velocity is larger than Vmax/2 (see Figure 3, blue lines on S1). Finally, the relative intensity is computed by averaging the cross-section velocity values over the estimated width. For each current vein crossing the six sections, we registered the monthly time series of the maximum intensity, width and relative intensity/strength. The latter could have been computed by just averaging velocities over the full identified portion of each current vein (e.g., positive or negative crossing signature), but the resulting values were found smaller and do not fully reflect the Hovmöller diagrams of Figure 3 and Figure 4 (Figure not shown). For the NBCR region and the NECC, the variability of the maximum velocity of two different flow branches from the same current and their corresponding location is also analyzed in the following sections in order to compare with the previous study of Fonseca et al. (2004), and mostly to understand the variability of their location in relation to the wind variability and the tropical Atlantic climate modes. In this study, the presence of two superimposed regions of the NBCR/NECC two-core structure is identified when the flow velocity profile shows 2 highest local maxima separated by a lowest local minimum in the NBCR region (considered between 4°-10°N)/NECC region (considered between 3°-11°N) (Figure 4S4-S6).

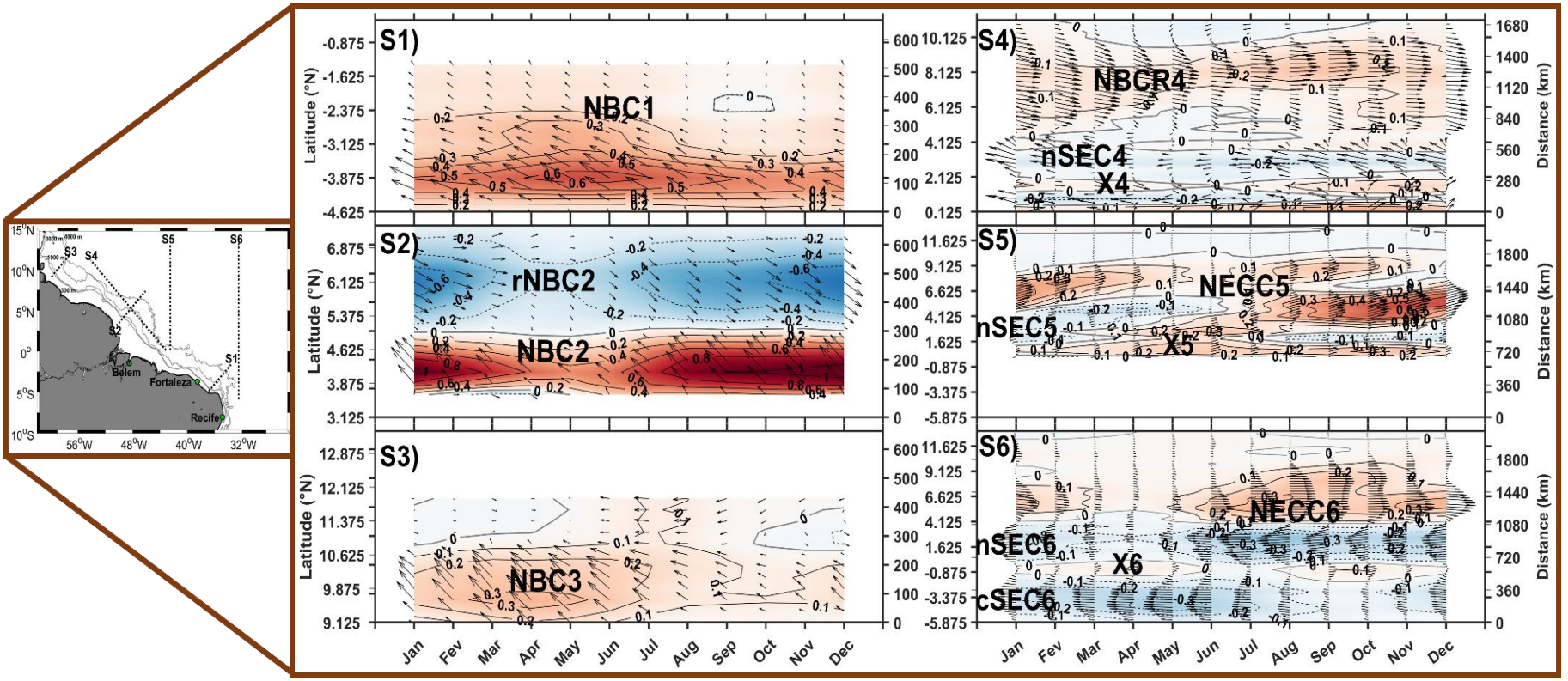

Figure 4. Monthly climatology of the current branches superimposed on the Hovmoller diagram of the monthly climatology of the cross-currents (m/s) over the 1993-2017 period. S1), S2), S3), S4), S5) and S6) are respectively for the cross-sections 1 to 6 represented over the study area (Left map). The grey lines represent the cross-currents isolines. nNECC and sNECC are respectively, the northern and southern branches of the North equatorial Countercurrent (NECC); NBC, the North Brazil Current; NBCR, the NBC retroflection limit; rNBC, the retroflected branch of the NBC, nSEC and cSEC, the northern and the central branches of the South Equatorial Current, respectively; and X, the equatorial surface eastward flow. The right sides of each diagram are the distances from the lowest point (in km) whereas the left sides are the latitudes (in degrees).

4. Seasonal variability of the western boundary circulation

The focus here is on the seasonal changes in the different current branches over the whole study area. Therefore, the monthly climatology of the cross-section currents shown in Figure 3 are calculated along the six sections (Figure 4). The corresponding seasonal climatological time series of each current intensity and other characteristics (core velocities and locations) of NBCR regions over section 4, NECC5 and NECC6 are also shown in Figure 5. Below, we analyze the different current components.

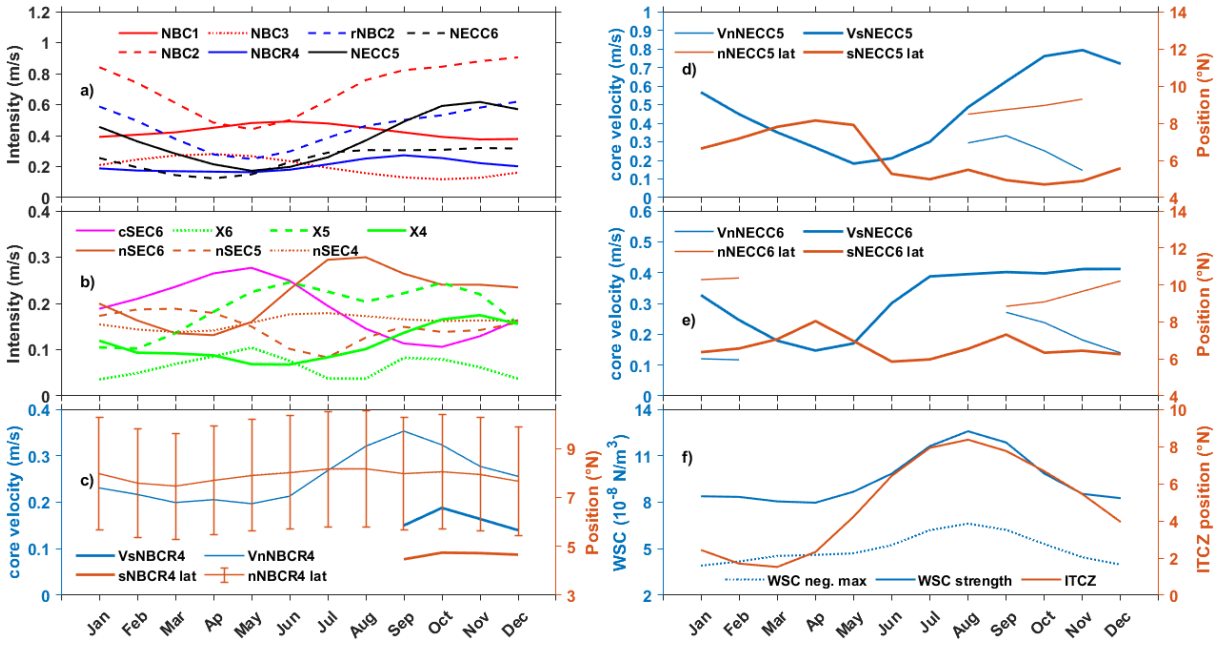

Figure 5. Monthly climatology of absolute values of the current branches' intensity (m/s) along their respective path on each cross-section: a) and b); the cores velocities and positions of the North Brazil Current Retroflection (NBCR) regions, and the North Equatorial Countercurrent (NECC) branches on the cross-section 4 (c) and the cross-sections 5-6 (d-e), respectively; and the absolute value of the maximum negative wind stress curl (WSC neg. max), the WSC strength and the ITCZ location (f). a): NBC1, NBC2 and NBC3 represents the North Brazil Current (NBC) on the cross-sections S1, S2 and S3, respectively; rNBC2 represents the NBC retroflected branch (rNBC) on the cross-section 2; NBCR4, represent the NBCR main flow on the cross-section 4; NECC5 and NECC6 represent respectively, the NECC on the cross-sections S5 and S6; b) nSEC4, nSEC5 and nSEC6 represents the northern branch of the South Equatorial Current (SEC) on the cross-sections S4, S5 and S6, respectively; cSEC6 represents the central branch of the SEC on the cross-section S6; and X4, X5 and X6 represent the equatorial surface eastward flow on the cross-sections S4, S5 and S6, respectively. On c), d) and e), the "V" initials at the beginning, and "lat" at the end of each acronym of the legends of figures represents the core velocity and position, respectively (blue and orange colors, respectively). The nNBCR/sNBCR and nNECC/sNECC represent the northern/southern retroflection and northern/southern NECC branch, respectively. The thin/tick lines represent the northern/southern retroflection (nNBCR/sNBCR) and southern/northern NECC branch (sNECC/nNECC), respectively. The bars on the nNBCR4 location represent the root mean square value of each month.

4.1. The North Brazil Current and its retroflection

From section 1 and 6 (Figure 4), the NBC and the cSEC are observed both located at ~4°N and present similar seasonal cycles with stronger flows during the first half of the year.

The cSEC6 maximum (0.3 m/s) / minimum (0.1 m/s) appears in May / October, and the NBC1 maximum (0.6 m /s) / minimum (0.4 m/s) appears between May-June / November-December (Figure 5a). Both annual cycles are similar to the the annual cycle of the NBUC transport found by Rodrigues et al. (2007) at 10°S and which is related to the bifurcation location of the sSEC. The authors show that, the NBUC transport reaches its maximum/minimum at that latitude in May-June/October-November when the sSEC bifurcates at its southernmost/northernmost location. This suggests that the seasonal variability of the NBC intensity approximately at 5°S might be influenced by the sSEC bifurcation location, which in turn is influenced by the annual cycle of the WSC over the area 5°–10°S, 25°–40°W (Rodrigues et al., 2007).

Comparing S1 to the sections S2 to S4 (Figure 4S1-S4 and Figure 5), the NBC depicts two different seasonal cycles along its northward path. The NBC2, NBCR4 and the rNBC2 show approximately the same seasonal cycles, in opposite phase with NBC1 and NBC3 which are approximatively in phase. NBC2 is narrower but relatively stronger than the NBC1. It decreases from January to May (up to 0.4 m/s), and is maximum in November-December (1m/s). The rNBC2 is larger (width of ~350 km) but less intense (maximum intensity of 0.6 m/s in November-December) than the NBC2 (~200 km). We observe a slow down of the NBC2 intensity in October, in phase with the rNBC2 (Figure 4S2). From September to January, the NBC shows another retroflection region between 4-6°N south of the main retroflection flow observed around 8°N, which is visible in section 4 (Figure 4S4 and Figure 5c). The flow of this new retroflection region (so-called sNBCR) reaches its maximum intensity in October while the main retroflection flow (nNBCR) reaches its maximum one month earlier. Then, the intensity of sNBCR starts decreasing after October and migrating northward to join the nNBCR; and both are completely merged at the beginning of the following year (Figure 4S4). The merged branch weakens to reach its minimum intensity in May. The annual cycles of NBC intensity crossing the section 2 and and the main retroflection flow crossing the section 4 (Figure 5a) depicts similar cycles to the NBC transport obtained by Johns et al. (1998) and Garzoli et al. (2004). The authors found using acoustic Doppler current profilers (ADCP)/Inverted Echos sounders/Pressure gauge data, minimum and maximum transports during boreal spring (April-May) and summer-fall (August-September-October), respectively. Jonhs et al. (1998) explained the seasonal cycle of the NBC by the influence of the remote wind stress curl forcing across the tropical Atlantic. In this study, we also show that the seasonal cycles of the NBC branches north of the equator (except its continuity along the Guyana coast) follow the remote wind stress curl strength with one to four months delay (Figure 5a and f).

The delay of more than the expected delay of two months can be explained by the inability of the NBC branches intensity as calculated here to reproduce well the shape of its transport annual cycle, or by the importance of the lateral diffusion near to the western boundary and the nonlinear terms (of the vorticity equation) which break down the Sverdrup balance west of 42°W (Garzoli and Katz, 1983; Verdy and Jochum, 2005). The northernmost location of the nNBCR maximum intensity occurs in August, when the maximum WSC strength is reached (Figure 5c and f). The root mean square (rms) of the monthly mean values of its location (Figure 5c) is nearly constant (~2.3°), and is consistent with the evidence that there may not be a preferred season for NBC ring formation (Garzoli et al., 2003; Goni and Johns, 2003).

Further north, the NBC continuity along the Guyana coast (NBC3) is twice wider (~440 km) and less intense than the NBC2 (Figures 4S2 and S3). It reaches a minimum in October (~0.1 m/s), and a maximum during March-May (0.3 m/s) when the NBCR4 is minimum (Figure 4S3-S4 and Figure 5). Its seasonal cycle is similar to the NBC1 and cSEC, and might also be influenced by the sSEC bifurcation location.

4.2. The North Equatorial Countercurrent

The NECC (NECC5 and NECC6) seasonal cycle is similar to the ones of the NBC2, NBCR4 and rNBC2 (Figure 4S2, S4, S5 and S6). It weakens along its pathway and its intensity is maximum in November-December (~0.6 m/s at 42°W and ~0.3 m/s at 32°W), and minimum in April-May (Figure 5a). It is stronger during the second half of the year and confirms the presence of a two-core/branch structure previously investigated by Urbano et al. (2006; 2008). The two cores/branches are seen first at 42°W in August, then at 32°W in September (Figure 4 and Figure 5d-e) and induce two current branches. The nNECC branch is narrower (located between 7°-9°N) and stronger (~0.3 m/s) in August-September at 42°W (Figure 4S5 and Figure 5d). It is even separated from the southern branch from October to December. At 32°W, the NECC appears with two non-separated branches from September (northern core velocity of ~0.2 m/s) to November. The northern core is gradually decreasing in intensity and shifting northward until forming a separated second branch, which is located between 9-11°N from December to February, and then becomes a very weak flow in March-April (Figure 4S5 and e). From June to July, the NECC signature (sNECC branch) is located between 3-4°N at 42°W and is connected from the south to the eastward flow associated with X5 in Figure 4S5. Urbano et al. (2008) show with ADCP data at 38°W that the eastward flow south of the NECC is the connection between the surfaced waters of the NEUC and the EUC during this period of the year. This suggests that the eastward flow X5 may be the one that favors the surfacing and the

connection of both currents during June-July. From June to November, the sNECC branch witnesses a continuous increase simultaneously with rNBCR2. However, it reaches its maximum one month early in November and decreases while the rNBC is still increasing. This confirms the geostrophic character of the NECC which is not only fed by the rNBC at the surface (Verdy and Jochum, 2005). The sNECC witnesses the same variability at 32°W, but reaches its minimum early in March-April when the climatological sNECC is described as a reversing flow or is missing at its usual location (Garzoli and Katz, 1983; Garzoli, 1992). It starts increasing from April-May, between 4°-6°N far from the eastward flow X, and grows until November. Burmeister et al. (2019) show that, in the central Atlantic, during the northward migration of the ITCZ from April to August (Figure 5f), the nSEC recirculated eastward to infiltrate the NEUC which strengthens and shoals the thermocline about its mean latitude of 5°N. The presence sNECC flow in April-May suggests that the NECC flow which is known to be in Sverdrup balance and is a geostrophic flow might be initiated by the recirculation of the mixed nSEC-NEUC water at the beginning, and then might be strengthened by this latter when developing until August. It reaches its first maximum in July-August together with the nSEC, and a second maximum in November (Figure 5a, b and e). At both locations, the sNECC core shows two northward migrations. The first migration occurs from June-July (June) to August (September) at 42°W (32°W), and the second occurs from October to April at both locations (Figures 5d-e). Fonseca et al. (2004) also found similar migrations but with some differences. They found two northernmost locations of the NECC in February and August, and two southernmost locations in June and December. The first northernmost location found by the authors in February was due to the lack of data between March and May, and the second southernmost location found in December might be due to their method used to compute the core position, which didn't allow them to also find the second core of the NECC. We found here that the nNECC core always migrates northward until disappear or be very weak to be captured at both locations (Figure 5d-e).

4.3. The central and northern branches of the South Equatorial Current

Although the westward cSEC and nSEC are two branches of the westward SEC, they don't show the same seasonal cycles (Figure 4S4-S5-S6). The nSEC4, nSEC5 and nSEC6 signatures are characterized by annual cycles with maxima at different periods of time. At 32°W, the nSEC (nSEC6) grows from April to reach a maximum of ~0.3 m/s in August following the northward migration of the ITCZ (Figure 5b and f). During this time, the nSEC branch at 42°W (nSEC5) migrates northward, and its intensity decreases to ralmost disappear

in July because of the presence of the eastward flow X (Figure 4S5). After July, the the nSEC5 increases to reach a maximum of ~0.2 m/s in March (Figure 4S5-S6 and Figure 5b). Over the shelf, most of the nSEC flow joins the NBC (section 4, around 2-4°N and 46°W) and another part is deviated southeastward to merge with the rNBC and form the eastward flow X4 which is captured over the cross-section 4 (Figure 4S4). The part that joins the NBC reaches its maximum of ~0.2 m/s between June and August also following the ITCZ northward migration (Figure 5b and f). However, the nSEC varies less at this location throughout the year (Figure 4S4). We remind that the amplitude the nSEC4 is estimated from the cross-section component of the oblique section 4 and might be reduced because of the inclination.

4.4. The eastward currents X

Figure 4S4, S5 and S6 shows an eastward surface flow near the equator. Such feature was already observed and mentioned by Hisard and Hénin (1987) and Bourles et al. (1999b) using hydrographic and ADCP data to capture the vertical structure of the currents in the WTA. We chose to study this flow in order to give more details about its spatial and temporal variability. In Figure 4S4, eastward flows are captured between 1-2°N (X4) and along the equator. As mentioned in the previous section, these flows should be composed of part of the nSEC that does not join the NBC and the rNBC which is kwown to feed the EUC in the thermocline layer. We remind that the intensity of X4 is weaker than X at 42°W (X5) because of the inclination of the cross-section 4 while the weaker X at 32°W (X6) is due to the weakening of the eastward flow. X4 and X5 are almost present throughout the year (Figure 4S4-S6) and their amplitude follows a similar semi-annual cycle (Figure 5b) to the EUC in the eastern Atlantic (Hormann et al. 2007). However, their maxima's time periods are slightly different from a location to another. The X4 amplitude displays a semi-annual cycle, with a weak maximum in March-April (~0.1 m/s) and another maximum in November (~0.2 m/s). At 42°W the eastward flow X5 is larger because of the merging of X4 with the eastward flow seen along the equator (Figure 4S5). Its maxima occur in June and October with similar intensity (more than 0.2 m/s) (Figure 5b). At 32°W, the eastward flow is weaker and reaches its maxima in May and September-October (less than 0.1 m/s). Since this eastward flow is less mentioned and discussed in the literature, it will be addressed in section 6.

5. Interannual variability of the upper-layer circulation

Despite the strong seasonal variability of the current branches, they also show year-to-year variabilities (Figure 2 and Figure 3). These year-to-year variabilities are even more

noticeable with the time series of the currents intensity, and the core velocity/ location of the flows with two-core structure (NECC) or in the NBCR regions (Figure 6). This section aims to analyze these variabilities and find the relationships with the tropical Atlantic climate modes.

The intensities of the cSEC on the section 6 and the NBC on the section 1 (NBC on the section 2) vary between 0.05-0.35 m/s and between 0.3-0.6 m/s (0.2-1.2 m/s), respectively, with mean intensities of 0.2 m/s ± 0.06 and 0.4 m/s ± 0.06 (0.7 m/s ± 0.2), respectively (Figure 6a-b). Crossing the section 3, the NBC intensity is weaker and ranges between 0.05-0.43 m/s with a mean intensity of 0.2 m/s ± 0.07. In the equatorial region (±5° of latitude), the nSEC intensity on the section 5 (section 6) varies between 0.05-0.3 m/s (0.1-0.4 m/s) with a mean intensity of 0.15 m/s ± 0.05 (0.2 m/s ± 0.07) (Figure 6b) while the eastward flow X intensity crossing the sections 4, 5 and 6 vary between 0.15-0.3 m/s, 0.05-0.4 m/s and 0-0.15 m/s, respectively, with mean values of 0.12 m/s ± 0.05, 0.2 m/s ± 0.07, and 0.06 m/s ± 0.03, respectively.

As mentioned in section 3, the interannual variability is more important in the eastern basin, and mostly in the NECC region. The two-core structure of the NECC and the NBCR regions show highest variability of their velocity field, characterized here by 2 core velocities and their corresponding location (Figure 6c-e). The NECC/NBCR intensity time series and the NECC/NBCR main flow core velocity time serie (sNECC and nNBCR) were found significantly correlated (>0.98) (Figure not shown). The NECC is much larger and decreases in intensity eastward. At 42°W, the sNECC (nNECC) core value varies between 0.1-1.2 m/s (0.05-0.55 m/s) with a mean value of 0.5 m/s ± 0.25 (0.25 m/s ± 0.1) while it is located between 3.6°-9.9°N (7.6°-10.4°N) with a mean location at 6.1°N ± 1.7° (8.9°N ± 0.8°) (Figure 6d). At 32°W, it varies between 0.05-0.8 m/s (0.05-0.5 m/s) with a mean velocity of 0.3 m/s ± 0.13 (0.2 m/s ± 0.09), and is located between 4.1°-12.4°N (7.4°-11.6°N) with a mean location of 6.6°N ± 1.4° (9.7°N ± 1.1°) (Figure 7e). The sNBCR (nNBCR) maximum velocity crossing the section 4 varies between 0.05-0.3 m/s (0.05-0.6 m/s) with a mean value of ~0.15 m/s ± 0.06 (0.25 m/s ± 0.08) while it is located between 3.9°-6.4°N (5.1°-9.1°N) with a mean location of 4.7°N±0.8° (7.9°N±0.8°). These results show important year-to-year variations in the current core location as well as in the velocity fields northeast of the equator.

For further analysis, the monthly anomalies of the time series of the currents characteristic relative to their monthly climatology have been computed (Figure 7). These monthly anomalies do not show any persistent patterns or obvious relationship between the currents over the period investigated. No evident relationship was also found between the NECC branches intensity/core value and their location, or the NBCR flows maximum velocity and their location. However,

some particular years, both the NECC intensity/core velocity and location show significant anomalies at 32°W. For example, the monthly anomalies of the sNECC6 location were atypically far north (south) in 2009 and 2010 (1996 and 2001) when the monthly anomalies of the sNECC6 intensity/core value were unusually weak (strong) (Figure 7f-g).

To investigate the relationship between the AMM, the AZM, and the current branches' characteristics (intensity and core value/location), we computed the three-month running mean anomalies of their monthly anomalies and of the climate mode indexes to generate time series of anomalies from 1993 to 2017 for each month (so-called 3-month anomalies). Then, the 3-month anomalies have been correlated with each other to find how their maximum interannual variability within each year are related over the 1993-2017 period (Figures not shown). Only the correlations greater than ±0.5 and which have been found significant with 95% of confidence level, performing the Student test are discussed below. They are grouped in Table 2.

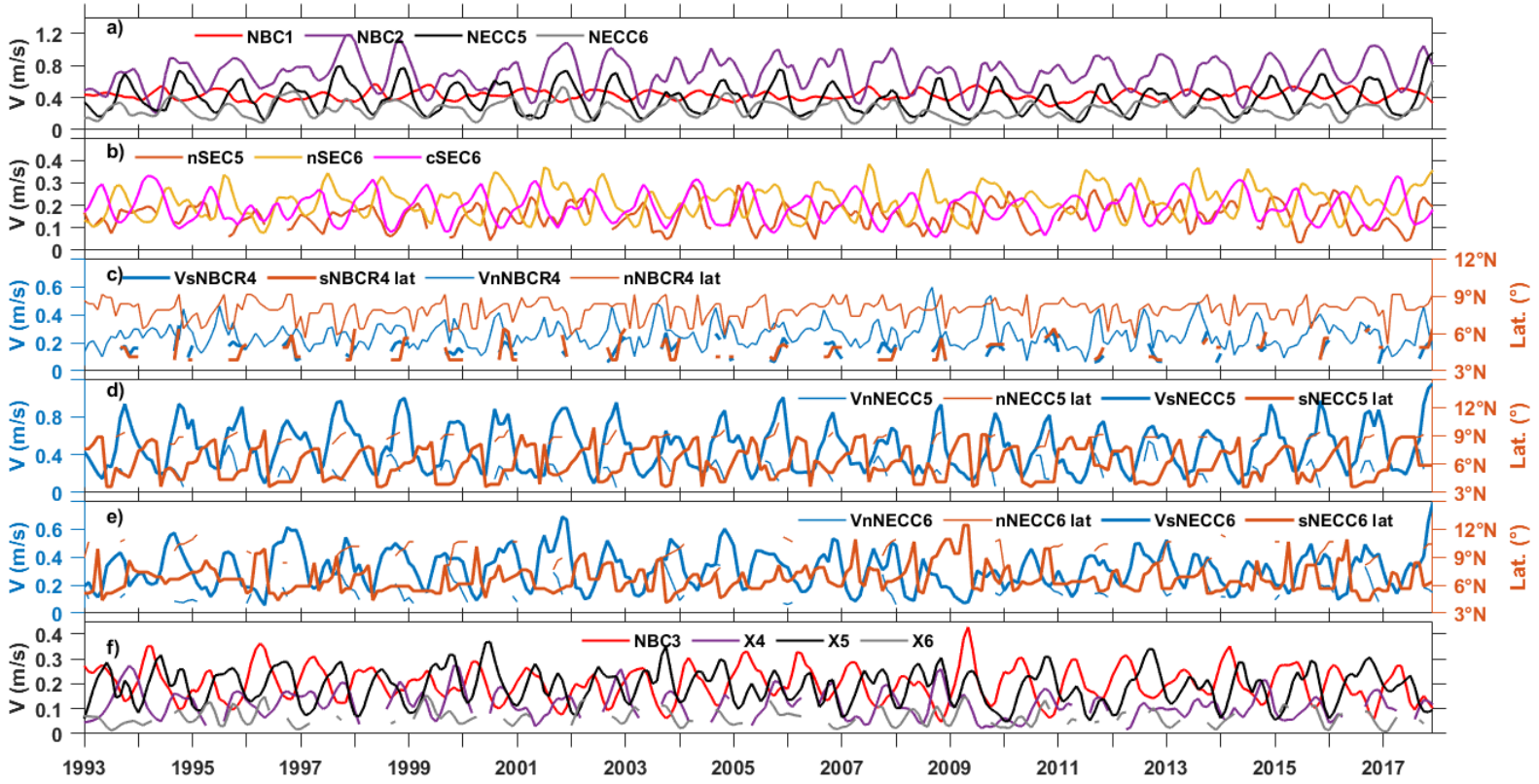

Figure 6. Time series of the 4-month low-pass filtered time series of the different characteristics of the geostrophic currents (a, b, c, d, e and f). a): intensity of NBC crossing the sections 1 (NBC1) and 2 (NBC2), and of the NECC crossing the sections 5 (NECC5) and 6 (NECC6). b): intensity of the cSEC crossing the section 6 (cSEC6) and of the nSEC crossing the sections 5 (nSEC6) and 6 (nSEC6). (c), (d) and (e) core velocities and the locations of the northern and southern cores of respectively the NBCR flows crossing the section 4 (NBCR4), and of the NECC cores on sections 5 (NECC5) and 6 (NECC6). f) NBC crossing the section 3 toward the Guyana coast (NBC3) and the equatorial surface eastward flow crossing the sections 4 (X4), 5 (X5) and 6 (X6). The "V" initials at the beginning, and "lat" at the end of each acronym of the legends of figures c) d) and e) represent the core velocity and location, respectively (blue and orange colors, respectively). The thin (tick) lines represent the northern (southern) branches of these currents/flows.

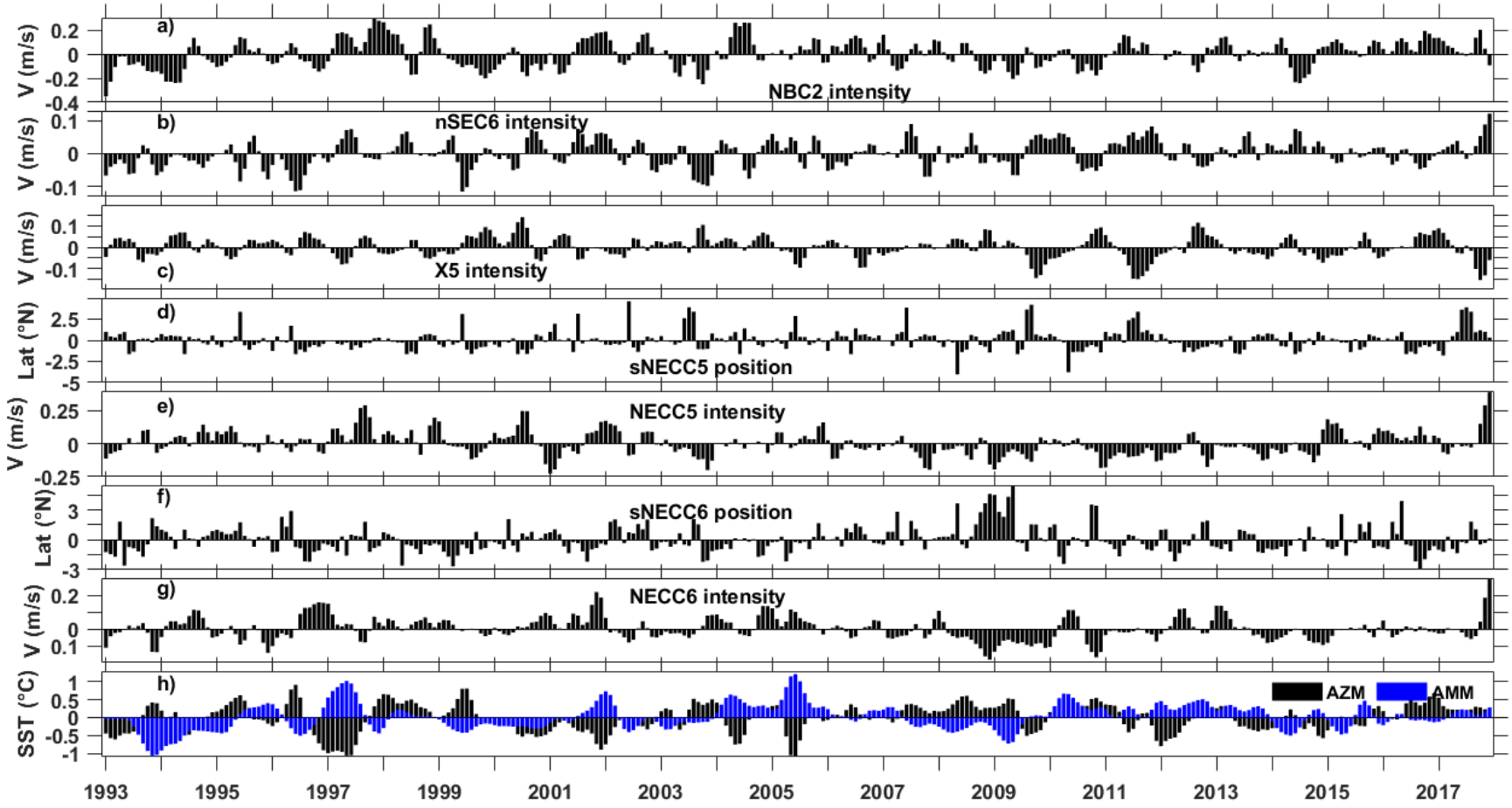

Figure 7. Monthly anomalies of: a), the NBC intensity on the section 2; b), the nSEC intensity on the section 6; c), the equatorial surface eastward flow X intensity on the section 5; d), the sNECC core position on the section 5; e) the NECC intensity on the section 5; f), the sNECC core position on the section 6; and g) the NECC intensity on the section 6; h) Normalized indexes of the tropical Atlantic meridional mode (AMM: blue color) and zonal mode (AZM; black color).

Table 2. Correlations of the current branches' characteristics with the Atlantic meridional and zonal modes (AMM and AZM, respectively). The cells where the correlations are found lower than 0.5 are marked insignificant with no period (none). The current branches are NBC: North Brazil Current, sNECC: southern branch of the NECC, nSEC: the northern branch of the South Equatorial Current, and the equatorial eastward flow X.

Current branches' characteristics		Atlantic meridional mode (AMM) during March-April-May	Atlantic Zonal mode (AZM) during June-July-August
NBC1 intensity (section 1)	Correlation	Higher than -0.51	Insignificant
	Period	June-July	None
NBC2 intensity (section 1)	Correlation	0.58	Insignificant
	Period	March-April-May	None
sNECC5 intensity (section 5)	Correlation	Insignificant	-0.51
	Period	None	September
sNECC6 intensity (section 6)	Correlation	Higher than 0.50	Insignificant
	Period	March-April-May	None
sNECC6 core location (section 6)	Correlation	Higher than 0.51	Insignificant
	Period	March-April-May	None
nNECC6 core location (section 6)	Correlation	-0.62	Insignificant
	Period	March	None
nSEC5 intensity (section 5)	Correlation	Insignificant	-0.52
	Period	None	November
nSEC6 intensity (section 6)	Correlation	Higher than 0.52	Insignificant
	Period	March-April-May	None
Equatorial eastward flow X (Sections 4 and 5)	Correlation	Higher than -0.55	Insignificant
	Period	May-June	None
Equatorial eastward flow X (Section 6)	Correlation	Higher than 0.62	Higher than -0.52
	Period	March-April-May	June-July

The 3-month anomalies of AMM index during March-April-May are found anticorrelated with the NBC intensity on the section 1, the nNECC core location on the section 6 and the equatorial eastward flow (X) intensity west of 42°W with respective coefficient of correlation (cc) higher than -0.51 during June-July, about -0.62 in March, and higher than -0.55 in May-June. These anti-correlations show the probability of the positive (negative) AMM phases to lead the negative (positive) anomalies of the nNECC core location at 32° W with 0-month delay, and the negative (positive) NBC intensity between 3°-5°S and the X flow intensity anomalies (west of 42°W) with 1- to 2-month and 0- to 1-month delay, respectively. However, the 3-month anomalies of AMM index during March-April-May are found correlated with the NBC intensity north of the equator before the retroflection (cc~0.58) and, the sNECC intensity/core

location and the nSEC intensity at 32°W (cc higer than 0.50/0.51 and cc higher than 0.52, respectively) during the same period of time. This suggests that the positive (negative) AMM phases probably lead the positive (negative) anomalies of the characteristics of the latter currents with no time lag.

The 3-month anomalies of AZM index during June-July-August are found anticorrelated with the sNECC/nSEC intensity at 42°W (cc=-0.51/-0.52) only in September/November. It suggests that the positive (negative) AZM phases probably lead the negative (positive) anomalies of the sNECC/nSEC intensity with 1- and 3-month delay, respectively.

The eastward flow X intensity at 32°W is found simultaneously correlated with AZM and AMM in June-July and March-April-May with cc higher than 0.62 and -0.52, respectively. This suggests that the positive (negative) anomalies of X at 32°W might be probably associated with both positive (negative) AZM and negative (positive) AMM phases with no delay.

Referring to Cabos et al. (2019), the relationships found between the currents and the AMM shows the influence of the strengthening (weakening) of the southeast trade winds in the southern hemisphere on the southward (northward) migration of the nNECC core at 32°W whereas the NBC intensity between 3°-5°S and the equatorial eastward flow X intensity west of 42°W decrease (increase). Conversely, the strengthening (weakening) of the southeast trade winds in the southern hemisphere should influence the northward (southward) migration of the sNECC core at 32°W whereas the NBC2, sNECC6 and nSEC6 intensities increase (decrease). Referring to the same authors, the relationship with the AZM should indicate the probable influence of the positive (negative) westerlies anomalies in the western part of the basin on the negative (positive) anomalies of the sNECC and nSEC intensities at 42°W. Concerning the eastward flow at 32°W the relationship with both the AZM and the AMM should indicate the strengthening (weakening) of X during the simultaneous events of positive (negative) westerlies anomalies in the western part of the basin and the negative (positive) southerlies winds anomalies in the southern hemisphere.

6. Discussion

The analysis of the seasonal map of the geostrophic currents in the whole WTA (Figure 8) allows to have a global view of the circulation. It confirms the analysis made on the basis of the the cross-currents sections in section 4 (seasonal and spatial variability) and highlights an interesting large cyclonic circulation which takes place between 35°-45°W and 0°-5°N during boreal spring (surrounded by blue ellipse). This large cyclonic circulation is formed by the nSEC coming from east and which is suddenly constrained to the northeast by an eastward flow

west of 32°W. Near to 44°W, around 5°N, the nSEC meets the rNBC which reaches it southernmost position during this season, and is constrained this time to the southeast. Reaching the equatorial region between 0°-2°N, where the equatorial eastward flow X is found (Figure 4), the resulting flow from the rNBC and the nSEC becomes stronger, and is deviated to the east to meet the nSEC at approximately 35°W and to close the circulation. This cyclonic circulation might answer the question of Schot et al. (1998) about the destination of the rNBC during the spring when the rNBC does not feed the NECC anymore. Before, during boreal winter, part NECC recirculates north-westward to encounter the rNBC and forms another cyclonic circulation is shown during the boreal winter between 44°-50°W and 5°-10°N (surrounder by blue ellipse in Figure 8). During both boreal winter and spring, a south-westward recirculation of the NECC appear to strengthen the nSEC located west of the 32°W. It is consistent the increase of the nSEC intensity on the section 4 compared to the nSEC intensity on the section 6 between February and May (Figure 5b).

During the second half of the year, Figure 8 shows a wider NECC which is extended north of 10°N. The NECC eastward flow is formed by a nNECC branch separated from the initial sNECC branch during the boreal fall between 38°-48°W whereas east of 38°W, both branches are apparently non-separated. This is consistent with Figure 4S5-S6. During the boreal summer, the connection of the nNECC branch at its western side with the northern part of the NBC retroflection suggests that the nNECC should be supplied by the NBC. This connection seems to fade during boreal fall.

In the equatorial region (2°S-2°N), Figure 8 also shows an eastward flow with lower amplitude which appears to be extended east of 32°W and stronger during boreal spring and fall. This equatorial eastward flow can be identified to the near-surface eastward flow mentioned by Hisard and Hénin (1987) and Bourlès et al. (1999b) on top of the EUC in the WTA. Hisard and Hénin (1987) explained the reason why it is less discussed in the literature by the difficulty of the measurement instruments like ADCPs to fully capture this flow in the upper layer and the difficulty to separate it from the EUC. They show that this near-surface current can reach amplitudes larger than 0.5 m/s between 23°W and 28°W. The seasonal map of the near-surface Ekman currents (Figure 9) shows westward current with larger amplitudes in this equatorial band (larger than 0.2 m/s). These westward currents can justify the lower amplitude of the near-surface found in this study (~0.1 m/s) particularly in the eastern basin (Figure 5b), which can be due to the divergence effect of the near-surface Ekman currents.

For the first time, the seasonal cycle of this equatorial eastward flow has been analyzed in the section 4.4 of this study (Figure 4S4-S5-S6 and Figure 5b). Its similar seasonal cycle with the EUC (semi-annual cycle with two maximum) might be due to the fact the most part of the flow come from the rNBC.

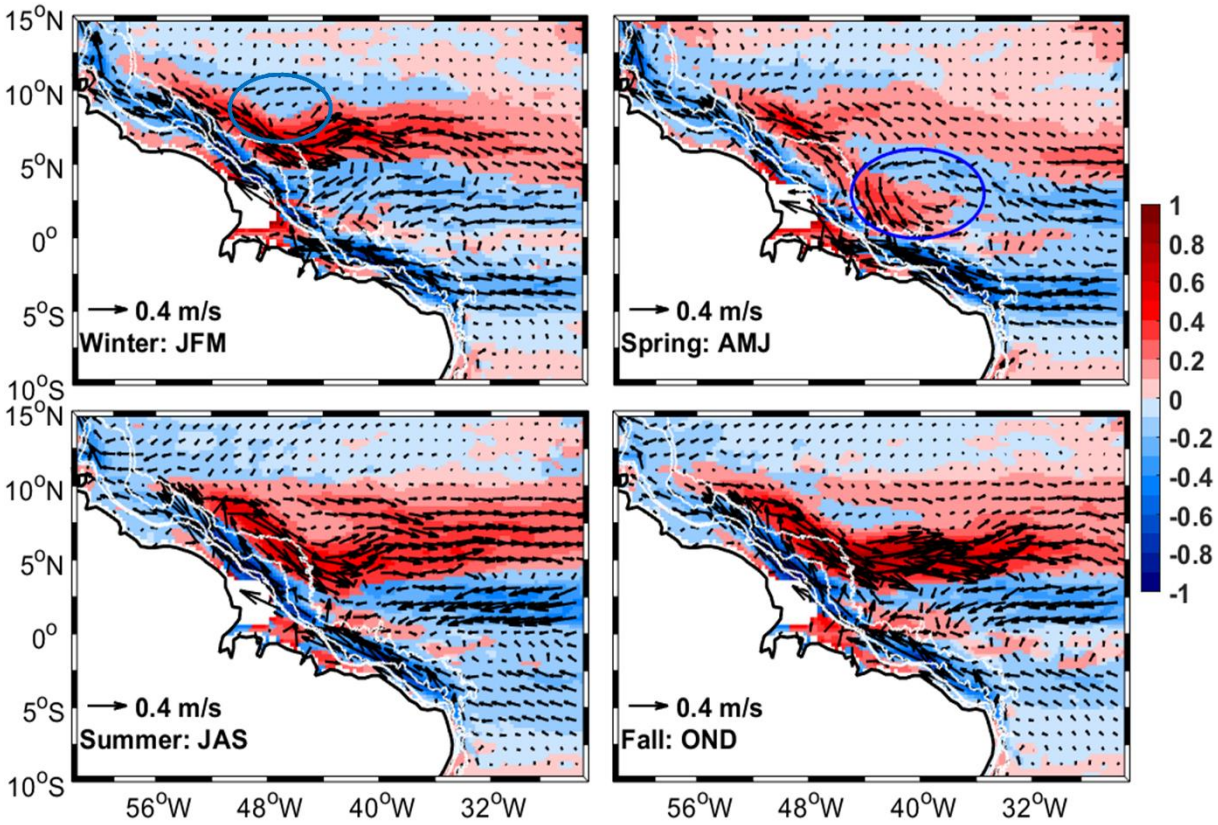

Figure 8. Seasonal map of the geostrophic currents in the western tropical Atlantic from 1993 to 2017. a), boreal winter (January-February-March); b), boreal spring (April-May-June); c), boreal summer (July-August-September); and d), boreal fall (October-November-December). The velocity arrows are superimposed on their speed. The cyclonic circulations during boreal winter and summer are surrounded by the blue ellipse on the spring map. The white lines near to the continent are from west to east, the 300 m, 1000 m, 3000 m and 4000 m isobaths.

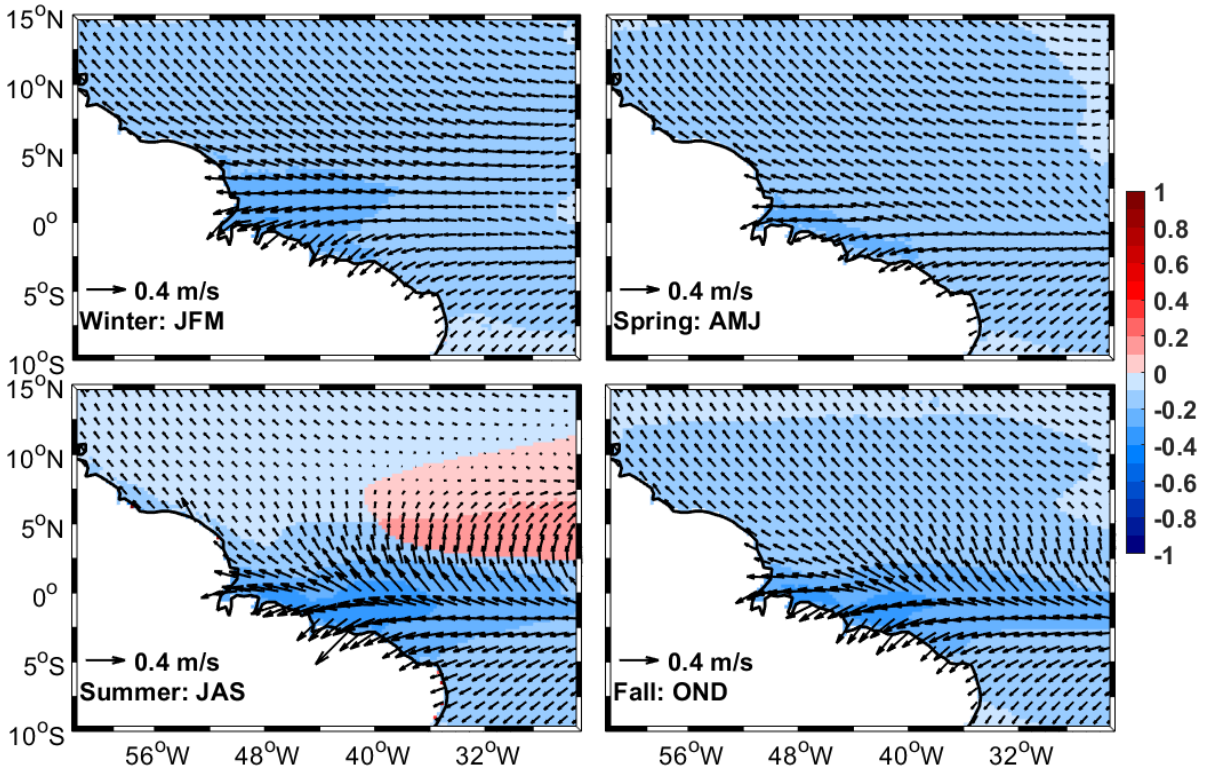

Figure 9. Seasonal map of the Ekman currents in the western tropical Atlantic from 1993 to 2017. a), boreal winter (January-February-March); b), boreal spring (April-May-June); c), the boreal summer (July-August-September); and d), the boreal fall (October-November-December). The velocity arrows are superimposed on their speed (m/s).

On the basis of the current branches' analysis made in section 4 and the analysis above, we have constructed a new schematic representation of the seasonal maps of the four seasons of the western boundary tropical Atlantic (Figure 10). The new current branches found in this study are in green color and the currents from north/south are in blue/yellow colors. The width of the current arrows is proportional to their amplitude and the dotted arrows represent the currents with the minimum amplitude. C1 and C2 are for respectively, the cyclonic circulations between 44°-50°W and 35°-45°W.

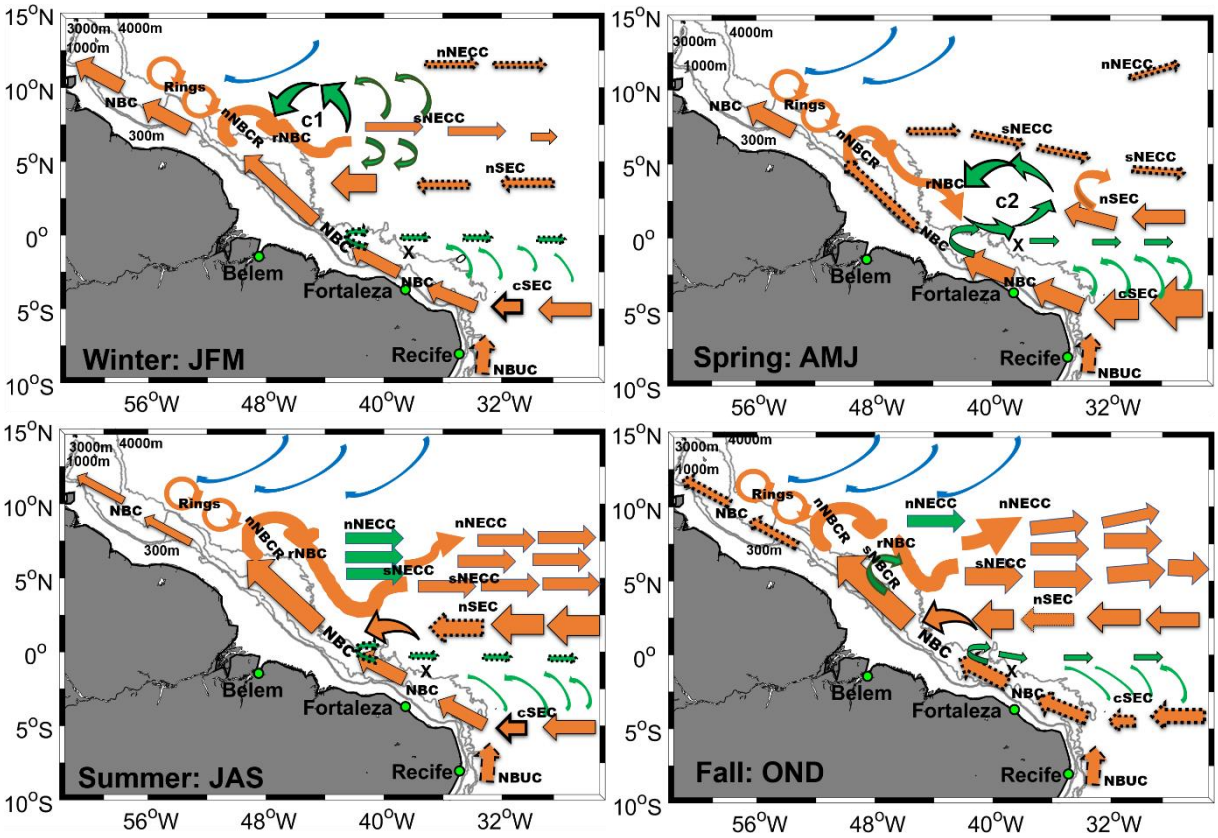

Figure 10. Schematic view of the seasonal maps of the tropical western boundary circulation. The closed circulations c1 and c2 represent the cyclonic circulations noticed in this study. The wider (dotted thin) arrows show current branches with maximum (minimum) intensity. The subsurface NBUC is represented by dashed arrows. The known (new) branches are in yellow/blue (green) color. The green arrows characterize the new branches observed by the altimetry-derived geostrophic currents. NBC is the North Brazil Current; nNBCR and sNBCR are the northern and the southern flows of the North Brazil Current retroflection, respectively; rNBC is the retroflected branch of North Brazil current; nNECC and sNECC are the northern and the southern branches of the North Equatorial Countercurrent (NECC), respectively; cSEC and nSEC are the central and the northern branches of the South Equatorial Current (SEC), respectively.

Concerning the interannual variability of the currents in the tropical Atlantic, Hormann et al. (2012) found by applying the complex empirical orthogonal function analyses on 17 year of altimetry and drifters' data, interesting scenarios about the NECC spatial and temporal variability. However, they couldn't clearly separate the sNECC from the nNECC. In their study, the authors have associated the strengthening of NECC in the whole basin to the AZM negative phase, and its northward shift to the positive AMM phase. Our results show different behaviors of the NECC system according to its branches and their cores location, and should be a precursor to future studies to be considered for investigations. We showed possible relationships between the southern NECC branch intensity and core location with the AMM phases at 42°W, and conversely possible relationships between the southern NECC branch intensity and core location with the AZM phases at 32°W.

7. Summary and perspectives

Twenty-five years of altimetry data provided by CMEMS over the 1993-2017 period were used in this study to improve the description of seasonal western boundary circulation of the tropical Atlantic by using six cross-currents sections along the main currents' veins of the upper layer, and investigate their year-to-year variabilities. C3S ERA5 wind estimates and the NOAA OI SST v2 product were also used over the same period to investigate the relationship between the large-scale remote wind variabilities and the tropical Atlantic climate modes on the seasonal and interannual variability of the currents, respectively.

The analysis of the 25 years gridded altimetry-derived currents highlights a complex western boundary circulation with significant seasonal and year-to-year variations of the currents' intensity and cores location. South of the equator, our results shows stronger/weaker central branch of the South Equatorial Atlantic (cSEC) and the North Brazil Current (NBC) during boreal spring/fall. North of the equator, the NBC continuity toward the Guyana coast also shows a similar annual cycle. However, the NBC before the retroflection is strongly strengthened by the northern branch of the South Equatorial Current (nSEC) which is stronger during boreal summer-fall. It shows a reverse cycle with larger amplitudes during boreal fall, 3-4 months after the peak of the remote wind stress curl (WSC) strength in August, and is weaker during boreal spring. The North Equatorial Countercurrent (NECC) is connected with the retroflected branch of the NBC, and both show similar annual cycle to the NBC. A secondary North Brazil Current Retroflection (NBCR) region was found for the first this in this study and is located between 4°-6°N during boreal fall. The two-core/branch structure of the NECC during the second half of the year was also confirmed and studied separately. From 32°W to 42°W, it has been found some changes in its intensity annual cycle. Between 0°-5°N and 35°-45°W, a surface cyclonic circulation develops during boreal spring and is found to initiate the growth of the NECC at 42°W in June. However, at 32°W, the NECC doesn't show any connection with the cyclonic circulation, but starts its cycle earlier in April with the ITCZ northward migration and the increase of the remote WSC strength. In the equatorial region between 2°S-2°N, the geostrophic currents show the presence of an equatorial surface eastward flow which shows similar seasonal variability with the Equatorial Undercurrent (EUC), and is influenced by the near-surface Ekman currents.

The analysis of the current branches' anomalies (intensity and core velocity/location) in relation to the tropical Atlantic climate modes shows different possible scenarios associated with one or both modes, and depends on the location of the currents.

This work shows the ability of the altimetry to characterize the seasonal variability of the western boundary surface circulation and complements the previous knowledge on the seasonal variability of the study area. It also confirms the two-core/branch structure of the NECC and shows the necessity to consider both cores for the study of its temporal variabilities, particularly at the interannual timescale. This opens the door to further investigations about the possible relationships of the Atlantic climate modes (ACM) on the current transports which is not possible with the altimetry. Combined use of regional modelling, altimetry complemented with observational data (in-situ, drifter, higher frequency radars) will allow to deepen the spatial and temporal variability. The oceanographic program cruises in the area of study will be also useful to better understand the dynamics of the regions, mostly in the equatorial region. The intraseasonal signals, particularly larger in the near-shore area (Figure 2d) are not studied here. It will be subject of a future study, based on a coastal altimetry product that will allow a significantly better spatial resolution and accuracy near the coast, compared to a gridded product.

Authors contribution

Djoirka M. Dimoune performed the data analyses as part of his PhD thesis. Florence Birol, Fabrice Hernandez, Fabien Leger and Moacyr Araujo supervised this research.

Acknowledgements

This work has been supported by: CAPES Foundation who funds the thesis of the first author, CAPES-Print (grants 88887.467360/2019-00) who funds his visit to LEGOS during the first six months spent in the laboratory, and LEGOS and CNES who fund the three last months of extension in the laboratory. The authors thank CMEMS, who processed the geostrophic currents data and made them available. They also thank ECMWF and NOAA respectively who made available the mean wind fields data and SST for the work. Thanks also to Joel Sudre from LEGOS who made wind-driven currents for this study. Special thanks also to Dr. Florence Birol and the CTOH team who made available all the operational resources to the success of this work. This work represents collaboration by the INCT AmbTropic, the Brazilian National Institute of Science and Technology for Tropical Marine Environments, CNPq/FAPESB (grants

565054/2010-4 and 8936/2011 and 465634/2014-1) and the Brazilian Research Network on Global Climate Change FINEP/Rede CLIMA (grants 01.13.0353-00). This is also a contribution to the LMI-TAPIOCA and to the TRIATLAS project, which has received funding from the European Union's Horizon 2020 research and innovation program under grant agreement No 817578

References

Aguedjou, H. M. A., Dadou, I., Chaigneau, A., Morel, Y., & Alory, G. (2019). Eddies in the Tropical Atlantic Ocean and their seasonal variability. *Geophysical Research Letters*, *46*(21), 12156-12164. https://doi.org/10.1029/2019gl083925.

Araujo, M., Noriega, C., Hounsou-Gbo, G. A., Veleda, D., Araujo, J., Bruto, L., ... & Neumann-Leitão, S. (2017). A synoptic assessment of the amazon river-ocean continuum during boreal autumn: From physics to plankton communities and carbon flux. *Frontiers in microbiology*, *8*, 1358. https://doi.org/10.3389/fmicb.2017.01358.

Arbic, B. K., Scott, R. B., Chelton, D. B., Richman, J. G., & Shriver, J. F. (2012). Effects of stencil width on surface ocean geostrophic velocity and vorticity estimation from gridded satellite altimeter data. *Journal of Geophysical Research: Oceans*, *117*(C3). https://doi.org/10.1029/2011jc007367.

Aroucha, L. C., Veleda, D., Lopes, F. S., Tyaquiçã, P., Lefèvre, N., & Araujo, M. (2020). Intra- and Inter-Annual Variability of North Brazil Current Rings Using Angular Momentum Eddy Detection and Tracking Algorithm: Observations From 1993 to 2016. *Journal of Geophysical Research: Oceans*, *125*(12), e2019JC015921. https://doi.org/10.1029/2019jc015921.

Burmeister K., Lübbecke, J. F.,Brandt, P., & Duteil, O. (2019). Interannual variability of the Atlantic North Equatorial Undercurrent and its impact on oxygen. *Journal of Geophysical Research: Oceans*, 124, 2348–2373. https://doi.org/10.1029/2018JC014760.

Bourles, B., Molinari, R. L., Johns, E., Wilson, W. D., & Leaman, K. D. (1999). Upper layer currents in the western tropical North Atlantic (1989–1991). *Journal of Geophysical Research: Oceans*, *104*(C1), 1361-1375. https://doi.org/10.1029/1998jc9000250.

Bourlès, B., Gouriou, Y., & Chuchla, R. (1999). On the circulation in the upper layer of the western equatorial Atlantic. *Journal of Geophysical Research: Oceans*, *104*(C9), 21151-21170. https://doi.org/10.1029/1999jc900058.

Brandt, P., Schott, F. A., Provost, C., Kartavtseff, A., Hormann, V., Bourlès, B., & Fischer, J. (2006). Circulation in the central equatorial Atlantic: Mean and intraseasonal to seasonal variability. *Geophysical Research Letters*, *33*(7). https://doi.org/10.1029/2005gl025498.

Brandt, P., Claus, M., Greatbatch, R. J., Kopte, R., Toole, J. M., Johns, W. E., & Böning, C. W. (2016). Annual and semiannual cycle of equatorial Atlantic circulation associated with basin-mode resonance. *Journal of Physical Oceanography*, *46*(10), 3011-3029. https://doi.org/10.1175/jpo-d-15-0248.1.

Cabos, W., de la Vara, A., & Koseki, S. (2019). Tropical Atlantic variability: observations and modeling. *Atmosphere*, *10*(9), 502. https://doi.org/10.3390/atmos10090502.

Cochrane, J. D., Kelly Jr, F. J., & Olling, C. R. (1979). Subthermocline countercurrents in the western equatorial Atlantic Ocean. *Journal of Physical Oceanography*, *9*(4), 724-738. https://doi.org/10.1175/1520-0485(1979)009<0724:scitwe>2.0.co;2.

Didden, N., & Schott, F. (1992). Seasonal variations in the western tropical Atlantic: Surface circulation from Geosat altimetry and WOCE model results. *Journal of Geophysical Research: Oceans*, *97*(C3), 3529-3541. https://doi.org/10.1029/91jc02860.

Dossa, A. N., Silva, A. C., Chaigneau, A., Eldin, G., Araujo, M., & Bertrand, A. (2021). Near-surface western boundary circulation off Northeast Brazil. *Progress in Oceanography*, *190*, 102475. https://doi.org/10.1016/j.pocean.2020.102475.

Ffield, A. (2005). North Brazil current rings viewed by TRMM Microwave Imager SST and the influence of the Amazon Plume. *Deep Sea Research Part I: Oceanographic Research Papers*, *52*(1), 137-160. https://doi.org/10.1016/j.dsr.2004.05.013.

Fonseca, C. A., Goni, G. J., Johns, W. E., & Campos, E. J. (2004). Investigation of the north Brazil current retroflection and north equatorial countercurrent variability. *Geophysical Research Letters*, *31*(21). https://doi.org/10.1029/2004gl020054.

Fratantoni, D. M., Johns, W. E., Townsend, T. L., & Hurlburt, H. E. (2000). Low-latitude circulation and mass transport pathways in a model of the tropical Atlantic Ocean. *Journal of Physical Oceanography*, *30*(8), 1944-1966. https://doi.org/10.1175/15200485(2000)030<1944:LLCAMT>2.0.CO;2.

Garzoli, S. L., & Katz, E. J. (1983). The forced annual reversal of the Atlantic North Equatorial Countercurrent. *Journal of Physical Oceanography*, *13*(11), 2082-2090. https://doi.org/10.1175/1520-0485(1983)013<2082:tfarot>2.0.co;2.

Garzoli, S. L. (1992). The Atlantic North Equatorial Countercurrent: Models and observations. *Journal of Geophysical Research: Oceans*, 97 (C11), 17931-17946. https://doi.org/10.1029/92jc01363.

Garzoli, S. L., Ffield, A., & Yao, Q. (2003). North Brazil Current rings and the variability in the latitude of retroflection. In *Elsevier Oceanography Series* (Vol. 68, pp. 357-373). Elsevier. https://doi.org/10.1016/s0422-9894(03)80154-x.

Garzoli, S. L., Ffield, A., Johns, W. E., & Yao, Q. (2004). North Brazil Current retroflection and transports. *Journal of Geophysical Research: Oceans*, *109*(C1). https://doi.org/10.1029/2003jc001775.

Garzoli, S. L., & Matano, R. (2011). The South Atlantic and the Atlantic meridional overturning circulation. *Deep Sea Research Part II: Topical Studies in Oceanography*, *58*(17-18), 1837-1847. https://doi.org/10.1016/j.dsr2.2010.10.063.

Gill, A. E., & Adrian, E. (1982). *Atmosphere-ocean dynamics* (Vol. 30). Academic press. https://doi.org/10.1016/s0074-6142(08)60025-x.

Góes, M., & Wainer, I. (2003). Equatorial currents transport changes for extreme warm and cold events in the Atlantic Ocean. *Geophysical Research Letters*, *30*(5). https://doi.org/10.1029/2002gl015707.

Goes, M., Molinari, R., da Silveira, I., & Wainer, I. (2005). Retroflections of the north brazil current during february 2002. *Deep Sea Research Part I: Oceanographic Research Papers*, *52*(4), 647-667. https://doi.org/10.1016/j.dsr.2004.10.010.

Goni, G. J., & Johns, W. E. (2003). Synoptic study of warm rings in the North Brazil Current retroflection region using satellite altimetry. In *Elsevier Oceanography Series* (Vol. 68, pp. 335-356). Elsevier. https://doi.org/10.1016/s0422-9894(03)80153-8.

Hazeleger, W., & De Vries, P. (2003). Fate of the Equatorial Undercurrent in the Atlantic. In *Elsevier oceanography series* (Vol. 68, pp. 175-191). Elsevier. https://doi.org/10.1016/s0422-9894(03)80146-0.

Hazeleger, W., de Vries, P., & Friocourt, Y. (2003). Sources of the Equatorial Undercurrent in the Atlantic in a high-resolution ocean model. *Journal of Physical Oceanography*, *33*(4), 677-693. https://doi.org/10.1175/1520-0485(2003)33<677:soteui>2.0.co;2.

Hisard, P., & Hénin, C. (1987). Response of the equatorial Atlantic Ocean to the 1983–1984 wind from the Programme Français Océan et Climat dans l'Atlantique Equatorial cruise data set. *Journal of Geophysical Research: Oceans*, *92*(C4), 3759-3768. https://doi.org/10.1029/jc092ic04p03759.

Hormann, V., & Brandt, P. (2007). Atlantic Equatorial Undercurrent and associated cold tongue variability. *Journal of Geophysical Research: Oceans*, *112*(C6). https://doi.org/10.1029/2006jc003931.

Hormann, V., Lumpkin, R., & Foltz, G. R. (2012). Interannual North Equatorial Countercurrent variability and its relation to tropical Atlantic climate modes. *Journal of Geophysical Research: Oceans*, *117*(C4). https://doi.org/10.1029/2011jc007697.

Jochum, M., & Malanotte-Rizzoli, P. (2003). On the generation of North Brazil Current rings. *Journal of Marine research*, *61*(2), 147-173. https://doi.org/10.1357/002224003322005050.

Johns, W. E., Lee, T. N., Schott, F. A., Zantopp, R. J., & Evans, R. H. (1990). The North Brazil Current retroflection: Seasonal structure and eddy variability. *Journal of Geophysical Research: Oceans*, *95*(C12), 22103-22120. https://doi.org/10.1029/jc095ic12p22103.

Johns, W. E., Lee, T. N., Beardsley, R. C., Candela, J., Limeburner, R., & Castro, B. (1998). Annual cycle and variability of the North Brazil Current. *Journal of Physical Oceanography*, *28*(1), 103-128. https://doi.org/10.1175/1520-0485(1998)028<0103:acavot>2.0.co;2.

Lagerloef, G. S., Mitchum, G. T., Lukas, R. B., & Niiler, P. P. (1999). Tropical Pacific near-surface currents estimated from altimeter, wind, and drifter data. *Journal of Geophysical Research: Oceans*, *104*(C10), 23313-23326. https://doi.org/10.1029/1999jc900197.

Large, W. G., & Pond, S. (1981). Open ocean momentum flux measurements in moderate to strong winds. *Journal of physical oceanography*, *11*(3), 324-336. https://doi.org/10.1175/1520-0485(1981)011<0324:oomfmi>2.0.co;2.

NRSC (2013). "OSCAT Wind stress and Wind stress curl products", Ocean Sciences Group, Earth and Climate Science Area, Hyderabad, India.

Peterson, R. G., & Stramma, L. (1991). Upper-level circulation in the South Atlantic Ocean. *Progress in oceanography*, *26*(1), 1-73. https://doi.org/10.1016/0079-6611(91)90006-8.

Provost, C., Arnault, S., Chouaib, N., Kartavtseff, A., Bunge, L., & Sultan, E. (2004). TOPEX/Poseidon and Jason equatorial sea surface slope anomaly in the Atlantic in 2002:

Comparison with wind and current measurements at 23W. *Marine Geodesy*, *27*(1-2), 31-45. https://doi.org/10.1080/01490410490465274.

Pujol, M. I., Faugère, Y., Taburet, G., Dupuy, S., Pelloquin, C., Ablain, M., & Picot, N. (2016). DUACS DT2014: the new multi-mission altimeter data set reprocessed over 20 years. *Ocean Science*, *12*(5), 1067-1090. https://doi.org/10.5194/os-2015-110.

Richardson, P. L., & Walsh, D. (1986). Mapping climatological seasonal variations of surface currents in the tropical Atlantic using ship drifts. *Journal of Geophysical Research: Oceans*, *91*(C9), 10537-10550. https://doi.org/10.1029/jc091ic09p10537.

Rodrigues, R. R., Rothstein, L. M., & Wimbush, M. (2007). Seasonal variability of the South Equatorial Current bifurcation in the Atlantic Ocean: A numerical study. *Journal of Physical Oceanography*, *37*(1), 16-30. https://doi.org/10.1175/jpo2983.1.

Schmitz Jr, W. J., & McCartney, M. S. (1993). On the north Atlantic circulation. *Reviews of Geophysics*, *31*(1), 29-49. https://doi.org/10.1029/92RG02583.

Schott, F. A., Stramma, L., & Fischer, J. (1995). The warm water inflow into the western tropical Atlantic boundary regime, spring 1994. *Journal of Geophysical Research: Oceans*, *100*(C12), 24745-24760. https://doi.org/10.1029/95jc02803.

Schott, F. A., Fischer, J., & Stramma, L. (1998). Transports and pathways of the upper-layer circulation in the western tropical Atlantic. *Journal of Physical Oceanography*, *28*(10), 1904-1928. https://doi.org/10.1175/1520-0485(1998)028<1904:tapotu>2.0.co;2.

Schott, F. A., McCreary Jr, J. P., & Johnson, G. C. (2004). Shallow overturning circulations of the tropical-subtropical oceans. *Washington DC American Geophysical Union Geophysical Monograph Series*, *147*, 261-304. https://doi.org/10.1029/147gm15.

Servain, J. (1991). Simple climatic indices for the tropical Atlantic Ocean and some applications. *Journal of Geophysical Research: Oceans*, 96 (C8), 15137-15146. https://doi.org/10.1029/91jc01046.

Silva, M., Araujo, M., Servain, J., Penven, P., & Lentini, C. A. (2009). High-resolution regional ocean dynamics simulation in the southwestern tropical Atlantic. *Ocean Modelling*, *30*(4), 256-269. https://doi.org/10.1016/j.ocemod.2009.07.002.

Stramma, L., & Schott, F. (1999). The mean flow field of the tropical Atlantic Ocean. *Deep Sea Research Part II: Topical Studies in Oceanography*, *46*(1-2), 279-303. https://doi.org/10.1016/s0967-0645(98)00109-x.

Stramma, L., & England, M. (1999). On the water masses and mean circulation of the South Atlantic Ocean. *Journal of Geophysical Research: Oceans*, *104*(C9), 20863-20883. https://doi.org/10.1029/1999jc900139.

Sudre, J., Maes, C., & Garçon, V. (2013). On the global estimates of geostrophic and Ekman surface currents. *Limnology and Oceanography: Fluids and Environments*, *3*(1), 1-20. https://doi.org/10.1215/21573689-2071927.

Trenberth, K. E., Large, W. G., & Olson, J. G. (1990). The mean annual cycle in global ocean wind stress. *Journal of Physical Oceanography*, *20*(11), 1742-1760. doi: 10.1175/1520-0485(1990)0202.0.CO;2.

Urbano, D. F., Jochum, M., & Da Silveira, I. C. A. (2006). Rediscovering the second core of the Atlantic NECC. *Ocean modelling*, *12*(1-2), 1-15. https://doi.org/10.1016/j.ocemod.2005.04.003.

Urbano, D. F., De Almeida, R. A. F., & Nobre, P. (2008). Equatorial Undercurrent and North Equatorial Countercurrent at 38 W: A new perspective from direct velocity data. *Journal of Geophysical Research: Oceans*, *113*(C4). https://doi.org/10.1029/2007jc004215.

Verdy, A., & Jochum, M. (2005). A note on the validity of the Sverdrup balance in the Atlantic North Equatorial Countercurrent. *Deep Sea Research Part I: Oceanographic Research Papers*, *52*(1), 179-188. https://doi.org/10.1016/j.dsr.2004.05.014.

Zebiak, S. E. (1993). Air–Sea Interaction in the Equatorial Atlantic Region. *Journal of Climate*, 6 (8), 1567-1586. doi: 10.1175/1520-0442(1993)006<1567:Aiitea>2.0.Co;2.

Zheng, Y., & Giese, B. S. (2009). Ocean heat transport in simple ocean data assimilation: Structure and mechanisms. *Journal of Geophysical Research: Oceans*, *114*(C11). https://doi.org/10.1029/2008jc005190.

6 VARIABILTY OF THE CURRENT BRANCHES BY USING GLORYS12V1 REANALYSIS

The chapter 5 has been dedicated to the main upper layer currents captured by satellite altimetry data in our study area. These currents are: the NBC, the rNBC, the NECC, the cSEC, the nSEC, and the eastward flow X. The EUC, the NEUC and the SEUC could not be clearly identified. In order to also investgate these latter, the G12V1 vertical profiles of the nine cross-sections described in Section 3.1 have been extracted to anlyze the current branches in the upper and the thermocline layers (0-100 m and 100-350 m depth, respectively), and follow the changes in their transport in order to provide a better view of the WBC. Before the investigations, the annual cycle of the NBC-NBUC system volume transport within the 0-70 m-depth and 70-350 m-depth have been estimated (see Table 4) and compared with previous studies (see Table 5; e.g., Schott et al., 1995; 2002; 2005; Bourlès et al., 1999b, Goes et al., 2005, Dossa et al., 2020) in order to assess the G12V1 realism. The transports estimated were found consistent with the results of the previous studies showing an increase (decrease) of the NBC-NBUC transport within 0-70 m depth (70-350 m depth) from south to north. On average, the annual mean of the transport estimated here are close to the values of the previous studies. These comparisons give credit to G12V1 to be used for the understanding of the evolution of the NBC-NBUC system, which was not yet clearly investigated in the literature. In this chapter, the analysis of the vertical structure of the NBC-NBUC system (from south to north) and the other currents mentioned above will be done. Then, the connection between all the currents in the upper and thermocline layers will be investigated separately by investigating the spatial variability of their volume transport. And finally, seasonal maps of the volume transport spatial variability will be proposed to further understand the evolution of the currents. In order to reduce the mesoscale activities due to eddies, the currents have been 4-month low-pass filtered before the investigations. We also chose to use the absolute value of the volume transports in order to facilitate the comparison, but keeping in mind that the northward (southward) and eastward (westward) transports are considered positives (negatives).

Table 4. Volume transport of the NBC-NBUC current calculated in the previous studies using ADCP data from 1993 to 2017. Note that in Stramma et al. (1995), the transport estimated is the geostrophic transport from CTD data.

Currents	Limits (of the sections)	Transports	0-70 m (Upper layer)	70-350 m (Lower layer)
NBC-NBUC system	3°-5°S, 35.5°37.5°W (NBC-NBUC1)	Mean	6.4 Sv	23 Sv
		Min/ boreal season (month)	4.4 Sv / Fall (November)	21.3 Sv/ Fall (October)
		Max/ boreal season (month)	9.1 Sv / Spring (May)	24.1 Sv/ Spring (May)
	0°-2°S, 42°-44°W (NBC-NBUCeq1)	Mean	8.6 Sv	18.3 Sv
		Min/ boreal season (month)	6.6 Sv/Fall (October)	17.2 Sv/ Fall (October)
		Max/ boreal season (month)	11.5 Sv/ Spring-Summer (June)	19.5 Sv/ Spring-Summer (June)
NBC	0°-2.2°N, 45.3°-47.5°W (NBCeq2)	Mean	10.2 Sv	17.5 Sv
		Min/ boreal season (month)	7.3 Sv/ Spring (April)	15 Sv/ Winter (February)
		Max/ Season (month)	10.2 Sv/ Summer (August)	20.4 Sv/ Summer (July)
	3°-5.5°N, 48°-50.5°W (NBC2)	Mean	11.6 Sv	16.5
		Min/ boreal season (month)	8.9 Sv/ Spring (May)	13.1 Sv/ Spring (May)
		Max/ boreal season (month)	13.5 Sv/ Fall (November)	20.9 Sv/ Summer (August)
	9°-10.5°, 58.5°-60°W (NBC3)	Mean	3.9 Sv	5.2 Sv
		Min/ boreal season (month)	1.7 Sv/ Fall (October)	3.1 Sv/ Fall (November)
		Max/ boreal season (month)	6 Sv/ Winter-Spring (March)	7.5 Sv/ Winter-Spring (March)

Source: The Author (2022).

.

Table 5. Volume transport of the NBC-NBUC current calculated in the previous studies using ADCP data from 1993 to 2017. Note that in Stramma et al. (1995), the transport estimated is the geostrophic transport from CTD data.

Reference	Section	0-70 m (Upper layer)	70-350 m (Lower layer)	Boreal season (Month)
Dossa et al. (2020)	3.3°-5°S, 34.7°-35.3°W	7.6 Sv ± 0.8	15.8 Sv ± 4.6	Fall (April-May 2017)
	3.3°-5°S, 35.3°-36°W	8.7 Sv ± 1.1	14.2 Sv ± 4.2	
	3.3°-4.1°S, 35.4°W	5.6 Sv ± 0.1	13.9 Sv ± 0.5	
	3.3°-4.1°S, 35.7°W	6.1 Sv ± 0.3	12.4 Sv ± 0.8	
	3.3°-4.1°S, 36.4°W	6.3 Sv ± 0.1	22.8 Sv ± 1.1	
Goes et al. (2005)	5°S, 34°-35°W	2.3 Sv	12.3 Sv	Winter (February 2002)
	3.8°-5.2°S, 35°W	6.5 Sv	16.9 Sv	
Schott et al. (2005)	5°S, 32°-35°W	3.8 Sv	14.2 Sv	Mean of 06 sections of different periods of 1990 and 2000
Schott et al. (2002)	5°S, 33°-35°W	2.7 Sv ± 1.8	13.4 Sv± 2.7	Mean of 09 sections of different periods from 2000 and 2004
Bourlès et al. (1999b)	5°S, 34°-35°W	3.8 Sv	10.6 Sv	Winter (February 1993)
	2°-5°S, 35°W	8.6 Sv	15.6 Sv	Spring (April 1996)
Schott et al. (1995)	3.2°-5°S, 35°W	5.1 Sv	13.1 Sv	Winter-Spring (March 1994)

Source: The Author (2022).

6.1 VARIABILITY OF THE VERTICAL STRUCTURES OF THE CURRENTS IN THE WESTERN BOUNDARY BY USING GLORYS12V1 REANALYSIS

6.1.1 The North Brazil Current

Between 5°S and 3°S, the climatology of the northward current (Figure 19) shows a vertical structure with apparently a relatively weak upper layer flow and a strong thermocline layer flow throughout the year. This region is described in the literature as the transition region between the NBUC and the NBC (Bourlès et al., 1999b). Here, ours results also show the non-homogeneous vertical structure of the northward flow crossing the equatorial section (Seq1) before the equator (Figure 20) from December to April. Across the section 1, the maximum core velocity in thermocline layer is stronger (0.9 m/s) and occurs in May while in the upper

layer flow (so called here NBC) the core is slightly weaker (0.7 m/s) and occurs during May-June (0.7 m/s). Near to the equator, the NBC starts presenting a uniform vertical structure which is shown from May to November with a maximum core velocity of 1 m/s in June-July. From December to April, both the upper layer and the thermocline layer cores are weaker and separated, and the latter is also weaker compared to the section 1. North of the equator, between 0°-3°N, the vertical structure of the NBC is now uniform throughout the year, and the flow from December to April strengthens (Figure 21). Its core continues strengthening and reaches 1 m/s between July-September. From August to March, the flow in the upper layer widens from about 3°N to 5°N. On its northward pathway, the NBC presents the same vertical structure with a maximum core velocity of about 1 m/s between August and December (Figure 22). However, its vertical structure shoals between March and May, and its intensity decreases to reach its minimum core velocity of 0.7 m/s in May. After the retroflection which mean location is about 8°N (See previous chapter), the rest of the NBC continues flowing northward, and its behaviour completely changes. Its vertical structure is shallower and thin, and its maximum core velocity of 0.7 m/s occurs between February and April (Figure 23). Its flow is shallowest and less extended with a miniimum core velocity of 0.3 m/s in October-November.

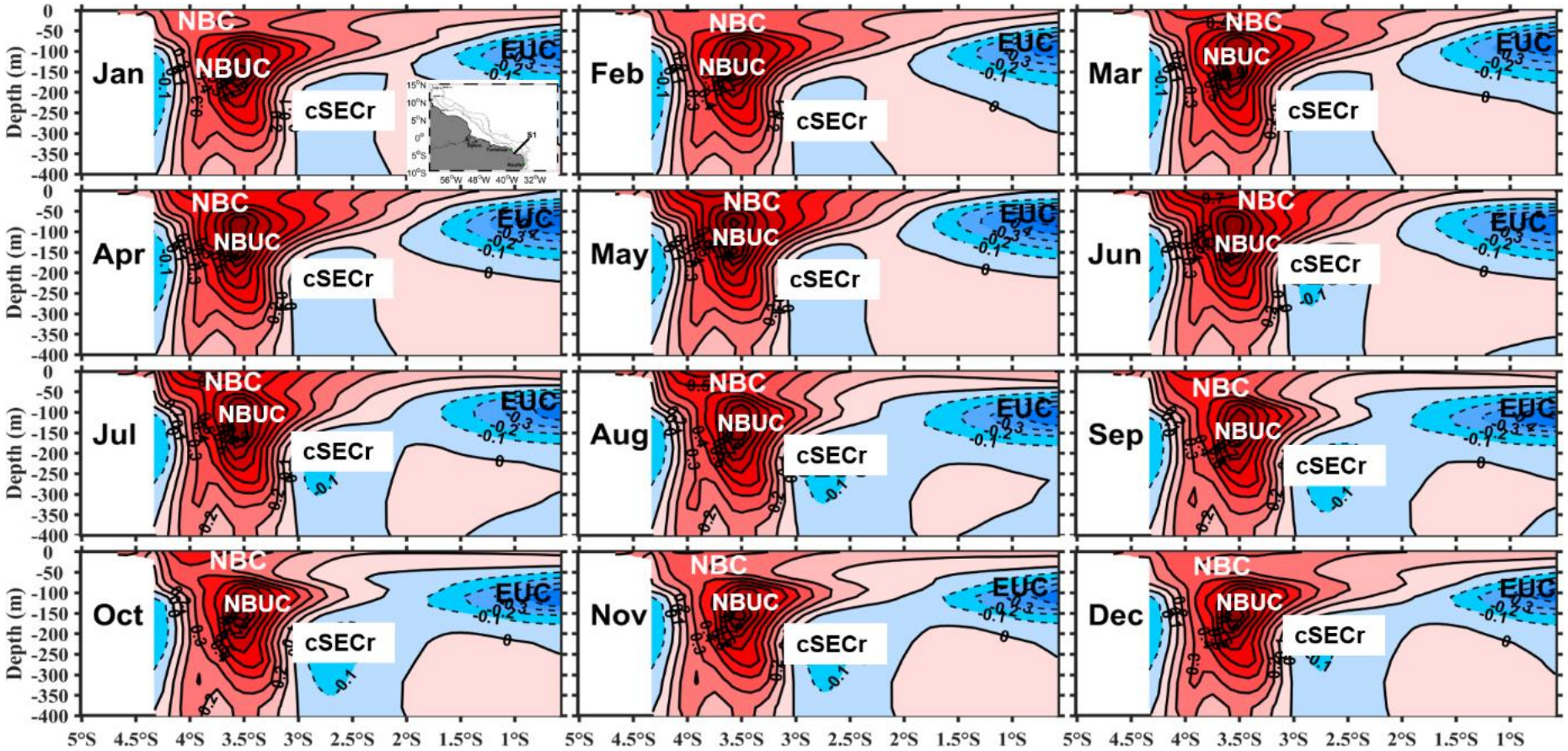

Source: The author (2022).

Figure 19. Monthly climatology of the vertical structure of the currents crossing the section S1 (shown on the map superimposed on the climatology of January). The contours intervals are every 0.1 m/s. The north-westward (south-eastward) flows are in red (blue). Currents are the North Brazil Current (NBC), the North Brazil Undercurrent (NBUC), the south-eastward recirculation of the cSEC (cSECr), and the southern part of the Equatorial Undercurrent (EUC).

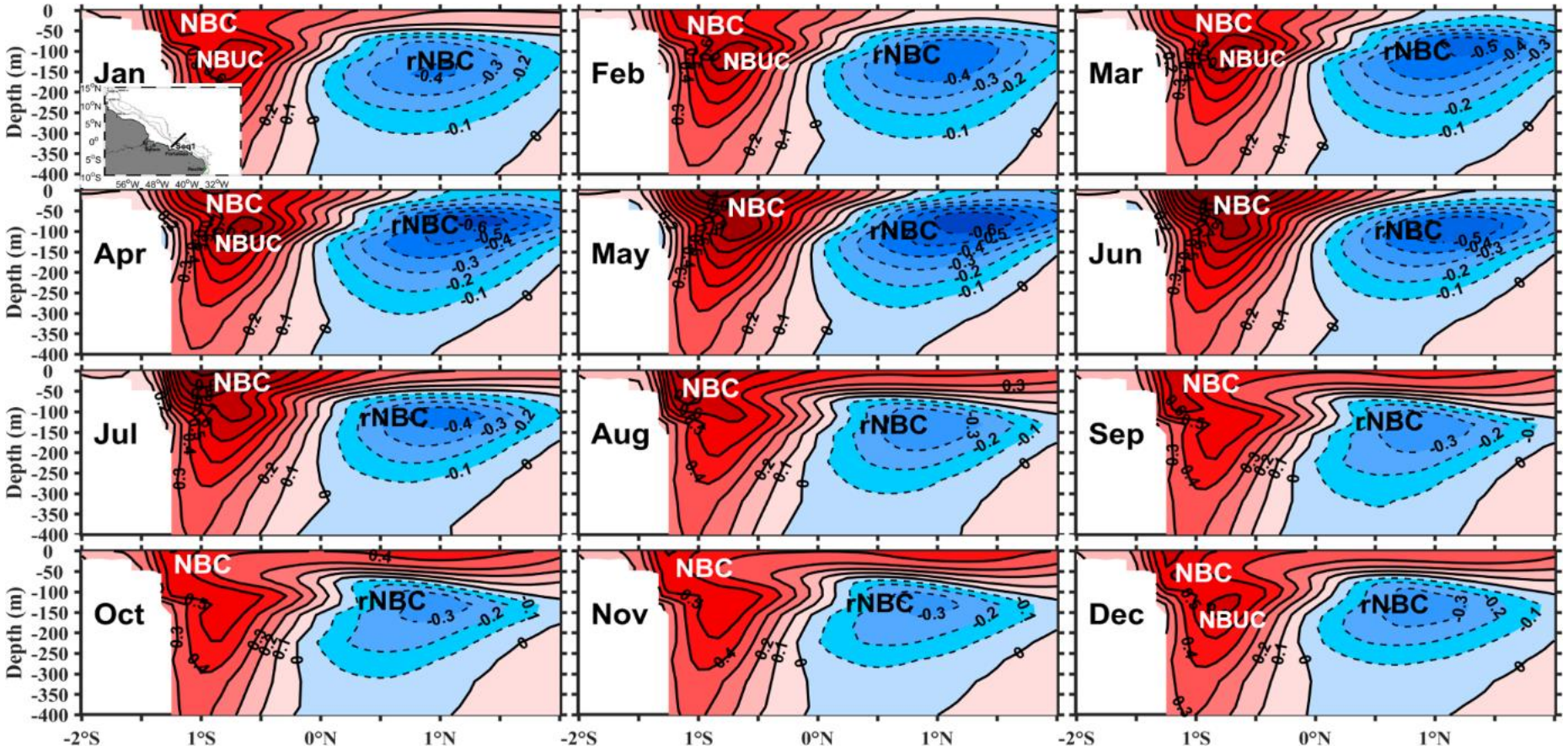

Source: The author (2022).

Figure 20. Monthly climatology of the vertical structure of the currents crossing the section Seq1 (shown on the map with superimposed on the climatology of January). The contours intervals are every 0.1 m/s. The north-westward (south-eastward) flows are in red (blue). Currents are North Brazil Current (NBC) and the retroflected branch of the North Brazil Undercurrent (rNBC).

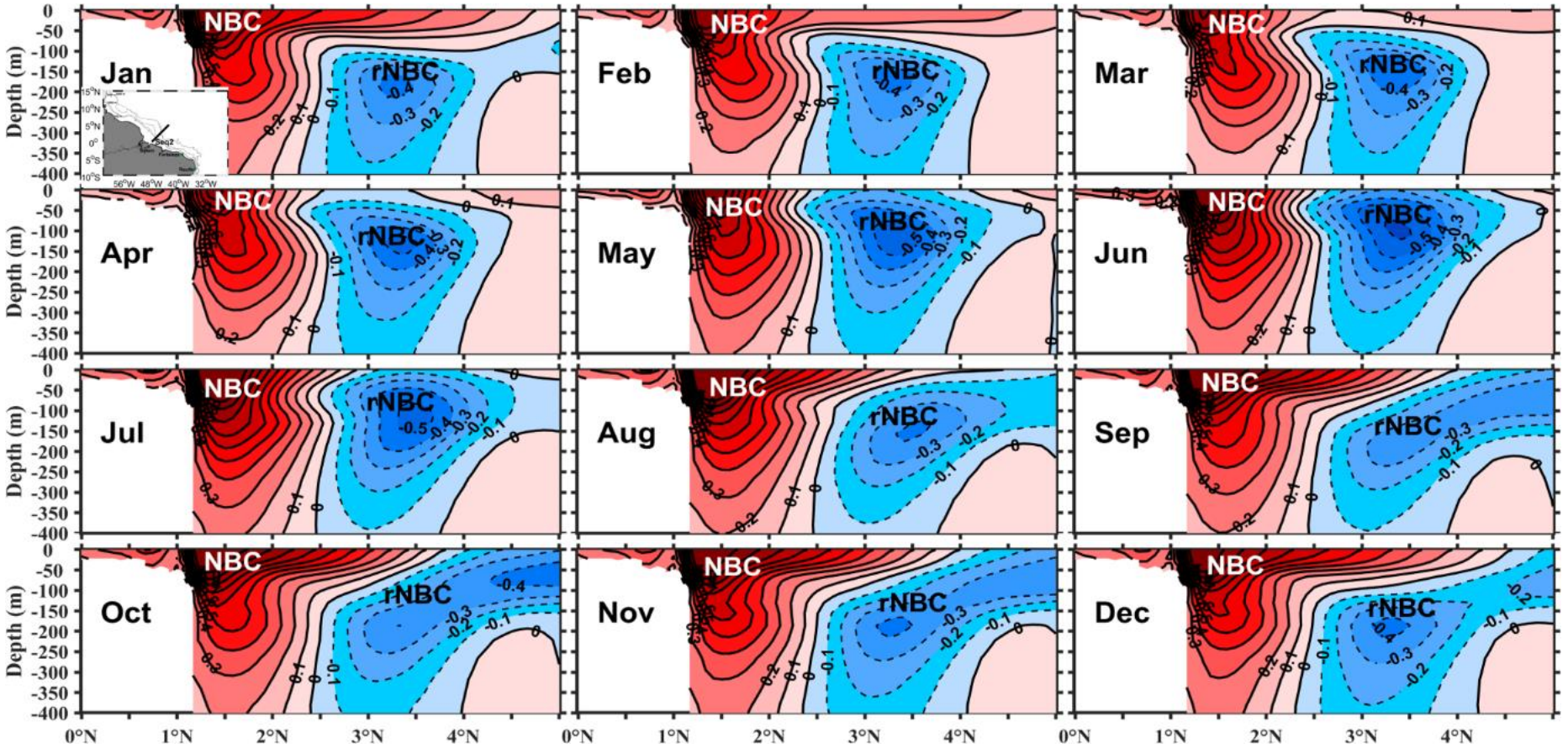

Source: The author (2022).

Figure 21. Monthly climatology of the vertical structure of the currents crossing the section Seq2 (shown on the map superimposed on the climatology of January). The contours intervals are every 0.1 m/s. The north-westward (south-eastward) flows are in red (blue). Currents are North Brazil Current (NBC) and the retroflected branch of the North Brazil Undercurrent (rNBC).

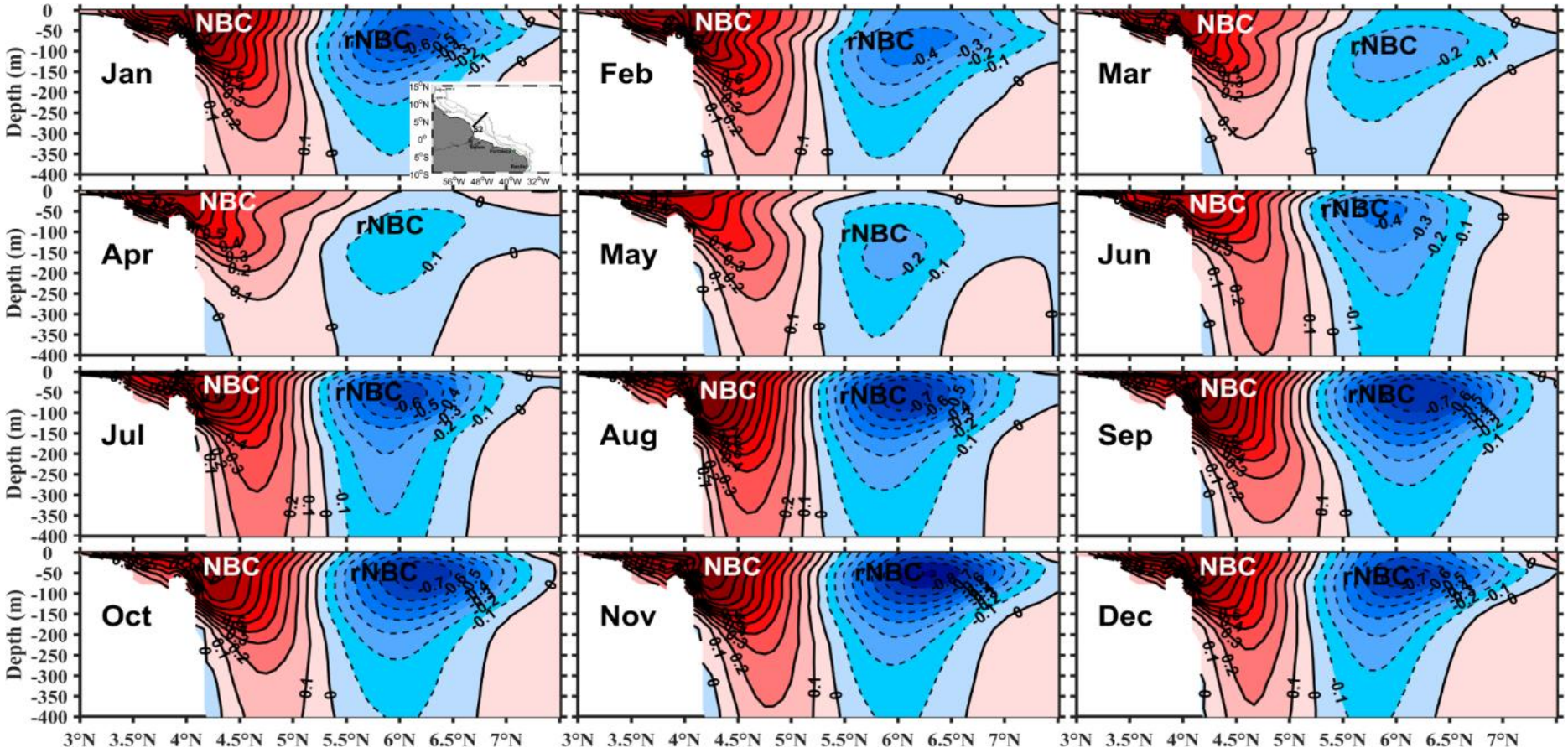

Source: The author (2022).

Figure 22. Monthly climatology of the vertical structure of the currents crossing the section S2 (shown on the map superimposed on the climatology of January). The contours intervals are every 0.1 m/s. The north-westward (south-eastward) flows are in red (blue). Currents are North Brazil Current (NBC) and the retroflected branch of the North Brazil Undercurrent (rNBC).

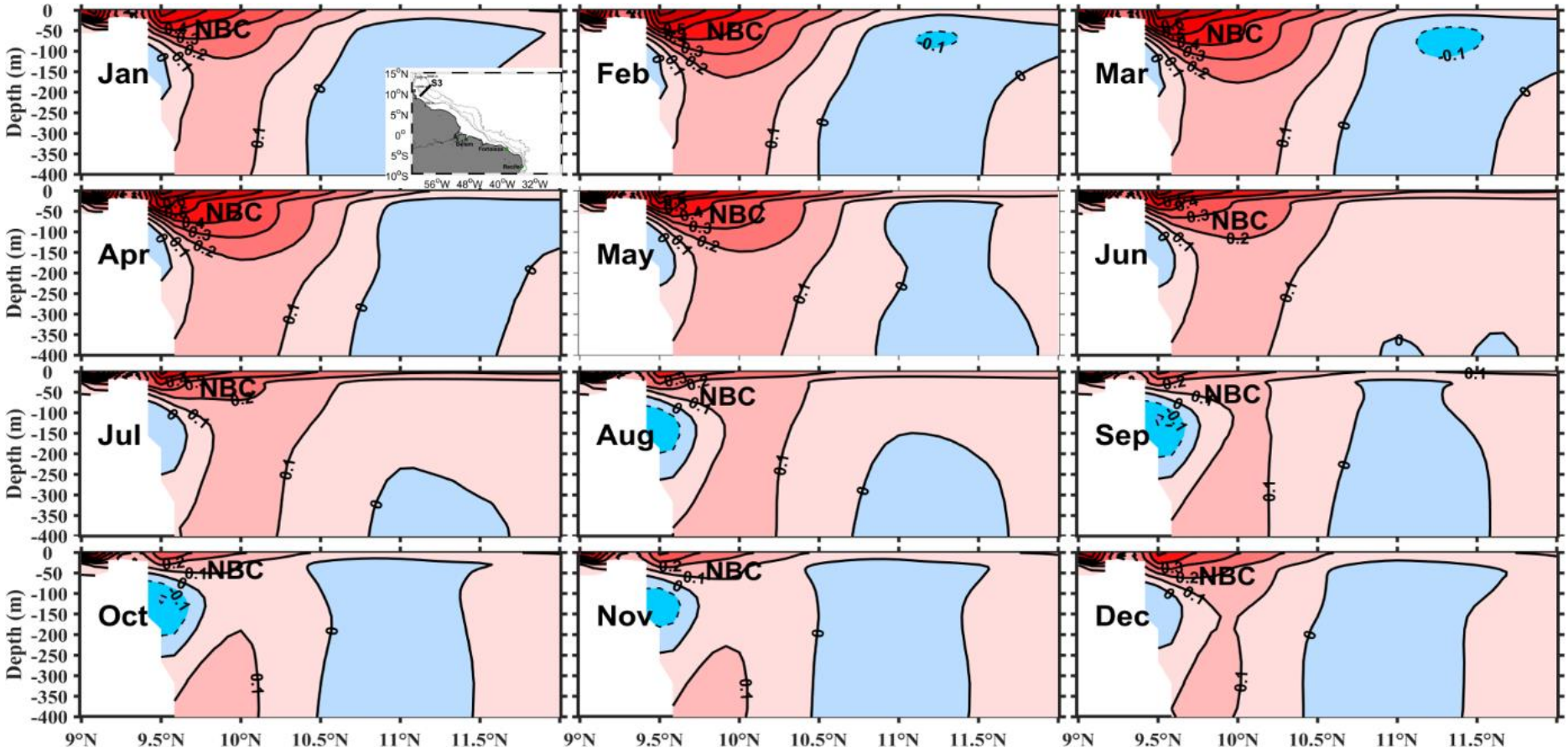

Source: The author (2022).

Figure 23. Monthly climatology of the vertical structure of the currents crossing the section S3 (shown on the map superimposed on the climatology of January). The contours intervals are every 0.1 m/s. The northward (southward) or westward (eastward) flows are in red (blue). NBC is the North Brazil Current toward the Guyana coas

6.1.2 The North Brazil Current Retroflection and its retroflected branch

The NBCR is captured through the cross-section 4 (Figure 24) which shows eastward recirculations of the NBC in the upper and thermocline layers. In the upper layer, the NBCR signature is permanent during the climatological year, but is very weak during the first half of the year, especially during boreal spring. This is consistent with previous studies (e.g., Fonseca et al., 2004; Garzoli et al., 2004). The retroflection starts intensifying from June until September when it appears another intense retroflection region south of the main one commonly called the NBCR. This southern flow (sNBCR) intensifies in October and extends northward to completely merge with the northern flow (nNBCR) in November-December. The resulting flow intensity decreases and becomes weaker during boreal spring. The mean position of the sNBCR and the nNBCR maximum intensities are found respectively at 5.5°N ± 0.8° and 8.1°N ± 0.9°. In the equatorial region, a less intense retroflection of the NBC occurs also between 0-100m and is wider and intense during boreal spring (Figure 24). In the thermocline layer, from the equator to about 6°N, the NBC also shows a deeper retroflection with a maximum velocity position centered between 3°-5°N which is present throughout the year, and is stronger from May to August.

After the retroflection, the retroflected flow (rNBC) is redirected southeastward and is captured by the section 2 (Figure 22) and, the sections Seq2 and Seq1 (Figure 20 and Figure 21). The zonal component of the rNBC flowing eastward, north of the equator is also captured by the section 5 (Figure 25). Crossing the section 2, the rNBC shows similar intensification to the NBC, showing weaker flow between March and May, and a minimum core of 0.1 m/s in April when most of the NBC is directed to the section 3. Its maximum core velocity of 0.8 m/s occurs in the upper layer in November. Equatorward, the rNBC starts deepening and flows in the thermocline layer (Figure 20 and Figure 21). Its intensity increases between March and July whereas its flow extends to the surface, and shows maximum core velocity of 0.5 m/s around 100 m-depth near to the equator. During the second half of the year, the core of the flow is deeper in the thermocline layer, and its core velocity varies between 0.3-0.4 m/s. The extension of the current crossing Seq2 north of 5°N (Figure 21) shows the eastward part of the retroflection out of the equatorial region. This part of the rNBC crosses the section 5 (Figure 25) and connects with a deeper and weak rNBC (0.2 m/s) and the NECC during this period. The deeper rNBC is supposed to feed the NEUC in the thermocline layer. Reaching the equatorial region (Figure 20), the rNBC still extends to the surface from March to June and strengthens to reach its maximum core velocity of 0.6 m/s in April-May between 50-100 m-

depth. The surfacing of the rNBC during this period should be due to the cyclonic circulation described in the previous chapter, which might be influenced by the retroflection of the NBC found in the equatorial region between 0-100m and which in turn should supply the eastward flow X.

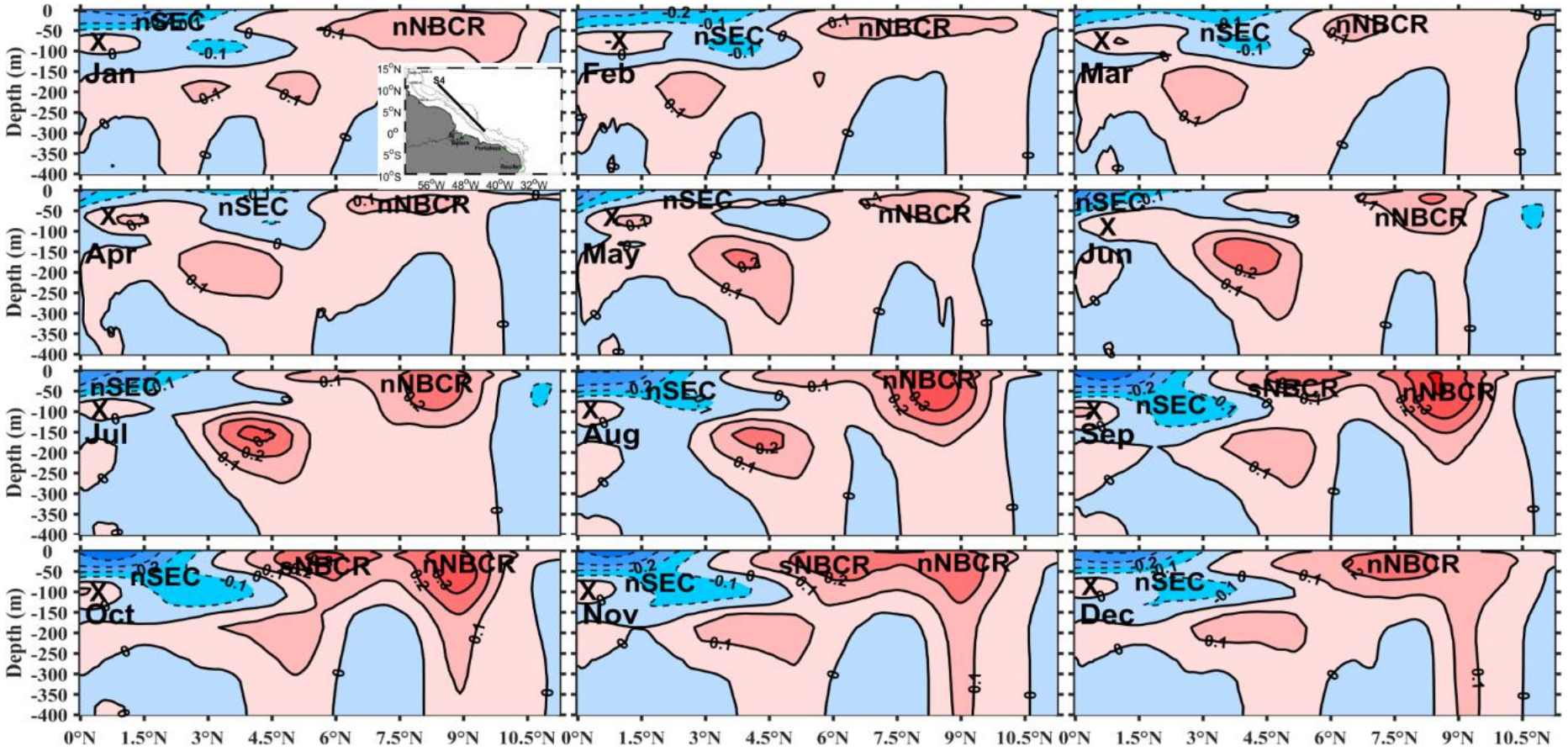

Source: The author (2022).

Figure 24. Monthly climatology of the vertical structure of the currents at the section S4 (shown on the map superimposed on the climatology of January). The contours intervals are every 0.1 m/s. The south-westward (north-eastward) flows are in blue (red). sNBCR and the nNBCR represent the southern and the northern core of the North Brazil Current Retroflection (NBCR) at the limit of the retroflection; nSEC represent the northern branch of the South equatorial Current; and X is retroflection within the upper layer in the equatorial region between 0-2°N.

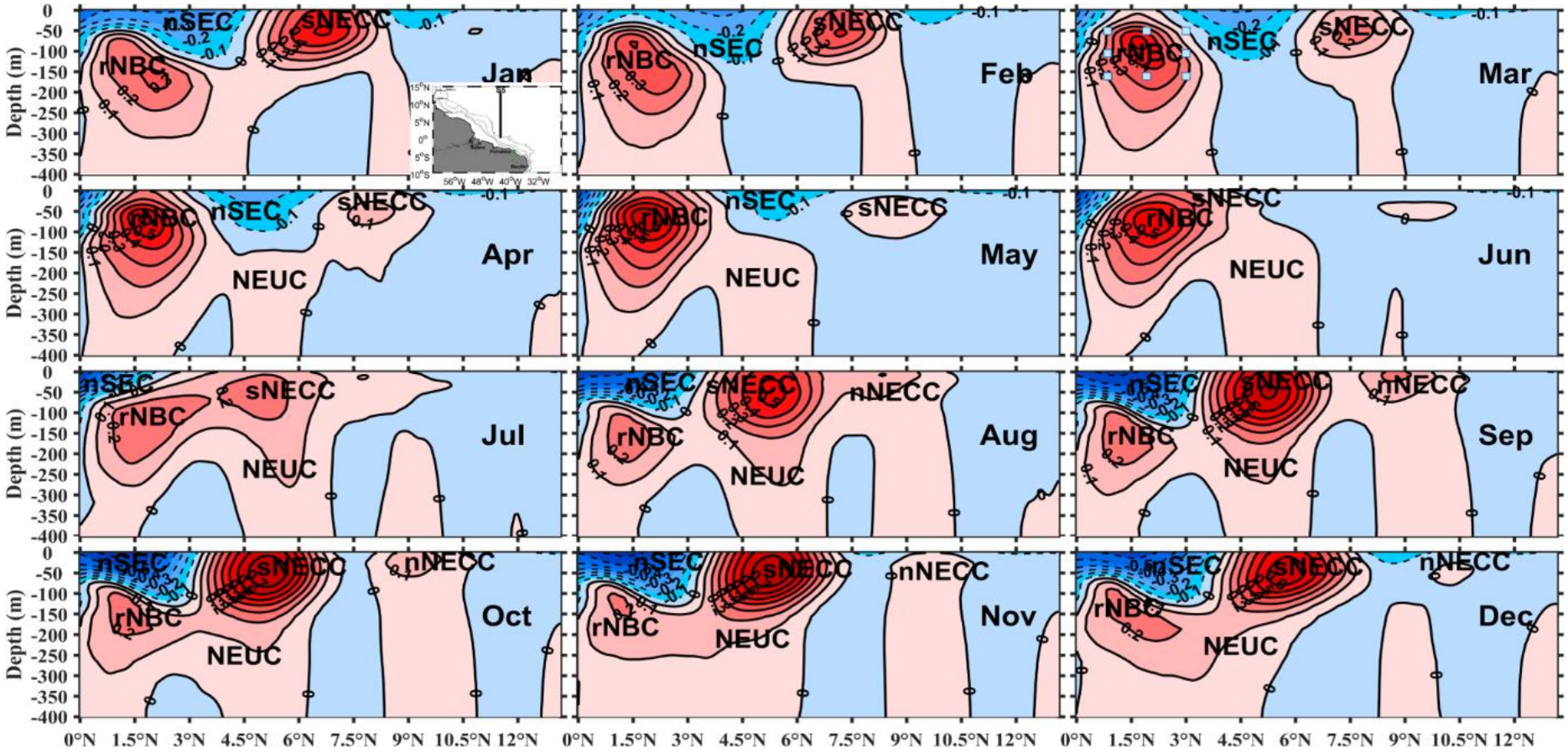

Source: The author (2022).

Figure 25. Monthly climatology of the vertical structure of the currents crossing the section S5 (shown on the map superimposed on the climatology of January). The contours intervals are every 0.1 m/s. The westward (eastward) flows are in blue (red). Currents are the northern and the southern branches of the North Equatorial Countercurrent (nNECC and sNECC) and the northern branch of the South equatorial current (SEC) in the upper layer, and the retroflected branch of the North Brazil Current (rNBC) and the North Equatorial Undercurrent (NEUC).

6.1.3 The North Equatorial Countercurrent

The NECC is known as a surface current which is in Sverdrup balance in the WTA between 22°-42°W (Garzoli and Katz, 1983; Fonseca et al., 2004; Verdy and Jochum, 2005). So, its variability is strongly affected by the wind regimes variability in the northern tropical Atlantic which is characterized by the northward migration of the ITCZ during the year from March to August (Figure 29f) and a presence of ADT ridge between the tropics and the equator during boreal summer and Fall (Rosell-Fieschi et al., 2015; Castellanos et al., 2015). During this period the NECC strength increases and it is partly supplied by the water from the surface NBCR. It starts decreasing after the ITCZ restarts migrating southward. From 42°W to 32°W, the eastward flow crossing ours sections (Figure 25, Figure 26, and Figure 27) shows a two-core structure of the NECC between 3°-12°N. At 42°W, near to the retroflection the NECC receives more water from the surface rNBC and is stronger whereas in the eastern part of the basin, the flow intensity progressively decreases. The maximum core intensity occurs in October-November with values of ~0.8 m/s, ~0.6 m/s and ~0.3 m/s at 42°W, 38°W and 32°W, respectively. At 42°W and 38°W, the southern core of the NECC (sNECC) starts growing from June when the NEUC surfaces in the upper layer and is connected to the EUC or the rNBC at its southern side (Figure 25 and Figure 26). This new sNECC continues growing until July-August when a northern core develops and finally separates from the former in October-November. Then, both branches migrate northward weakening until the nNECC completely disappears during boreal winter while the sNECC remain weaker until a new brand sNECC grows in June. The weaker sNECC finally connects with the new brand sNECC of the following in year in June to form a unique flow which grows and form later another northern branch to continue the cycle. At 32°W, the seasonal cycle still remains the same but the new brand sNECC growth starts earlier in May when the NEUC surfaces earlier (Figure 27). Then, it continues growing till September-October when the northern core develops, and both migrate northward and weakening until the nNECC disappears and the remaining sNECC connects with the new brand sNECC of the next year in May.

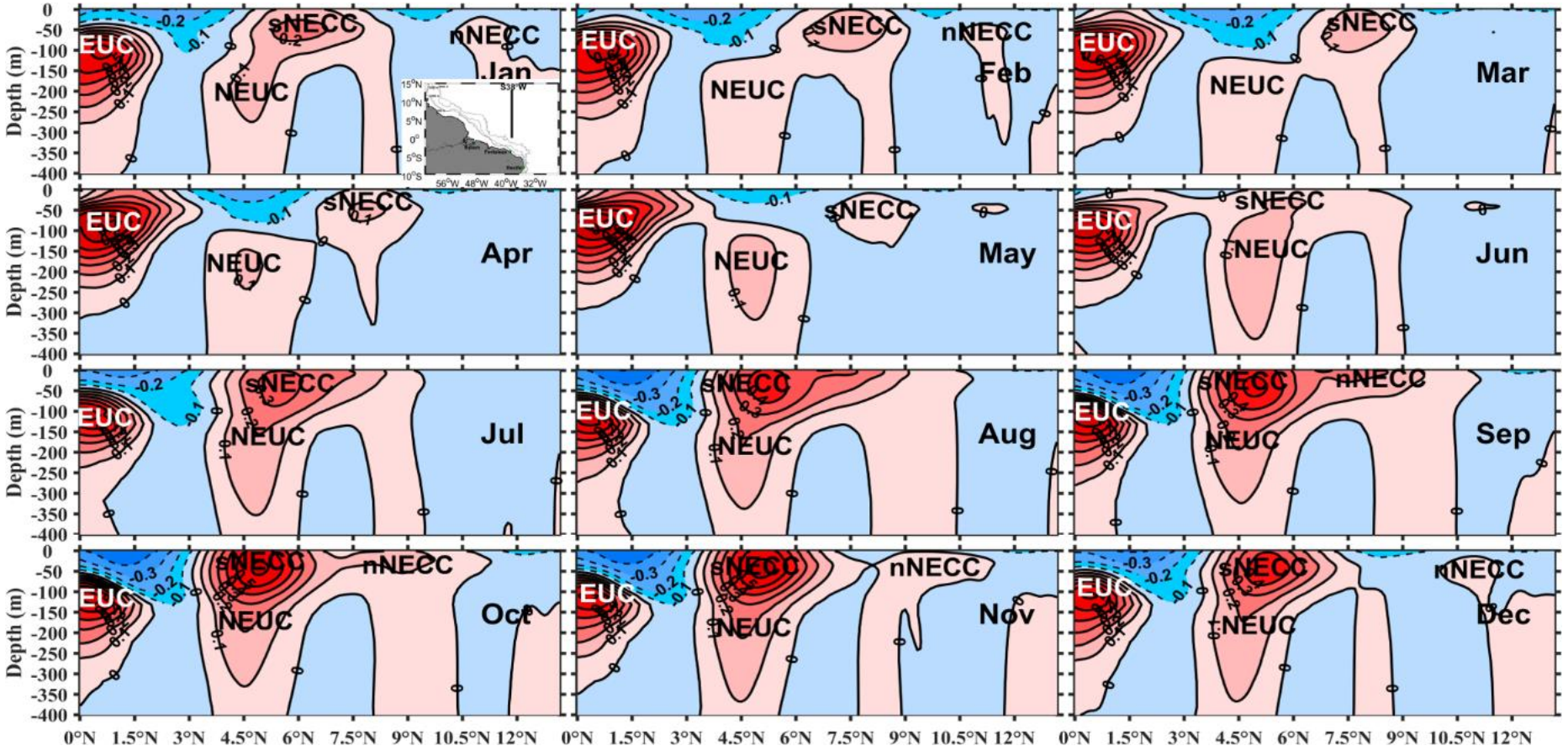

Source: The author (2022).

Figure 26. Monthly climatology of the vertical structure of the currents crossing the section S38°W (shown on the map superimposed on the climatology of January). The contours intervals are every 0.1 m/s. The westward (eastward) flows are in blue (red). Currents are the northern branches of the North Equatorial Countercurrent (nNECC and sNECC), the northern and the central branches in the upper layer crossing the section 5, the Equatorial Undercurrent and the North equatorial Undercurrent (NEUC) in the thermocline layer.

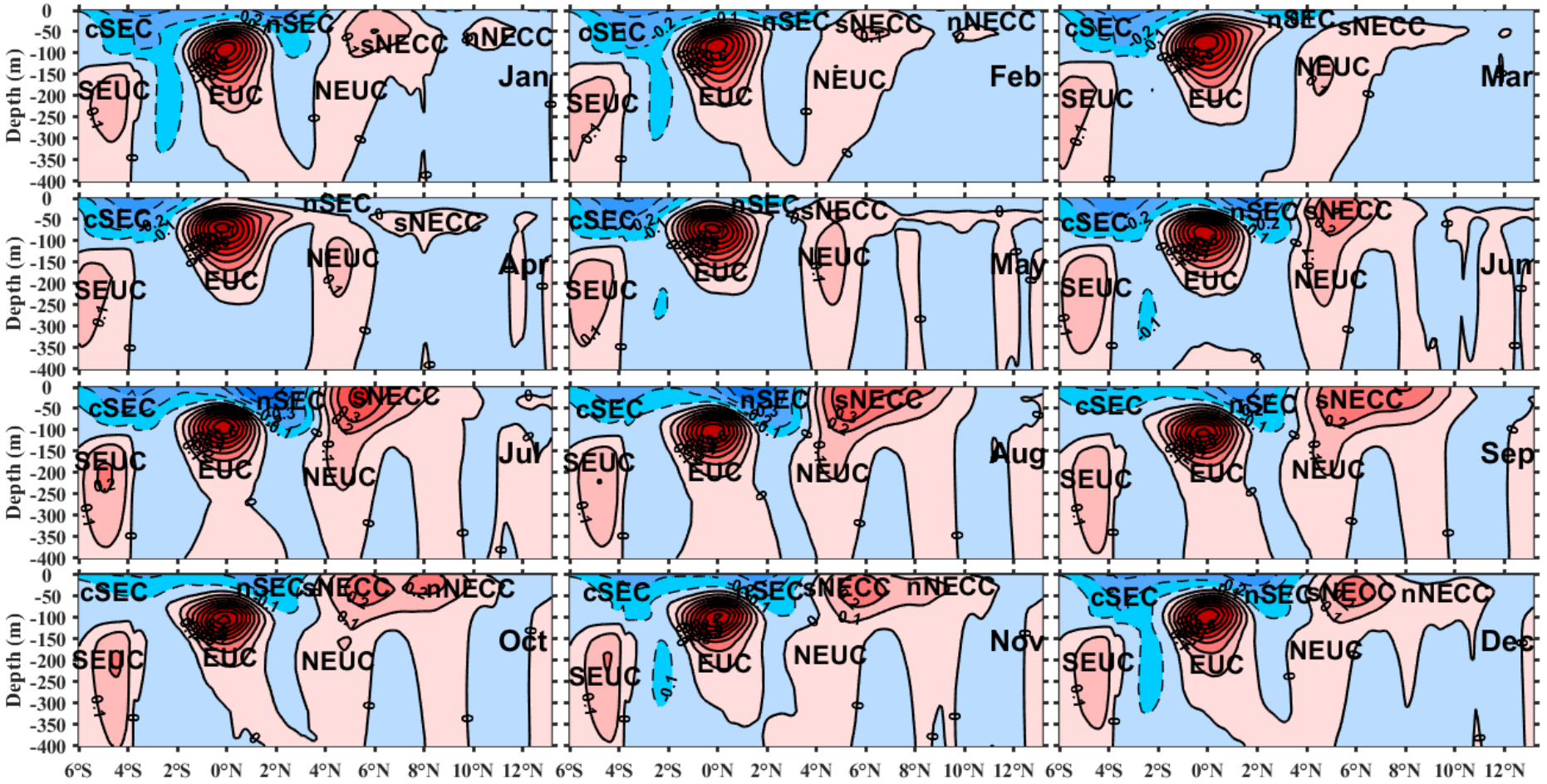

Source: The author (2022).

Figure 27. Monthly climatology of the vertical structure of the currents crossing the section 6 (shown on the map superimposed on the climatology of January). The contours intervals are every 0.1 m/s. The westward (eastward) flows are in blue (red). Currents are the northern and the southern branches of the North Equatorial Countercurrent (nNECC and sNECC), the northern and the central branches in the upper layer crossing the section 5, the Equatorial Undercurrent, the North equatorial Undercurrent (NEUC) and the South Equatorial Undercurrent (SEUC) in thermocline layer.

6.1.4 The central and northern branches of the South Equatorial Current

Crossing the sections located at 32°W, 38°W and 42°W the SEC branches show different behaviours depending on the location, especially for the northern branch (nSEC) (Figure 25, Figure 26 and Figure 27). At 32°W (Figure 27), both branches are connected in the equatorial region, except in boreal spring when the EUC is supposed to surface. The central branch (cSEC) is stronger (weaker) between May-June (in October) with maximum (minimum) core velocity higher (lower) than 0.3 m/s (0.2 m/s) whereas the nSEC is stronger (weaker) in July (April) with a maximum (minimum) core velocity larger (lower) than 0.4 m/s (0.1 m/s). The nSEC at 32°W and 38°W shows the same core velocities. However, at 38°W, it is stronger between August and October and weaker in June when the NECC starts growing. At 42°W, it becomes stronger but shows a similar seasonal cycle to the cycle at 38°W with a maximum (minimum) core velocity about 0.7 m/s (0.1 m/s) between September and November (in June).

6.1.5 The thermocline layer currents and their connections: The North Equatorial Undercurrent, the Equatorial Undercurrent and the South Equatorial Undercurrent.

As thermocline layer currents, the NEUC and the EUC are known to be supplied by the deeper part of the NBCR/rNBC (Bourlès et al., 1999b; Schott et al., 1995; 2004). The sections from 4 to the east confirms the previous studies and shows that the NEUC should be directly supplied by part of the retroflection flow in the thermocline layer located between 3°6°N which probably does not deviate (Figure 24, Figure 25, Figure 26 and Figure 27). The strong rNBC besides of the NEUC at 42°W (Figure 25) is the zonal component of the southeastward rNBC which might be joined by the equatorial retroflection of the NBC described in the section 6.1.2, and then, goes to feed the EUC in the equatorial region. It can be also seen through the equatorial cross-section Seq1 between 40°-42°W. This rNBC continues flowing to reach the equator and feed the EUC. Following the flow crossing the section 4, the NEUC maximum core velocity occurs between May and August, and its flow weakens when it is moving eastward to reach 0.1 m/s at 32°W (Figure 25). During this time, the EUC which is directly fed by the southeastward rNBC shows a seasonal cycle similar to this latter when crossing Seq1 (see section 6.1.2). It intensifies to the east and shows maximum core velocity of ~0.8 m/s during the spring when its flow surfaces.

South of the equator, the SEUC flows between 3°-6°S (Figure 27). It is stronger than the NEUC and shows a maximum core velocity higher than 0.2 m/s in July and October between

200-250 m depth. The flow of the cross-section S1 averaged between 100-350 m depth (Figure 28) shows a recirculation of a deep westward flow toward the SEUC between 2.2°-3.3°S, mostly the second half of the year. This evidences the fact that the SEUC might be supplied by the cSEC recirculation so-called here cSECr (see Figure 19) which flows at this location and confirms the previous studies of Schott et al. (1998) and Dossa et al. (2020).

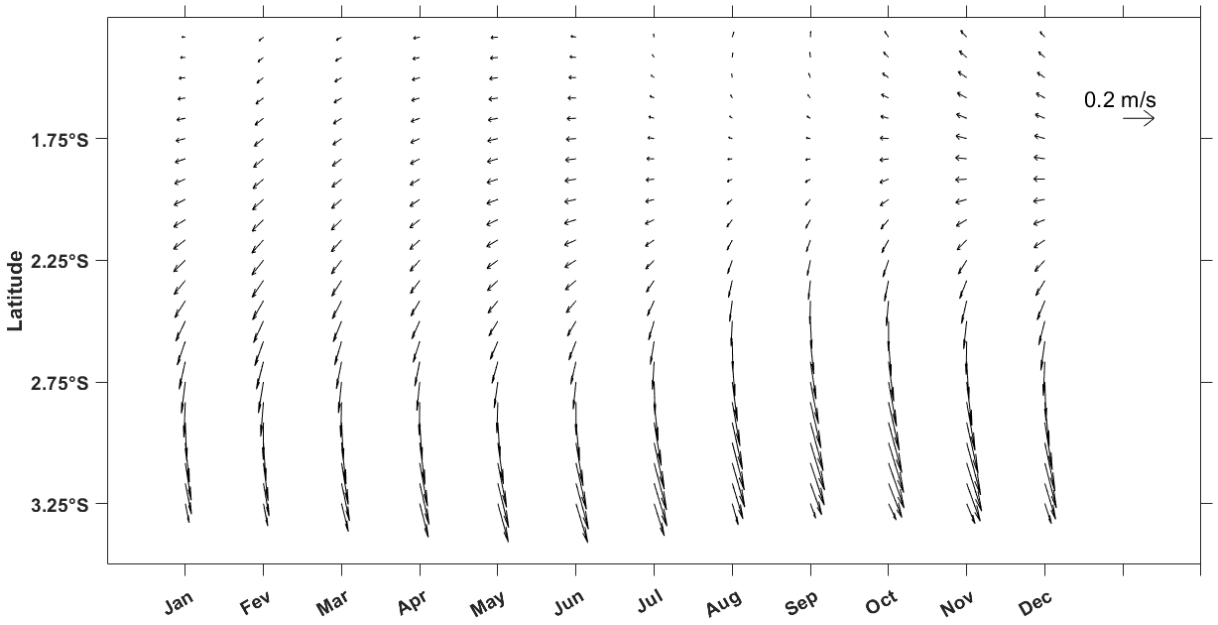

Source: The author (2022).
Figure 28. 100-350 m-depth mean average flow of the cross-section S1 between 1°-3.3°S.

6.2 THE SEASONAL VARIABILITY OF THE WESTERN BOUNDARY CURRENT TRANSPORTS AND THE INTERDEPENDENCE BETWEEN THE NBC AND THE OTHER CURRENTS.

From south to north, the NBC transport shows different annual cycles depending on its exchanges with the other WB currents in the upper layer and/or in the thermocline layer. In the transition region between the NBUC and the NBC (3°-5°S), the volume transport monthly climatology of the upper layer flow called here NBC1 (Figure 29a) shows similar cycle to that of the cSEC (Figure 29e) with maxima in May (12.8 Sv and 5.8 Sv, respectively). The surplus of NBC1 transport relatively to the cSEC input throughout the climatological year informs about the contribution of the NBUC, which is slightly larger than that of the cSEC in the upper layer at this location. Before reaching the equator, the northward upper layer transport witnesses some changes due to the cSEC contribution north of 3°S. Indeed, the cSEC flowing north of 3°S contributes to increase the transport which reaches a maximum of 14.9 Sv in June (Figure 29b). In parallel, the cSEC transport between 0°-5°N shows larger transports during the first

half of the year with a mean value of ~8.5 Sv and a maximum of ~9 Sv in June (Figure 29e). This latter shows that, all the cSEC transport in the upper layer does not reach the NBC (e.g., Figure 30a). Part of this transport might be directed equatorward to create a connection with the nSEC and/or probably recirculate eastward. A cSEC annual mean transport of 1.9 Sv should be joining the nSEC transport in the upper layer transport (Figure 30a).

Crossing the equator, the NBC is clearly influenced by the nSEC which reaches its maximum transport (~16 Sv) in September (Figure 29e). The NBC transport increases following a similar cycle to that of the nSEC, but reaches its maximum of 15.5 Sv in August when the WSC strength reaches its maximum value and the ITCZ is at its northernmost position (Figure 29c and f). The NBC transport continues increasing under the influence of the nSEC and reaches a new maximum (minimum) value from August to November (May) when crossing the section S2 (Figure 29d). A similar annual cycle was also found by Garzoli et al. (2004) who used the Inverted Echo sounders (IES) and Pressure gauge data to calculate the geostrophic transport between 2°-4°N. The authors found with dataset of ~2 years a maximum NBC transport of 20 Sv between August and November within the first 300 m-depth, and two different maximum peaks in August and October. We found here that the transport reaches its first maximum peak in August, decreases from August to October and reaches the largest value of 17.1 Sv in November. Its minimum of 10.4 Sv occurs in May and is also consistent with the authors. The decrease from August to October should be explained by the importance of the southern NBCR region found in the previous chapter, which might move part the NBC water to the east before reaching the section S2. The rNBC transport crossing the section S2 also depicts a similar annual cycle but varies between the 3.3 Sv in April and 16.9 Sv in November within upper layer (Figure 31c). The difference between the NBC transport crossing the section S2 and the rNBC transport might be due to the non-retroflected NBC crossing S3 and probably to the northward transport generated by the rings. The estimation of the NBC transport crossing the section S3 varies from the 1.9 Sv in November to 7.5 Sv in March (Figure 29a). The negative difference between the NBC transport before the retroflection and the sum of rNBC and NBC transports crossing the sections S2 and S3, respectively in both the upper and the thermocline layers (Figure 30c) shows that, the rNBC should be supplied by another source coming from the north. The previous studies of Bourlès et al. (1999a) and Goes et al. (2005) who proved that the NECC is supplied by the NEC. This suggests that the NEC waters might be introduced into the NECC by the rNBC. However, the input of water into the rNBC makes difficult the estimatation of transport due to the rings. The positive difference shown between March and May in the upper layer (Figure 30c) should indicate that the rings during this period may be the

ones which contributes more to the annual mean transport of the rings without be able to precisely estimate the amount of water transported by the rings to the north assuming the conservation of transport.

From S2 to Seq2, the rNBC transport in the upper layer is influenced by northern part of the equatorial retroflection described in section 6.1.2 and increases rapidly from 4.4 Sv to 11 Sv between April and June, and decreases after to reach a minimum transport of 0.7 Sv in January-February (Figure 31b and c, and Figure 24). After crossing Seq2, the rNBC increases from January to reach its maximum value of 10.1 Sv in May and then decreases till the end of the year (Figure 31a). This increase of the transport in the upper layer during boreal spring is due to the influence of the transport due to the equatorial retroflection between 0°-2°N (Figure 32a), which is strengthened by the rNBC coming from the northern retroflection and fully directed to the equatorial region. This rNBC during boreal spring will be the one that engages the equatorial cyclonic circulation located between 0°-5°N, 35°W45°W. The rest of the year whereas the rNBC is deeper, the transport in the thermocline layer remains higer compared to the upper layer (Figure 31a-c).

The NECC transport decreases from 42°W to 32°W (Figure 31d, e and f). At 42°W/38°W, it shows a same annual cycle with a minimm in May (2.8 Sv/2 Sv) and a maximum in November (21.7 Sv/17.8 Sv). However, at 32°W, the extrema of the NECC annual cycle are reached earlier. The minimum (maximum) of 2.1 Sv (13.4Sv) occurs in April (August).

The undercurrents also present different seasonal cycles. The SEUC transport shows an annual cycle varying from 5.8 Sv in April to 7.6 Sv in July. Its amplitude compared to the cSECr transport shows that the SEUC may be supplied by another current such as the NBUC (Figure 32d). The NEUC transport is slightly weaker than that of the SEUC and shows an annual cycle varying from 4.4 Sv in December to 6.7 Sv in August (Figure 32c). In the equatorial region the EUC is the stronger current in the thermocline layer and follows a semi-annual cycle with two maxima of 20 Sv and 25 Sv in April and September, respectively; and two minima of 18.5 Sv and 19.7 Sv in June-July and November-December, respectively.

In the following section the information about all the transport of the current in both layers will be used to propose a new schematic map of the seasonal circulation of the WB.

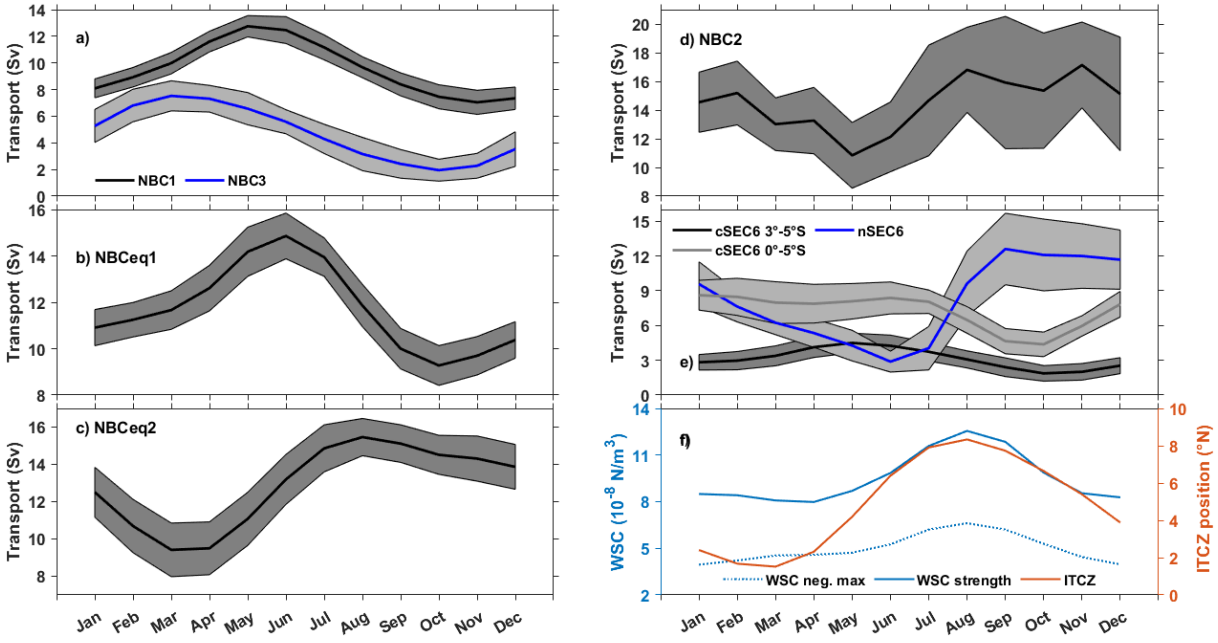

Source: The author (2022).

Figure 29. Monthly climatology of the current transports in the upper layer (0-100 m depth): a) the North Brazil Current (NBC) crossing the section 1 and 3; b) and c) the NBC crossing the equatorial sections eq1 and eq2, respectively; d) the NBC crossing the section 2; e) the central and the northern branches of the South Equatorial Current (SEC) crossing the section 6 and 5, respectively; and the monthly climatology of the wind parameters: the absolute value of the maximum negative wind stress curl (WSC neg. max), the difference between the maximum positive and negative wind stress curl (WSC strength) and the location of the intertropical convergence zone (ITCZ). The shaded areas surrounding the monthly means in a), b), c) d) and e) correspond to the standard deviation of the transport associated with each current.

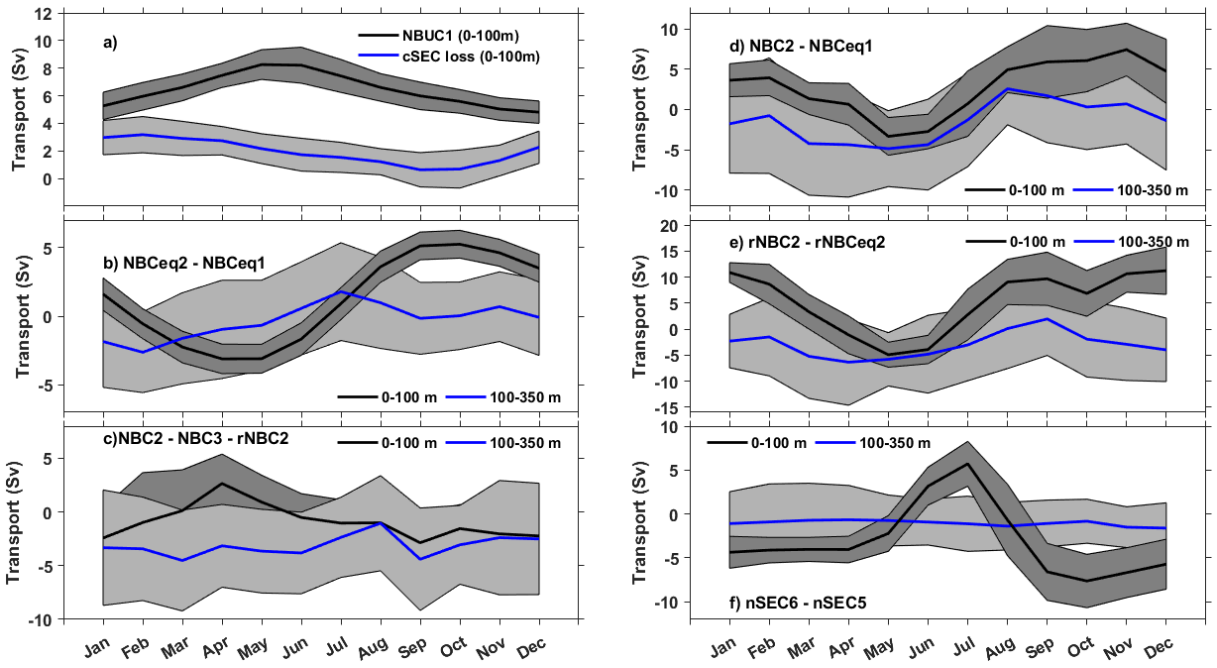

Source: The author (2022).

Figure 30. Monthly climatology of the difference of the absolute values of the current transports in the upper layer (0-100 m depth black lines):and in the thermocline layer (100-350 m depth: blue lines): NBUC1 and cSEC loss in a) are the contribution of the North Brazil Undercurrent (NBUC) to flow crossing S1 and part of the central branch of the South Equatorial Current (cSEC) joining the northern branch (nSEC), respectively; NBCeq2 – NBCeq1 in b) is the difference between the transports of the North brazil Current (NBC) crossing Seq2 and Seq1; NBC2-NBC3-rNBC2 in c) is the difference between the transport crossing S2 and the sum of the transport of the NBC crossing S3 and transport of the retroflected branch of the NBC (rNBC) crossing S2; NBC2-NBCeq1 in d) is the difference between the transports of the NBC crossing S2 and Seq1; NBCeq1-NBC1 in e) is the difference between the transports of the NBC crossing Seq1 and S1; and nSEC6-nSEC5 in f) is the difference between the transports of the nSEC croissing S6 and S5. The shaded areas surrounding the monthly means correspond to the standard deviation of the values of the differences.

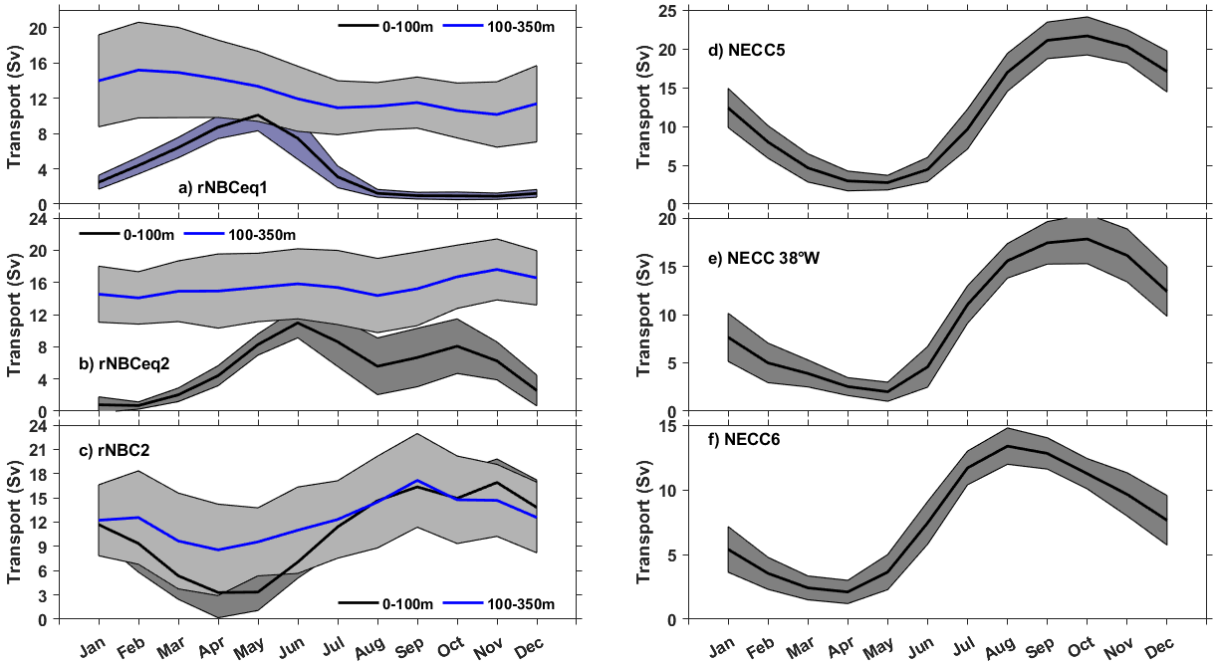

Source: The author (2022).

Figure 31. Monthly climatology of the current transports of the retroflected branch of the North Brazil Current (rNBC) crossing Seq1 (a), Seq2 (b) and S2 (c), and of the North Equatorial Countercurrent (NECC) crossing S5, S38°W and S6. The blue and black lines are the transport in the upper layer (0-100 m depth) and in the thermocline layer (100-350 m depth), respectively. The shaded areas surrounding the monthly means correspond to the standard deviation of the transport associated with each current.

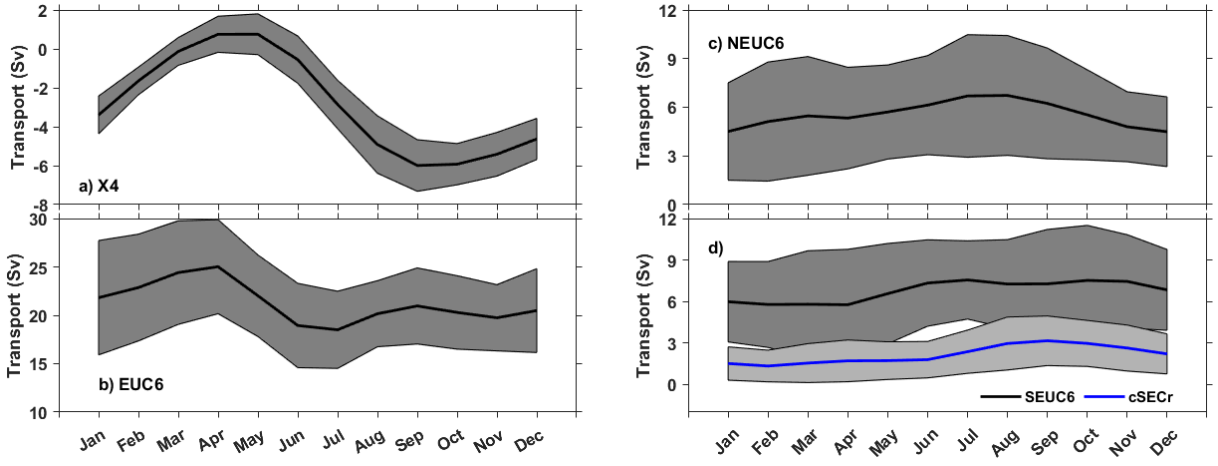

Source: The author (2022).

Figure 32. Monthly climatology of the current transports. The currents are a) the eastward flow coming from the equatorial retroflection within the first 100 meters and crossing S4 (X4); b) the Equatorial Undercurrent crossing S6 (EUC6) within 0-350 m depth; c) the North Equatorial Undercurrent crossing S6 (NEUC) withing 100-350 m depth; and d), the South Equatorial Current crossing S6 (SEUC6) and the southeastward recirculation of the cSEC crossing S1 (cSECr) within 100-350 m depth. The shaded areas surrounding the monthly means correspond to the standard deviation of the transport associated with each current. The transport of X4 is estimated by summing the transport of the eastward and the westward current in order to shows the importance of this flow.

6.3 SYNTHESIS AND SCHEMATIC MAP OF THE SEASONAL CIRCULATION OF THE WESTERN BOUNDARY CIRCULATION FOLLOWING THE NBC TRANSPORT DISTRIBUTION

To propose a new schematic circulation in the upper and thermocline layers, we choose to follow the NBC transport along its pathway and analyze how this is dispatched in the WB. To do so, the cross-sections of the current, mostly the cross-sections S1, Seq1, Seq2, S2 and S3 are considered. The inputs of the NBUC transport in the upper layer can be estimated by subtracting the cSEC transport from the transport of the northwestward current crossing S1 (Figure 30a). Its variations depict an annual cycle similar to the cSEC and the NBC between 3°-5°S with a maximum (7.3 Sv) in May and a minimum (4.8 Sv) in December. Since we know that the NBC undergoes a retroflection along its pathway, and its transport is influenced in the southern and northern hemispheres by the cSEC and the nSEC, respectively, the estimations of its variations from a location to another allowed to determinate the inputs or the outputs of transports. For an increase of transport between two sections, the NBC is considered receiving a surplus of transport from the cSEC or the nSEC while a decrease indicates an eastward retroflection. The monthly climatology of differences between transports of all the currents also allowed to understand the possible connections between them. Figure 30 presents the climatology of the transport differences between some sections to analyze their spatial and seasonal variations. For example, the difference between the absolute values of the current transports of the northward current between 3°-5°S and the cSEC crossing S1 (e.g., Figure 30a) indicates the contribution of the NBUC to the NBC before the equator; and the difference between the total transport of the NBC at this location and the next location indicates whether an eastward retroflection (loss) or an input from an westward current (gain). The difference of volume transports of the northwestward (southeastward) NBC (rNBC) between both equatorial sections Seq1 and Seq2 (e.g., Figure 30b) shows the amount of the nSEC/X entering/leaving the NBC (rNBC) between 0°-2°N. The difference of transport between the NBC crossing S2 and the sum of the absolute value of the NBC transport crossing S3 and the rNBC transport crossing the S2 (e.g., Figure 30c) indicates whether there is a flow joining the rNBC from north and/or there is a loss of volume transport due to the rings. To compensate a positive difference, it should have a loss of transport due to the rings while in the contrary case, it should have an input from northern water coming probably from the NEC. The difference of the NBC (rNBC) transports crossing Seq1 and S2 (e.g., Figure 30d and e) indicates whether there is a nSEC contribution to the NBC (the rNBC contribution to the NECC/NEUC in the upper/thermocline layer or no contribution) or an eastward retroflection. The negative difference for both the NBC

and rNBC in these locations in the upper layer during boreal spring shows a loss of transport and confirm the strong NBC retroflection between 0°-2°N during this period (Figure 30d-e). In the thermocline layer, the difference is lower, but permanently negative, indicating the presence of a permanent weak retroflection between 100 and 350 m depth which is also shown in Figure 24. The difference between the nSEC transports at 32°W and 42°W (e.g., Figure 30f) indicates the recirculation of the nSEC into the NECC during boreal summer and the possible southeastward recirculation of the NECC into the nSEC the rest of the year.

The variation of the NBC transport along its pathway and its possible connections in upper and the thermocline layers have been computed for each season and summarized in Figure 33 and Figure 34, respectively to update the WBC. From south to north, the NBC transport in the upper layer of the equatorial region is higher during boreal spring and lower during the boreal fall. The larger value of the transport in boreal spring is due to the inputs of both the cSEC and the NBUC which are larger during this period compared to the others seasons as mentioned in the previous section (8 Sv and 5.9 Sv, respectively). These larger values might explain the existence of the cyclonic circulation found between 0°-5°N and 35°-45°W. Over 10% of the total transport (1.8 Sv) retroflects to strengthen the weaker rNBC which carries 4.6 Sv and constrains the nSEC (3.1 Sv) to the southeast direction. Then, the resulting current transporting 9.5 Sv flows eastward along the equator to meet the lower part of the nSEC. On its pathway surplus of the transport flows along the equator and connects with the EUC which is seen shallower during this period. North of the equator, the NBC transport is larger during the second half of the year, especially during boreal fall when the inputs from the NBUC and the cSEC are lower (5.1 Sv and 4.6 Sv, respectively). The strengthening of the NBC to reach a maximum transport of 15.9 Sv in the northern hemisphere even though it was weakest before the equator is due to the larger contribution of the nSEC (6.1 Sv). These results suggest that the strengthening of the NBC between 0°-2°S should be due to the larger transports of the cSEC and the NBUC which favor the equatorial retroflection in the upper layer whereas its strengthening north of the equator depends only on the nSEC inputs. The transport of the rNBC is in phase with the variations of the NBC before the retroflection. The larger NBC transports before the retroflection induce higher transport of the rNBC which feeds the NECC accordingly. The higher contribution to the NECC is shown during boreal fall whereas in boreal spring, there is almost no contribution. Inversely, the NBC flowing toward the Guyana coast are less fed during the second half of the year. It appears that the weaker (stronger) northward continuity of the NBC during boreal fall (spring) might depend on the situation when both the cSEC and the NEUC transports are lower (higher). In the northern hemisphere and the equatorial region, the

northern and the equatorial NBC retroflections in the upper layer are shown to depend on the NBC strength north of the equator and on the cSEC-NBUC strength south of the equator, respectively. Regarding the transport due to NBC rings which are shed along the year (Aroucha et al., 2019), the conservation of the volume transport shows that, only during boreal spring, there is a remaining transport which should be carried by the rings. This transport should be larger than 1.1 Sv in case of northern waters inputs from the northern hemisphere (NEC) into the rNBC. During the rest of the year, the conservation of transport shows that there should always have inputs of waters higher than 1 Sv from the northern hemisphere.

In the thermocline layer (Figure 34), between 3°-5°S, the input of the NBUC does not vary too much. The mean transport is about 17.2 Sv. Unlike the upper layer, the flow in thermocline layer shows possible retroflection of the current before reaching the equator probably toward the EUC. However, this retroflection has a lower transport compared to that of the northern hemisphere. The higher outputs of transport occur during the second half of the year when the negative WSC maximum and WSC strength are maximum and the ITCZ is at its northernmost location (Figure 29f) (2.6 Sv and 2.7 Sv during boreal summer and fall, respectively). Because of the water outputs created by this southern retroflection during the second half of the year, the NBC transport becomes lower after crossing the equator. In the northern hemisphere, it has been also found that, the contribution of the northern hemisphere waters to the rNBC transport in the thermocline layer might be larger than in the upper layer. The conservation of transport does not show any particular season for a probably larger transport carried by the rings. However, it has been shown that the higher contribution of the northern hemisphere waters should occur during boreal spring, with larger than 12.6 Sv volume transport into the rNBC, and a higher contribution to the EUC transport accordingly. The higher contribution to both the EUC and the NEUC appears to be stronger during season with higher northern waters inputs into the rNBC (22.3 Sv and 20 Sv during boreal spring and fall, respectively). The maximum contribution to both undercurrents occurs for the EUC (16.5 Sv) and the NEUC (9.3 Sv) during boreal spring and fall, respectively. The variability of the NBC transport flowing toward the Guyana coast remains the same as in the upper layer but is lower.

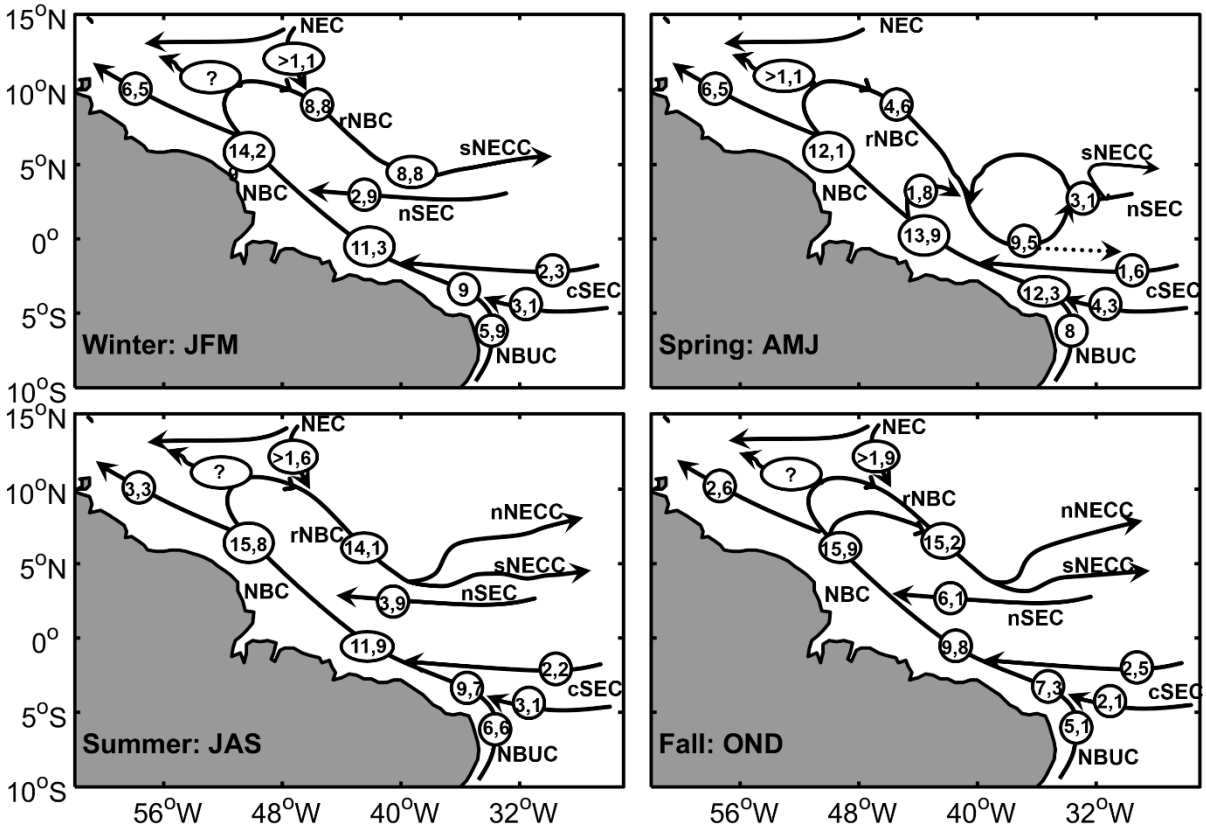

Source: The author (2022).

Figure 33. Schematic representation of the North brazil Current (NBC) transport along its pathway and the repartition of this transport toward the southern and the northern branches of the North Equatorial Countercurrent (sNECC and nNECC, respectively) in the upper layer (0–100 m) during the boreal seasons. Seasonal NBC transport values are calculated from GLORYS12V1 reanalysis considering the sections S1 within 0°-5°N, 33°-38°W, the section Seq1 within 2°S-2°N, 42.5°47°W, the section S2 within 3°-7.5°N, 46°-50.5°W and the section 3 within 9°-12°N, 57°-60°W. The incoming North Brazil Undercurrent (NBUC) transport and the additional transport coming from the central and the northern branches of the South Equatorial Current (cSEC and nSEC, respectively) are also mentioned and schematized. Region of the NBC rings, where the transports are not calculated are labelled by question marks and the possible surplus of transport to the NBC retroflected branch (rNBC), coming from north probably via the North Equatorial Current (NEC) are also mentioned considering conservation of the transport if the ring transport is assumed to be null.

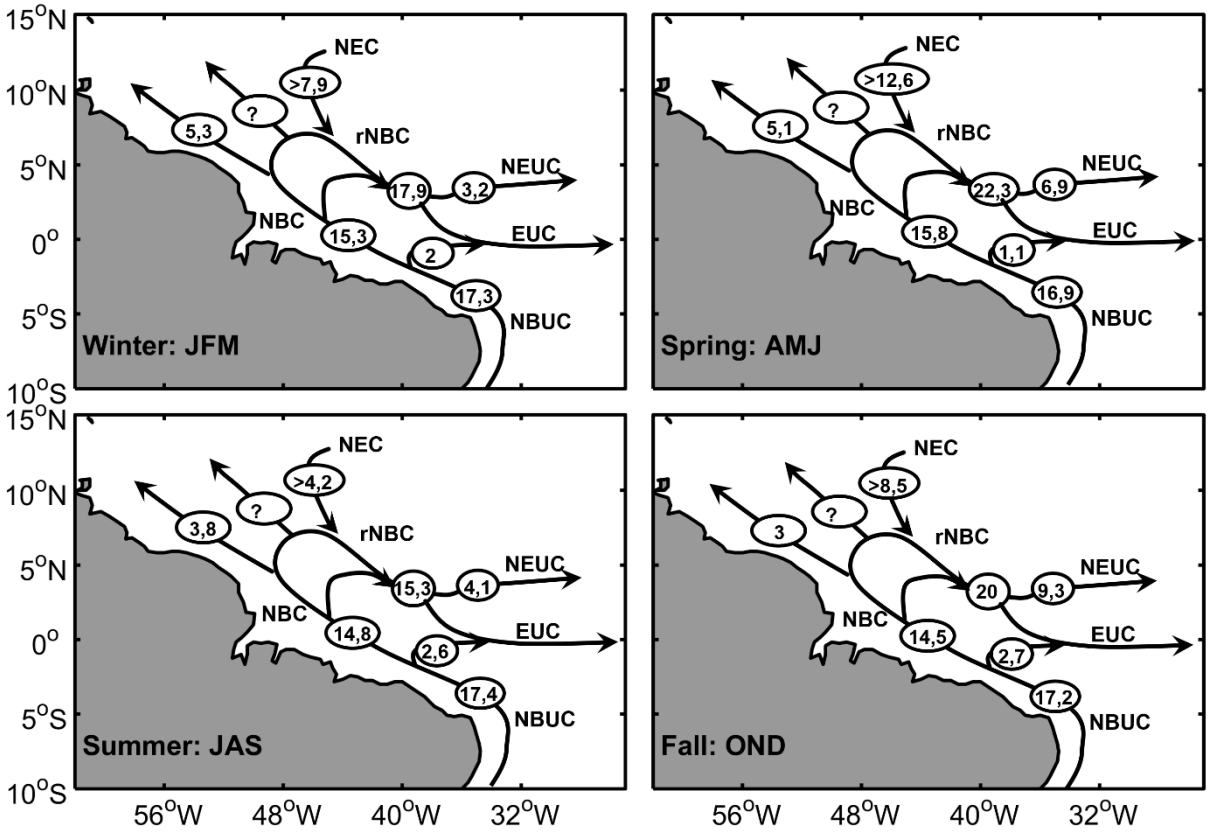

Source: The author (2022).

Figure 34. Schematic representation of the North brazil Current (NBC) transport along its pathway and the repartition of this transport this transport toward the North Equatorial Undercurrent (NEUC) and the Equatorial Undercurrent (EUC) in the thermocline layer (100–350 m depth) during the boreal seasons. Seasonal NBC transport values are calculated from GLORYS12V1 reanalysis with the same sections used for Figure 33. Region of the NBC rings, where the transports are not calculated are labelled by question marks; and the incoming North Brazil Undercurrent (NBUC) transport and the additional transport coming north, probably from the North Equatorial Current (NEC) are also mentioned and schematized. The possible surplus of transport to the NBC retroflected branch (rNBC), coming from north probably via the North Equatorial Current (NEC) is also mentioned considering conservation of the transport if the ring transports are assumed to be null.

7 SYNTHESIS OF THE KNOWLEDGE, CONCLUSIONS AND PERSPECTIVES

The tropical Atlantic western boundary is one the most dynamic region of world ocean by connecting several zonal and meridional surface and subsurface currents which dispatch water mass, heat and salt in the whole basin. Its two main upper layer currents are the North Brazil Current (NBC) and the North Equatorial Countercurrent (NECC) because of their strength and impact on the whole basin. First, the NBC is the continuity of the North Brazil Underurrent (NBUC) and represents one of the routes of the return branch of the Atlantic overturning circulation (AMOC) by carrying warm waters from the southern to northern hemisphere (Talley 2003; Ganachaud 2003; Lumpkin and Speer 2003). And second the NECC which is an eastward current redistributes at the surface, the heat and salt carried by the NBC to the eastern and northern basins. The whole basin witnesses strong interactions with atmosphere which affect its regional climate, the precipitations, and the currents variability, especially at seasonal, interannual and even decadal timescale (Chang et al, 2006). The main purpose of this thesis was to give a more attentive look to the western boundary currents by analysing altimetry-derived satellite data and GLORYS12V1 reanalysis from a common time period of 25 years, complemented with 15 sections of acoustic Doppler current profiler data collected during the Prediction and Research Moored Array in the Tropical Atlantic program cruises maintained by Brazil (PIRATA-BR) and drifter data. The focus of our studies was on the seasonal and the interannual variability of the currents, and the first goal was to select individual sections crossing the main currents in order to also follow their spatial variability and propose an updated seasonal map of the circulation. The second goal was to investigate the role of the winds and the Atlantic climate modes on the current branches at each location.

To start, the ADCP data from PIRATA-BR and CAMADAS-FINAS III cruises were processed, and compared with the GLORYS12V1 reanalysis at 38°W. The GLORYS12V1 reanalysis was also compared to the drifter's currents climatology data in the whole basin. Both comparisons helped to check the ability of the reanalysis to the reproduce the two-core structure of the NECC in order to confirm its usefulness which has been already proven in the southern hemisphere. After reassessing the GLORYS12V reanalysis, it was used to investigate the seasonal and interannual variability of the two-core structure of the NECC at 38°W over the 1993-2018 period. Ours results showed that, at 38°W, the NECC cycle starts in June when the North Equatorial Undercurrent (NEUC) and the Equatorial Under Current (EUC) rise at the surface, then grows and migrates northward under the influence of the wind stress curl until August. From July-August, a northern core appears, grows, and moves northward creating a

second branch which extends deeply and finally separates from the southern branch in November. From November, the northern branch continues migrating northward and decays to almost disappear during boreal spring. After the separation of the northern branch, the southern branch also migrates northward until June of the following year when the new brand NECC starts developing and growing. This new sNECC finally merges with the former in July to maintain a new cycle. To identify the limit between both branches of the NECC, its velocity field has been averaged in the first 100 m depth (considered as the mean depth of the thermocline in the western boundary), and the location of the two core is represented by the two highest local maxima separated by the lowest local minimum. The location of each local maxima corresponds exactly to the core latitude of the vertical structure of each branch. The limit between both branches is identified as the latitude corresponding to the lowest minimum which is negative for separated branches and positive for non-separated branches. The investigations of the seasonal variability of the transport of both branches show that they depict different annual cycles influenced by the remote wind stress curl (WSC) strength flowing in the region bounded by 6°S– 16°N and 0°–30°W. The northern branch (nNECC) transport is almost null the first half of the year, and is maximum, one month later the maximum wind stress curl (WSC) strength in August while the southern core (sNECC) transport is minimum in May and maximum in October, two months later the maximum of WSC strength. These delays are consistent with the response time of the upper ocean to the wind stress curl variability in the western boundary (Garzoli and Katz, 1983) and correspond to the travel time of Rossby waves propagating from Africa coast to the NECC region in the WB (Fonseca et al., 2004, Urbano et al., 2006). The investigation of the interannual variability shows that the positive transport anomalies of the NECC might be associated to the opposite phases of the Atlantic meridional mode (AMM) and the Atlantic zonal mode (AZM) while the negative anomalies might be associated to the same phases of both modes or an AMM phase with a neutral AZM phase.

The analysis of the altimetry-derived data has been done by considering 6 sections crossing at least one time the NBC, its retroflected branch (rNBC), the retroflection at the frontier between the NBC and the rNBC (NBCR), the NECC and the northern and the central branches of the Southern Equatorial Current (nSEC and cSEC, respectively). The analysis of the cross-sections allowed to identify some new features of the currents and confirm once more the two-core structure of the NECC, well developed during the second half of the year. It has been found that, south of the equator, the amplitude of the NBC depicts the same seasonal variability as cSEC, with minimum (maximum) amplitudes during boreal fall (spring). Unlike, in the northern hemisphere, its annual cycle and that of all the currents, except for the NBC

flowing toward the Guyana coast and the nSEC is reversed. The continuity of the NBC toward the Guyana coast presents the same seasonal cycle as for the currents in the southern hemisphere. The nSEC shows different cycles at each location. In the northern hemisphere, the annual cycles are associated with the wind variability, but with 3-4 months' time delay relatively to the remote wind stress curl strength. This delay was explained by the importance of the lateral diffusion known near to the western boundary and/or the mesoscale activities in the WB. We also found that the NBC show two retroflection regions during the second half of the year, from September to December. The southern retroflection flow is intense in October and merges later with the northern one to form a unique retroflection flow from December to September. The mean locations of the maximum velocity of the southern and the northern flows are 4.7°N±0.8° and 7.9°N±0.8°, respectively. It has been also found that the NECC cycle at 32°W starts one month earlier than at 42°N. In the equatorial region, we found a surface eastward flow called X which is fed by the rNBC in the upper layer during boreal spring, and engages a cyclonic circulation between 0°-5°N, 35°-45°W. The amplitude of the eastward surface flow decreases toward the east and shows a similar cycle to the Equatorial Undercurrent (EUC) in the tropical Atlantic. The year-to-year variations of the the currents amplitude shows possible associations of the interannual anomalies of the NBC with the AMM phases with two opposite scenarios depending on the location of the NBC. At 42°W, the interannual variability of the NECC's amplitude/core location, and the nSEC's amplitude also appear to be associated to the AMM phases while they are associated to the AZM phases at 32°W.

To investigate the vertical distribution of the currents and their transport at the 6 sections location used for the altimetry data analysis, the same GLORYS12V1 sections have been extracted, and three new sections have been added for a better description of the currents and their transports. Two of the new sections are located in the equatorial region to investigate what happens between 2°S and 2°N (Seq1 and Seq2) and the third one is the meridional sections located at 38°W between 0°-15°N. For our investigations, we have considered two layers: the upper layer (0-100m) and the thermocline layer (100-350 m). The vertical structure analysis of the currents confirms the presence of the two NBC retroflection regions and the two-core structure of the NECC found with the altimetry data in the upper layer. In the thermocline layer, we also found a NBC retroflection which is present thoughout the year with a maximum velocity centered between 3°-6°N. The annual cycle of the NBC transport in the upper layer also confirms the results of the altimetry-derived currents data. It has been found that, south of the equator, the NBC transport is influenced by the cSEC variability, but also by the NBUC variability. Both data show maximum/minimum NBC values in boreal spring/fall while in the

northern hemisphere, the NBC cycle is reversed due to the nSEC inputs and the wind influence. We found that the strengthening of the NBC before the equator during boreal spring gives rise to an equatorial retroflexion within the 0-100m between 0°-2°N which combines with the rNBC to constrain the nSEC to the east, and finally create a cyclonic circulation with the remaining nSEC branch to the east. This cyclonic circulation process is established when NBC transport south of the equator reaches its maximum transport due the intensification of both the NBUC and the cSEC which led to the equatorial retroflection between 0°-2°N. Further north of the equatorial region, the rNBC is in phase with the NBC before the retroflection and connects directly with the NECC except during boreal spring.

In thermocline layer, the transport does not vary to much between 3°-5°S. We found two NBC retroflection regions thorough the year, one in the southern hemisphere and the other in the northern hemisphere. The first one flow is weaker relatively to the second but strengthens during the second half of the year, with the larger values 2 to 4 month later the WSC strength and the negative WSC maxima in the eastern basin when the ITCZ is at its northernmost location. Unlike in the upper layer, the rNBC which supplies the NEUC and the EUC seems to be strongly impacted by the NEC which highly increases its transport throughout the year. The maximum input is found during boreal spring and fall. The EUC transport climatology also shows an increase during the same period whereas the NEUC maximum occurs during boreal fall. During our investigations, we found that, south of the equator, the SEUC is surely supplies the recirculation flow of the cSEC throughout the year with a higher contribution during the second half of the year. However, the positive difference of transport between the recirculation of the cSEC and the SEUC at 32°W suggests that the SEUC might also be supplied by the NBUC south of 5°S.

This study highlights the new aspects of the seasonal western boundary circulation by using the gridded altimetry-derived satellite data and GLORYS12V1 reanalysis from which different sections crossing the currents have been extracted to carry out our study. The interannual variavility of the currents amplitude in the whole basin also shows interesting results related to the tropical Atlantic climate modes (ACM) which can be deepen by investigating the interannual variability of the current transports at different locations as initiated at 38°W. For future steps the investigation of the interannual variability of the currents volume transport in the whole tropical Atlantic is feasible. Other study can be also conducted to understand for instance, the influence of the cyclonic circulation found in the equatorial region during boreal spring on the biogeochemistry process in its surrounding regions. Since we also found a dominant intraseasonal signal in western boundary, another step would also be

to investigate the intraseasonal variability of the Atlantic western boundary. The future satellites missions like SWOT (Surface Water and Ocean and Topical) would be helpful by providing more improved and newer database with good spatial and temporal resolution to highlights the intraseasonal variability of western boundary. The oceanographic programs like PIRATA-BR, he AMOZOMIX and ABRAÇOS would be always crucial to qualify the numerical model outputs and improve their quality by performing assimilations.

REFERENCES

Aguedjou, H. M. A., Dadou, I., Chaigneau, A., Morel, Y., & Alory, G. (2019). Eddies in the Tropical Atlantic Ocean and their seasonal variability. *Geophysical Research Letters*, *46*(21), 12156-12164. https://doi.org/10.1029/2019gl083925.

Araujo, M., Limongi, C., Servain, J., Silva, M., Leite, F. S., Veleda, D., & Lentini, C. A. D. (2011). Salinity-induced mixed and barrier layers in the southwestern tropical Atlantic Ocean off the northeast of Brazil. *Ocean Science, 7(1), 63–73.* doi:10.5194/os-7-63-2011.

Araujo, M., Noriega C., Hounsou-Gbo, G. A., Veleda, D., Araujo, J., Bruto, L., et al. (2017). A Synoptic Assessment of the Amazon River-Ocean Continuum during Boreal Autumn: From Physics to Plankton Communities and Carbon Flux. *Frontiers in Microbiology*. doi: 10.3389/fmicb.2017.01358.

Araujo, M., Dimoune, D. M., Trotte-Duhá, J., Nobre, P., Rodrigues, R., Cotrim, L., et al. (2021). Brazilian PIRATA cruises: S-ADCP data. *SEANOE*. https://doi.org/10.17882/80771.

Araujo, M., Dimoune, D. M., Noriega, C., Hounsou-Gbo, G. A., Veleda, D., Araujo, J., et al. (2021). Camadas Finas III - BR cruise: S-ADCP data. *SEANOE*. https://doi.org/10.17882/80828.

Arbic, B. K., Scott, R. B., Chelton, D. B., Richman, J. G., & Shriver, J. F. (2012). Effects of stencil width on surface ocean geostrophic velocity and vorticity estimation from gridded satellite altimeter data. *Journal of Geophysical Research: Oceans*, *117*(C3). https://doi.org/10.1029/2011jc007367.

Aroucha, L. C., Veleda, D., Lopes, F. S., Tyaquiçã, P., Lefèvre, N., & Araujo, M. (2020). Intra- and Inter-annual variability of NBC rings using AMEDA algorithm: observations from 1993 to 2016. *Journal of Geophysical Research: Oceans*. doi:10.1029/2019jc015921.

Artana, C., Lellouche, J.-M., Sennéchael, N., & Provost, C. (2018). The Open-Ocean Side of the Malvinas Current in Argo Floats and 24 Years of Mercator Ocean High-Resolution (1/12) Physical Reanalysis. *Journal of Geophysical Research: Oceans*, 123(11), 8489–8507. doi:10.1029/2018jc014528.

Artana, C., Provost, C., Lellouche, J., Rio, M., Ferrari, R., & Sennéchael, N. (2019). The Malvinas Current at the Confluence With the Brazil Current: Inferences From 25 Years of Mercator Ocean reanalysis. *Journal of Geophysical Research: Oceans*. doi:10.1029/2019jc015289.

Athie, G., & Marin, F. (2008). Cross-equatorial structure and temporal modulation of intraseasonal variability at the surface of the tropical Atlantic Ocean. *Journal of Geophysical Research: Oceans*, *113*(C8).

Assunção, R. V., Silva, A. C., Roy, A., Bourlès, B., Henrique S. Silva, C., Ternon, J.-F., … Bertrand, A. (2020). 3D characterisation of the thermohaline structure in the southwestern tropical Atlantic derived from functional data analysis of in situ profiles. *Progress in Oceanography, 102399.* doi:10.1016/j.pocean.2020.10239.

Barnier B., Blaker A.T., Biatosch A., Böning C.W., Coward A., Deshayes J., et al. (2014). DRAKKAR: developing high resolution ocean components for European Earth system models. CLIVAR Exchange, 65 - 19(2), 18-21. Open Access version : https://archimer.ifremer.fr/doc/00326/43698/.

Bourles, B., Molinari, R. L., Johns, E., Wilson, W. D., & Leaman, K. D. (1999). Upper layer currents in the western tropical North Atlantic (1989–1991). *Journal of Geophysical Research: Oceans*, *104*(C1), 1361-1375. https://doi.org/10.1029/1998jc9000250.

Bourlès, B., Gouriou, Y., & Chuchla, R. (1999). On the circulation in the upper layer of the western equatorial Atlantic. *Journal of Geophysical Research: Oceans*, 104 (C9), 21151-21170. doi: 10.1029/1999jc900058.

Bourlès, B., Lumpkin, R., McPhaden, M. J., Hernandez, F., Nobre, P., Campos, E., et al. (2008). The PIRATA program: History, Acomplishments, and Future Directions. *Bulletin of the American Meteorological Society* , 89 (8), 1111-1125. doi: 10.1175/2008BAMS2462.1.

Bourlès, B., Araujo, M., McPhaden, M. J., Brandt, P., Foltz, G. R., Lumpkin, R., et al. (2019). PIRATA: A Sustained Observing System for Tropical Atlantic Climate Research and Forecasting. *Earth and Space Science*. doi: 10.1029/2018EA000428.

Brandt, P., Schott, F. A., Provost, C., Kartavtseff, A., Hormann, V., Bourlès, B., & Fischer, J. (2006). Circulation in the central equatorial Atlantic: Mean and intraseasonal to seasonal variability. *Geophysical Research Letters*, *33*(7). https://doi.org/10.1029/2005gl025498.

Brandt, P., Caniaux, G., Bourles, B., Lazar, A., Dengler, M., Funk, A., ... & Marin, F. (2011). Equatorial upper-ocean dynamics and their interaction with the West African monsoon. *Atmospheric Science Letters*, *12*(1), 24-30.

Brandt, P., Claus, M., Greatbatch, R. J., Kopte, R., Toole, J. M., Johns, W. E., & Böning, C. W. (2016). Annual and semiannual cycle of equatorial Atlantic circulation associated with basin-mode resonance. *Journal of Physical Oceanography*, *46*(10), 3011-3029. https://doi.org/10.1175/jpo-d-15-0248.1.

Breugem, W.-P., Chang, P., Jang, C. J., Mignot, J., & Hazeleger, W. (2008). Barrier layers and tropical Atlantic SST biases in coupled GCMs. *Tellus A: Dynamic Meteorology and Oceanography, 60(5), 885–897.* doi:10.1111/j.1600-0870.2008.00343.x.

Burmeister K., Lübbecke, J. F.,Brandt, P., & Duteil, O. (2019). Interannual variability of the Atlantic North Equatorial Undercurrent and its impact on oxygen. *Journal of Geophysical Research: Oceans*, 124, 2348–2373. https://doi.org/10.1029/2018JC014760.

Cabanes, C., Grouazel, A., von Schuckmann, K., Hamon, M., Turpin, V., Coatanoan, C., et al. (2013). The CORA dataset: validation and diagnostics of in-situ ocean temperature and salinity measurements. *Ocean Science*, 9 (1), 1-18. doi: 10.5194/os-9-1-2013.

Cabos, W., de la Vara, A., & Koseki, S. (2019). Tropical Atlantic Variability: Observations and Modeling. *Atmosphere*, 10 (9), 502.

Carton, J. A., Cao X., Giese, B. S., & Silva, A. M. D. (1996). Decadal and Interannual SST Variability in the Tropical Atlantic Ocean. Journal of *Physical Oceanography*, 26 (7), 1165-1175. doi: 10.1175/1520-0485(1996)026<1165:Daisvi>2.0.Co;2.

Castellanos, P., Pelegrí, J. L., Campos, E. J. D., Rosell-Fieschi, M., & Gasser, M. (2015). Response of the surface tropical Atlantic Ocean to wind forcing. *Progress in Oceanography*, 134271-292. doi: 10.1016/j.pocean.2015.02.005.

Chang, P., Saravanan, R., Ji, L., & Hegerl, G. C. (2000). The effect of local sea surface temperatures on atmospheric circulation over the tropical Atlantic sector. *Journal of Climate*, *13*(13), 2195-2216.

Chang, P., Yamagata, T., Schopf, P., Behera, S. K., Carton, J., Kessler, W. S., et al. (2006). Climate Fluctuations of Tropical Coupled Systems—The Role of Ocean Dynamics. *Journal of Climate*, 19 (20), 5122-5174. doi: 10.1175/jcli3903.1.

Chiang, J. C., & Vimont, D. J. (2004). Analogous Pacific and Atlantic meridional modes of tropical atmosphere–ocean variability. *Journal of Climate*, *17*(21), 4143-4158.

Cleveland, W. S., & Devlin, S. J. (1988). Locally Weighted Regression: An Approach to Regression Analysis by Local Fitting. *Journal of the American Statistical Association*, 83 (403), 596-610. doi: 10.1080/01621459.1988.10478639.

Coles, V. J., Brooks, M. T., Hopkins, J., Stukel, M. R., Yager, P. L., & Hood, R. R. (2013). The pathways and properties of the Amazon River Plume in the tropical North Atlantic Ocean. *Journal of Geophysical Research: Oceans*, 118 (12), 6894-6913. doi: 10.1002/2013jc008981.

Cochrane, J. D., Kelly Jr, F. J., & Olling, C. R. (1979). Subthermocline countercurrents in the western equatorial Atlantic Ocean. *Journal of Physical Oceanography*, *9*(4), 724-738. https://doi.org/10.1175/1520-0485(1979)009<0724:scitwe>2.0.co;2.

Crespo, L. R., Keenlyside, N., & Koseki, S. (2019). The role of sea surface temperature in the atmospheric seasonal cycle of the equatorial Atlantic. *Climate Dynamics*, *52*(9), 5927-5946.

Davidson, F., Alvera-Azcárate, A., Barth, A., Brassington, G. B., Chassignet, E. P., Clementi, E., et al. (2019). Synergies in Operational Oceanography: The Intrinsic Need for Sustained Ocean Observations. *Frontiers in Marine Science*, 6450. doi: 10.3389/fmars.2019.00450.

de Boyer Montégut, C., Madec, G., Fischer, A. S., Lazar, A., & Iudicone, D. (2004). Mixed layer depth over the global ocean: An examination of profile data and a profile-based climatology. *Journal of Geophysical Research: Oceans*, *109*(C12).

de Boyer Montégut, C., Mignot, J., Lazar, A., & Cravatte, S. (2007). Control of salinity on the mixed layer depth in the world ocean: 1. General description. *Journal of Geophysical Research: Oceans*, *112*(C6).

Diakhaté, M., Lazar, A., de Coëtlogon, G., & Gaye, A. T. (2018). Do SST gradients drive the monthly climatological surface wind convergence over the tropical Atlantic?. *International Journal of Climatology*, *38*, e955-e965.

Didden, N., & Schott, F. (1992). Seasonal variations in the western tropical Atlantic: Surface circulation from Geosat altimetry and WOCE model results. *Journal of Geophysical Research: Oceans*, 97 (C3), 3529-3541. doi: 10.1029/91jc02860.

Dossa, A., Da-Allada, C., Herbert, G., & Bourlès, B. (2019). Seasonal cycle of the salinity barrier layer revealed in the northeastern Gulf of Guinea. *African Journal of Marine Science*, 41(2), 163–175. doi:10.2989/1814232x.2019.161661.

Dossa, A. N., Silva, A. C., Chaigneau, A., Eldin, G., Araujo, M., & Bertrand, A. (2021). Near-surface western boundary circulation off Northeast Brazil. *Progress in Oceanography*, *190*, 102475. https://doi.org/10.1016/j.pocean.2020.102475.

Drévillon, M., Régnier, C., Lellouche, J.-M., Garric, G., Bricaud, C., & Hernandez, O. (2018). QUALITY INFORMATION DOCUMENT For Global Ocean Reanalysis Products GLOBAL-REANALYSIS-PHY-001-030 v1.2. (CMEMS-GLO-QUID-001-030), ed. by Mercator Ocean International, pub. by C. M. E. M. Service, 48 pp pp. [Available at http://marine.copernicus.eu/documents/QUID/CMEMS-GLO-QUID-001-030.pdf.]

Egbert, G. D., & Erofeeva, S. Y. (2002). Efficient inverse modeling of barotropic ocean tides. *Journal of Atmospheric and Oceanic technology*, *19*(2), 183-204. Doi: doi: 10.1175/1520-0426(2002)019<0183:EIMOBO>2.0.CO;2.

Enfield, D. B., & Mayer, D. A. (1997). Tropical Atlantic sea surface temperature variability and its relation to El Niño-Southern Oscillation. *Journal of Geophysical Research: Oceans*, *102*(C1), 929-945.

Enfield, D. B., Mestas-Nuñez, A. M., Mayer, D. A., & Cid-Serrano, L. (1999). How ubiquitous is the dipole relationship in tropical Atlantic sea surface temperatures? *Journal of Geophysical Research: Oceans*, 104 (C4), 7841-7848. doi: 10.1029/1998jc900109.

Ffield, A. (2005). North Brazil current rings viewed by TRMM Microwave Imager SST and the influence of the Amazon Plume. *Deep Sea Research Part I: Oceanographic Research Papers*, *52*(1), 137-160. https://doi.org/10.1016/j.dsr.2004.05.013.

Foltz, G. R., Semyon, A. G., & Carton, J. A. (2003). Seasonal mixed layer heat budget of the tropical Atlantic Ocean. *Journal of Geophysical Research*, 108(C5). doi:10.1029/2002jc001584.

Foltz, G. R., & McPhaden, M. J. (2006). The Role of Oceanic Heat Advection in the Evolution of Tropical North and South Atlantic SST Anomalies*. *Journal of Climate*, 19(23), 6122–6138. doi:10.1175/jcli3961.

Foltz, G. R., & McPhaden, M. J. (2010). Interaction between the Atlantic meridional and Niño modes. *Geophysical Research Letters*, *37*(18).

Foltz, G. R., McPhaden, M. J., & Lumpkin, R. (2012). A Strong Atlantic Meridional Mode Event in 2009: The Role of Mixed Layer Dynamics. *Journal of Climate*, 25 (1), 363-380. doi: 10.1175/JCLI-D-11-00150.1.

Foltz, G. R., Schmid, C., & Lumpkin, R. (2015). Transport of surface freshwater from the equatorial to the subtropical North Atlantic Ocean. *Journal of Physical Oceanography*, *45*(4), 1086-1102.

Foltz, G. R., Hummels, R., Dengler, M., Perez, R. C., & Araujo, M. (2020). Vertical turbulent cooling of the mixed layer in the Atlantic ITCZ and trade wind regions. *Journal of Geophysical Research: Oceans*, *125*(2), e2019JC015529.

Fonseca, C. A., Goni, G. J., Johns, W. E., & Campos, E. J. D. (2004). Investigation of the North Brazil Current retroflection and North Equatorial Countercurrent variability. *Geophysical Research Letters*, 31 (21). doi: 10.1029/2004gl020054.

Fox-Kemper, B., Adcroft, A., Böning, C. W., Chassignet, E. P., Curchitser, E., Danabasoglu, G., et al. (2019). Challenges and Prospects in Ocean Circulation Models. *Frontiers in Marine Science*, 6 (65). doi: 10.3389/fmars.2019.00065.

Fratantoni, D. M., Johns, W. E., Townsend, T. L., & Hurlburt, H. E. (2000). Low-latitude circulation and mass transport pathways in a model of the tropical Atlantic Ocean. *Journal of Physical Oceanography*, *30*(8), 1944-1966. https://doi.org/10.1175/15200485(2000)030<1944:LLCAMT>2.0.CO;2.

Gaillard, F., Reynaud, T., Thierry, V., Kolodziejczyk, N., & von Schuckmann, K. (2016). In Situ–Based Reanalysis of the Global Ocean Temperature and Salinity with ISAS: Variability of the Heat Content and Steric Height. *Journal of Climate*, 29 (4), 1305-1323. doi: 10.1175/jcli-d-15-0028.1.

Garzoli, S. L., & Katz, E. J. (1983). The Forced Annual Reversal of the Atlantic North Equatorial Countercurrent. *Journal of Physical Oceanography*, 13 (11), 2082-2090. doi: 10.1175/1520-0485(1983)013<2082:Tfarot>2.0.Co;2.

Garzoli, S., & Richardson, P. L. (1989). Low-frequency meandering of the Atlantic North Equatorial Countercurrent. *Journal of Geophysical Research: Oceans*, 94 (C2), 2079-2090. doi: 10.1029/JC094iC02p02079.

Garzoli, S. L. (1992). The Atlantic North Equatorial Countercurrent: Models and observations. *Journal of Geophysical Research: Oceans*, 97 (C11), 17931-17946. doi: 10.1029/92jc01363.

Garzoli, S. L., Ffield, A., & Yao, Q. (2003). North Brazil Current rings and the variability in the latitude of retroflection. In *Elsevier Oceanography Series* (Vol. 68, pp. 357-373). Elsevier. https://doi.org/10.1016/s0422-9894(03)80154-x.

Garzoli, S. L., Ffield, A., Johns, W. E., & Yao, Q. (2004). North Brazil Current retroflection and *transports. Journal of Geophysical Research: Oceans*, 109 (C1). doi: 10.1029/2003jc001775.

Garzoli, S. L., & Matano, R. (2011). The South Atlantic and the Atlantic meridional overturning circulation. *Deep Sea Research Part II: Topical Studies in Oceanography*, *58*(17-18), 1837-1847. https://doi.org/10.1016/j.dsr2.2010.10.063.

Gill, A. E., & Adrian, E. (1982). *Atmosphere-ocean dynamics* (Vol. 30). Academic press. https://doi.org/10.1016/s0074-6142(08)60025-x.

Góes, M., & Wainer, I. (2003). Equatorial currents transport changes for extreme warm and cold events in the Atlantic Ocean. *Geophysical Research Letters*, *30*(5). https://doi.org/10.1029/2002gl015707.

Goes, M., Molinari, R., da Silveira, I., & Wainer, I. (2005). Retroflections of the north brazil current during february 2002. *Deep Sea Research Part I: Oceanographic Research Papers*, *52*(4), 647-667. https://doi.org/10.1016/j.dsr.2004.10.010.

Goni, G. J., & Johns, W. E. (2001). A census of North Brazil Current Rings observed from TOPEX/POSEIDON altimetry: 1992–1998. *Geophysical Research Letters*, 28 (1), 1-4. doi: 10.1029/2000gl011717.

Goni, G. J., & Johns, W. E. (2003). Synoptic study of warm rings in the North Brazil Current retroflection region using satellite altimetry. In *Elsevier Oceanography Series* (Vol. 68, pp. 335-356). Elsevier. https://doi.org/10.1016/s0422-9894(03)80153-8.

Good, S. A., Martin, M. J., & Rayner, N. A. (2013). EN4: Quality controlled ocean temperature and salinity profiles and monthly objective analyses with uncertainty estimates. *Journal of Geophysical Research: Oceans*, 118 (12), 6704-6716. doi: 10.1002/2013jc009067.

Gordon, A. L. (1986). Interocean exchange of thermocline water. *Journal of Geophysical Research: Oceans*, *91*(C4), 5037-5046.

Ham, Y. G., Kug, J. S., & Park, J. Y. (2013). Two distinct roles of Atlantic SSTs in ENSO variability: North tropical Atlantic SST and Atlantic Niño. *Geophysical Research Letters*, *40*(15), 4012-4017.

Hazeleger, W., & De Vries, P. (2003). Fate of the Equatorial Undercurrent in the Atlantic. In *Elsevier oceanography series* (Vol. 68, pp. 175-191). Elsevier. https://doi.org/10.1016/s0422-9894(03)80146-0.

Hazeleger, W., de Vries, P., & Friocourt, Y. (2003). Sources of the Equatorial Undercurrent in the Atlantic in a high-resolution ocean model. *Journal of Physical Oceanography*, *33*(4), 677-693. https://doi.org/10.1175/1520-0485(2003)33<677:soteui>2.0.co;2.

Hisard, P., & Hénin, C. (1987). Response of the equatorial Atlantic Ocean to the 1983–1984 wind from the Programme Français Océan et Climat dans l'Atlantique Equatorial cruise data set. *Journal of Geophysical Research: Oceans*, *92*(C4), 3759-3768. https://doi.org/10.1029/jc092ic04p03759.

Hormann, V., & Brandt, P. (2007). Atlantic Equatorial Undercurrent and associated cold tongue variability. *Journal of Geophysical Research: Oceans*, 112 (C6). doi: 10.1029/2006jc003931.

Hormann, V., & Brandt, P. (2009). Upper equatorial Atlantic variability during 2002 and 2005 associated with equatorial Kelvin waves. *Journal of Geophysical Research*, *114(C3).* doi:10.1029/2008jc005101.

Hormann, V., Lumpkin, R., & Foltz, G. R. (2012). Interannual North Equatorial Countercurrent variability and its relation to tropical Atlantic climate modes. *Journal of Geophysical Research: Oceans*, 117 (C4). doi: 10.1029/2011jc007697.

Hounsou-Gbo, G. A., Araujo, M., Bourlès, B., Veleda, D., & Servain, J. (2015). Tropical Atlantic contributions to strong rainfall variability along the Northeast Brazilian coast. *Advances in meteorology*, *2015*.

Hounsou-Gbo G. A., Servain, J, Araujo, M, Martins, E. S., Bourlès, B. & Canaix, G. (2016). Oceanic Indices for Forecasting Seasonal Rainfall over the Northern Part of Brazilian Northeast. *American Journal of Climate Change*, 5: 261-274.

Jochum, M., & Malanotte-Rizzoli, P. (2003). On the generation of North Brazil Current rings. *Journal of Marine Research*, 61, 147- 173.

Jochum, M., Malanotte-Rizzoli, P., & Busalacchi, A. (2004). Tropical instability waves in the Atlantic Ocean. *Ocean Modelling*, 7(1-2), 145–163. doi:10.1016/s1463-5003(03)00042-8.

Johns, W. E., Lee, T. N., Schott, F. A., Zantopp, R. J., & Evans, R. H. (1990). The North Brazil Current retroflection: Seasonal structure and eddy variability. *Journal of Geophysical Research*, 95(C12), 22103. doi:10.1029/jc095ic12p22103.

Johns, W. E., Lee, T. N., Beardsley, R. C., Candela, J., Limeburner, R., & Castro, B. (1998). Annual Cycle and Variability of the North Brazil Current. *Journal of Physical Oceanography*, 28(1), 103–128. doi:10.1175/1520-0485(1998)028<0103:acavot>.

Jouanno, J., Hernandez, O., & Sanchez-Gomez, E. (2017). Equatorial Atlantic interannual variability and its relation to dynamic and thermodynamic processes. *Earth System Dynamics*, *8*(4), 1061-1069.

Keenlyside, N. S., & Latif, M. (2007). Understanding equatorial Atlantic interannual variability. *Journal of climate*, *20*(1), 131-142.

Kermabon, C., Lherminier, P., Le bot, P., & Gaillard, F. (2018). Chaine Automatisée de Suivi des Courantomètres Acoustiques Doppler Embarqués. CASCADE V7.2: Logiciel de validation et de visualisation des mesures ADCP de coque. Documentation utilisateur et maintenance. (ODE/LOPS 18), edited by Ifremer, Brest, France, 115 pp. [Available at ftp://ftp.ifremer.fr/ifremer/lpo_permanents/cascade/CASCADE_V72_V2.pdf.]

Kushnir, Y., Robinson, W. A., Chang, P., & Robertson, A. W. (2006). The physical basis for predicting Atlantic sector seasonal-to-interannual climate variability. *Journal of Climate*, *19*(23), 5949-5970.

Large, W. G., & Pond, S. (1981). Open ocean momentum flux measurements in moderate to strong winds. *Journal of physical oceanography*, *11*(3), 324-336. https://doi.org/10.1175/1520-0485(1981)011<0324:oomfmi>2.0.co;2.

Lagerloef, G. S., Mitchum, G. T., Lukas, R. B., & Niiler, P. P. (1999). Tropical Pacific near-surface currents estimated from altimeter, wind, and drifter data. *Journal of Geophysical Research: Oceans*, *104*(C10), 23313-23326. https://doi.org/10.1029/1999jc900197.

Laurindo, L. C., Mariano, A. J., & Lumpkin, R. (2017). An improved near-surface velocity climatology for the global ocean from drifter observations. *Deep Sea Research Part I: Oceanographic Research Papers*, 12473-92. doi: 10.1016/j.dsr.2017.04.009.

Lellouche, J.-M., Greiner, E., Le Galloudec, O., Garric, G., Regnier, C., Drevillon, M., et al. (2018). Recent updates to the Copernicus Marine Service global ocean monitoring and forecasting real-time 1⁄12° high-resolution system. *Ocean Science*, 14 (5), 1093-1126. doi: 10.5194/os-14-1093-2018.

Lellouche, J.-M., Greiner, E., Bourdallé-Badie, R., Garric, G., Melet, A., Drévillon, M., et al. (2021). The Copernicus Global 1/12° Oceanic and Sea Ice GLORYS12 Reanalysis. *Frontiers in Earth Science*, 9 (585). doi: 10.3389/feart.2021.698876.

Lindzen, R. S. and Nigam, S. (1987). On the role of sea surface temperature gradients in forcing low-level winds and convergence in the tropics. *Journal of The Atmosphere Sciences*, 44, 2418-2436.

Lumpkin, R., & Garzoli, S. L. (2005). Near-surface circulation in the Tropical Atlantic Ocean. *Deep Sea Research Part I: Oceanographic Research Papers*, 52 (3), 495-518. doi: 10.1016/j.dsr.2004.09.001.

Ma, H. (1996). The dynamics of North Brazil Current retroflection eddies. *Journal of Marine Research*, *54*(1), 35-53.

Madec, G. (2008): NEMO ocean engine - Version 3.1. Note du Pôle de modélisation, (27), edited by Institut Pierre-Simon Laplace (IPSL), Paris, France1288-1619, 201 pp.

Marin, F., Caniaux, G., Bourlès B., Giordani, H., Gouriou, Y., & Key, E. (2009). Why were sea surface temperatures so different in the eastern equatorial Atlantic in June 2005 and 2006? *Journal of Physical Oceanography*, 39, 1416–1431, doi:10.1175/2008JPO4030.1.

Masson, S., & Delecluse, P. (2001). Influence of the Amazon River runoff on the tropical Atlantic. *Physics and Chemistry of the Earth, Part B: Hydrology, Oceans and Atmosphere*, 26(2), 137-142.

Merle, J. (1980). Variabilité thermique annuelle et interannuelle de l'océan Atlantique équatorial est. L'hypothèse d'un El Niño Atlantique. *Oceanologica Acta*, *3*(2), 209-220.

Metcalf, W. G., Voorhis, A. D., & Stalcup, M. C. (1962). The Atlantic Equatorial Undercurrent. *Journal of Geophysical Research, 67(6), 2499–2508.* doi:10.1029/jz067i006p02499.

Mignot, J., de Boyer Montégut, C., Lazar, A., & Cravatte, S. (2007). Control of salinity on the mixed layer depth in the world ocean: 2. Tropical areas. *Journal of Geophysical Research: Oceans*, *112*(C10).

Nof, D., & Pichevin, T. (1996). The retroflection paradox. *Journal of physical oceanography*, *26*(11), 2344-2358.

NRSC (2013). "OSCAT Wind stress and Wind stress curl products", Ocean Sciences Group, Earth and Climate Science Area, Hyderabad, India.

Okumura, Y., & Xie, S. P. (2004). Interaction of the Atlantic equatorial cold tongue and the African monsoon. *Journal of Climate*, *17*(18), 3589-3602.

Peterson, R. G., & Stramma, L. (1991). Upper-level circulation in the South Atlantic Ocean. *Progress in oceanography*, *26*(1), 1-73. https://doi.org/10.1016/0079-6611(91)90006-8.

Philander, S. G. H., & Pacanowski, R. C. (1986). The mass and heat budget in a model of the tropical Atlantic Ocean. *Journal of Geophysical Research: Oceans*, 91 (C12), 14212-14220. doi: 10.1029/JC091iC12p14212.

Poli, L., Artana, C., Provost, C., Sirven, J., Sennéchael, N., Cuypers, Y., & Lellouche, J. (2020). Anatomy of subinertial waves along the Patagonian shelf break in a 1/12° global operational model. *Journal of Geophysical Research: Oceans*. doi:10.1029/2020jc016549.

Provost, C., Arnault, S., Chouaib, N., Kartavtseff, A., Bunge, L., & Sultan, E. (2004). TOPEX/Poseidon and Jason equatorial sea surface slope anomaly in the Atlantic in 2002: Comparison with wind and current measurements at 23W. *Marine Geodesy*, *27*(1-2), 31-45. https://doi.org/10.1080/01490410490465274.

Pujol, M. I., Faugère, Y., Taburet, G., Dupuy, S., Pelloquin, C., Ablain, M., & Picot, N. (2016). DUACS DT2014: the new multi-mission altimeter data set reprocessed over 20 years. *Ocean Science*, *12*(5), 1067-1090. https://doi.org/10.5194/os-2015-110.

Rayner, N. A. A., Parker, D. E., Horton, E. B., Folland, C. K., Alexander, L. V., Rowell, D. P., ... & Kaplan, A. (2003). Global analyses of sea surface temperature, sea ice, and night marine air temperature since the late nineteenth century. *Journal of Geophysical Research: Atmospheres*, *108*(D14).

Reynolds, R. W., Rayner, N. A., Smith, T. M., Stokes, D. C., & Wang, W. (2002). An Improved In Situ and Satellite SST Analysis for Climate. *Journal of Climate*, 15 (13), 1609-1625. doi: 10.1175/1520-0442(2002)015<1609:Aiisas>2.0.Co;2.

Richardson, P. L., & Walsh, D. (1986). Mapping climatological seasonal variations of surface currents in the tropical Atlantic using ship drifts. *Journal of Geophysical Research: Oceans*, *91*(C9), 10537-10550. https://doi.org/10.1029/jc091ic09p10537.

Richardson, P. L., & Reverdin, G. (1987). Seasonal cycle of velocity in the Atlantic North Equatorial Countercurrent as measured by surface drifters, current meters, and ship drifts. *Journal of Geophysical Research: Oceans*, 92 (C4), 3691-3708. doi: 10.1029/JC092iC04p03691.

Rodrigues, R. R., Rothstein, L. M., & Wimbush, M. (2007). Seasonal variability of the South Equatorial Current bifurcation in the Atlantic Ocean: A numerical study. *Journal of Physical Oceanography*, *37*(1), 16-30. https://doi.org/10.1175/jpo2983.1.

Rosell-Fieschi, M., Pelegrí, J. L., & Gourrion, J. (2015). Zonal jets in the equatorial Atlantic Ocean. *Progress in Oceanography*, *130*, 1-18.

Salisbury, J., Vandemark, D., Campbell, J., Hunt, C., Wisser, D., Reul, N., & Chapron, B. (2011). Spatial and temporal coherence between Amazon River discharge, salinity, and light

absorption by colored organic carbon in western tropical Atlantic surface waters. *Journal of Geophysical Research: Oceans*, *116*(C7).

Saravanan, R., & Chang, P. (2004). Thermodynamic coupling and predictability of tropical sea surface temperature. *Washington DC American Geophysical Union Geophysical Monograph Series*, *147*, 171-180.

Schmitz Jr, W. J., & McCartney, M. S. (1993). On the north Atlantic circulation. *Reviews of Geophysics*, *31*(1), 29-49. https://doi.org/10.1029/92RG02583.

Schott, F. A., & Böning C. W. (1991). The WOCE model in the western equatorial Atlantic: Upper layer circulation. *Journal of Geophysical Research: Oceans*, 96 (C4), 6993-7004. doi: 10.1029/90jc02683.

Schott, F., Fischer, J., Reppin, J., & Send, U. (1993). On mean and seasonal currents and transports at the western boundary of the equatorial Atlantic. *Journal of Geophysical Research: Oceans*, *98*(C8), 14353-14368.

Schott, F. A., Stramma, L., & Fischer, J. (1995). The warm water inflow into the western tropical Atlantic boundary regime, spring 1994. *Journal of Geophysical Research: Oceans*, *100*(C12), 24745-24760. https://doi.org/10.1029/95jc02803.

Schott, F. A., Fischer, J., & Stramma, L. (1998). Transports and pathways of the upper-layer circulation in the western tropical Atlantic. *Journal of Physical Oceanography*, 28 (10), 1904-1928. doi: 10.1175/1520-0485(1998)028<1904:tapotu>2.0.co;2.

Schott, F. A., McCreary Jr, J. P., & Johnson, G. C. (2004). Shallow overturning circulations of the tropical-subtropical oceans. *Washington DC American Geophysical Union Geophysical Monograph Series*, *147*, 261-304. https://doi.org/10.1029/147gm15.

Schouten, M. W., Matano, R. P., & Strub, T. P. (2005). A description of the seasonal cycle of the equatorial Atlantic from altimeter data. *Deep Sea Research Partt I: Oceanographic Research Papers*, 52 (3), 477-493. doi: 10.1016/j.dsr.2004.10.007.

Servain, J., Picaut, J., & Busalacchi, A. J. (1985). Chapter 16 Interannual and Seasonal Variability of the Tropical Atlantic ocean depicted by Sixteen years of Sea-Surface Temperature and wind stress. *Elsevier Oceanography Series*, 211–237. doi:10.1016/s0422-9894(08)70712-8.

Servain, J. (1991). Simple climatic indices for the tropical Atlantic Ocean and some applications. *Journal of Geophysical Research: Oceans*, 96 (C8), 15137-15146. doi: 10.1029/91jc01046.

Servain, J., & Merle, J. (1993). Interannual climate variations over the tropical Atlantic Ocean. In *Prediction of interannual climate variations* (pp. 153-172). Springer, Berlin, Heidelberg.

Silva, M., Araujo, M., Servain, J., Penven, P., & Lentini, C. A. (2009). High-resolution regional ocean dynamics simulation in the southwestern tropical Atlantic. *Ocean Modelling*, *30*(4), 256-269. https://doi.org/10.1016/j.ocemod.2009.07.002.

Snowden, D. P., & Molinari, R. L. (2003). Subtropical cells in the Atlantic Ocean: An observational summary. *Elsevier Oceanography Series, 287–312.* doi:10.1016/s0422-9894(03)80151-4.

Storto, A., Alvera-Azcárate, A., Balmaseda, A., Barth, A., Chevallier, M., Counillon, F., et al. (2019). Ocean reanalyses: Recent advances and unsolved challenges. *Frontiers in Marine Science*, 6418. doi: 10.3389/fmars.2019.00418.

Stramma, L. (1991). Geostrophic transport of the South Equatorial Current in the Atlantic. *Journal of Marine Research*, *49*(2), 281-294.

Stramma, L., & Schott, F. A. (1999). The mean flow field of the tropical Atlantic Ocean. *Deep Sea Research Part II: Tropical Studies in Oceanography*, 46 (1-2), 279-303. doi: 10.1016/s0967-0645(98)00109-x.

Stramma, L., & England, M. (1999). On the water masses and mean circulation of the South Atlantic Ocean. *Journal of Geophysical Research: Oceans*, *104*(C9), 20863-20883. https://doi.org/10.1029/1999jc900139.

Schott, F. A., Dengler, M., Zantopp, R., Stramma, L., Fischer, J., & Brandt, P. (2005). The shallow and deep western boundary circulation of the South Atlantic at 5–11 S. *Journal of Physical Oceanography*, *35*(11), 2031-2053.

Stramma, L., S. Schmidtko, J. Luo, J. Hoolihan, M. Visbeck, D. Wallace, P. et al. (2012). Expansion of oxygen minimum zones may reduce available habitat for tropical pelagic fishes. *Nature Climate Change*, 2, 33-37, doi:10.1038/nclimate1304.

Sudre, J., Maes, C., & Garçon, V. (2013). On the global estimates of geostrophic and Ekman surface currents. *Limnology and Oceanography: Fluids and Environments*, *3*(1), 1-20. https://doi.org/10.1215/21573689-2071927.

Trenberth, K. E., Large, W. G., & Olson, J. G. (1990). The mean annual cycle in global ocean wind stress. *Journal of Physical Oceanography*, *20*(11), 1742-1760. doi: 10.1175/1520-0485(1990)0202.0.CO;2.

Tsuchiya, M. (1986). Thermostads and circulation in the upper layer of the Atlantic Ocean. *Progress in Oceanography*, *16*(4), 235-267.

Tuchen, F. P., Lübbecke, J. F., Brandt, P., & Fu, Y. (2020). Observed transport variability of the Atlantic Subtropical Cells and their connection to tropical sea surface temperature variability. *Journal of Geophysical Research: Oceans*, 125, e2020JC016592. https://doi.org/10.1029/2020JC016592.

Urbano, D. F., Jochum, M., & da Silveira, I. C. A. (2006). Rediscovering the second core of the Atlantic NECC. *Ocean Modelling*, 12 (1), 1-15. doi: 10.1016/j.ocemod.2005.04.003.

Urbano, D. F., De Almeida, R. A. F., & Nobre, P. (2008). Equatorial Undercurrent and North Equatorial Countercurrent at 38°W: A new perspective from direct velocity data. *Journal of Geophysical Research: Oceans*, 113 (C4). doi: 10.1029/2007jc004215.

Varona, H. L., Veleda, D., Silva, M., Cintra, M., & Araujo, M. (2019). Amazon River plume influence on Western Tropical Atlantic dynamic variability. *Dynamics of Atmospheres and Oceans*, (85) 1-15. doi: 10.1016/j.dynatmoce.2018.10.002.

Verdy, A., & Jochum, M. (2005). A note on the validity of the Sverdrup balance in the Atlantic North Equatorial Countercurrent. *Deep Sea Research Part I : Oceanographic Research Papers*, 52 (1), 179-188. doi: 10.1016/j.dsr.2004.05.014.

von Schuckmann, K., Brandt, P. & Eden, C. (2008). Generation of tropical instability waves in the Atlantic Ocean, *Journal of Geophysical Research,* 113, (C8), doi:10.1029/2007JC004712.

Wallace, J. M., & Hobbs, P. V. (1977). Atmosphere science-an introductory survey. *Atmosphere science-an introductory survey*, V.

Weingartner, T. J., & Weisberg, R. H. (1991). A description of the annual cycle in sea surface temperature and upper ocean heat in the equatorial Atlantic. *Journal of Physical Oceanography*, *21*(1), 83-96.

Xie, S. P. (2004). The shape of continents, air-sea interaction, and the rising branch of the Hadley circulation. In *The Hadley Circulation: Present, Past and Future* (pp. 121-152). Springer, Dordrecht.

Xie, S. P., & Carton, J. A. (2004). Tropical Atlantic variability: Patterns, mechanisms, and impacts. *Earth's Climate: The Ocean-Atmosphere Interaction, Geophys. Monogr*, *147*, 121-142.

Zebiak, S. E. (1993). Air–Sea Interaction in the Equatorial Atlantic Region. *Journal of Climate*, 6 (8), 1567-1586. doi: 10.1175/1520-0442(1993)006<1567:Aiitea>2.0.Co;2.

Zheng, Y., & Giese, B. S. (2009). Ocean heat transport in simple ocean data assimilation: Structure and mechanisms. *Journal of Geophysical Research: Oceans*, *114*(C11). https://doi.org/10.1029/2008jc005190.

APPENDIX A - INVESTIGATING OF THE TWO-CORE STRUCTURE OF THE ATLANTIC NORTH EQUATORIAL COUNTERCURRENT WITH THE GLORYS12V1 REANALYSIS

This appendix presents some of our results accepted to be published in the Journal of Tropical Oceanography.

Investigating of the two-core structure of the Atlantic North Equatorial Countercurrent with the GLORYS12V1 reanalysis

Djoirka M. Dimoune[1*], Fabrice Hernandez[1,2], and Moacyr Araujo[1,3]

[1]Laboratório de Oceanografia Física Estuarina e Costeira (LOFEC), Departamento de Oceanografia da Universidade Federal de Pernambuco (UFPE), Cidade Universitária, Avenida Arquitetura s/n, 50740-550 Recife, PE, Brasil.

[2]LEGOS, Université de Toulouse, CNES, CNRS, IRD, UPS (Toulouse), 18 avenue Edouard Belin, 31400 France.

[3]Brazilian Research Network on Global Climate Change (Rede CLIMA), Av. dos Astronautas, 1758, 01227-010 São José dos Campos, SP, Brazil.

*Corresponding author: Dimoune Djoirka Minto (pmintodimoune@gmail.com)

Abstract

Twenty-six years of the high-resolution global ocean reanalysis GLORYS12V1 are used to investigate the temporal and spatial variability of the two-core structure of the North Equatorial Counter Current (NECC) in the western and central tropical Atlantic. The two cores of the NECC exhibit mean positions of 6.3°N±1.4° and 9.7°N±1°, and of 5.4°N±1.1° and 8.9°N±0.9° respectively in the area west of 32°W and in the area between 32°W and 22°W. Both areas witness a semi-annual cycle of the position of the southern core with northernmost positions, respectively in May and July, and in March and July. The transport of the branch associated with the southern cores shows annual cycles with maxima occurring in August (>17 Sv) and July (>7 Sv), respectively, in the western and central areas. The annual cycle in the West is influenced by the wind stress curl (WSC) strength. The central area might be influenced by a return flow of the northern branch of the South Equatorial Current over the central Atlantic. On

the opposite, the NECC's northern core transport shows the same annual cycles, with maxima occurring in September in both areas. This NECC transport shows seasonal cycles led by the WSC strength with a 1-month lag. 83% and 71% of the total transport between the first 150 m-depth is above the thermocline respectively in the western and central areas. In the West, the northern core transport shows year-to-year variations associated with the WSC strength, while the southern core position of the NECC in the central tropical Atlantic appears influenced by the InterTropical Convergence Zone migration.

Introduction

In the tropical Atlantic (TA), one of the most important zonal surface currents is the North Equatorial Countercurrent (NECC), part of the complex TA wind-driven circulation. This current flows eastward between 3°-15°N across the basin, flanked by the North Equatorial Current (NEC) and the northern branch of the South Equatorial Current (nSEC) (Figure 1). In the west, it is fed at the surface by the retroflected branch of the North Brazil Current Retroflection (rNBC) and transports fresher and oxygen-rich waters, and heat from the western boundary to the northern and the eastern basin (Philander and Pacanowski,1986; Schott et al., 2004; Urbano et al., 2006; 2008; Castellanos et al., 2015; Varona et al., 2019). The North Equatorial Undercurrent (NEUC) also flows eastward underneath the NECC, fed by the subthermocline water from the rNBC, but is influenced by the waters from the nSEC, which are characterized by oxygen-poor waters (Burmeister et al., 2019). The NECC and the NEUC are well separated in the western TA during the first half of the year when the NEUC is stronger, especially during the boreal spring, and are completely merged below the thermocline surface during the second half of the year (Urbano et al., 2006).

To understand the seasonal variability of the TA circulation, many studies have been conducted so far to infer the NECC evolutions and their relationship with the wind's pattern variability. Garzoli and Katz (1983) analyzed the shallow water vorticity equation using historical hydrographic data and identified two main areas with different behaviors. Between 22°-42°W, the authors found that the NECC flow is in the Sverdrup balance. West of 42°W, this balance fails due to the importance of the nonlinear advective and local winds friction terms in the vorticity equation. In the first region, they found a delay of 1 to 2 months between the thermocline displacement and the wind stress curl (WSC) over the basin, which was explained by the influence of the westward propagating Rossby waves on the thermocline. Using numerical modeling, Verdy and Jochum (2005) confirm the importance of the nonlinear terms of the meridional and zonal advection of the mean flow and the eddies, which breaks down the

balance between the divergence of the Ekman pumping and the divergence of the geostrophic currents. They also found that this region is extended to 32°W (area 1: Gray square in Figure 1). Fonseca et al. (2004) and Urbano et al. (2006) confirmed this finding and showed that the NECC transport is approximately in Sverdrup balance but lags the WSC strength by 1 to 2 months. In particular, Urbano et al. (2006) used Acoustic Doppler Profilers (ADCP) and modeling at 35°W to investigate the two-core structure of the NECC previously mentioned by Schott and Böning (1991) and Didden and Schott (1992). They explained the one month lag found between the NECC's total transport from the surface to below the below thermocline and the "Sverdrup balance" transport at 35°W by the traveling time of the first mode baroclinic Rossby waves from the African coast to 35°W. Their results also showed that their model underestimates the NECC transports above the thermocline, overestimating a 1 to 2-month time lag. East of 32°W (area 2: Gray square in Figure 1), both Garzoli and Katz (1983) and Verdy and Jochum (2005) found that the nonlinear terms effects on the seasonal variability of the transport of the NECC are negligible.

The purpose of this study is to investigate the two-core structure of the Atlantic North Equatorial Countercurrent (NECC) and the associated transport of both cores above the thermocline in relation to the seasonal variability of the remote wind blowing in the eastern basin as considered by Fonseca et al. (2004), represented by the blue rectangle in Figure 1. However, they could not evidence any particular relationship at the interannual timescales due to the short 8-year available data period. Therefore, we propose to benefit from the longer time series (i.e., 1993-2018) provided by the state-of-art GLORYS12V1 global ocean reanalysis (G12V1) over the TA. This reanalysis has been proved to be globally realistic, particularly in the South Atlantic Ocean (e.g., Artana et al., 2018, 2019; Poli et al., 2020). To achieve our goal, areas 1 and 2 will be considered to investigate the influence of the wind fields on the NECC characteristics (branches and cores positions and associated transports).

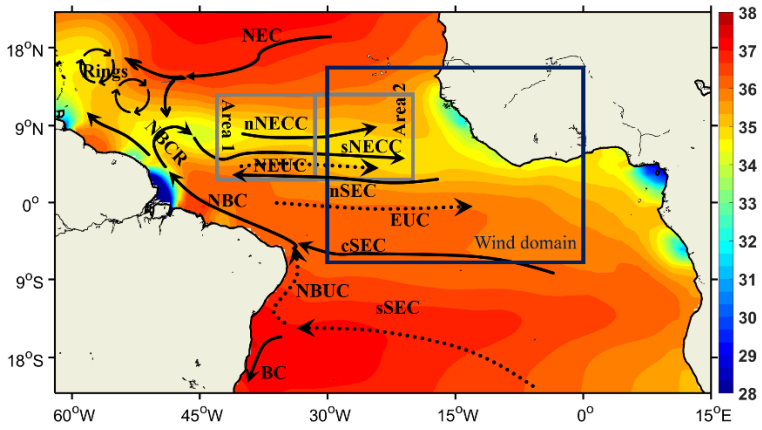

Figure 1. Mean Sea Surface Salinity (SSS) map for Sep-Oct-Nov averaged from 1993 to 2018 in the tropical Atlantic. Superimposed surface and thermocline currents (respectively thick solid and dashed black lines) in the study area based on John et al. (1990), Schott et al. (2004) and Halm et al. (2017): North Equatorial Current (NEC), North Equatorial Undercurrent (NEUC), North Equatorial Countercurrent (NECC), its northern branch (nNECC), Equatorial Undercurrent (EUC), southern, northern and central branches of the South Equatorial Current (sSEC, nSEC, cSEC), North Brazil Undercurrent (NBUC), North Brazil Current and its retroflection (respectively, NBC and NBCR), the rings shed during the NBCR; and Brazil Current (BC). The gray boxes define the region where the NECC parameters are calculated (area 1 and area 2); and the blue box define where the wind parameters are calculated. The SSS dataset used here is the CORA SSS reanalysis (INSITU_GLO_TS_OA_REP_OBSERVATIONS_013_002_b product) made available by Copernicus Marine Service (CMEMS) at https://resources.marine.copernicus.eu/products

1. Data and Methods

Three datasets are used in this study:

1) The G12V1 reanalysis of monthly zonal current components (product name GLOBAL_REANALYSIS_PHY-001-030) available at the Copernicus Marine Service (CMEMS: https://marine.copernicus.eu/), with a 1/12° horizontal grid resolution and 50 irregular vertical levels from the surface to the bottom ocean. This reanalysis, comprehensively detailed and validated at global scale by Lellouche et al. (2018; 2021) is based on a 1/12° high resolution global ocean configuration using the NEMO model forced by the ECMWF ERA-Interim wind reanalysis. Its realism is obtained through data assimilation of along-track altimeter sea level anomaly (SLA), satellite sea surface temperature (SST), satellite sea ice concentration, and in situ temperature and salinity (T/S) vertical profiles from the CORA database corrected from the slowly evolving large-scale biases in temperature and salinity (Madec, 2008; Cabanes et al., 2013; Good et al., 2013; Lellouche et al., 2018; 2021). Here, the zonal velocities have been extracted first in areas 1 (between 2°N– 15°N and 32°–42°W) and 2 (between 2°N– 15°N and 22°–32°W) over the 1993-2018 period. Then, they have been interpolated vertically with 1 m resolution, and finally, zonally averaged in each area.

2) The vertical profiles of G12V1 monthly temperature estimates have also been extracted and interpolated vertically with 1 m resolution, then zonally averaged in both areas. This allows computing the depth of the 21.5°C isotherm, usually considered the thermocline upper limit in the TA (e.g., Urbano et al., 2006).

3) The monthly surface wind velocity fields from ERA5 provided by the European Centre for Medium-Range Weather Forecasts (ECMWF, http://www.ecmwf.int) in 1/4° grid have also been used to investigate the influence of the wind on the NECC over the same period. Following Fonseca et al. (2004), the wind stress components are zonally averaged in a region bounded by 6°S– 16°N and 0°–30°W (Figure 1) and are used to calculate the WSC. Its strength is obtained by the difference between its maximum negative and positive values every month. The WSC is also used to find the location of the ITCZ, determined by the position of the WSC zero value, following Fonseca et al. (2004).

2. Characterization of the two-core structure of the NECC in the tropical Atlantic

To show the two-core structure of the NECC, we compute the zonal current monthly climatology of the NECC in area 1 (Figure 2) and area 2 (Figure 3), considering the 1993-2018 period. We distinguish near the surface over the year, one or two eastward branches of the NECC characterized by a vertical two-core structure, separated or not in both areas. The presence of the two-core structure in area 1 is consistent with Urbano et al. (2006). These NECC structures appear weaker in area 2, indicating that it weakens along their pathway. In area 1, the northern core of the NECC (nNECC) is permanent during the second half of the year, mostly from September to February; It appears fully separated from the southern core at the end of its cycle from December to February. For the rest of the year, the nNECC is only present some years. On the opposite, the sNECC is almost present all the year but is well established from October to December and from March to May when the nNECC is separated from the sNECC. The maximum (minimum) core velocity of the sNECC occurs in area 1 in October-November (May) with a value of 0.5 m/s (<0.1 m/s), while in the area 2, it occurs in June-July (March) with a value of 0.3 m/s (<0.05 m/s). In both areas, most of the NECC flows above the thermocline.

To characterize the two branches of the NECC associated with the two cores pattern, in order to calculate the transport associated with the branches (Figure 4), particularly when the flow weakens in area 2, we calculate the depth-average of the zonal velocity from the surface to the mean depth of the thermocline in both areas. The mean depth climatology (Figure 5c) exhibits

averaged values over the year of 91 m ± 5 in area 1, and 68 m ± 4 in area 2. The values in both areas are consistent with those found by Garzoli and Katz (1993). This method aims to identify in each depth-averaged horizontal profile of the current the limit between the sNECC and the nNECC branches which in practice is the position of the lowest local minimum between two highest positive local maxima. The position of the two highest positive local maxima represents, in this case, the core position of each core/branch. The NECC is considered a unique branch (sNECC) when the depth-average of the zonal velocity exhibits either only one positive local maximum or several positive local maxima and no local minima. The NECC presents two separated branches when the lowest local maximum is negative. This method helps to find the sNECC and the nNECC core positions and compute the transport of the branches associated with the cores of the NECC illustrated by figure 4 over the years. The zonal transports are calculated following Burmeister et al. (2019) as follows:

$$Tr = \int_{Di}^{Df} \int_{Zs}^{Z} U.d\,x.dz \qquad \text{(Equation 1)}$$

Where U is the eastward (positive velocity) flow; x is the latitude, converted into meters, and z is the depth of the water column, also in meters. Di and Df are respectively the lower and the higher latitude of U; and Zs and Z are respectively the reference depth at the surface, which is 0 m in this study, and the depth limit for calculating of the transport.

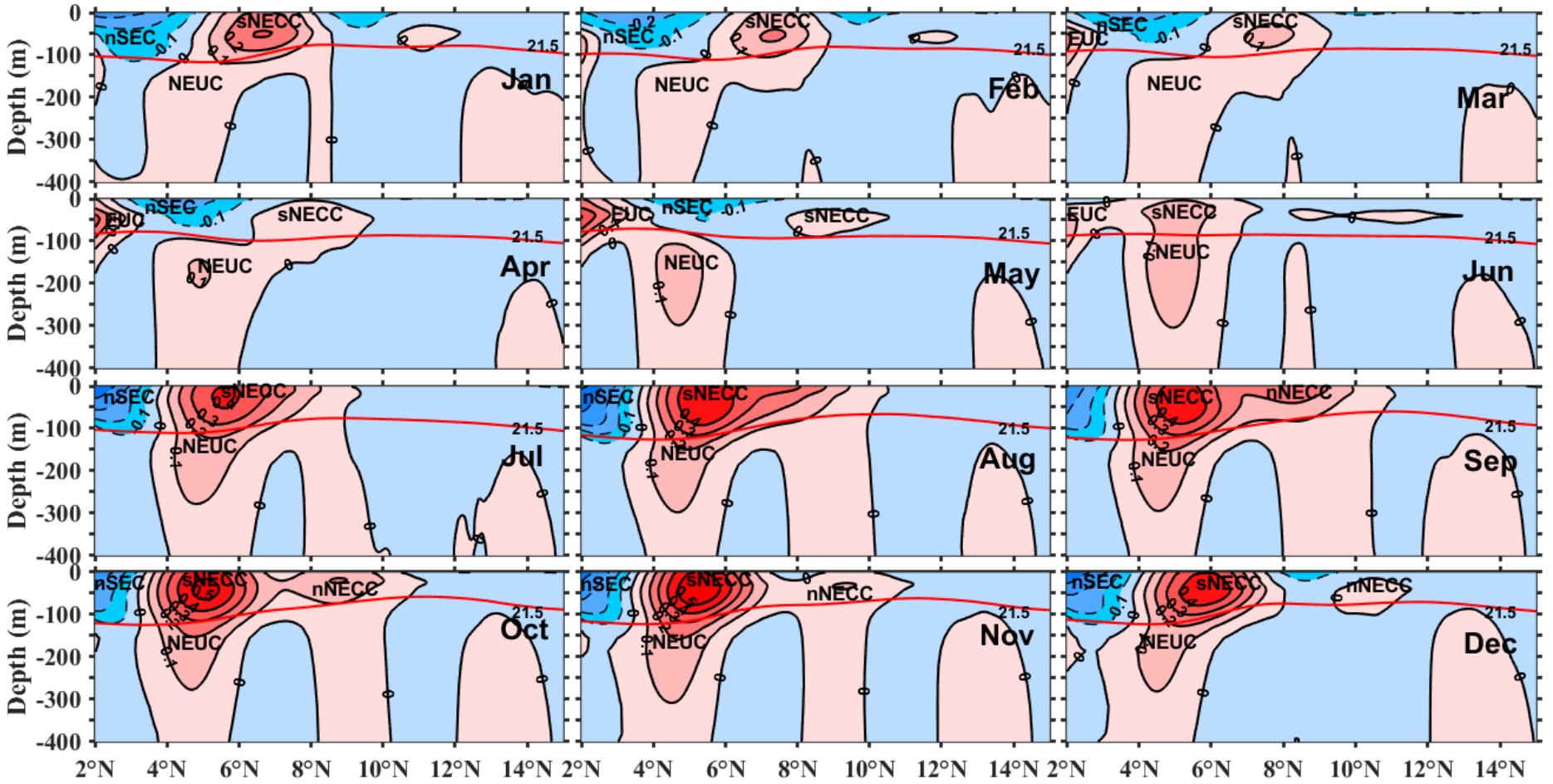

Figure 2. Monthly climatology of the meridional sections of G12V1 zonal velocity in area 1 (32°-42°W, 2°-15°N). The contour interval is 0.1 m/s, and dashed lines represent negative (westward) velocities also represented by the blue color. The red color represents the eastward velocities. The 21.5 °C isotherm is overlaid (red line) and represents TA thermocline upper limit.

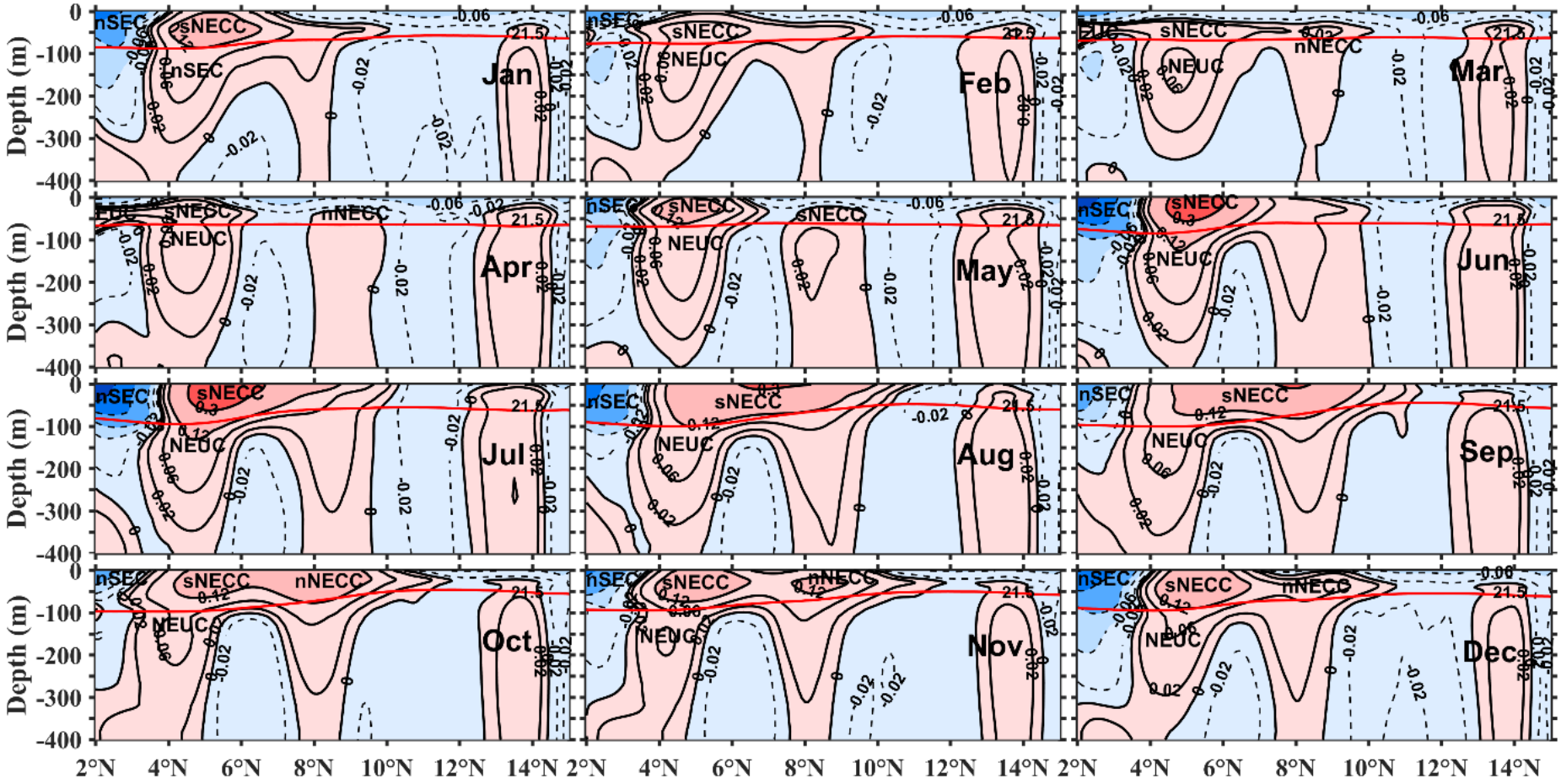

Figure 3. Monthly climatology of the meridional sections of G12V1 zonal velocity in area 1 (22°-32°W, 2°-15°N). The contour lines are irregular and represent isolines of the velocity of the currents. The dashed lines (blue color) represent negative (westward) velocities. The red colors show the eastward velocities. The 21.5 °C isotherm is overlaid (red line) and represents the TA thermocline upper limit.

3. Variability of the two cores of the NECC and their associated transports in areas 1 and 2

The time series of the positions of the NECC cores and their associated transport above the thermocline (Figure 4) show a strong seasonal variability, which is consistent with the variability of the tropical Atlantic (e.g., Garzoli and Katz, 1983; Garzoli and Richardson, 1989; Garzoli, 1992; Polonsky and Artamonov, 1997; Yang and Joyce, 2006). Figure 4 also showsyear-to-year variations. Our results show a larger NECC in area 1 than in area 2. Moreover, the mean location of the sNECC (nNECC) is at 6.3°N ± 1.4° (9.7°N ± 1°) in area 1, and 5.4°N ± 1.1° (8.9° ± 0.9°) in area 2. The sNECC (nNECC) core lies latitudinally between approximately 3.5°N (7.7°N) and 11.3°N (11.4°N) in area 1, and between 3.5°N (6.7°N) and 9.7°N (10.9°N) in area 2. Fonseca et al. (2004), who used 8 years of TOPEX/Poseidon altimeter-derived sea height anomaly and climatological hydrographic data, found the sNECC's core confined between 3°-10°N. Their methods for determining the NECC's location could not allow the identification of the northern core of the NECC, nor the core position of the weaker flow of the NECC between March and June. This might explain the difference in our results. The monthly climatology of NECC's core location (Figure 5 b and e) also does not show the two northernmost locations of the sNECC in February and August for both areas. Our results show in area 1 a slightly northward migration of the sNECC from June to July, leading to a northern core of the NECC that starts growing and migrating northward from August to February in area 1. After February, the nNECC flow is weaker and shallower, and the core becomes difficult to capture by our method in area 1. In area 2, the mean location of the nNECC varies slightly. The root mean square (rms) of the mean monthly location in both areas shows larger values for the nNECC than the sNECC. This shows that the core position for the nNECC is more significant than for the sNECC, which is consistent with Urbano et al. (2006). The northward migration of the sNECC is clearly shown in both areas, respectively, between November and May in area 1, and November and March in area 2.

Table 1. Percentage of the transport of the NECC's branches above the thermocline relatively to the transport above 150 m-depth

Percentage of transport above thermocline in area 1			Percentage of transport above thermocline in area 2		
sNECC	nNECC	NECC	sNECC	nNECC	NECC
84%	70%	83%	74%	62%	71%

Before the analysis of the time series of transport of the NECC branches above the thermocline, the transports above 150 m-depth has also been calculated considering that the core of the NEUC is deeper than 150 m-depth (e.g., Urbano et al., 2006) and its contribution to the NECC during the year is weaker above 150 m-depth. A comparison between the transports above the thermocline and above 150 m-depth (Table 1) shows higher percentages of transport above the thermocline in area 1 compared to area 2. The nNECC transport percentage above the thermocline is lower, with 70% in area 1 and 62% in area 2. It indicates that a more significant part (>30%) of the nNECC remains between the thermocline surface and the 150 m-depth. The percentages of the sNECC transport and the total transport show values higher than 80% and 70% respectively in area 1 and area 2 and confirm that the sNECC is the main contributor to the total NECC transport in both areas. This also shows that the more significant part of the NECC transport is above the thermocline. The correlations between both transports (Figure not shown) for the branches and the total flow show significant correlations with a coefficient greater than 0.99 and 0.97, respectively, in area 1 and area 2. This shows that transports above 150-m can be used to study the NECC and investigate mechanisms which drive its seasonal and interannual variability.

The analysis of the time series of the transports of the NECC branches above the thermocline (Figure 4a, i, d, and l) shows higher values as expected in area 1 compared to area 2. The transport of the sNECC (nNECC) varies from approximately 0 to 21 Sv (0 to 7.2 Sv) in area 1 compared to 0 to 11 Sv (0 to 8.3 Sv) in area 2. Maximum values of the sNECC transport in area 1, associated with locations of the core at about 5.4°N, usually occur during August, in good agreement with the Sverdrup transport proposed by Urbano et al. (2006). In area 2, we find an earlier maximum in July at about 5.3°N (Figures 5a and 5d). Maximum values of the nNECC transport in both areas occur in September, associated with locations of the cores at about 8.5°N. Overall, the NECC is weaker during the first half of the year. Then stronger during July and August for the sNECC and September for the nNECC. The rms values during the first half of the year witnessed the weak variability of the NECC, which is very weak or even disappears during this period.

The relationship between the transport and the location of the NECC's cores shows two different scenarios for area 1 and area 2 (Figures 4a, 4d, 5a, 5b, and 4i, 4l, 5d, 5e). In area 1, during the onset phase of the sNECC in June–July, the current witnesses an increase in its strength and location. The current shifts southward after while its strength continues to increase. The maximum strength of the sNECC occurs in August when the ITCZ reaches its northernmost

position. The sNECC remains about the same location until November. Then it moves northward again when the nNECC is about 9.8°N. In area 2, the onset phase of the sNECC starts in April-May. Its branch witnesses an increase in strength and location until July, followed by a decrease of both strength and location until October-November when the nNECC migrates northward. The onset phase of the nNECC transports in areas 1 and 2 are similar and starts between July and August, two months later than the onset of the sNECC in area 1. The maximum strength of the nNECC occurs in September, one month later than the northernmost position of the ITCZ in August, and decreases after when the nNECC is still moving northward.

The monthly anomalies relative to the monthly climatology of the NECC's location and the transport-associated to the corresponding cores do not show any persistent patterns or obvious correlation for the sNECC over the period investigated. However, the location and transport show significant anomalies relative to their climatological values during specific years. For example, the monthly anomalies of the sNECC location were atypically far north (south) in 1995 and 2009 (1996, 1999, and 2012), and the monthly anomalies of the sNECC transport were unusually strong (weak) in 1994, 1996, and 2017 (1995 and 2009). The strong anomalies between 1993 and 2000 were also found by Fonseca et al. (2004). In area 2, the correlation between the core position of the sNECC and the associated transport is higher than in area 1 (0.34). Between area 1 and area 2, some coincident anomalies are found for the transport of the sNECC during the years 1994, 1995, and 1996. The highest correlations are found between the nNECC's location and its cores associated transports (-0.41 and -0.60 for areas 1 and 2). The correlation of area 2 shows that strong (weak) nNECC indicates a southernmost (northernmost) location of its core. We remind the correlations mentioned above are significant with 95% of confidence level, performing the Student test.

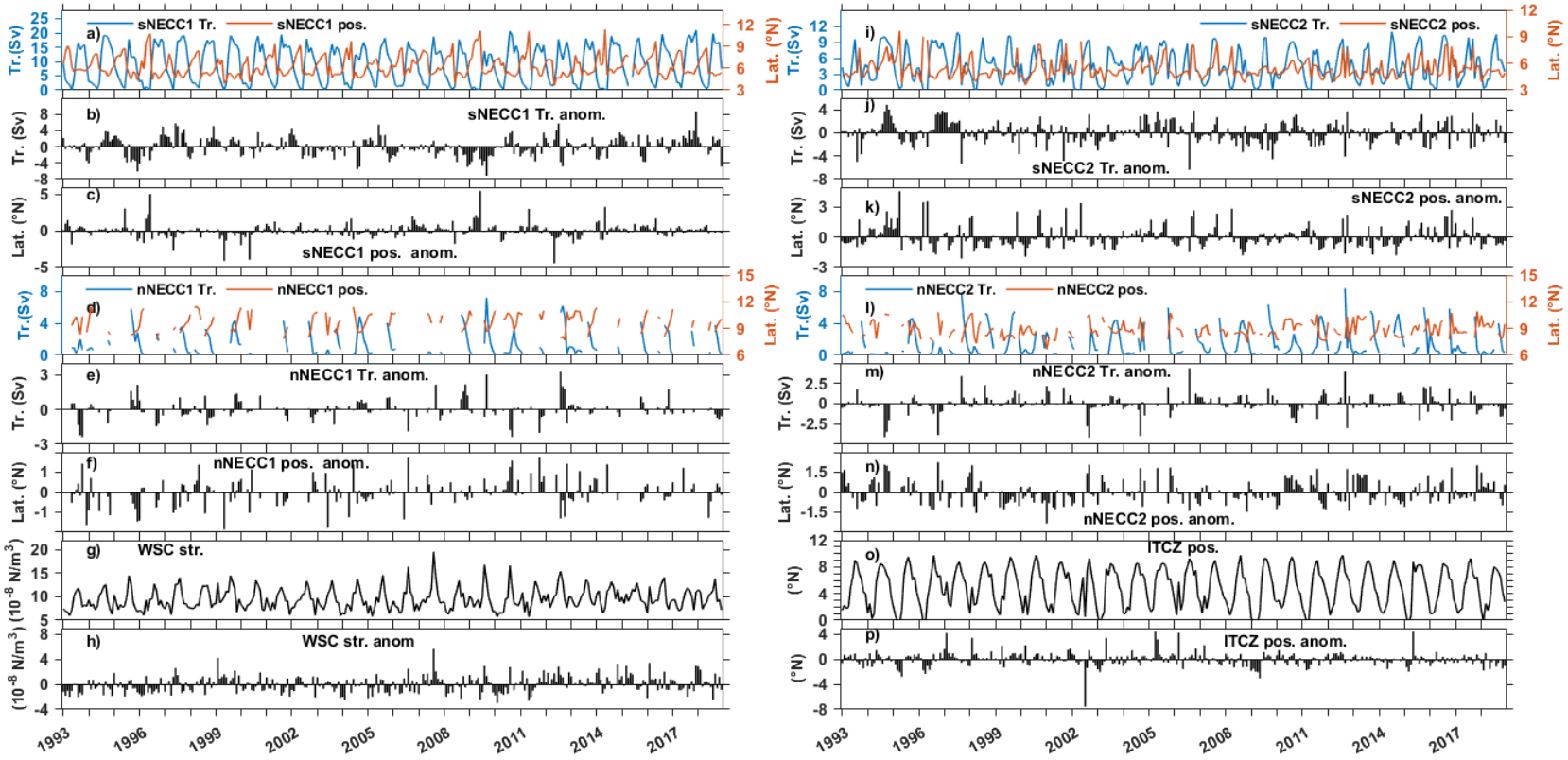

Figure 4. Time series of the core positions of the southern and northern branches of the North Equatorial Countercurrent (respectively, sNECC and nNECC), the transport above the thermocline associated to the cores and their anomalies in area 1 (first column: a-f) and in area 2 (second column: i-n), together with the time series of the wind stress curl (WSC) strength and the Intertropical Convergence Zone (ITCZ) position and their anomalies (respectively, g-h and o-p). (a and i) position of the sNECC core (orange line) and its associated transport (blue line) respectively, in area 1 and area2; (b and j) and (c and k) monthly anomalies of respectively, the position of the sNECC core and its associated transports in area 1 and area 2. (d and l) position of the nNECC core (orange line) and its associated transport (blue line) respectively,in area 1 and area2, (e and m) and (f and n) monthly anomalies of respectively,the position of the nNECC core and its associated transports in area 1 and area 2. (g and o) WSC strength and ITCZ position in the tropical Atlantic, respectively; and (h and p) their monthly anomalies.

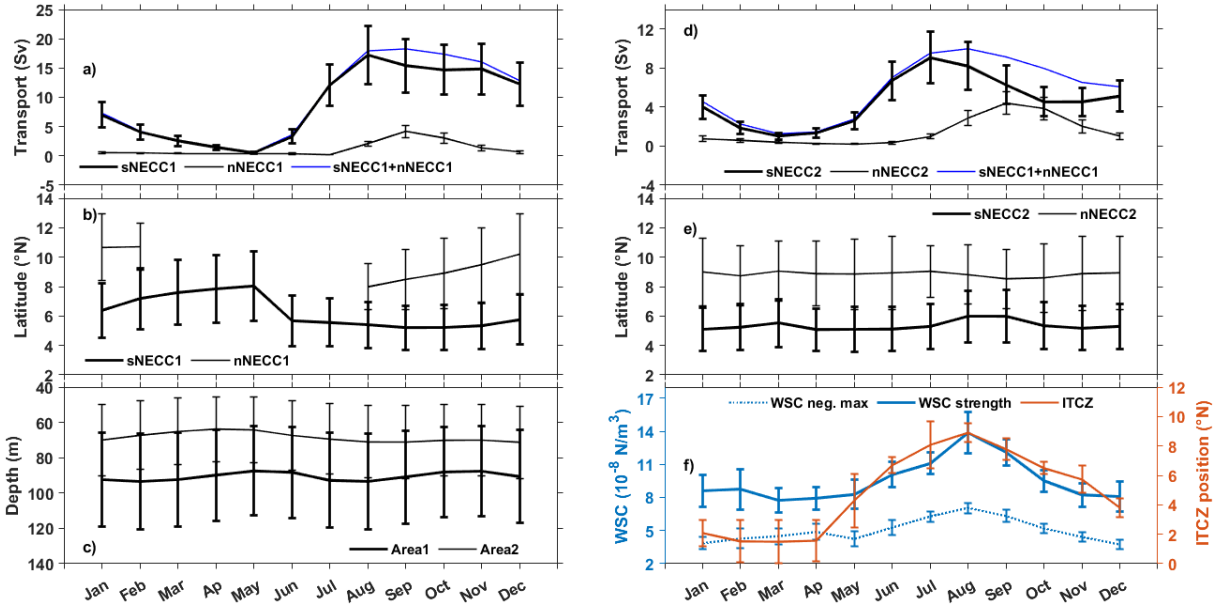

Figure 5. Monthly climatology from 1993 to 2018, of (a and d) the transport of the branches of the NECC, respectively in area 1 and area 2 (thick line: sNECC; thin line: nNECC and blue line: sum of both branches); (b and e) the position of the sNECC core (thick line) and the nNECC core (thin line), respectively in area 1 and area 2; (e) the mean depth of the thermocline in area 1 (thick line) and area 2 (thin line); and (f) the wind parameters: position of the ITCZ (orange line), WSC strength (thick blue line) and absolute value of the maximum in the negative WSC (thin blue line). The vertical bars indicate the root mean square values for each month.

4. Relationship between the NECC and the wind fields in area 1 and area 2

To investigate the relationship between the NECC and the wind in TA, the wind domain, shown in Figure 1, has been used to compute the minimum and maximum zonally averaged WSC. Then deduce the WSC strength as the difference between these maximum and minimum WSC values following Fonseca et al. (2004). The ITCZ has been identified as the location of the WSC zero value. As found by Fonseca et al. (2004), the annual cycle of the ITCZ varies between its northernmost location at 9°N in August and the southernmost location at 1°N in March. The WSC strength minimum is also found in March (Figure 5f). Unlike Fonseca et al. (2004), who found the peak of the maximum negative WSC in July, we found a peak in August, coinciding with the maximum WSC strength and the northernmost position of the ITCZ (Figure 5f). The difference with our result can be due to the short length of the time series considered for their studies or the errors in satellite data used.

In the TA, the NECC transport is related to the influence of both the positive WSC north of the ITCZ and the negative WSC south of the ITCZ, and by the way, their difference is represented

by the WSC strength (Fonseca et al., 2004). In area 1, the maximum total transport occurs in September (Figure 5a), and the minimum total transport occurs in May. The one to two-month lags of the NECC transport relative to the WSC strength cycle is consistent with expected delays due to Rossby wave propagation in the area (e.g., Garzoli and Katz, 1983, Urbano et al., 2006). The sNECC and nNECC transport peaks in August and September, respectively, show that the phase lag between the WSC strength and the thermocline occurs in the nNECC region.

In area 2, the total transport of the NECC follows exactly the cycle of the WSC strength with a minimum in March and maximum in August with no lag. However, the transport associated with the NECC branches shows different cycles with different maximum. The transport-associated to the sNECC grows from April and reaches its maximum in July, one month before the peak of the WSC strength. Rosell-Fieschi et al. (2015) show that from April to July-August, the NECC is fed by an eastward retroflected branch of the nSEC which reaches its maximum during June-July in the central Atlantic and follows the ITCZ displacement. Burmeister et al. (2019) also show that the NEUC is supplied by the nSEC during this period and strengthens when the thermocline is shoaling (Xie & Carton, 2004). This means that the transport of the sNECC in area 2 should be influenced by the nSEC and the NEUC. In Figure 3, the uniform flow reaching the surface in April strengthens later, then migrates northward should be composed of a mixture of the nSEC eastward recirculating branch and the NEUC. The nNECC transport shows the same seasonal cycle for area 1, which confirms our findings that the phase lag between the WSC strength and the thermocline occurs in the region of its branching in the TA. The one-month lag delay in area 2 is consistent with Garzoli and Katz (1983) and Urbano et al. (2006) findings.

The July-August northernmost location of the sNECC in both areas (Figure 5b and 5e) coincides with the northernmost location of the ITCZ. Fonseca et al. (2004) found the same results. This suggests that the location of the sNECC during March-August is wind-driven. This confirms previous findings of Richardson and McKee (1984), Richardson and Reverdin (1987), Garzoli and Richardson (1989). Furthermore, the northward migration of the sNECC is consistent with Urbano et al. (2008) that found during this period a presence of zero line of the WSC north of 10°N that should influence this migration. Therefore, we assume that the northward migration of the nNECC from August to February should be due to the same mechanism, primarily in area 1.

At interannual timescales, correlations between the WSC strength monthly anomalies of the ITCZ and the monthly anomalies of the location of the NECC cores and the associated transports are not significant. Thus, to investigate the influence of the maximum WSC strength and the NECC's northernmost position due to the ITCZ, we performed a 3-month running mean of the maximum values of the WSC and the highest positions of the ITCZ for each year. They were correlated with the 3-month running averages of the locations of the cores and their associated transport. Correlations were significant only for nNECC, which shows a 0.52 correlation between its associated transport and the WSC strength in area 1 during September; and -0.59 between its core location and the ITCZ in June. This means that, on interannual timescales, the variability of the nNECC's location and its associated core transport might be related to the variability of the wind fields. The result opens the door for future investigations to infer the possible mechanisms that drive the two-core structure of the NECC and their associated transport on interannual timescales.

Conclusion

This study using the GLORYS12V1 reanalysis, aims to re-visit the variability of the location of both cores of the NECC and their associated transport in relation to the wind fields blowing over the Tropical Atlantic. We found that G12V1 represents the NECC system consistent with previous studies of Garzoli and Katz (1983). In the past, Urbano et al. (2006) showed inconsistency between the NECC transport estimated from their model and a transport that would be solely due to ocean circulation response to the wind forcing using the Sverdrup balance. We found here that G12V1 NECC transport seasonal cycle does not present this inconsistency. It appears that this is caused by an underestimation of the NECC transport above the thermocline.

Our results also show the importance of considering the second core/branch of the NECC, the wind fields' influence on the entire NECC system at the seasonal timescales, and mainly on the nNECC on the interannual timescales. However, some investigations still need to be made, especially on interannual timescales. For example, Góes and Wainer (2003) used numerical modeling results to show that the long period wind variability was linked to warm and cold events in the tropical Atlantic which impacted the strength of the tropical Atlantic circulation. Recently, Hormann et al. (2012) used altimetry data in the tropical Atlantic to show the influence of the Atlantic zonal mode on the NECC strength and the meridional mode on its

location. Therefore, future studies might investigate the variability of the NECC two-core structures with the tropical Atlantic modes. In addition, specific vessel measured sections can also be used in the NECC regions to understand better the NECC's behavior at the seasonal and interannual timescales.

Acknowledgements

We are grateful to the CMEMS and the ECMWF who made available the ocean reanalysis, and the mean wind fields for this work. We are also thankful to CAPES Foundation. Fabrice Hernandez supervised this work as part of the TAPIOCA Laboratoire Mixte International funded by IRD and CAPES/MEC in Brazil. Moacyr Araujo thanks the support of the Brazilian Research Network on Global Climate Change FINEP/Rede CLIMA (grants 01.13.0353-00). This work has been supported by the French LEFE/GMMC funded project Merca2Recife (42-DS-GMMC-MERCA2RECIFE – REF. CNRS N° 197932) and represents a contribution to the INCT AmbTropic, the Brazilian National Institute of Science and Technology for Tropical Marine Environments, CNPq/FAPESB (grants 565054/2010-4 and 8936/2011 and 465634/2014-1), and to the TRIATLAS project, which has received funding from the European Union's Horizon 2020 research and innovation program under grant agreement No 817578.

References

Artana, C., Lellouche, J.-M., Sennéchael, N., & Provost, C. (2018). The Open-Ocean Side of the Malvinas Current in Argo Floats and 24 Years of Mercator Ocean High-Resolution (1/12) Physical Reanalysis. *Journal of Geophysical Research: Oceans*, 123(11), 8489–8507. doi:10.1029/2018jc014528.

Artana, C., Provost, C., Lellouche, J., Rio, M., Ferrari, R., & Sennéchael, N. (2019). The Malvinas Current at the Confluence With the Brazil Current: Inferences From 25 Years of Mercator Ocean reanalysis. *Journal of Geophysical Research: Oceans*. doi:10.1029/2019jc015289.

Burmeister K., Lübbecke, J. F.,Brandt, P., & Duteil, O. (2019). Interannual variability of the Atlantic North Equatorial Undercurrent and its impact on oxygen. *Journal of Geophysical Research: Oceans*, 124, 2348–2373. https://doi.org/10.1029/2018JC014760

Cabanes, C., Grouazel, A., von Schuckmann, K., Hamon, M., Turpin, V., Coatanoan, C., et al. (2013). The CORA dataset: validation and diagnostics of in-situ ocean temperature and salinity measurements. *Ocean Science*, 9 (1), 1-18. doi: 10.5194/os-9-1-2013.

Castellanos, P., Pelegrí, J. L., Campos, E. J. D., Rosell-Fieschi, M., & Gasser, M. (2015). Response of the surface tropical Atlantic Ocean to wind forcing. *Progress in Oceanography*, 134271-292. doi: 10.1016/j.pocean.2015.02.005.

Didden, N., & Schott, F. (1992). Seasonal variations in the western tropical Atlantic: Surface circulation from Geosat altimetry and WOCE model results. *Journal of Geophysical Research: Oceans*, 97 (C3), 3529-3541. doi: 10.1029/91jc02860.

Fonseca, C. A., Goni, G. J., Johns, W. E., & Campos, E. J. D. (2004). Investigation of the North Brazil Current retroflection and North Equatorial Countercurrent variability. *Geophysical Research Letters*, 31 (21). doi: 10.1029/2004gl020054.

Garzoli, S. L., & Katz, E. J. (1983). The Forced Annual Reversal of the Atlantic North Equatorial Countercurrent. *Journal of Physical Oceanography*, 13 (11), 2082-2090. doi: 10.1175/1520-0485(1983)013<2082:Tfarot>2.0.Co;2.

Garzoli, S., & Richardson, P. L. (1989). Low-frequency meandering of the Atlantic North Equatorial Countercurrent. *Journal of Geophysical Research: Oceans*, 94 (C2), 2079-2090. doi: 10.1029/JC094iC02p02079.

Garzoli, S. L. (1992). The Atlantic North Equatorial Countercurrent: Models and observations. *Journal of Geophysical Research: Oceans*, 97 (C11), 17931-17946. doi: 10.1029/92jc01363.

Goes, M. P., and Wainer, I. (2003). Equatorial currents transport changes for extreme warm and cold events in the Atlantic Ocean Equatorial currents transport changes for extreme warm and cold events in the Atlantic Ocean, (March), 2–6. https://doi.org/10.1029/2002GL015707

Good, S. A., Martin, M. J., & Rayner, N. A. (2013). EN4: Quality controlled ocean temperature and salinity profiles and monthly objective analyses with uncertainty estimates. *Journal of Geophysical Research: Oceans*, 118 (12), 6704-6716. doi: 10.1002/2013jc009067.

Hahn, J., Brandt, P., Schmidtko, S., & Krahmann, G. (2017). *Decadal oxygen change in the eastern tropical North Atlantic. Ocean Science, 13(4), 551–576.* doi:10.5194/os-13-551-2017

Hormann, V., Lumpkin, R., & Foltz, G. R. (2012). Interannual North Equatorial Countercurrent variability and its relation to tropical Atlantic climate modes. *Journal of Geophysical Research: Oceans*, 117 (C4). doi: 10.1029/2011jc007697.

Johns, W. E., Lee, T. N., Schott, F. A., Zantopp, R. J., & Evans, R. H. (1990). The North Brazil Current retroflection: Seasonal structure and eddy variability. *Journal of Geophysical Research*, 95(C12), 22103. doi:10.1029/jc095ic12p22103 Lellouche, J.-M., Greiner, E., Le Galloudec, O., Garric, G., Regnier, C., Drevillon, M., et al. (2018). Recent updates to the Copernicus Marine Service global ocean monitoring and forecasting real-time 1⁄12° high-resolution system. *Ocean Science,* 14 (5), 1093-1126. doi: 10.5194/os-14-1093-2018.

Lellouche, J.-M., Greiner, E., Bourdallé-Badie, R., Garric, G., Melet, A., Drévillon, M., et al. (2021). The Copernicus Global 1/12° Oceanic and Sea Ice GLORYS12 Reanalysis. *Frontiers in Earth Science*, 9 (585). doi: 10.3389/feart.2021.698876.

Madec, G. (2008): NEMO ocean engine - Version 3.1. Note du Pôle de modélisation, (27), edited by Institut Pierre-Simon Laplace (IPSL), Paris, France1288-1619, 201 pp

Philander, S. G. H., & Pacanowski, R. C. (1986). The mass and heat budget in a model of the tropical Atlantic Ocean. *Journal of Geophysical Research: Oceans*, 91 (C12), 14212-14220. doi: 10.1029/JC091iC12p14212.

Poli, L., Artana, C., Provost, C., Sirven, J., Sennéchael, N., Cuypers, Y., & Lellouche, J. (2020). Anatomy of subinertial waves along the Patagonian shelf break in a 1/12° global operational model. *Journal of Geophysical Research: Oceans*. doi:10.1029/2020jc016549.

Polonsky, A. B., and Y. V. Artamonov (1997), North Equatorial Counter- current in the tropical Atlantic: Multi-jet structure and seasonal variability, *Ocean Dynamics*, 49, 477–495. doi: 10.1007/bf02764342.

Richardson, P. L., and T. K. McKee (1984), Average seasonal variation of the Atlantic equatorial currents from historical ship-drifts, *Journal of Physical Oceanography*, 14, 1226–1238. Doi: 10.1175/1520-0485(**1984**)014<1226:ASVOTA>2.0.CO;2.

Richardson, P. L., & Reverdin, G. (1987). Seasonal cycle of velocity in the Atlantic North Equatorial Countercurrent as measured by surface drifters, current meters, and ship drifts. *Journal of Geophysical Research: Oceans*, 92 (C4), 3691-3708. doi: 10.1029/JC092iC04p03691.

Rosell-Fieschi, M., Pelegrí, J.L., Gourrion, J. (2015). Zonal jets in the equatorial Atlantic Ocean. Progress in Oceanography 130, 1–18. doi: 10.1007/bf02764342.

Schott, F. A., & Böning C. W. (1991). The WOCE model in the western equatorial Atlantic: Upper layer circulation. *Journal of Geophysical Research: Oceans*, 96 (C4), 6993-7004. doi: 10.1029/90jc02683.

Schott, F.A., McCreary, J.P., Johnson, G.C. (2004). Shallow overturning circulations of the tropical–subtropical oceans. In: Wang, C., Carton, J., Xie, S.-P. (Eds.), Ocean–Atmosphere Interaction and Climate Variability. AGU, Washington, pp. 261– 304.

Urbano, D. F., Jochum, M., & da Silveira, I. C. A. (2006). Rediscovering the second core of the Atlantic NECC. *Ocean Modelling*, 12 (1), 1-15. doi: 10.1016/j.ocemod.2005.04.003.

Urbano, D. F., De Almeida, R. A. F., & Nobre, P. (2008). Equatorial Undercurrent and North Equatorial Countercurrent at 38°W: A new perspective from direct velocity data. *Journal of Geophysical Research: Oceans*, 113 (C4). doi: 10.1029/2007jc004215.

Varona, H. L., Veleda, D., Silva, M., Cintra, M., & Araujo, M. (2019). Amazon River plume influence on Western Tropical Atlantic dynamic variability. *Dynamics of Atmospheres and Oceans*, (85) 1-15. doi: 10.1016/j.dynatmoce.2018.10.002.

Verdy, A., & Jochum, M. (2005). A note on the validity of the Sverdrup balance in the Atlantic North Equatorial Countercurrent. *Deep Sea Research Part I: Oceanographic Research Papers*, 52 (1), 179-188. doi: 10.1016/j.dsr.2004.05.014.

Xie, S., & Carton, J. (2004). Tropical Atlantic variability: Patterns, mechanisms, and impacts. *Geophysical Monograph Series*, 147, 121–142. https://doi.org/10.1029/147GM07

Yang, J., and T. M. Joyce (2006), Local and equatorial forcing of seasonal variations of the North Equatorial Countercurrent in the Atlantic Ocean, J. *Journal of Physical Oceanography*, 36, 238–254. doi: 10.1175/JPO2848.1